

This item was submitted to Loughborough University as a PhD thesis by the author and is made available in the Institutional Repository (<https://dspace.lboro.ac.uk/>) under the following Creative Commons Licence conditions.



For the full text of this licence, please go to:  
<http://creativecommons.org/licenses/by-nc-nd/2.5/>



University Library

Author/Filing Title CASAS-RODRIGUEZ, J. P.

Class Mark T

Please note that fines are charged on ALL  
overdue items.

--	--	--

0403819350







# Damage in adhesively bonded joints: sinusoidal and impact fatigue

by


Juan Pablo Casas Rodríguez

*A Doctoral Thesis  
Submitted in partial fulfilment of the requirements  
for the Award of  
Doctor of Philosophy of Loughborough University*

Wolfson School of Mechanical and Manufacturing Engineering

December 2008

© by Casas-Rodríguez, J.P. 2008

 Lancashire County Council Public Library
Date 12/12/09
Class T
Acc No. 0403219350

## Abstract

The main aim of this research was to investigate the behaviour of adhesive joints exposed to repeated low-velocity impact i.e. *impact fatigue* (IF), and to compare this loading regime with standard fatigue (SF), i.e. non-impacting, constant amplitude, sinusoidal loading conditions. Two types of lap joint configuration using rubber toughened modified epoxy adhesives were used and exposed to various loading conditions in order to determine the fatigue behaviour of the joints for each load conditions.

The fatigue life was investigated using bonded aluminium alloy (7075-T6) single lap joint (SLJ) specimens, where it was seen that IF is an extremely damaging load regime compared to SF. Different trends were visible in force-life plots for these two types of loading. In SF a gradual decrease in the fatigue life with increasing load was observed, whereas, in IF a significant decrease in life was seen at relatively modest levels of maximum force after relatively few cycles. Comparisons of the fatigue life show a considerably earlier failure in IF than in SF for comparable levels of force and energy. Additionally, it was demonstrated that the maximum force per cycle, loading time, stiffness and strength decreased as a result of damage generated in the sample during IF.

Fatigue crack growth was investigated using bonded carbon fibre reinforced polymeric (CFRP) lap strap joints (LSJs). It was seen that IF had the potential to initiate a crack and to cause its rapid propagation at levels of loading that were significantly lower than quasi-static and dynamic strengths and even the fatigue durability of joints. Two typical patterns of failure were seen; a cohesive failure in the adhesive, which was related to slow fatigue crack growth, and a mixed-mechanism failure that was associated with fast fatigue crack growth. It was also seen that a change in the mechanism pattern of failure from cohesive to the mixed-mechanism fracture acted an accelerator of the crack growth in specimens tested in SF. In IF a mixed-mechanism path was seen in all samples tested. Differences between IF and SF were also seen with regard to the crack speed. It was found that in the initial stages of the crack propagation, the crack rate was 10 times higher in IF than in SF. It was

found that the introduction of a relatively small number of in-plane impacts between blocks of SF drastically changed the dynamics of fracture in the specimen, with the IF blocks having a damage accelerating effect. It was also observed that the toughening mechanism of the rubber particles present in the adhesive was affected by cyclic in-plane impacting. The rapid crack growth in the adhesive associated with IF was characterised by a lack of rubber particle cavitation.

Various methods of cracking and predicting IF have been proposed and compared with the experimental data. It was seen that impact energy was a linear function of the logarithm of cycles to failure in IF, when failure mechanism was taken into account. In addition, the *modified load-time model* and the *normalized load-time model* were proposed; these proved to be suitable for characterization of IF in adhesively bonded joints. The first model relates the total cumulative loading time of the primary tensile load wave to the mean maximum force. The second model attempts to characterise sample damage under IF by relating the maximum force normalised with respect to initial maximum force to the accumulated loading time normalised with respect to the total accumulated loading time. Furthermore, changes in specimen stiffness during IF and SF were represented by a sigmoidal curve, which could be used to predict the percentage of the fatigue life.

The fatigue crack growth rate curve was seen to be a valid representation of fatigue propagation under SF and IF, where a combination of experimental data and finite element analysis (FEA) enable the curve to be constructed. It was seen that the curve shows a normal fatigue relation shape with clearly distinction of a linear and critical regions. It was concluded that this curve can be used to analyse crack propagation in IF and also in SF.

It was seen that the back face strain (BFS) technique could be used to monitor crack growth in LSJs in both SF and IF, however, the location of the gauge is critical, with the best location being on the strap adherend and placed along the length at the position in which the greatest accuracy is required. Ideally, a series of crack gauges along the length of the strap should be used. It was also seen that semiconductor strain gauges should be used rather than a standard electrical resistance gauge, both for

noise suppression and to achieve the high sampling rates needed to characterise the strain response during impact.

Changes of the fracture mechanism in specimens were modelled by the mixed mechanism fracture model (MMFM), which represented the experimentally observed acceleration of fatigue crack growth rate when the cracks path changes.

A damage shift model in conjunction with the numerical crack growth integration technique was proposed to analyse combined impact and standard fatigue (CISF). This proved to be a suitable technique to account damage for the zone ahead of the main crack tip produced by small blocks of IF.

## **Keywords**

Fatigue, adhesives, impact fatigue, high load rate, CFRP, Damage tolerance, Fracture mechanics



## Acknowledgements

The author gratefully acknowledges Dr I.A. Ashcroft for his support, encouragement, knowledge, friendship and overall patience over the entire project. At the same level the author wants to thank Prof. V. Silberschmidt for his faith, assistance, knowledge, understanding and motivation through the entire project. Both give the confidence to enrich my academic and personal life in so many aspects that I wish to be reflected in so many aspects of my life.

The author is grateful to all staff and research students of Wolfson School of Mechanical and Manufacturing Engineering, Loughborough University especially at to technicians that have been extremely friendly, making my life comfortable inside the department; at Dr. Diana Segura and Miss Lina Huertas for being like my family here in the UK; at Mr Vikram Shenoy and Mr. Aamir Mubashar, for those wonderful fundamental conversations that sometimes we had.

Additionally, the author would like to thank Dr Lucas F. M. da Silva and Dr G. Critchlow for their efforts as external and internal examiners respectively.

Finally, the author would like to dedicate this work at my relatives that always were there helping and supporting me during this time; my mother, my father and Veronica.

## Publications

1. Casas-Rodriguez JP, Ashcroft IA and Silberschmidt VV, *Propagation of delamination zones in bonded joints*, Proc. Estonian Acad. Sci., 56 (2007) 170-176. ISSN 1406-0086.
2. Casas-Rodriguez JP, Ashcroft IA and Silberschmidt VV, *Effect of impact-fatigue on damage in adhesive joints*, Key Eng. Mat., 347 (2007) 653-658. ISSN 1013-9826.
3. Casas-Rodriguez JP, Ashcroft IA and Silberschmidt VV, *Damage evolution in adhesive joints subjected to impact fatigue*, J. Sound Vib 308 (2007) 467-478.
4. Silberschmidt VV, Casas-Rodriguez JP and Ashcroft IA, *Impact fatigue of adhesive joints*, Key Eng Mat 399 (2009) 71-78.
5. Casas-Rodriguez JP, Ashcroft IA and Silberschmidt VV, *Delamination in adhesively bonded CFRP joints: standard fatigue, impact fatigue and intermittent impact*. Comp. Sci. Technol. 68 (2008) 2401-2409.
6. Casas-Rodriguez JP, Ashcroft IA and Silberschmidt VV, *Damage in adhesively bonded CFRP joints: sinusoidal and impact fatigue*, Comp. Sci. Technol. 68 (2008) 2663-2670.
7. Silberschmidt VV, Casas-Rodriguez JP and Ashcroft IA, *Impact fatigue in adhesive joints*, J. Mech. Eng. Sci., 222 (2008) 1981-1994.
8. Ashcroft IA, Casas-Rodriguez JP and Silberschmidt VV, *Mixed mode crack growth in bonded composite joints under standard and impact fatigue loading*, J. Mat. Sci., 43 (2008) 6704-6713.

# Table of contents

<b>Acknowledgements .....</b>	<b>iv</b>
<b>Publications.....</b>	<b>v</b>
<b>Abbreviations.....</b>	<b>xviii</b>
<b>CHAPTER 1 Introduction.....</b>	<b>1</b>
1.1. Background .....	1
1.2. Aim of the research .....	4
1.3. Research objectives .....	4
1.4. Outline of the thesis.....	5
<b>CHAPTER 2 Fatigue in adhesive joints .....</b>	<b>7</b>
2.1. Introduction.....	7
2.2. Theoretical considerations .....	9
2.2.1 Basic concepts of fracture mechanics .....	9
2.2.2 Numerical methods for fracture mechanics.....	14
2.3. Effect of joint geometry.....	17
2.3.1 Single lap joint.....	19
2.3.2 Lap strap joint .....	20
2.4. General consideration of fatigue .....	23
2.4.1 Constant amplitude fatigue .....	23
2.4.2 Variable Amplitude fatigue .....	24
2.5. Fatigue models .....	24
2.5.1 Phenomenological models.....	25
2.5.2 Fatigue crack growth rate curve approach.....	35
2.6. Discussion.....	42
2.7. Conclusions.....	42
<b>CHAPTER 3 Impact fatigue .....</b>	<b>43</b>
3.1. Introduction.....	43
3.2. Impact tests .....	45
3.3. Impact in composites.....	47
3.3.1 FRPC under a impact .....	48
3.3.2 FRPC under impact and fatigue.....	50
3.3.3 Modelling impacts in FRPC .....	52

3.4. Impact in polymers.....	53
3.5. Impact in adhesives .....	56
3.5.1 Adhesives under an impact.....	56
3.5.2 Adhesives under impact fatigue.....	58
3.5.3 Modelling impacts in adhesives.....	59
3.6. Phenomenological models of impact fatigue.....	60
3.6.1 Fatigue life.....	61
3.6.2 Accumulated load-time model.....	61
3.7. Summary.....	62
CHAPTER 4 Material and Experimental techniques .....	64
4.1. Introduction.....	64
4.2. Materials .....	65
4.2.1 Composite adherends .....	65
4.2.2 Aluminium adherends .....	66
4.2.3 Adhesives.....	67
4.3. Adhesive material properties .....	67
4.3.1 Bulk adhesive sample manufacture.....	67
4.3.2 FM-73M material properties.....	68
4.3.3 Material properties of EA 9628-UNS .....	70
4.4. Surface preparation .....	71
4.5. Adhesive joint configuration .....	72
4.5.1 Single Lap Joints.....	72
4.5.2 Lap Strap Joints.....	74
4.6. Experimental Test Procedures .....	76
4.6.1 Quasi-static (Qs) testing .....	76
4.6.2 Standard fatigue (SF) .....	76
4.6.3 Impact fatigue (IF) .....	77
4.6.4 Combined impact and standard fatigue (CISF) .....	80
4.7. Crack growth measurements.....	80
4.7.1 Optical measurements .....	81
4.7.2 Crack gauge and Fractomat system.....	82
4.7.3 Backface strain.....	82
4.7.4 Comparison between crack gauge and optical measurements.....	84
4.8. Fatigue crack growth rate .....	85

4.9. Fractography .....	86
4.10. Summary.....	86
CHAPTER 5 Finite Element Modelling Methods .....	87
5.1. Introduction.....	87
5.2. Development of quasi-static model.....	87
5.2.1 Material.....	88
5.2.2 Geometry and Boundary conditions.....	88
5.2.3 Element choice.....	89
5.2.4 Mesh convergence.....	90
5.2.5 Geometrical consideration.....	94
5.2.6 Specimen size differences .....	95
5.2.7 Back face strain gauge in LSJs .....	97
5.3. Development of dynamic model.....	98
5.3.1 Dynamics of single impact .....	99
5.3.2 Support calibration.....	103
5.3.3 Impact in LSJ without crack.....	106
5.4. Model to determine the strain energy release rate .....	108
5.4.1 Quasi-static model.....	109
5.4.2 Dynamic model.....	111
5.5. Summary.....	112
CHAPTER 6 Quasi-static testing and fatigue life of aluminium bonded single lap joints .....	113
6.1. Introduction.....	113
6.2. Quasi-static testing of SLJs .....	114
6.2.1 Test results.....	114
6.2.2 Fracture surface.....	114
6.2.3 Discussion.....	118
6.3. Fatigue life of SLJs in SF .....	119
6.3.1 Test results.....	119
6.3.2 Examination of fracture surface.....	124
6.3.3 Discussion of SF .....	127
6.4. Fatigue life of SLJs in IF .....	128
6.4.1 Test results.....	128
6.4.2 Examination of fracture surfaces .....	135

6.4.3 Repeatability of impact fatigue data .....	138
6.4.4 Discussion of IF .....	140
6.5. Comparison of IF and SF .....	140
6.6. Conclusions .....	142
CHAPTER 7 Quasi-static and fatigue crack growth in bonded CFRP lap strap joints .....	143
7.1. Introduction .....	143
7.2. Quasi-static testing of LSJs .....	144
7.3. Fatigue crack growth in LSJs during SF .....	145
7.3.1 Fatigue crack growth in LSJ <sub>long</sub> specimens .....	145
7.3.2 Fatigue crack growth of LSJ <sub>short</sub> specimens in SF .....	150
7.3.3 Discussion of FCG in SF .....	155
7.4. Fatigue crack growth of short LSJ in IF .....	156
7.4.1 Fatigue crack growth .....	156
7.4.2 Examination of fracture surfaces .....	159
7.5. Fatigue crack growth in LSJ short specimens in CIFS .....	165
7.5.1 Fatigue crack growth .....	165
7.5.2 Examination of fracture surfaces .....	166
7.5.3 Discussion of FCG during CIFS .....	169
7.6. Discussion .....	169
7.7. Conclusions .....	172
CHAPTER 8 Predicting Fatigue in adhesively bonded joints under Standard and Impact fatigue .....	174
8.1. Introduction .....	174
8.2. Phenomenological models .....	175
8.2.1 Energy-life approach .....	175
8.2.2 Stiffness degradation model .....	176
8.2.3 The modified load-time model .....	178
8.2.4 The normalized load-time model .....	180
8.3. Fatigue crack growth approach .....	181
8.3.1 Fracture mechanics in LSJs .....	181
8.3.2 Fatigue crack growth rate curves in LSJs .....	186
8.3.3 Mixed mechanism fracture model (MMFM) .....	189
8.4. Numerical crack growth integration .....	192

8.4.1 Cohesive failure during SF .....	192
8.4.2 CISF .....	192
8.5. Discussion.....	198
8.6. Conclusions.....	200
CHAPTER 9 Discussion.....	202
9.1. General.....	202
9.2. Experimental techniques.....	203
9.3. Fatigue life in aluminium bonded SLJ .....	203
9.3.1 Standard fatigue .....	203
9.3.2 Impact fatigue .....	204
9.4. Fatigue crack growth in lap strap joints .....	204
9.5. Modelling SF, IF and CISF .....	206
9.5.1 Modelling impact fatigue .....	206
9.5.2 Mixed mechanism fracture model (MMFM).....	207
9.5.3 Modelling CISF .....	207
CHAPTER 10 Conclusions and future work.....	208
10.1. Conclusions.....	208
10.2. Future work.....	210

## List of figures

Figure 1.1 Schematic application of CFRP in Airbus A380 .....	3
Figure 2.1 Load Modes.....	11
Figure 2.2 VVC models: (a) four-node elements, (b) eight-node elements; .....	16
Figure 2.3 Typical adhesive joints. ....	21
Figure 2.4 Parameters of Papini's method.....	22
Figure 2.5 Typical stress level variations in fatigue.....	23
Figure 2.6 Block representation in Variable Amplitude fatigue .....	24
Figure 2.7 Typical $S-N_f$ diagram.....	26
Figure 2.8 Typical stiffness degradation curves in composite materials.....	30
Figure 2.9 Schaff and Davidson's method.....	34
Figure 2.10 Typical fatigue crack growth curve .....	36
Figure 2.11 Damage shift model.....	39
Figure 3.1 Schematic representation of an impact block test .....	46
Figure 3.2 Schematic representation of a wedge impact specimen.....	47
Figure 3.3 Schematic of impact of SLJ .....	60
Figure 4.1: FM-73M Bulk adhesive specimens .....	68
Figure 4.2: Changes in the tensile strength in FM-73M as increasing of the displacement rate .....	69
Figure 4.3 Stress-strain curves for bulk adhesive (FM-73M) at different displacement rates.....	70
Figure 4.4 Changes in the tensile strength in FM-73M as increasing of the displacement rate .....	70
Figure 4.5 Typical stress-strain curves for bulk adhesive at different displacement rate (EA 9628-UNS).....	71
Figure 4.6 Image of a typical aluminium (7075-T6) surface after grid blasting.....	71
Figure 4.7 Dimensions of SLJ <sub>long</sub> .....	73
Figure 4.8 Dimensions of SLJ <sub>short</sub> .....	73
Figure 4.9 Dimensions of lap strap joint specimens. a) LSJ <sub>long</sub> for SF; b) LSJ <sub>short</sub> for IF .....	75
Figure 4.10 Schematic of specimen fixture for impact fatigue.....	78



Figure 4.11 Schematic of the instrument vice on the impact fatigue machine, a) top view, b) front view .....	78
Figure 4.12: Schematic of impact-fatigue test and data acquisition.....	80
Figure 4.13 Positions of the back face strain gauges.....	84
Figure 4.14 Comparison between crack gauge and optical crack measurements .....	85
Figure 5.1 Boundary conditions of a generalized LSJ specimen .....	89
Figure 5.2 Detail of a cohesive failure in a LSJ <sub>long</sub> specimen.....	91
Figure 5.3 Comparison of energy release rate using different methods in a cohesive failure of 3.35 mm: a) low order element; b) high order element.....	93
Figure 5.4 Mixed mode dependency on element size .....	93
Figure 5.5 Comparison of stress distributions over the middle adherend in 2D and 3D FEA models: (a) peel stresses; (b) shear stresses.....	95
Figure 5.6 Comparison of stress distributions over the adhesive middle line for short and long LSJ specimens: (a) peel stress; (b) shear stress. ....	96
Figure 5.7 Back face strain for different location on the lap adherend .....	98
Figure 5.8 Back face strain for different locations on the strap adherend.....	98
Figure 5.9 Schematic representation of aluminium bar.....	100
Figure 5.10 Experimental data for aluminium plate in tensile impact: .....	102
Figure 5.11 Bending effect in the aluminium bar .....	102
Figure 5.12 Description of a 2D model of impact.....	104
Figure 5.13 Comparison between experimental and calculated reaction force: a) completely rigid support; b) elastic support.....	105
Figure 5.14 Comparison of experimental and FEA BFS for aluminium plate .....	107
Figure 5.15 Comparison of experimental and FEA results for force in support. Specimen without damage .....	108
Figure 5.16 Comparison of experimental and FEA results for axial strain in strap at 15 mm from the fillet. Specimen without damage.....	108
Figure 5.17 Finite-element meshes of areas with cracks: (a) cohesive fracture of adhesive, (b) interfacial fracture, (c) fracture in 1 <sup>st</sup> ply of CFRP (adhesive layer in grey).....	110
Figure 5.18 Changes of crack propagation direction for cohesive failure in short LSJ .....	112
Figure 6.1 Force-displacement plot for SLJ <sub>short</sub> specimen tested under quasi-static loading .....	115

Figure 6.2 Force-displacement plot for SLJ <sub>long</sub> specimen tested under quasi-static loading .....	116
Figure 6.3 Opposing fracture surfaces after quasi-static testing: (a) upper adherend, (b) lower adherend.....	116
Figure 6.4 Schematic representation of fracture path in specimens tested under quasi-static loading .....	117
Figure 6.5 High-magnification SEM of specimen tested under quasi-static loading conditions.....	117
Figure 6.6 Detail of a typical failure under quasi-static conditions .....	117
Figure 6.7 Description of a generalized SLJ specimen .....	118
Figure 6.8 Shear stress distributions for SLJ <sub>long</sub> and SLJ <sub>short</sub> specimens in quasi-static loading .....	119
Figure 6.9 Peel stress distribution comparison for SLJ <sub>long</sub> and SLJ <sub>short</sub> specimens in quasi-static loading.....	120
Figure 6.10 $F - N_F$ diagrams for SLJ in standard fatigue .....	121
Figure 6.11 $E - N_F$ diagram for SLJ <sub>long</sub> samples standard fatigue .....	122
Figure 6.12 Deterioration of SLJ <sub>long</sub> stiffness as damage accumulate during SF for three specimens tested at a maximum load of 9, 8, and 7 kN.....	123
Figure 6.13 Strength wearout of SLJ <sub>short</sub> .....	124
Figure 6.14 Failure in SF conditions at high force levels (90% of $F_{Qs}$ );.....	125
Figure 6.15 Fracture surface of SF specimens tested at 35% of $F_{Qs}$ :(a) schematic presentation, (b) macroscopic image .....	126
Figure 6.16 Fracture surface of Zone 1 in specimens tested.....	127
Figure 6.17 Fracture surface in Zone 2 in specimens tested.....	127
Figure 6.18 Evolution of forces in SLJ <sub>short</sub> in various cycles of impact fatigue .....	129
Figure 6.19 Definitions of loading time in Tanaka's model [135] (a) and in the current model (b).....	129
Figure 6.20 Evolution of maximum force and loading time during IF .....	130
Figure 6.21 $F - N_F$ diagrams for SLJ's under impact fatigue.....	131
Figure 6.22 $E - N_F$ diagrams for IF.....	132
Figure 6.23 Effect of initial energy of hammer on total energy absorbed in IF to failure.....	133
Figure 6.24 Effect of initial energy on energy dissipation in impacts.....	134
Figure 6.25 Deterioration of the stiffness of SLJ <sub>short</sub> samples during IF .....	134

Figure 6.26 Typical fracture surface in adhesive joint after IF at high energy levels in SLJ <sub>short</sub> .....	135
Figure 6.27 Failure in specimen tested at 1 J.....	136
Figure 6.28 Cavitated rubber particles in IF at high energy levels .....	136
Figure 6.29 Detail of the cohesive failure at high impact energy in IF.....	137
Figure 6.30 Details of failure in Zone 1 in low energy IF (adherend side).....	137
Figure 6.31 Detail of failure in Zone 3 in low energy IF (adhesive side) .....	138
Figure 6.32 Cavitated rubber particles in impact fatigue at low energy levels.....	138
Figure 6.33 $E-N_F$ diagrams for two groups of specimens in IF .....	139
Figure 6.34 Comparison of $E-N_F$ diagrams for SLJ's in IF and SF .....	141
Figure 6.35 Comparison of $E-N_F$ diagrams for SLJ's in IF and SF .....	141
Figure 6.36 Strength wearout for SLJs, at samples tested at 1J in: (a) IF and (b) SF	142
Figure 7.1 Quasi-static value of failure of LSJ <sub>short</sub> .....	144
Figure 7.2 Crack growth rate of LSJ <sub>long</sub> in standard fatigue .....	146
Figure 7.3 Comparison between experimental and FEA back face strains (a) gauge at 16 mm from the fillet on the lap adherend, (b) gauge at 15 mm from the fillet on the strap adherend .....	147
Figure 7.4 Failure surface of sample tested in standard fatigue using LSJ <sub>long</sub> .....	148
Figure 7.5 Crack initiation and propagation in standard fatigue using LSJ <sub>long</sub> .....	148
Figure 7.6 Scanning electron micrographs of fracture surfaces in LSJ <sub>long</sub> samples tested in standard fatigue: (a) region I; (b) region II; (c) and (d) region III .....	150
Figure 7.7 Crack growth of LSJ <sub>short</sub> specimens in SF.....	151
Figure 7.8 Crack growth rate of LSJ <sub>short</sub> specimens in SF .....	152
Figure 7.9 BFS on the strap adherend in LSJ <sub>short</sub> specimen SF2 .....	152
Figure 7.10 Detail of cohesive failure in SF1 LSJ <sub>short</sub> specimen tested in SF .....	153
Figure 7.11 Type SF2 crack propagation of LSJ <sub>short</sub> in standard fatigue.....	154
Figure 7.12 Transverse cross section through region II fracture surface in LSJ <sub>short</sub> .	155
Figure 7.13 Crack growth of LSJ <sub>short</sub> specimens in IF.....	157
Figure 7.14 Crack growth rate of LSJ <sub>short</sub> specimens in IF .....	157
Figure 7.15 Force and strain results for a typical impact in impact fatigue and LSJ <sub>short</sub> .....	158
Figure 7.16 Change in back face strain with crack length during IF using LSJ <sub>short</sub> ..	159
Figure 7.17 Comparison between experimental and FEA back face strains of LSJ <sub>short</sub> specimens under IF.....	160

Figure 7.18 Failure surface of $LSJ_{short}$ tested in impact fatigue .....	160
Figure 7.19 Fracture in region A in specimens with fast crack growth tested in impact fatigue conditions IF7 .....	161
Figure 7.20 Failure in IF specimen IF7 with fast FCG behaviour: (a) details of failure in region B of the lap; (b) details of failure in region C .....	162
Figure 7.21 SEM of fracture surfaces in sample IF5 tested in IF with a slow FCG behaviour. (a) Region A, (b) Region B of the lap, (c) and (d) region C.....	164
Figure 7.22 Damage across the strap width near to the crack tip under IF .....	165
Figure 7.23 Crack growth in combined impact and standard fatigue.....	166
Figure 7.24 Crack growth rate in combined impact and standard fatigue.....	166
Figure 7.25 SEM of fracture surfaces in samples with a fast FCG behaviour tested in CISF: (a) region A, (b) region C .....	167
Figure 7.26 SEM of fracture surfaces in specimens with a cohesive failure tested in CISF: (a) SF region, (b) IF region. ....	168
Figure 7.27 Comparison of the crack growth rate in CISF and SF.....	169
Figure 8.1 Power law fit to energy-life plot for SLJs in IF .....	176
Figure 8.2 Log-linear law fit to energy-life plot for SLJs in IF .....	176
Figure 8.3 Stiffness deterioration during SF.....	178
Figure 8.4 Stiffness deterioration during IF.....	178
Figure 8.5 Modified load-time model.....	179
Figure 8.6 Effect of accumulated loading time on damage evolution in $SLJ_{short}$ .....	181
Figure 8.7 Comparison of different fracture parameters for cohesive fracture of $LSJ_{short}$ .....	182
Figure 8.8 Changes in $G_I$ and $G_{II}$ from a geometric non-linear model as a function of the crack size in $LSJ_{short}$ .....	183
Figure 8.9 Comparison of $G_{gnl}$ for different fracture paths.....	183
Figure 8.10 Comparison of $G_{gnl}$ mode ratio ( $G_I/G_{II}$ ) for different fracture paths in $LSJ_{short}$ .....	184
Figure 8.11 Changes in the dynamic strain energy release rate with a cohesive crack size of 11 mm in a $LSJ_{short}$ .....	185
Figure 8.12 Comparison of $G_{gnl}$ for different fracture paths in $LSJ_{short}$ .....	185
Figure 8.13 Comparison of $G_{dyn}$ and $J_{dyn}$ with a linear or elasto-plastic adhesive material in a $LSJ_{short}$ .....	186
Figure 8.14 Fatigue crack growth during Standard fatigue .....	187

Figure 8.15 Mixed mode fracture model .....	188
Figure 8.16 Fatigue crack growth during Impact fatigue .....	189
Figure 8.17 Failure in mixed fracture model under SF. ....	190
Figure 8.18 Optimization of $n$ in the mixed mechanism fracture model.....	191
Figure 8.19 NCGI prediction of cohesive failure in a $LSJ_{short}$ under SF.....	192
Figure 8.20 NCGI of a cohesive failure LSJs under CISF .....	193
Figure 8.21 Schematic representation of CISF in Damage Shift model .....	194
Figure 8.22 Schematic representation of FCG rate changes from IF to SF in CISF.	195
Figure 8.23 NCGI curve using $DSM_{abr}$ .....	195
Figure 8.24 FCGR-curve for a CISF assuming $DSM_{abr}$ .....	196
Figure 8.25 NCGI curve using $DSM_{lin}$ .....	196
Figure 8.26 FCGR-curve for CISF assuming $DSM_{lin}$ .....	197
Figure 8.27 NCGI curve using $DSM_{frac}$ .....	197
Figure 8.28 FCGR-curve for CISF assuming $DSM_{fra}$ .....	198

**List of Tables**

Table 4-1: Properties of 5245C matrix at room temperature [..... 65

Table 4-2: Properties of T800 fibres ..... 66

Table 4-3: Properties of T800/5245C composite at room temperature ..... 66

Table 4-4: Properties of 7075-T6 in clad condictiones ..... 66

Table 5-1 Lap strap dimensions ..... 89

Table 6-1 Single lap dimensions ..... 119

## **Abbreviations**

Back face strain (BFS)  
Constant amplitude (CA) fatigue  
Continuum damage mechanics (CDM)  
Carbon Fibre Reinforced Polymers (CFRP)  
Combined IF and SF (CISF)  
Cycle mix factor (CM)  
Compact tension shear (CTS)  
Cohesive zone elements (CZE)  
Dynamic fracture mechanics (DFM)  
Fatigue crack growth rate (FCGR)  
Finite element method (FEM)  
Fracture mechanics (FM);  
Fibre-reinforced polymeric composite (FRPC)  
Linear elastic fracture mechanics (LEFM)  
Impact fatigue (IF)  
Lap strap joints (LSJ)  
Mix mode fracture model (MMFM),  
Numerical crack growth integration (NCGI)  
Nonlinear elastic fracture mechanics (NLEFM)  
Standard fatigue (SF)  
Single lap joints (SLJ)  
Split Hopkinson pressure bar (SHPB)  
Variable amplitude fatigue (VA)  
Virtual crack closure (VCC)

## Nomenclature

$a$	Crack length
$A$	Area
$B$	Width
$C$	Material compliance
$c_R$	Rayleigh wave speed
$d$	Displacement
$D$	Damage accumulation
$D_0$	Initial damage
$E$	Elastic modulus, Energy
$\bar{E}_t$	Average accumulated energy
$E_{Qs}$	Energy necessary to break a specimen in quasi-static conditions
$E_j$	Energy absorbed by each impact
$\bar{E}_t$	Average energy absorbed per impact
$E_0$	Initial potential energy, Initial stiffness.
$F_{wo}$	Strength wear out
$F_{max}$	Maximum force
$\bar{F}_{max}$	Mean maximum force
$F_{max}^{static}$	Maximum quasi-static force
$F_{Qs}$	Static load at failure
$F_{ij}$	Force in node $ij$
$\bar{F}_{max}$	Mean maximum force
$G_T$	Total energy release rate
$G_{IR}$	Inter-laminar fracture toughness resistance
$G_{IC}$	Critical strain energy release rate in mode $I$
$G_{th}$	Threshold strain energy release rate
$G_C$	Critical strain energy release
$G_{Brus}$	$G_T$ based on Brussat model
$G_{gnl}$	Geometric non-linear strain energy release rate
$G_{dyn}$	Dynamic strain energy release rate
$\gamma_s,$	Surface energy



$J_I$	J-integral evaluated under contour $i$
$J_{\text{dyn}}$	Dynamic non-linear strain energy release rate
$K$	Stress intensity factor
$K_{IC}$	Critical stress intensity factor in mode I
$K(n^*)$	Stiffness deterioration
$l$	Overlap length.
$N_F$	Number of cycles needed to generate failure
$n$	Number of cycles
$P$	Load
$R$	load ratio (minimum to maximum load or stress)
$r_p$	ratio of the plastic zone
$\Gamma$	Path surrounding the crack tip,
$\sigma$	Applied stress
$\sigma_c$	Fracture stress.
$\sigma_{\text{max}}$	maximum stress
$\sigma_{\text{min}}$	minimum stress
$\sigma_m$	mean stress
$\sigma_a$	stress amplitude
$\sigma_R(n)$	Residual strength
$\sigma_c$	Compressive strength
$\sigma^{\text{static}}$	Rupture stress in static conditions.
$\sigma_{ys}$	Yield stress.
$\tau_{SF}^{\text{max}}$	Maximum shear strength
$\tau$	Total cumulative loading time
$T_{FI}$	Contact time for the impact $i$ ,
$T_g$	Glass transition temperature
$\vec{t}$	Traction vector,
$\vec{u}$	Displacement vector
$U_{jk}$	Displacement in node $ij$
$V$	Velocity
$V_0$	Initial velocity
$W$	Strain energy density

# **CHAPTER 1**

## **Introduction**

### **1.1. Background**

Joining small parts is a common method of modern design to produce complex and/or multi-material structures. Designers have used different types of joints such as rivets, bolts, etc, to assemble components and structures known as mechanically fastened joints. However, with development of new polymer materials and better understanding of their mechanical properties another type of joint has become more prominent; the adhesively bonded joint. In this work, the term “adhesive” is defined as the material that is applied to (pre-treated) surfaces to be joined together to resist the separation after curing the adhesive; the materials that are going to be bonded together are referred to as adherends. The last generation of structural adhesively bonded joints began to be used mainly by the aeronautic industry, but with time and thanks to new research developments, other types of industries such as automotive, marine, are implementing this technique as a common method to joint mechanical parts.

Advantages of adhesive bonding with regard to mechanical fastened joints have been mentioned by various researchers, the main being: a decrease in stress concentration; a high strength-to-weight ratio; a capacity to join different adherends; a capacity to join thin-sheet materials and good corrosion resistance (because they do not need holes or welds where corrosion can appear). In fact, the absence of holes, good fatigue

properties and low weight of adhesively bonded joints make this technique a better option in many cases; but adhesive bonding is not suitable when disassembly of the joints is necessary. In general, adhesively bonded joints are considered to have a good fatigue performance; adhesive perform better under fatigue than many adherend. This allowed to suggest a rule to design adhesive joints [1] ensuring failure in metallic adherends rather than in the adhesive since damage in adherend in many cases is easier to detect and repair in contrast to a damage in the adhesive where non destructive technique should be usually used to detect damage.

The use of advanced materials in the aeronautic industry is continuously increasing. In the last decades advanced composites, such as Carbon Fibre Reinforced Polymers (CFRP) have become one of the most important structural materials in the aeronautic industry due to their excellent stiffness and low strength-to-weight ratio. Figure 1.1 presents a schematic of the use of CFRP in Airbus A380 airplane. It is reported by the manufacturer that 16% of the structural weight are composites, with a typical example being the centre wingbox with 60 wt % 45 mm-thick CFRP laminates [2]. Still, lightweight materials such as aluminium still remain a commonly used material in aerospace applications; Airbus A380 has 66 wt% of aluminium alloys [3].

The adhesive joining technology in aeronautic industry is mainly used to attach stringers to fuselage and wing skins in order to stiffen the structure against buckling. In addition, it is also used to manufacture lightweight structures of metal honeycomb for flight control components like elevators, ailerons, spoilers, etc. [4]. Like most of the engineering materials, structural adhesives are susceptible to fatigue. Hence, this phenomenon should be analysed in detail in order to compare performance of adhesive joints in fatigue with that other types of joints. This should be another parameter for a designer to consider when selecting a structural adhesive along with factors such as; joint shape, type of surface, pre-treatment, etc.

Fatigue is a common phenomenon linked to cyclic loading, which occurs in service operation of structural components and can result in premature failure of the material compared to quasi-static conditions. In addition, complex patterns of real loads in-service have an effect on the progress of failure in composites or adhesives compared

to results obtained under fatigue with constant load amplitude. Failure by fatigue in laminate composites is manifested by various types of damage: fibre breaking, transverse matrix cracking, de-bonding between fibres and matrix and de-bonding of adjacent plies of the laminate commonly referred as delamination. In adhesives, failure by fatigue is identified as cohesive cracks in the adhesive, as cracks at the interface of the joint between adhesive and adherent or crack in the adherend in the case of adhesively bonded CFRP joints. With respect to fatigue, the term damage usually refers to micro or macro cracks-discontinuities in the material changing the initially continuous medium.

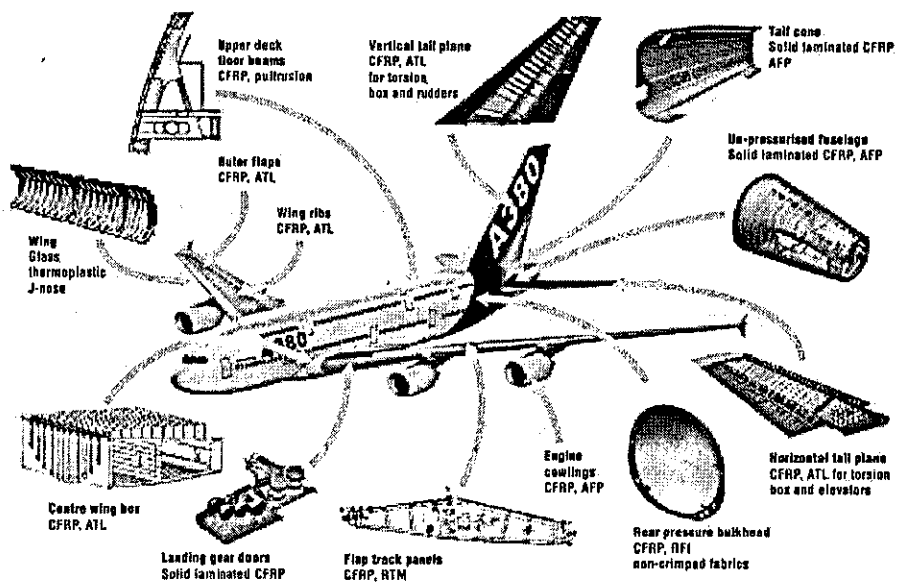


Figure 1.1 Schematic application of CFRP in Airbus A380 [2]

Though adhesive joints, as mentioned, have a good fatigue performance, there is still a concern that cyclic low-velocity impact experienced by mechanical structures e.g. in aeronautic systems, can lead to deterioration of their integrity and produce failure of bonded joints in cases when a long service life is expected. In operation, as was described by researchers [5, 6], aeronautic, automotive, naval and other structures can be exposed to cyclic or singular low-velocity impacts resulting in delamination damage of parts with fibre-reinforced polymeric composite (FRPC) as adherends. Obviously, from the mechanical point of view, impact results in stress waves that propagate, through the structure affecting all their interacting components. Hence, if

adhesive joints are used in such structures they are also exposed to such dynamic loading.

## **1.2. Aim of the research**

The purpose of this project is to evaluate the durability and degradation of adhesively bonded joints used in the aeronautical industry, for various regimes of fatigue: (i) sinusoidal with a constant-load amplitude, (ii) repetitive low-velocity, low-energy impacts and (iii) combination of these two loading regimens conditions.

## **1.3. Research objectives**

Although adhesively bonded joints usually demonstrate a good fatigue performance, their response to, and behaviour under, cyclic tensile impacts, known as *impact fatigue* (IF) is not fully studied. Fatigue in aerospace structure materials is commonly studied using a constant amplitude sinusoidal load pattern (referred in this project as standard fatigue (SF)); however, the results obtained for loading condition cannot be extended to the fatigue behaviour of adhesively bonded joints under IF. Hence, such studies could overestimate the life in service of real components exposed to complex loading histories that also contain low-amplitude impacts.

This project specifically aims to analyse the fatigue performance of adhesively bonded joints particularly under SF, IF and combined IF and SF (CISF). In order to do this, it is essential to study the behaviour of adhesively bonded joints under each loading conditions. The objectives are listed below.

- To study the historical development of research in IF and the state of the art in this area (see Chapter 3)
- To identify the mechanism of fracture and their dependency with the specimens size in single lap joints (SLJ) and lap strap joints (LSJ) (see Chapters 5 and 6)
- To develop finite-element models suitable to analyze IF and SF (see Chapter 5)
  - To evaluate the best locations for strain gages to monitor back face strain (BFS) in LSJs in order to analyse crack propagation;

- To evaluate the use of the technique based on BFS gages to monitor fatigue during SF and IF;
  - To optimise the boundary conditions of a dynamic model using experimental data.
- To analyse the fatigue life of adhesively bonded SLJs under SF and IF (see Chapter 6)
  - To investigate the existence of a fatigue limit under IF in SLJs;
  - To understand the fracture mechanism of failure in SLJs exposed to IF and SF;
  - To analyse the evolution of measure parameters in SLJ specimens tested in IF;
- To evaluate the strength wearout of SLJs under IF and SF (see Chapter 6);
- To analyse the fatigue crack growth in LSJs under standard fatigue, impact fatigue and their combination (CISF) (see Chapter 7)
  - To analyse the fatigue limit for LSJs under IF;
  - To analyse the effect of small block of IF into SF loading.
  - To analyse the fracture mechanisms of LSJs under IF, SF and CISF;
  - To analyse differences in the fatigue crack growth rate (FCGR) during IF and SF;
- To describe a methodology to evaluate FCGR-curve for LSJ specimens (see Chapter 8).
- To propose phenomenological model suitable analysis of IF and to evaluate its suitability to analyse CISF (see Chapter 8).

## 1.4. Outline of the thesis

The rest of the thesis is organized into the following chapters:

Chapter 2 introduces some basic concepts of fracture mechanics, especially for adhesively bonded joints, followed by a description of common fatigue methods used to study standard fatigue. These methods include the fatigue life model, phenomenological models and the fatigue crack growth approach.

Chapter 3 provide a review of previous studies in the area of impact and impact fatigue for different materials, relevant to the topic of this research: composites, polymers and adhesives.

Chapter 4 introduces the materials studied in this investigation including details of the types of joints used in experiments and simulations as well as experimental procedures used in this project.

Chapter 5 describes the methodology used to develop various finite-element models- quasi-static LSJ model, dynamic LSJ model. The specific features of the calibration and use of these models to analyse IF and SF in LSJ is described.

The main aim of Chapter 6 is to understand and quantify the fatigue life of adhesive joints exposed to multiple low-velocity tensile impacts. The chapter deals with a detailed experimental analysis of SLJ loaded in SF and IF conditions.

Chapter 7 is focused on an investigation of the fatigue crack growth behaviour of bonded CFRP LSJ subjected to three loading regimes: SF, IF and CISF.

Chapter 8 deals with implementations of some models used to analyse IF, CISF as well as changes of fracture mechanisms on specimens.

Chapter 9 presents a detailed discussion of the main experimental and theoretical results.

Chapter 10 provides the main conclusions obtained in this research, presenting also the suggested areas for future work.

## **CHAPTER 2**

### **Fatigue in adhesive joints**

#### **2.1. Introduction**

Engineers consider the phenomenon of fatigue as deterioration of the material properties of a component/structure caused by repetitive load application with relatively low amplitude that eventually results in a failure. Analysing loading histories of engineering structures, it is observed that in the majority of cases, components are exposed to cyclic loads generating a typical pattern of failure by fatigue. However, such ideal fatigue phenomena can also be affected by some failure accelerating factors such as corrosion, environmental effects, single or repetitive impacts. Damage initiation by fatigue in polymers is explained by researchers [7] as a process that occurs only when a cyclic plastic strain exists. However, the presence of small defects in materials before loading acting as stress concentrators can result in fracture by fatigue even at a nominal stress applied to the material being below the yield stress of the material. As mentioned above, different factors can accelerate a failure process caused by cyclic loading, making each of these factors a centre of interest of new research areas. The most important areas for polymers are:

- Creep fatigue, resulting from cyclic loads at higher temperatures.
- Thermo-mechanical fatigue, caused by fluctuating temperature and mechanical loads.
- Corrosion fatigue due to a combined action of recurrent loads and chemical agents or an environment that affects the adhesive properties.



However, in the last decade a new or, rather a re-discovered area, called *impact fatigue* (IF) has drawn the attention of researchers, mainly due to the potentially severe damage that can be produced under repetitive impacts [8]. This work focuses predominantly on the latter type of fatigue.

Failure by fatigue in adhesives is considered as a mix of many mechanisms. Structural adhesives can be considered as nanocomposites [9] because they are typically multi-component materials. Structural adhesives commonly use epoxy resins as a matrix with rubber particles and/or inorganic fillers [10] to generate a toughening mechanism. Extensive research has been undertaken to study the effect of those inclusions on the epoxy matrix. This effect can be summarized in terms of three main mechanisms [11]. The first is cavitation of rubber particles. This mechanism is characterised by the presence of holes in the fracture surface of the adhesive. A second mechanism is formation of shear bands. This can occur in areas with a high number of rubber particles, increasing the possibility of the onset of plasticity. A third mechanism is rubber bridging, in which rubber particles bridge a gap between the fractured surfaces, thus impeding crack propagation. These mechanisms are dependent on the volume fraction of rubber particles and their size [9]. Failure by fatigue in adhesives can be affected by one or all of those mechanisms and is manifested by the following: matrix micro-cracking, filler particle fracture or debonding, cavitation of rubber toughening particles and debonding of carrier fibres. For instance, failure in an adhesive joint can also involve damage in a region under the adherend making the process of crack generation and propagation in adhesive joints a complex and stochastic phenomenon. This presupposes a need to identify each of those mechanisms of failure in order to understand and predict the phenomenon of fatigue in adhesive joints.

The main purpose of this Chapter is to provide background information on the issues to be analysed in this study and to emphasize the relevance of this research. In order to reach this aim the following objectives of the research are used:

- To review the main concept of fracture mechanics (FM);
- To review numerical methods used to calculate FM parameters;

- To review models used to determine FM parameters for some specific specimen configurations;
- To review phenomenological models proposed to analyse fatigue in adhesives;
- To describe the load effect in the fatigue crack growth behaviour in adhesive joints.

## **2.2. Theoretical considerations**

Before reviewing the mechanisms of fatigue in adhesive joints as well as the respective methodology, a short review of the fracture theory in adhesive joints is given and the specific terminology is introduced.

### **2.2.1 Basic concepts of fracture mechanics**

Failure in materials and structures can be divided into two main categories: yield-dominant or crack-dominant. Fracture mechanics is associated with a crack-dominant failure [12]; it links fracture to the initiation and propagation of flaws or cracks until their critical length is reached causing material failure. Examples of this kind of failure were reported during the Second World War when an unstable catastrophic failure on welded ships was observed pressing researchers to gain understanding of that phenomenon [13]. Linear elastic fracture mechanics (LEFM) is a theory describing conditions for crack propagation in elastic media, where two main approaches have been used: the energy-balance approach and the stress-field approach. A brief description of each of these approaches is conducted below.

#### **2.2.1.1 Energy-Balance approach**

The starting point of fracture mechanics is the studies by A.A. Griffith [14], who proposed a theory of cracks based on measurements performed on glass rods. His theory explains conditions for crack growth in brittle solids and defined the concept of strain energy release rate ( $G$ ). The Griffith's theory suggests that the failure criterion due to a crack growth is based on energy balance between the strain energy and surface energy. Applying this idea together with the principle of minimum energy to the loaded body gives that the critical stresses required for fracture initiation can be described as:

$$\sigma = \sqrt{\frac{2E'\gamma_s}{\pi a}}, \quad (2.1)$$

where  $\gamma_s$ ,  $a$ ,  $\sigma$  and  $E'$  are the surface energy, the crack length, the remotely applied stress and the elastic modulus ( $E$ ) in case of plane stress, respectively. Furthermore, introducing the concept of the critical stress energy ( $G_c$ ) that is defined as the critical value of  $G$  that is necessary for a crack growth in quasi-static conditions, and assuming that material behaves in a linear elastic manner  $G_c$  can be expressed as [15]:

$$G_c = \frac{\pi a \sigma_c^2}{E'} \quad (2.2)$$

where  $\sigma_c$  is the fracture stress. Researchers have developed expressions to identify  $G$ , one of the common expressions is assuming a linear compliance in a fracture elastic material, where  $G$  can be expressed as:

$$G = \frac{P^2}{2B} \frac{\delta C}{\delta a}, \quad (2.3)$$

where  $P$ ,  $B$  and  $C$  are the critical load necessary for a crack to propagate, the width of the specimen and the material compliance, respectively.

#### 2.2.1.2 Modes of loading

Before introducing the stress-field approach it is necessary to analyse the type of loading of materials with cracks. Fracture in materials is related to the stress distributions that exist near the crack tip, and consequently, with the way which these materials are loaded. There are generally three modes of loading that have been used to analyse a cracked body based on the crack surface displacements that are common in fracture problems; these modes are presented in Figure 2.1. Mode *I* is the opening or peel mode, in which the crack faces are separated in the direction normal to the crack plane. Mode *II* is the sliding or in-plane shear mode, in which the crack faces are separated in the direction of the crack front propagation. Mode *III* is the tearing or anti-plane shear mode, in which the crack faces are sheared parallel to the crack front.

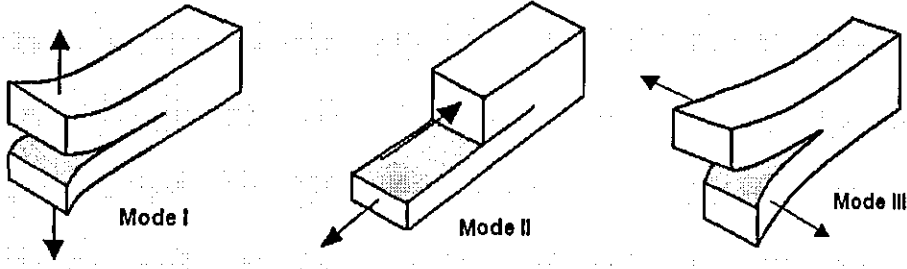


Figure 2.1 Load Modes

### 2.2.1.3 Stress-field approach

Irwin [15] continued the studies by Griffith and Inglis [16], finding that the amplitude of the stress distribution in the area near to the singularity can be expressed in terms of a scalar quantity called stress intensity factor ( $K$ ). His study was based on the results developed by Westergaard who defined an analytic function satisfying the Airy conditions for elastic problems. It was proposed that the stress field around a crack tip at mode  $I$  of loading at a position with coordinates  $r$  and  $\theta$  (using polar coordinates) can be expressed as:

$$\begin{aligned}\sigma_{xx} &= \frac{K_I}{\sqrt{2\pi r}} \cos \frac{\theta}{2} \left( 1 - \sin \frac{\theta}{2} \sin \frac{3\theta}{2} \right), \\ \sigma_{yy} &= \frac{K_I}{\sqrt{2\pi r}} \cos \frac{\theta}{2} \left( 1 + \sin \frac{\theta}{2} \sin \frac{3\theta}{2} \right), \\ \tau_{xy} &= \frac{K_I}{\sqrt{2\pi r}} \cos \frac{\theta}{2} \sin \frac{\theta}{2} \sin \frac{3\theta}{2},\end{aligned}\tag{2.4}$$

where  $K_I$  depends on geometry, the crack size, load level and load mode [17]. A useful relation, also defined by Irwin, was developed, correlating  $K$  with  $G$  using the Young's modulus:

$$G = \frac{K^2}{E'},\tag{2.5}$$

where  $E' = E/(1-\nu^2)$  for a plane strain state, and  $E' = E$  for a plane stress one;  $\nu$  is the Poisson's ratio. If the body is exposed to more than one load mode, then a superposition expression for the total energy release rate ( $G_T$ ) can be used [18]:

$$G_T = G_I + G_{II} + G_{III} = \frac{K_I^2}{E'} + \frac{K_{II}^2}{E'} + (1+\nu) \frac{K_{III}^2}{E}, \quad (2.6)$$

where the sub-indices denote each of the load modes.

#### 2.2.1.4 Crack tip plasticity

Theoretically, LEFM analysis of a sharp crack predicts infinite stresses at a crack tip. This theory does not account for inelastic deformations that can exist as plasticity or crazing and produce stress relaxation due to the yield phenomenon near the crack tip; as a result of this relaxation, a plastic zone is formed which is characterised by defects and voids [12]. To sort out this inconsistency, Irwin considered that in a structural material loaded above the yield stress, a plastic zone is formed around the crack tip and it needs to be properly accounted, this approach is known as nonlinear elastic fracture mechanics (NLEFM). A first approximation to determine the contour of the plastic zone is to consider that it has a circular shape with a radius  $r_p$ , using Equation 2.4 at  $\theta = 0$  and analysing only stresses in  $y$  direction. Then it can be calculated that the radius of plastic zone  $r_p$  in mode  $I$  is

$$r_p = \left( \frac{K_I}{\sigma_{ys}} \right)^2 \frac{1}{3\pi} \text{ for plane strain,} \quad (2.7)$$

$$r_p = \left( \frac{K_I}{\sigma_{ys}} \right)^2 \frac{1}{\pi} \text{ for plane stress,} \quad (2.8)$$

where  $\sigma_{ys}$  is the yield stress. However, a more accurate plastic zone shape was determined by others researchers, with the most popular based on the von Mises and Tresca yield criteria.

### 2.2.1.5 J integral

Rice [19] developed a model to characterise fracture mechanics in nonlinear elastic materials when large plastic zones due to yielding are present. His model was based on plane analysis for an isotropic material, monotonic loading and static equilibrium conditions. Along a close path an integral

$$J = \oint_{\Gamma} W dy - \oint_{\Gamma} \left( \bar{t}_x \frac{\partial \bar{u}_x}{\partial x} + \bar{t}_y \frac{\partial \bar{u}_y}{\partial y} \right) ds \quad (2.9)$$

is always equal to zero; here  $\Gamma$  is any path surrounding the crack tip,  $W$  is the strain energy density,  $\bar{t}$  is the traction vector,  $\bar{u}$  is the displacement vector and  $s$  is the distance along the path  $\Gamma$ . One of the principal restrictions is that the load must be monotonic; it means that  $J$  cannot be evaluated in unloading conditions. In addition, Rice also demonstrated that the J-integral is the potential energy change with respect to the crack size for nonlinear elastic solids and can be reduced to the strain energy release rate for linear elastic materials:  $J = G$  [20].

### 2.2.1.6 Dynamic fracture mechanics

Using a more detailed approach to loading conditions, researchers found more factors that can affect the fracture behaviour of materials, especially when dynamic conditions are accounted. In real life, the majority of structures are loaded under dynamic conditions, however, when the rate of loading or motion is low or neglected, structures can be analysed as static and only appropriate constitutive equations for the material are needed. However, when real dynamic problems are analysed, load oscillations caused by a dynamic load in addition to the inertia effects, the area of dynamic fracture mechanics (DFM) should be applied that is briefly described in this literature review.

Various dynamic scenarios and methodologies were employed in DFM. In general, those methodologies were focused on description of DFM parameters that can be used as an analogy of  $K$  in static analyses. However, the main difference between LEFM or NLFM and DFM is that in the last one the wave propagation produced by a load in

the material should be studied, with geometrical discontinuities like cracks changing drastically the wave propagation process. From the dynamic mechanical point of view and using the classical theory of wave propagation the load wave can travel in a material with the characteristic wave velocity  $c$ . Hence, the strain in each part of the material depends on the load rate,  $c$  and, obviously, boundary conditions. An example of this has been reported in [21], where the effect of a sample size on the impact strength of polymethyl methacrylate was analysed using cracked specimens with similar notch sizes but different sample lengths. It was observed that the fatigue life for short specimens was less than for long specimens, and those differences were explained by superposition of the wave propagation effect in short specimens. Another factor that can be analysed in DFM is that the crack also has its own dynamic behaviour with the crack velocity that can affect the wave propagation in the material.

A classical formulation for the dynamic stress intensity factor is based on the conventional static stress intensity formula (Equation 2.4) replacing  $K_I$  for  $K_I^{\text{dyn}}(t)$ . In [22] it is commented that under certain circumstances  $K_I^{\text{dyn}}(t)$  can be related to the static  $K_I$  with a function of crack speed  $k_I(V)$

$$K_I^{\text{dyn}} = k_I(V) K_I^{\text{static}}, \quad (2.10)$$

where

$$k_I(V) \equiv \frac{1 - V/c_R}{\sqrt{1 - V/c_D}}, \quad (2.11)$$

$c_R$  is the Rayleigh wave speed,  $c_D$  is a function of some materials properties and  $V$  is the speed of the incident crack. More results for this area can be found in [23, 24].

### 2.2.2 Numerical methods for fracture mechanics

Various methods are commonly used in numerical simulations to evaluate fracture resistance of components and structures; the most popular are discussed below.

### 2.2.2.1 Virtual crack closure

In [25], a technique for evaluating the strain energy release rate for modes *I* and *II* is defined, based on the evaluation of the crack closure integral. A linear four-node element was used to evaluate  $G$ ; a close agreement was found between this method and solutions based on analytical estimates of the energy release rate, J-integral and beam theory. This technique is called virtual crack closure (VCC) and is based on the physical interpretation of the definition of  $G$ , calculating the energy necessary to close a crack with a size equal to the element size  $\Delta a$ .

In [26], the work conducted in [25] is summarised and the VCC is extended to different quadratic elements. The simplest model, described the work per unit area necessary to be performed for each node to move it from the final position to the initial one, was developed in [25] using 4 nodes with  $G$  defined for a unit width in the following form: (Figure 2.2a)

$$G_I = \frac{1}{2\Delta a} F_{y1} U_{y3}, \quad (2.12)$$

$$G_{II} = \frac{1}{2\Delta a} F_{x1} U_{x3}. \quad (2.13)$$

An alternative model for elements with 8 nodes gives (Figure 2.2b):

$$G_I = \frac{1}{2\Delta a} (F_{y1} U_{y5} + F_{y2} U_{y4}), \quad (2.14)$$

$$G_{II} = \frac{1}{2\Delta a} (F_{x1} U_{x5} + F_{x2} U_{x4}). \quad (2.15)$$

Finally, a model developed for quarter-point singular elements gives (Figure 2.2c):

$$G_I = \frac{U_{y4}}{\Delta a} (F_{y2} + (1.5\pi - 4)F_{y1}), \quad (2.16)$$



$$G_I = \frac{U_{x4}}{\Delta a} (F_{x2} + (1.5\pi - 4)F_{x1}). \quad (2.17)$$

where  $F_{ij}$  and  $U_{jk}$  are introduced in Figure 2.2. A common supposition defined for all these methods is that  $\Delta a \rightarrow 0$ ; this implies that the results will be dependent on the quality of the mesh.

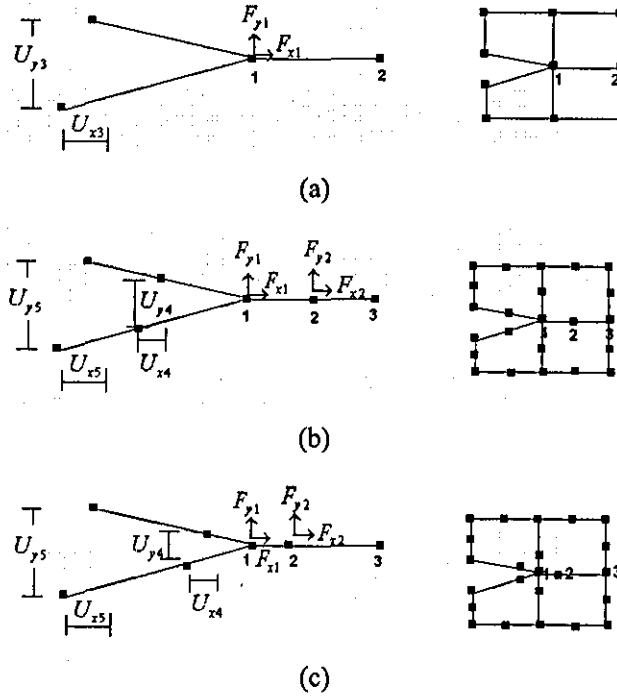


Figure 2.2 VVC models: (a) four-node elements, (b) eight-node elements; (c) quarter-point singular elements.

#### 2.2.2.2 J integral in FEA

The concept of J integral provides a useful method to evaluate numerically this fracture mechanics parameter based on Equation 2.9. However, to implement this, a line integral is converted to an integral over an area that surrounds the crack tip. Usually this is implemented as:

$$J = \int_A \left( \sigma_y \frac{\partial u_j}{\partial x_1} - W \partial x_1 \right) \frac{\partial q_1}{\partial x_1} dA, \quad (2.18)$$

where  $q_1$  is the function that changes the line integrals into the area one and has a value of 1 when the point is inside the area and zero when it is outside the area. In [27] two principal advantages of this approach are described. Firstly, the method can be used when the plastic zone size is significant; secondly, it is not strongly mesh-dependent.

### 2.2.2.3 Energy balance method

The energy release rate method is a simple variation of the VCC method. This is based on the amount of work related to a crack opening. The difference with regard to VCC is that  $G$  is calculated by two analyses; the first is developed for a crack length  $a$ , and the second for a crack length  $a+\Delta a$ . The energy release rate is calculated as

$$G = -\frac{U_{a+\Delta a} - U_a}{B\Delta a}, \quad (2.19)$$

where  $U_{a+\Delta a}$  is the strain energy for a crack length  $a+\Delta a$  and  $U_a$  is the strain energy for  $a$ . This method has the disadvantage that only the total strain energy release rate  $G_T$  is determined.

## 2.3. Effect of joint geometry

Fracture mechanics is a common methodology, used to analyse failure in adhesive joints. One of the first works that applied this theory to adhesive joints was by Ripley et al. [28]. In that work, it was identified that adhesive materials which contained flaws such as bubbles, unbounded regions or dust particles, affect the strength of the joint. In order to analyse the failure in bonded joints, the fracture mechanics-based theory was proposed, where measurements of fracture toughness were conducted in specimens analysing effects of some variables such as geometry, the section size and strain rate. It was found that the fundamental factor that affects fracture toughness of the joint is the crack speed, when a cohesive failure is observed. Slow crack propagation results in a higher toughness; however, when cracks appear as an immediate cohesive failure a lower fracture toughness was observed. In addition, it

was considered that a change from a peel fracture mode to a shear one results in an increase in fracture toughness.

Unfortunately, researchers showed that the experimental values obtained from tests are not necessarily a material property even when only a cohesive failure is observed. A comparison of the fracture energy for similar specimen geometry but with different adhesive bonding thickness was conducted in [29]; it was observed that for a rubber-toughened modified epoxy, increases in the adhesive thickness produced an increase in the fracture energy. However, that tendency reached a peak when the thickness of the adhesive layer was equivalent to the plastic zone  $2r_p$ . Changes in the adhesive fracture energy were also reported for different adherends. Similar results were reported in [30], with fracture surfaces and fracture toughness being affected by the bonding thickness; this was explained as a result of a competition between two different mechanisms. The first mechanism linked to the fact that for a small bond line thickness the fracture toughness changes linearly with the thickness. The second mechanism results in the toughness decrease after reaching the maximum value due to a blunting effect since a decrease in the crack tip radius results in the growth of stress at the crack tip. These differences in the fracture parameter when properties are experimentally obtained for bulk specimens and adhesive joints make it necessary to analyse fracture mechanics under bonded joints configurations since the stress distribution at the crack tip is affected by thickness of the adhesive and adherend.

Joint design is an important task that needs to be carefully studied. At a preliminary stage of design of a bonded joint, a cheaper adhesive and a simple process method to produce it can be selected; however, this process should be conducted with more detail because joints are designed to support significant levels of loads under particular conditions. Hence, the stress distribution, geometry singularities, dependency of the adhesive properties on the environment, absorption quality between the adhesive and adherends and other factors should all be accounted for. From the mechanical point of view, joints in structural components are designed to be loaded mainly in shear, however, elastic deformation of the adherends produces a combination of peel (mode *I*) and shear stresses (mode *II*) in the adhesive. In general, adhesive joints are strong in shear and weak in peeling; so the latter type of load needs

to be minimized [31]. In a recent paper [32] it was experimentally observed that strength of a joint decreases as the adhesive thickness increases. That was explained with the use of results reported in [33], where it was described that an increase in thickness enhanced a bending effect, increasing the mode *I* and, eventually, decreasing strength of the joint.

Numerous types of joints have been developed to optimize the manufacturing process and stress distributions in joints, examples of those together with the main configurations that are used in this work are shown in Figure 2.3. A brief description of these geometric configurations is given below.

### 2.3.1 Single lap joint

The lap joint is one of the most popular joint configurations used by industry, with the single lap joint (SLJ) (Figure 2.3) broadly used in standard tests to evaluate the adhesive performance and quality. This kind of joint is easy to make and the test results obtained for specimens are mainly sensitive to the adhesive quality and adherend preparation. In this kind of joint, when specimens are loaded with a tensile load, a part of the shear force acting in the adhesive, a bending moment is also applied to it caused by the non-collinear forces. As a result, both peel and shear stresses should be included into analysis of the stress state in adhesive in a SLJ.

A simple way to analyse such joints is to consider adherends as rigid bodies and consequently, the adhesive can only deform in shear. This supposition results in constant shear stresses supported by the adhesives for the entire adhesive section and described as:

$$\tau = \frac{P}{Bl}, \quad (2.20)$$

where *P* is the load, *B* is the adhesive width, and *l* is overlap length. In addition, it is supposed that the tensile stress over the overlap region for the upper adherend decreases from the maximum value at the first fillet to zero (at the second fillet). However, more realistic models were proposed by various researchers to analyse the stress distribution in SLJ, where they supposed that the adherend is an elastic

deformable material; those models are typically referred by the name of the author. A review of many analytical and numerical solutions for the SLJ are provided in [34].

### **2.3.2 Lap strap joint**

In this thesis special attention is paid to the lap strap joint (LSJ) (Figure 2.3), which has been referred to using different names by various researchers: as a cracked lap shear specimen [35, 36], with cracks usually growing in the middle of the adhesive, and strap-lap joint [37]. These joints are tested with a tensile force or even in three point bending. In this work this specimen is used only in tensile conditions. The lap strap joint (LSJ) is a representative joint for many aeronautic structures such as stiffened panels and shells, selective plate reinforcement, bonded edge doubler for flush mechanical attachments etc. This kind of joint is useful to researchers when the fracture behaviour of bonded joints under mixed-mode loading at one overlap end needs to be analysed. The LSJ has been used to study metal joints, composite joints, joints between composites and metals as well as inter-laminar fracture. In [35], a typical relation of  $G_I/G_{II}$  for LSJ between 0.2 and 0.3 was determined using a non-linear geometric finite element analysis. During experimentation, analytical solutions for  $G$  are required in order to verify the obtained results but also to determine the fracture energy of the adhesive joint. A recent publication [38] summarises the research conducted on this kind of joint. A summary providing details for the most important close-form models to determine  $G$  follows, for the crack growth in the middle of the adherend.

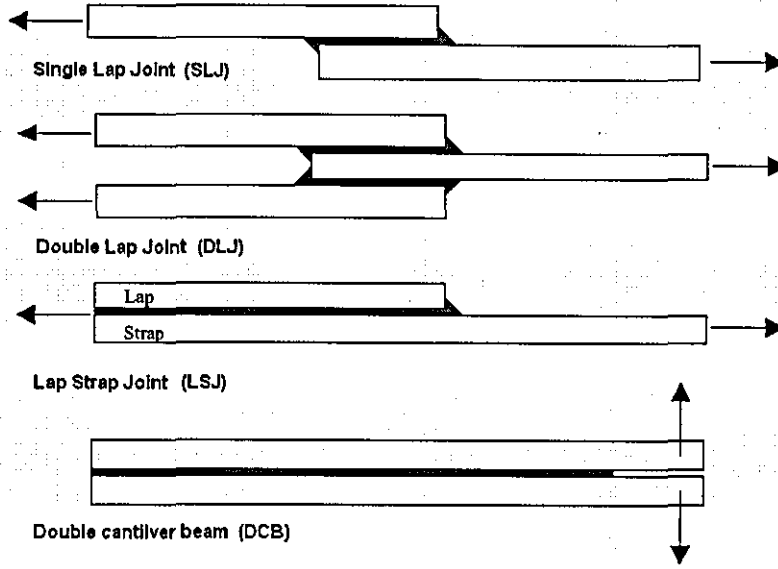


Figure 2.3 Typical adhesive joints.

#### 2.3.2.1 Brussat's model

Brussat [39] was the first researcher to work with the LSJ. His model, based on an infinite beam and the beam theory defined  $G_T$  in a LSJ with constant thickness as follows:

$$G_T = \frac{P^2}{2B(EA)_2} \left[ 1 - \frac{(EA)_2}{(EA)_0} \right], \quad (2.21)$$

where  $P$  is the load,  $B$  is the specimen width,  $(EA)_2$  is the tensile rigidity of the strap and  $(EA)_0$  is the total rigidity (lap + strap). Analysing Equation 2.21, it can be identified that  $G_T$  does not depend of the crack size, defining it as a constant along any crack size.

#### 2.3.2.2 Yeh-Hung's model

In [40], a model based on the Goland-Reissner [41] analysis of the SLJ was proposed. This model accounts for the bending moments per unit of width,  $M_1$  and  $M_2$ , found at the end of the strap and at the crack tip, respectively. For plane stress, it was established that:

$$G_r = \frac{P^2}{2(E_1 + E_2)(h_1 + h_2)} \left\{ \left( 1 + \frac{1}{\Sigma} \right) \left[ \left( 1 + \frac{1}{\eta} \right) + 12\hat{M}_1^2 \left( 1 + \frac{1}{\eta} \right)^3 \right] - (1 + \Sigma) \left( \frac{(1 + 1/\eta)}{A} + \hat{M}_0^2 \frac{(1 + 1/\eta)^3}{I} \right) \right\}, \quad (2.22)$$

where  $h_1$  and  $h_2$  represents thickness of the strap and lap respectively,  $I = g(E_1, E_2, h)$ ;  $\Sigma = h(E_1, E_2)$ ;  $\eta = p(h_1, h_2)$ ;  $A = t(\eta, \Sigma)$ ;  $\hat{M}_1 = f(M_1)$ ;  $\hat{M}_2 = f(M_2)$ ;  $M_1$  and  $M_2$  are the non-dimensional bending moments, which are functions of the reaction forces and bending at each restriction,  $E_1$  is the Young's modulus of the strap adherend and  $E_2$  is the Young's modulus of the lap adherend. This model was compared with FEM solutions; a good correlation for  $G$  but poor agreement for the fracture mode ( $K_I/K_{II}$ ) was found. The principal advantage of the method is that  $\hat{M}_0$  and  $\hat{M}_1$  depend on the crack size.

### 2.3.2.3 Papini's model

In [36] a model was developed based on the large-deformation beam theory for a thin adhesive layer; it described that  $G$  in a LSJ could be expressed as:

$$G = Eh^5 \lambda_1^4 \left( \frac{1}{576} + \frac{\tanh^2(\lambda_1 L_1) - \tanh^2(\lambda_2 L_2)}{768 \left[ \sqrt{1/8} \tanh^2(\lambda_1 L_1) + \tanh^2(\lambda_2 L_2) \right]^2} \right), \quad (2.23)$$

where  $E$  is the Young's modulus of the adherend,  $\lambda_i = f(P, D_i)$ ;  $D_i$  is the flexural rigidity per unit width of element  $i$ ;  $P$  is load;  $L_1$  and  $L_2$  are the lengths shown in Figure 3.5. The advantage of this model is an account for crack propagation that can be included into the model by changing the magnitudes of  $L_1$  and  $L_2$  (Figure 2.4).

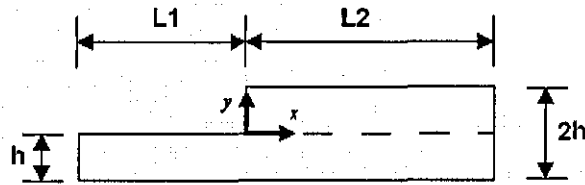


Figure 2.4 Parameters of Papini's method

## 2.4. General consideration of fatigue

During operation, structures are exposed to a variety of loads with the varying frequency, amplitude and direction entirely depending on the location and moment where those features are analysed. For example, in the design of ships, structures suffer load fluctuation as a results of variation with time of the sea waves producing a cyclic load during the time that structure is in use [42]. However, in laboratory simulations, these load conditions usually are represented as a sinusoidal load wave. Other load shapes can be used as: square, trapezium, saw-tooth and spikes that can have a constant load level or a variable-loads block pattern. The presence of such load patterns results in introduction of different approaches in fatigue studies-constant amplitude (CA) fatigue and variable amplitude (VA) fatigue.

### 2.4.1 Constant amplitude fatigue

CA fatigue, commonly using a sinusoidal waveform, is normally characterised by the its loading or displacement pattern but also by a number of parameters such as the maximum ( $\sigma_{\max}$ ) and minimum ( $\sigma_{\min}$ ) stress, frequency and load or displacement control. These parameters are used to identify the following parameters: mean stress ( $\sigma_m$ ), stress amplitude ( $\sigma_a$ ) and load ratio  $R$  (minimum to maximum load or stress) as shown in Figure 2.5. In this thesis, this kind of load conditions is referred to as standard fatigue (SF).

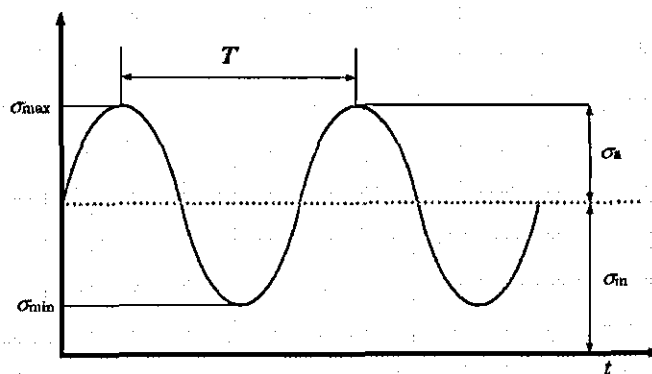


Figure 2.5 Typical stress level variations in fatigue



### 2.4.2 Variable Amplitude fatigue

Mechanical loading histories can be approximated with the use of variable amplitude. However, in order to simulate real load-time events, expensive and time-consuming experiments need to be performed. For this reason, variable amplitude fatigue is frequently simulated using blocks of CA fatigue loads, as shown in Figure 2.6. This simplification helps to analyse VA with the same techniques used in CA tests. However, researchers have pointed out the necessity to include also effects that are produced only by the change of the monotony on the load conditions. For instance, it was found in [43] working with FRPCs that the transition from a low mean stress to a high one was more harmful than the reverse, with the tendency being strongly dependent on the number of transitions.

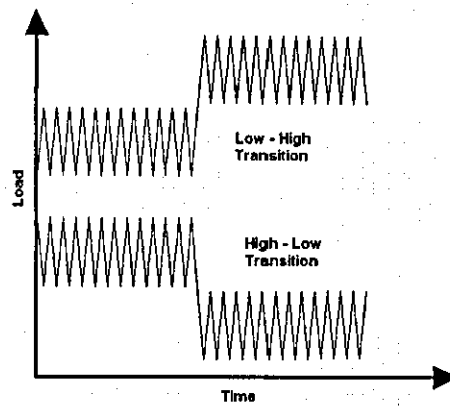


Figure 2.6 Block representation in Variable Amplitude fatigue

### 2.5. Fatigue models

Extensive research on fatigue modelling on adhesively bonded has been done during the last decades; where the main models that have been proposed could group in three: phenomenological, crack growth rate and continuum damage mechanics. In order to have a spectrum of fatigue models, some models specifically for adherends, i.e. CFRP, are reviewed. For a more detailed study of phenomenological and crack growth rate models specially for fibre reinforced polymeric composites, the author refers the reader to reference [44]. In addition, for a deep understanding of continuum damage mechanics, the author recommends to references [45-47]

### 2.5.1 Phenomenological models

The phenomenological models are based on changes in the macroscopic mechanical characteristics of the sample after fatigue damage; these characteristics commonly use fatigue life, stiffness and strength.

#### 2.5.1.1 Fatigue life approach

Experimental fatigue results are commonly presented as  $S-N_F$  curves or Wöhler plots. In this plots, a testing condition like stress, strain, load or displacement is related to the number of cycles,  $N_F$ , needed to generate failure in a specimen under a specific type of load (i.e. constant  $R$  and constant frequency), see Figure 2.7. Usually, this graph is plotted in semi-log scale where a quasi-linear behaviour is detected and some empirical curve fitting is used, the most common being

$$\begin{aligned}\sigma &= C + D \log(N_F) \\ \sigma &= A(N_F)^\alpha\end{aligned}\tag{2.24}$$

where constants  $C$ ,  $D$ ,  $A$  and  $\alpha$  are obtained from experimental results. It is necessary to emphasise that changing any of the loading conditions would change the graph and, consequently, the value of the constant. In Figure 2.7 a generic presentation of a  $S-N_F$  diagram is given. It is seen that, in general, this curve is divided into two different sections. The first is the fatigue zone, where a quasi-linear behaviour is observed when data are plotted in a log-log scale. The second section is called the endurance zone, for which an endurance limit is expected. For adhesives that do not have an endurance limit, a second zone can be linked to the load that adhesives can support at least  $10^6$  cycles without failure. In studies of fatigue in adhesives it was seen that a  $S-N_F$  graph can have a slightly different form from the hypothetical linear relation in the fatigue zone. Studies of fatigue in adhesively bonded joints have detected that the endurance limit is between 20% and 50% of the stress at static failure [48].

Though researchers pointed out limitations of this model, basically it can be stated that  $S-N_F$  graphs are still useful to analyse fatigue. However, such graphs do not give information of crack initiation and propagation, this technique is not suitable to analyse fatigue in such cases. Some effects of loading condition on  $S-N_F$  graphs for adhesive joints have been described by researchers. In [49], the effect of the load ratio was analysed and it was observed that for a given fatigue life a lower load range is expected to produce failure when  $R$  increases. It was suggested that the fatigue process is more controlled by the maximum load rather than by the load range. The variation of  $R$  results in the increase in the slope of  $S-N_F$  graphs as  $R$  decreases.

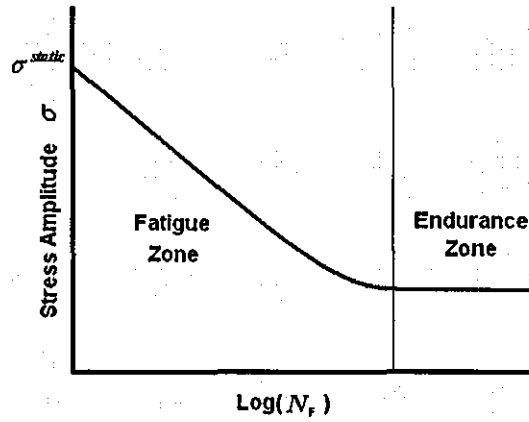


Figure 2.7 Typical  $S-N_F$  diagram

A series of cumulative models was proposed by researchers in order to use the data obtained with  $S-N_F$  graphs to predict the fatigue life of specimens under varying cyclic conditions. Let us note here that the majority of the models that are presented below are related with those used to analyse fatigue in adhesively bonded joints, however, some of them are more commonly used to analyse fatigue in FRPC.

#### ***Palmgren-Miner (P-M) model***

This is the most common method to analyse fatigue life. This method was initially proposed by Palmgren [50] and then developed by Miner [51]. This method is based on the assumption that a constant work is absorbed in each cycle. For a CA load, the Miner's rule is defined as:

$$C = \frac{n}{N_F}, \quad (2.25)$$

where  $n$  is the number of cycles at a given stress amplitude  $\sigma_a$ ,  $N_F$  is the number of cycles to failure at  $\sigma_a$ ;  $C$  is called the Miner's sum and is theoretically equal to one at the point of complete rupture.

Approximations for cumulative damage in VA fatigue can be developed using the Miner's rule. Such methods are based on the determination of damage accumulation ( $D$ ) as a linear combination of damage for each load block.

$$D = \sum_{i=1}^j \left( \frac{n}{N_F} \right)_i \quad (2.26)$$

where  $j$  is the number of CA blocks. Rupture is expected when  $D = 1$ . It was shown that this kind of model can give satisfactory results in many cases. However, it was proved in [52] that when it was used to predict the fatigue life in adhesively bonded joints under VA fatigue it produced unconservative fatigue life predictions as a result of crack growth acceleration due to load interaction.

#### ***Marco-Starkey's model***

This model is a simple extension of the Palmgren-Miner's model. In this method, damage is defined as [53]:

$$D = \left( \frac{n}{N_F} \right)^\alpha \quad (2.27)$$

where  $\alpha$  is an independent constant.

#### ***Howe-Owen's model***

The model of Howe and Owen is supported by experimental work that demonstrated non-linear cumulative damage in glass-reinforced composites:

$$D = \sum_{i=1}^j \left[ A \left( \frac{n_i}{N_i} \right) + B \left( \frac{n_i}{N_i} \right)^2 \right] \quad (2.28)$$

where A and B are material's parameters. This model was developed since the Miner's linear damage rule did not accurately predict the behaviour of their samples [54].

#### *Adam-Harris's model*

A model called "constant-life analysis" was suggested in [55] for CA fatigue based on the experimental work with CFRP. The authors showed that for experiments using positive and negative  $R$ -ratios but with similar  $\sigma_{\max}$ , comparable levels of life were obtained, suggesting that:

$$\frac{\sigma_a}{\sigma_t} = f \times \left(1 - \frac{\sigma_m}{\sigma_t}\right)^u \left(\frac{\sigma_c}{\sigma_t} + \frac{\sigma_m}{\sigma_t}\right)^v, \quad (2.29)$$

where  $\sigma_a = (\sigma_{\max} - \sigma_{\min})/2$ ,  $\sigma_m = (\sigma_{\max} + \sigma_{\min})/2$ ,  $\sigma_t$  is tensile strength and  $\sigma_c$  is compressive strength. Additionally,  $u$  and  $v$  are material parameters having a linear relation with  $\log(N_F)$  and  $f$  is the fatigue parameter defined by the following relation:

$$f = \frac{\sigma_{ah}/\sigma_t}{\left(1 - \sigma_m/\sigma_t\right)\left(\sigma_c/\sigma_t + \sigma_m/\sigma_t\right)}. \quad (2.30)$$

Further work [56] defined a model for VA fatigue based on experimental studies of CFRP. As a simplification, this model was first defined for two load blocks and then extrapolated to  $i$  blocks supposing that a specimen has initial damage  $D_0$ . After the first block of load the damage level increases to  $D_1$  defined by the Marco-Starkey's model[53]:

$$D_1 = \left( D_0 + \left( \frac{n}{N_F} \right)_1 \right)^{\alpha_1}. \quad (2.31)$$

The effect of block loads transition is included into this model using an equivalent fractional life model  $(n/N)_{2,1}$ ; the latter is defined for the first block in terms of  $\alpha$  for the second load block ( $\alpha_2$ ) and for the first load block ( $\alpha_1$ ):

$$\left(\frac{n}{N_F}\right)_{2,1} = (D_1)^{\alpha_1/\alpha_2}. \quad (2.32)$$

Finally, damage before the second block is defined assuming  $d_0 = 0$ :

$$D_2 = \left[ \left( 0 + \left(\frac{n}{N_F}\right)_1 \right)^{\alpha_1/\alpha_2} + \left(\frac{n}{N_F}\right)_2 \right]^{\alpha_2}. \quad (2.33)$$

Generalising the damage model in Equation 2.32, damage for  $i$  blocks is defined:

$$D = \left( \left( \left( \left( 0 + \left(\frac{n}{N_F}\right)_1 \right)^{\alpha_1/\alpha_2} + \left(\frac{n}{N_F}\right)_2 \right)^{\alpha_2/\alpha_3} + \left(\frac{n}{N_F}\right)_3 \right)^{\alpha_3/\alpha_4} + \dots + \left(\frac{n}{N_F}\right)_i \right)^{\alpha_i}, \quad (2.34)$$

where exponent  $\alpha_i$  is the constant of the Marco-Stanley's model for the  $i$ -th block.

#### ***Jen and Lee's model***

The paper [57] extended the static unidirectional Tsai-Hill model to cyclic loading. Their model is defined in terms of the stress supported by a plate with fibres oriented at an angle  $\theta$  to the load axis. They showed that for multidirectional laminates, subjected to plane-stress multi-axial fatigue loading with positive  $R$ , the following equation applies:

$$\left(\frac{\sigma_{11}}{L}\right)^2 + \left(\frac{\sigma_{22}}{t}\right)^2 - \left(\frac{\sigma_{11}\sigma_{22}}{L^2}\right) + \left(\frac{\sigma_{12}}{\tau}\right)^2 = 1, \quad (2.35)$$

where direction 1 and 2 are parallel and perpendicular to the fibre respectively,  $L = L(n, R_{11})$ ;  $t = t(n, R_{22})$ ;  $\tau = \tau(n, R_{12})$  and  $R_{ii} = (\sigma_{ii})_{\min}/(\sigma_{ii})_{\max}$  and  $N$  are the cycles under stress ratio  $R_{ii}$ .

### 2.5.1.2 Residual stiffness models

The stiffness-based models deal with changes in material or structural components under fatigue. Such changes are caused by a combination of all damage mechanisms, making it difficult to differentiate between the effects of each of these mechanisms. Hence, they are analysed with phenomenological models that, as mentioned in [58], have the advantage compared with the strength models because the residual stiffness data have lower scatter than the strength data, that is highly sensitive to damage progression. In addition, this method can be used as a non-destructive measure that can be used during service. In [59], it is stated that a typical experimental result on stiffness degradation in composites in fatigue can be presented as a three-stage graph, schematically shown in Figure 2.8. The character of stiffness deterioration in composites is characterised by an initial stage with an observed reduction of 2-5% caused by transversal cracks, the second stage with an additional decrease between 1-5% with damage dominated by the edge delamination and longitudinal cracks, and the final stage when an abrupt failure happens.

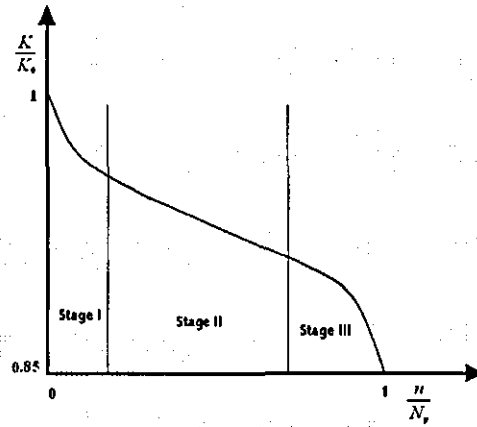


**Figure 2.8 Typical stiffness degradation curves in composite materials**

Various models to analyse the stiffness decrease in composites that can be used for adhesives have been suggested by different researchers, with [60, 61] presenting summaries of the most important ones.

### *Yang's model*

Experimental work on CFRP composites under fatigue at  $R = 0.1$  and different stress levels was used to propose the following stiffness degradation model for a fibre-dominant composite laminate [62] :

$$\begin{aligned} K(n) &= K_0 [1 - Qn^\nu], \\ \nu &= a_3 + B\sigma_{\max}, \\ Q &= a_1 + a_2\nu, \end{aligned} \quad (2.36)$$

where  $a_1, a_2, a_3$  are parameters independent of the applied stress level  $\sigma_{\max}$ ;  $B$  is a random variable with a lognormal distribution and  $K_0$  is the initial stiffness. A stiffness deterioration law for fatigue in such laminates can be written as:

$$\frac{\partial K(n)}{\partial n} = -K_0 Q \nu n^{\nu-1}. \quad (2.37)$$

### *Whitworth's model*

In his studies of composites, two main phenomenological models were proposed. The first model was suggested in [63] as:

$$\frac{K^a(n/N_F)}{K_0} = 1 - H \left[ 1 - \frac{\Delta\sigma}{\sigma_{\max}^{\text{static}}} \right]^a (n/N_F), \quad (2.38)$$

where  $a$  and  $H$  are experimental parameters that can be determined from experimental data and  $K_0$  is the initial stiffness. A cumulative damage model was proposed as:

$$D = \left[ \frac{H \left( 1 - \Delta\sigma / \sigma_{\max}^{\text{static}} \right)^a}{1 - \left( \Delta\sigma / \sigma_{\max}^{\text{static}} \right)^a} \right] \frac{n}{N_F}. \quad (2.39)$$

The second model assumes that the residual stiffness is a monotonically decreasing function of the fatigue cycle, with a degradation law defined for CA as [64]

$$\frac{\partial K^{\text{eff}}(n)}{\partial n} = \frac{-a}{(n+1)K^{\text{eff}}(n)^{m-1}}, \quad (2.40)$$



where  $K^{eff}(n)=K(n)/K(N_F)$  is the ratio between the residual stiffness  $E(n)$  and the failure stiffness;  $a$  and  $m$  are parameters that depend on the applied stress, loading frequency and environmental conditions. Integrating Equation 2.40 and introducing a stress failure criterion, assuming that failure occurs when the fatigue stress reaches the ultimate stress, the residual modulus is:

$$K(n) = K_0 \left( \frac{\sigma_{max}}{c_1 \sigma_{static}} \right)^{1/c_1} \left[ -h \ln(n+1) + \left( c_1 \frac{\sigma_{static}}{\sigma_{max}} \right)^{m/c_2} \right]^{1/m}, \quad (2.41)$$

where  $c_1$  and  $c_2$  are experimentally obtained constants,  $h$  is  $a \cdot m$  and  $\sigma_{static}$  is rupture stress in static conditions.

#### **Zhan's model**

In a recent study of adhesively bonded joints (DLJ and SLJ) with a GFRP composite as the adherend two phenomenological models were proposed by Zhan [58], one for each joint configuration, suitable to predict the stiffness degradation caused by fatigue. Those models are described, in general, as linear stiffness degradation for DLJ and a non-linear model for SLJ. The reason of these differences is due to various types of failure observed during the experimental work: delamination in adherends in SLJs and failure in the adhesive in DLJs; that difference in failure scenarios can be explained by different stress distributions in those joints. For DLJ it was proposed that:

$$\frac{K(n)}{K_0} = 1 - k_1 \left( \frac{F}{F_{max}} \right)^{k_2} n, \quad (2.42)$$

where  $k_1$  and  $k_2$  are independent cycle and applied load parameters and  $n$  is the number of cycles. In the case of SLJ, a nonlinear model was proposed:

$$\frac{K(n)}{K_0} = \left( \frac{n \times k^m}{V - n} \right)^{\frac{1}{m}}, \quad (2.43)$$

where  $V$ ,  $k$  and  $m$  are parameter estimated by fitting the experimental data.

### 2.5.1.3 Residual strength models

#### *Yao-Himmel's model*

This model considers that experimental data has a sinusoidal character (similar at the three stages observed in Figure 2.8) when the residual strength  $\sigma_R$  is plotted versus the normalized fatigue life, and is defined in the following form:

$$\sigma_R = \sigma^{static} - (\sigma^{static} - \sigma_{max}) \frac{\sin(\beta \frac{n}{N_F}) \cos(\beta - \alpha)}{\sin(\beta) \cos(\beta \frac{n}{N_F} - \alpha)}, \quad (2.44)$$

where  $\beta$  and  $\alpha$  are empirically defined parameters [65].

The Yao-Himmel's model was extended in [66] to variable amplitude fatigue defining a cumulative damage rule for each load block  $i$  with respect to residual strength  $\sigma_{Ri}$  for the block  $i$ , as follows:

$$D_i = \frac{\sigma^{static} - \sigma_{Ri}}{\sigma^{static} - \sigma_{maxi}}. \quad (2.45)$$

Assuming that no interaction exists, and that the specimen ruptures when the residual strength is equal to the maximum loading level, it follows that:

$$D_i = \frac{\sin(\beta(n/N_F)_i) \cos(\beta - \alpha)}{\sin(\beta) \cos(\beta(n/N_F)_i - \alpha)}. \quad (2.46)$$

#### *Schaff and Davidson's model*

A methodology to analyse the evolution of damage in composites was defined in [67]. That model was based on the residual strength  $\sigma_R(n)$  of a specimen during fatigue.

This model assumes that the initial residual strength is equal to  $\sigma^{static}$  (static strength) and it decreases as the number of cycles increases. Failure occurs after  $N_F$  cycles when  $\sigma_R(n)$  reaches the same value that has the maximum stress from the sinusoidal load spectrum ( $\sigma_{max}$ ) ( $\sigma_R(N_F)=\sigma_{max}$ ). It is considered that in cycle  $n$ ,  $\sigma_R(n)$  has the following magnitude:

$$\sigma_R(n) = \sigma^{static} - (\sigma^{static} - \sigma_{max}) \left( \frac{n}{N_F} \right)^{\nu}, \quad (2.47)$$

where  $\nu$  is a degradation parameter. In VA fatigue, introduction of a second block at the model makes it necessary to introduce an equivalent number of cycles ( $n_{eff}$ ) that is shown in Figure 2.9. Here, curve ABCD represents the residual strength after completing two load blocks. In this case, by definition  $\sigma_{R1} > \sigma_{R2}$ , and  $\sigma_{R1}$  has a linear strength degradation ( $\nu_1=1$ ). This model assumes that the specimen will be at point B when it is loaded at  $\sigma_{1max}$  by  $n_1$  cycles and the strength will be defined by Equation 2.47. However, when the second load block is introduced, the system will follow ACD and point C represents an equivalent strength that a specimen has before being loaded at  $\sigma_{2max}$ .

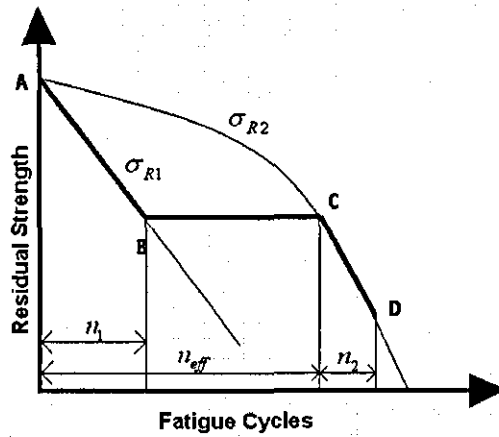


Figure 2.9 Schaff and Davidson's method

To correlate B and C, an effective number of cycles should be determined assuming that the specimen has the same strength between these points:

$$n_{eff} = \left[ \frac{\sigma^{static} - \sigma_{R1}(n)}{\sigma^{static} - \sigma_{2max}} \right]^{1/v_2} n_2. \quad (2.48)$$

Finally, strength of point D is defined in terms of the effective number of cycles at C plus  $n_2$  as:

$$\sigma_R(n_1 + n_2) = \sigma^{static} - (\sigma^{static} - \sigma_{2max}) \left( \frac{n_{eff} + n_2}{N_2} \right)^{v_2}. \quad (2.49)$$

Additionally, the authors developed an important model to evaluate loading sequences with small cycle blocks. In order to include changes in the magnitude of the mean stress from one segment to the next, it was proposed to include the cycle mix (CM) factor; correcting the residual strength:

$$(\sigma_R(n))_{eqv} = \sigma_R(n) - CM, \quad (2.50)$$

where CM is the mix factor defined as:

$$CM = C_m \sigma^{static} \left[ \frac{\Delta \sigma_{mn}}{\sigma_R(n)} \right]^{(\Delta \sigma_p / \Delta \sigma_m)^2}, \quad (2.51)$$

where  $\Delta \sigma_p$  is the change in the peak stress magnitude, and  $\Delta \sigma_m$  is the change in the mean stress magnitude. In [68], a modification of the CM factor was presented in order to predict complex load patterns such as block load changes in CA and inclusion of overloads. This term was included in a linear residual degradation expression for  $\sigma_R(n)$  making it capable to predict  $N_F$  for a complex load pattern with high accuracy.

## 2.5.2 Fatigue crack growth rate curve approach

The fatigue crack growth rate curve (FCGR-curve) approach is a common technique used to characterise the fatigue crack growth rate ( $da/dn$ ), at which the crack grows,

as a function of the number of cycles with respect to some fracture mechanics parameter. A typical way to show these results is by plotting  $\log(da/dn)$  vs.  $\log(G_{\max})$ , where  $G_{\max}$  is the strain energy release rate, calculated from the maximum load (Equation 2.3). Three different regions can be identified in this graph as seen in Figure 2.10. Region I is characterised by a threshold value, below which no fatigue failure is present. In region II, there is a quasi-linear relation between  $\log(G_{\max})$  and  $\log(da/dn)$ . Finally, in region III the crack has a fast-growth tendency, having an asymptotic value  $G_c$  ( $G_c$  is the energy release rate for failure in quasi-static conditions).

Usually, for adhesives and composites  $G$  is used as the fracture mechanics parameter in preference to  $K$ . In addition, it is common to use  $G_{\max}$  rather than  $\Delta G$  (i.e.  $G_{\max} - G_{\min}$ ) because the cracked surface can be affected by friction in the unloading process. This factor increases the real value of  $G_{\min}$  [48].

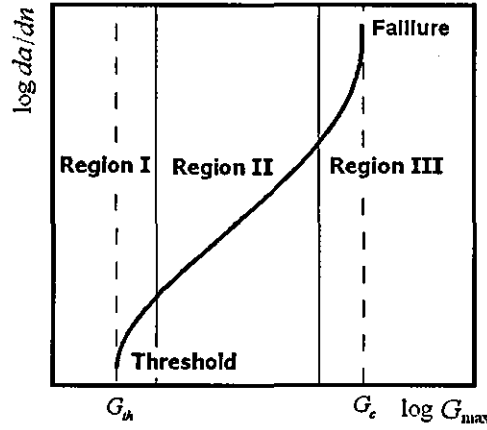


Figure 2.10 Typical fatigue crack growth curve

### 2.5.2.1 Empirical model of Fatigue Crack Growth

An empirical relation between  $(da/dn)$  and  $K$  was defined in [69] and commonly referred to as Paris law. His studies concluded that for region II the FCG has the following tendency:

$$\frac{da}{dN} = C \Delta K^m, \quad (2.52)$$

where  $C$  and  $m$  are material constants,  $\Delta K$  ( $K_{\max} - K_{\min}$ ) is the amplitude stress intensity factor, with stress intensity factors determined for the maximum and minimum load. Some studies replace the parameter  $\Delta K$  by  $\Delta G$ .

In [70] a total life model for composite samples subjected to Mode I fatigue loading was developed. That model was based on the inter-laminar fracture toughness resistance ( $G_{IR}$ ), which is defined as the instantaneous material resistance as a function of the crack size and the critical material fracture toughness ( $G_{IC}$ ). Experimentally, it was observed that  $G_{IR} = G_{IC}$  when the delamination begins to grow; however, as the crack size increases  $G_{IR}$  begins to be higher than  $G_{IC}$ . This phenomenon is explained as cause of matrix cracking and fibre bridging in the case of unidirectional composites. It was also supposed that  $(da/dn)$  was proportional to the cyclic force  $G_{I\max}$  but inversely proportional to the resistance  $G_{IR}$ . Finally,  $(da/dn)$  was limited by the threshold energy release rate  $G_{IR}$  ( $da/dn = 0$ ) and  $G_R$  ( $da/dn = \infty$ ):

$$\frac{da}{dn} = C \left( \frac{G_{\max}}{G_{IR}} \right)^m \left[ \frac{1 - \left( G_{th} / G_{I\max} \right)^{m1}}{1 - \left( G_{\max} / G_{IR} \right)^{m2}} \right], \quad (2.53)$$

where  $C$ ,  $m$ ,  $m1$  and  $m2$  are material constants.

### 2.5.2.2 Numerical crack growth integration

The numerical crack growth integration (NCGI) is a technique used to predict the crack size under VA conditions from the FCGR-curves of CA tests. In this approach an initial crack size,  $a$ , is related with a  $G_{\max, i}$ , which is assumed constant throughout the stage  $i$ . FCG rate, for the stage  $i$  can be obtained from the Paris law relation. Multiplication of this rate by the number of cycles in the stage  $n_i$  gives the increase on the crack growth during the stage  $i$ . This process is repeated for the number of cycles interested.

$$a_{i+1} = a_i + n_i \frac{da}{dn} (G_{\max, i}(a_i)) \quad (2.54)$$

### 2.5.2.3 Damage shift model

A model to analyse VA fatigue in adhesive joints based on the fatigue crack growth approach is presented in [71]. It was supposed that under CA block  $a$ , fatigue could be analysed using the FCG approach and represented by  $G_{th}$ ,  $G_C$ , and two Paris constants  $C$  and  $m$  (Equation 2.52). For instance, it was determined that when a constant amplitude load block referenced as  $a$  was applied (with Paris's law constants  $C_a$  and  $m_a$ ), it produced  $\Delta G_a$ , that resulted in a growth rate  $(da/dn)_a$ . However, when an overload was imposed to the load pattern  $a$ , the damage level in the process zone could increase and, therefore, decrease the resistance to crack propagation. It was proposed that such increases of damage would shift the FCGR-curve by  $\psi_E$ . It was proposed that as the crack grows in the damage zone, an equilibrium position of the FCG was reached and the parameter  $\psi_E$  could be calculated as

$$\psi_E = f(N_R, R_{ol}), \quad (2.55)$$

where  $N_R$  is the number of overloads and  $R_{ol}$  is the ratio between  $\Delta G_a$  and  $\Delta G_{ol}$  (the latter is  $\Delta G$  at the overload). Special attention should be taken, as emphasised by the author, when  $\Delta G_a$  increases as the crack grows because it is possible that it reaches the critical value  $(\Delta G_a)_C$  for the shifted FCGR-curve (Figure 2.11). It was suggested that in that case an unstable or quasi-static crack appeared producing a catastrophic failure of the specimen. However, in the case when the  $\Delta G_a$  decreased as the crack grew, it was possible that eventually the crack would stop but with an arrest strain energy release  $(\Delta G_{arr})$  lower than the value that was without overload.

That model was proposed in order to explain the acceleration phenomenon observed experimentally when an intermittent overload was introduced into a CA load pattern. In the case that a failure grows inside of the FRPC adherend, X-ray analyses of adhesively bonded structures showed the existence of a damage region ahead of the crack tip where small debonding or fibre debonding could exist generating a decrease in the energy necessary for a crack growth [71]. In the case when the overload was imposed, an increase of the damage zone could be detected confirming a faster crack growth [68].

### 2.5.2.4 Load effects in fatigue crack growth

Researchers have analysed the effect of loading conditions on the FCG in order to identify crack acceleration phenomena and how they change the normal behaviour of the FCGR-curve. A review of the effect produced by variation of each of the test parameters follows.

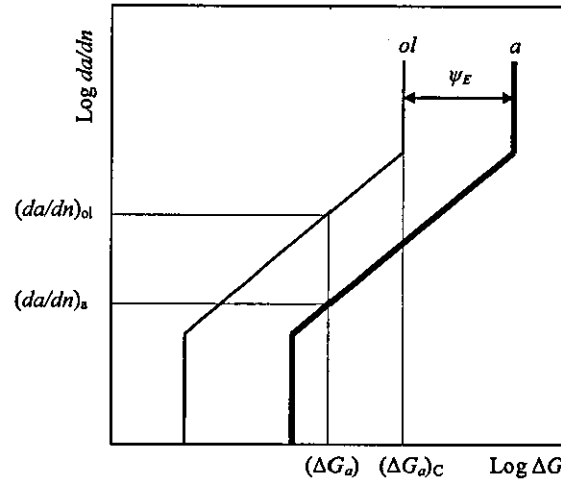


Figure 2.11 Damage shift model

#### *Effect of frequency*

It was found that adhesive joints were sensitive to the frequency of applied loading. The effect of different frequencies on the FCG behaviour on DCB steel bonded joints was studied in [72] where two types of adhesives were used, tested at three frequencies of 0.02, 0.2 and 2 Hz. No significant effect on the FCG was detected for one adhesive. However, in another adhesive it was found that a decrease in frequency caused a reduction in the threshold value and acceleration on the crack growth. Such behaviour is justified by an increase in the load application time in experiments performed at positive load ratios and low frequency, making the creep behaviour more likely to appear. These conclusions can also be used to analyse the results presented in [73]. In these tests, three frequency levels with adhesively bonded CRFP and mild steel specimens it was also observed that the FCG increased and the fatigue threshold decreased as the frequency decreased.



### ***Effect of R-ratio***

In [68], changes of the FCG caused by the load ratio were investigated using a DCB specimen with CFRP-epoxy adhesive system. It was observed that the fatigue threshold decreased with the decreasing load ratio. For instance, the FCGR-curve showed quasi-similar tendencies when they were plotted as a function of  $\Delta G$ ; however, when curves were plotted as a function of  $G_{max}$ , it was observed that as  $R$  decreased a high crack growth occurred. Similar changes of graphs were also reported in [74]. In [75], the influence of  $R$  and the frequency on the FCGR-curve was analysed, concluding that the effect of the frequency is much lower than that of  $R$ ; it was explained that such behaviour was due to viscoelastic properties of the adhesive.

### ***Effect of bonding thickness***

As mentioned before, thickness of the adhesive layer was shown to affect the fracture energy measured for adhesive specimens, basically, due to a relation between thickness and the size of a plastic region. However, some researchers mentioned that relation could affect the FCG only for particular specimen configurations [76]. In [77], working with a DCB specimen and a specific adhesive range thickness, it was observed that the greater the thickness, the lower is the FCG rate. That effect was explained by an increasing stress level at the crack tip with declining thickness of the adhesive, consequently, increasing the FCG rate. However, there exists a limit thickness, for which no changes on the FCG can be perceived [78].

### ***Effect of mode mix***

It was analysed by various researcher that fracture toughness under mode  $I$  in quasi-static conditions is lower than in mode  $II$  [79]; this suggests that under fatigue a lower FCG resistance can be expected in mode  $I$  than in mode  $II$ . This kind of tendency was observed in [80] using a LSJ in three point bending where a lower FCG was found under a mix-mode than in a pure mode  $I$  of loading. On the other hand, comparison of the  $G_{th}$  value at various temperatures was presented in [81] working with different joint configurations DCB, LSJ and DLJ. It was observed that for all temperatures measured ( $-50^{\circ}\text{C}$ ,  $22^{\circ}\text{C}$  and  $90^{\circ}\text{C}$ ) the variation of  $G_{th}$  followed the relation  $(G_{th})_{DLJ} < (G_{th})_{DCB} < (G_{th})_{LSJ}$ , being almost constant for the temperature range used except for low temperatures in DLJ. However, differences in the definition of thresholds in specimens can affect these tendencies; in the case of DCB it was defined as a level, at which the crack suffered an arrest but in LSJ and DLJ it was defined as the load that

could support  $10^6$  cycles in the specimen without formation of a macro-crack. In a recent work [82], the FCG of an aluminium alloy adhesively bonded under pure mode *I*, mode *II* and controlled mixed modes was analysed using a compact tension shear (CTS) specimen. An increase in the FCG resistance in the mixed mode and mode *II* was found with respect to mode *I*, confirming similar results found before. However, those results did not support the difference found for quasi-static values. It was proposed in [82] that for some adhesives the viscoelastic behaviour could produce such changes in addition to the heating at the crack tip due to hysteresis where a softened material can exist during fatigue. It would result in a stress redistribution that differs from that for the quasi-static behaviour. In conclusion, the effect of the FCG under pure mode *I*, mode *II* and the mixed mode is not always obvious and depends, in particular, on the type of adhesive that is used.

#### *Effect of environment*

Analyses of the FCG in CFRP composites, adhesively bonded in DCB beams, were carried out at different temperatures in [81]. They found that when the temperature increased,  $G_{th}$  increased and the ratio  $G_{th}/G_c$  decreased; the failure occurred in the composite adherends at low temperature and in the adhesive layer, cohesively, at higher temperature. A similar behaviour was presented in [75] with changes in the FCGR-curve slope being caused by changes of the temperature; the environmental factor was studied using LSJs under four-point bending. It was observed for specimens tested at room temperature that as the temperature increased the FCG resistance increased. However, when specimens were tested at higher temperatures (90°C) the behaviour changed decreasing considerably the FCG resistance; no explanation to that behaviour was given. An additional conclusion that was obtained in that work is that at constant temperature a change in environment condition from air to a salt water environment decreases FCG resistance in all the cases.

Effects on  $G_{th}$  at different temperatures and humidity levels were studied in [37], where similar values of  $G_{th}$  in dry conditions were found for LSJ tested at different temperatures. In addition, it was found that specimens tested at high temperatures or high moisture content did not demonstrate significant changes in  $G_{th}$ ; however, when LSJs were tested at both conditions a drastic decrease in  $G_{th}$  was found. The authors explained that behaviour indicating that  $G_{th}$  decreased when test conditions were near

to the glass transition temperature ( $T_g$ ); and  $T_g$  was reduced by the moisture level observed in LSJs tested at high temperatures. Finally, it was suggested that fatigue crack initiation, damage patterns and failure modes were influenced by environmental conditions.

## 2.6. Discussion

To understand the fatigue behaviour of adhesively bonded joints various researchers used various approaches based on fracture mechanics theory. Obviously, this theory has limitations such as an assumption that the material is in the undamaged state in front of the plastic region (in the case of NLEFM) or near the crack tip (for LEFM) neglecting the effect of a damage zone in front of the crack tip. Still, it can be useful; especially to understand features crack initiation and propagation.

Although application of the fracture mechanics approach to predict the fatigue life in adhesively bonded joints was successful, there is further work to be undertaken in this area. Previous research was mainly focussed on common joint configurations like SLJ, DLJ, DCB; under standard fatigue, however, other types of joints like LSJ that are present in many real components and structures have attracted little attention. It is hoped that the work of this thesis will address the issue of this type of geometry with the use of fracture mechanics in predicting fatigue in LSJ in SF and *impact fatigue*.

## 2.7. Conclusions

This chapter reviewed the basic principles of fracture mechanics and its implementation. In addition, describe applications of fracture mechanics to some geometry of adhesively bonded joints and the models that are suitable to analyse the fatigue behaviour of adhesively bonded joints. From understanding of these principles it is possible to investigate in detail the fracture behaviour of adhesively bonded joints under fatigue conditions. A review of the previous research into *impact fatigue* is presented in the next Chapter.

## CHAPTER 3

### Impact fatigue

#### 3.1. Introduction

Prediction of the performance of various structures and components under real-life loads are usually based on models upon fundamentals material behaviour. These models are validated by experimental studies performed on specimens using relevant types of mechanical loads; an isothermal case is considered in this thesis. Such loads are a generalisation of loads experienced in service and normally limited to quasi-static, cyclic, dynamic, creep and relaxation tests. A need for these various types of tests is linked to different responses of the same materials to various loading conditions, and there is a general understanding that results, obtained in experiments of one type can hardly be sufficient to predict outcomes for other experiments. One of the examples is a dynamic overshoot factor, roughly doubling the maximum magnitude of the load due to the weight if it is suddenly applied to a component. Still, one type of the load has yet not obtained the attention, which it undoubtedly deserves. This is a repetition of low-velocity impacts, with each impact being insufficient to cause the total failure of a structure or component. This type of loading is known as *impact fatigue* (IF) and at in the centre of this study.

It is a well-established fact [83] that research into IF started effectively at the same time as the one into standard fatigue, i.e. in the middle of the 19th century [84]. More

than a century ago a ‘shock-fatigue’ test, defined as a one ‘involving a large number of relatively small blows’ was used to study a response of steels to this type of loading in comparison with a static test and a ‘single-blow’ test [85]. Those tests were performed with specially designed testing machines for impacts in bending, tension and compression. The tests in bending were implemented for loading histories of up to  $10^6$  cycles while those for tensile impacts – ‘owing to the relatively slow speed of the direct-impact tester’ – were limited to 50000 impacts [85]. A difference between effects due to IF and both single-impact loading and standard fatigue was apparent at that time as well as the absence of a durability limit (named ‘limiting resistance’).

Still, more than a hundred years after those conclusions the area of IF is considerably less studied than that of standard fatigue. There are several reasons for such a situation. One of them is ambiguity in the choice of the loading parameter. For a standard fatigue, an obvious parameter is the stress amplitude that comes back to the notion of Wöhler’s  $S-N_F$  diagrams in stress-controlled fatigue. In IF, a maximum stress magnitude can be hardly used as a sole parameter since, depending on the loading conditions, especially the impact velocity, the same level of this parameter can correspond to different levels of the applied energy. As a result, different authors have been using various loading parameters in their studies.

Another reason is the specificity of IF realisation in different types of materials. Already in 1908 Stanton and Bairstow [85] noticed ‘remarkable endurance for lighter blows’ in brittle specimens. Some authors even mention a higher resistance of specimens exposed to impact-fatigue conditions as compared to standard fatigue. This can be explained by a link between the levels of impact energy, contact duration and damping properties resulting in a specific type of spatial localization of the stresses and their decay with propagation from the contact area. This linkage can differ with kinematics of impact-induced deformation and the specimen geometry and type of fixture. One extreme example is shot peening, which is a process of repetitive impacting with tiny particles, resulting in improved fatigue performance due to strengthening of a near-surface layer [86]. Another example is repetitive impacting of laminated composites in drop-weight test systems (see e.g. [87, 88]), where the most

affected zone is situated below the contact area, resulting in delamination initiation in this part of laminate and its subsequent spreading to other parts of tested specimens.

Impact events that arise in aerospace structures and components due to; gusts, storms and landing can be masked in loading history diagrams, presenting thousands loading cycles with various amplitudes. The existing methods to treat such diagrams, e.g. so-called 'rainflow technique' [89], are considered with a proper way of counting events, making no distinction between impacts and relatively slow cycles that can be treated as non-IF events. This can be very dangerous, since impacts with lower amplitude can be more damaging than non-impact cycles with higher amplitudes.

The main purpose of this Chapter is to provide background information on impact fatigue and to emphasize the relevance of this research. In order to reach this aim the following objectives of the research are suggested:

- To review the impact test standards;
- To review the area of IF in adhesives;
- To review the area of IF in composites;
- To review the area of IF in polymers.

### **3.2. Impact tests**

Research into impact loading of materials is mostly limited to analysis of the material's response to a single impact, studying its dependency on the impact velocity, impact force and impact direction (transversal, in-plane impacts or oblique impacts). Three main types of tests are used to analyse the effect of impacts: (i) experiments with pendulum impact testers with impact rates below 5 m/s; (ii) drop-weight tests, with rates up to 10 m/s, and (iii) a split Hopkinson pressure bar (SHPB) testing technique for rates up to 100 m/s [90]. Specifically in the area of adhesives, two standard tests were proposed to evaluate the impact strength in adhesives: ASTM D950-03 Standard Test Method for Impact Strength of Adhesive Bonds [91] and ISO 11343:2003 Adhesives - Determination of dynamic resistance to cleavage of high-strength adhesive bonds under impact conditions, the wedge impact method [92]. The first of these standard methods employs two bonded together blocks as seen in Figure 3.1; the bottom block is rigidly secured in the test rig, and a pendulum hammer strikes

the top block, generating a shear load in the adhesive layer. In [93], the block impact test was analysed and it was concluded that the stress condition was uncertain due to complex dynamic effects generated by uncertainties in the contact interface between the block and hammer. The second method was originally proposed in [93]; this test method employs a wedge inserted into the specimen as seen in Figure 3.2; as the wedge is moved under impact the adherends starts to deform producing a peeling loading in the adhesive. Disadvantages of this method were also discussed by the authors describing that the local stress in the adhesive depended strongly on deformation of the adherend as well as on the angle of the wedge; in addition, the friction between the wedge and the broken adhesive could not be measured. Another disadvantage is that high levels of energy are consumed by plastic deformation of the adherend which increases as the thickness grows. In [94], this technique was used experimentally and modelled by FEM to analyse a variety of rubber-toughened epoxy adhesives. In that work it was found that the shape affected test measurements, and the obtained FEM results depended on the friction coefficient  $\mu$  between the wedge and the fracture surface and, obviously, on the  $G_c$  value of the adhesive. However, as expected, the results depended mainly on  $G_c$  than on  $\mu$  but the latter also caused differences in the results.

Local setups were proposed by various researchers to analyse impact in adhesive joints. The single lap impact test in [1] was proposed as an alternative; and it was reported in [94] that the deformation of the adherend is affected by the plastic deformation of the adherends. However, this is a more similar technique than those normally used to analyse standard fatigue or quasi-static fracture behaviour.

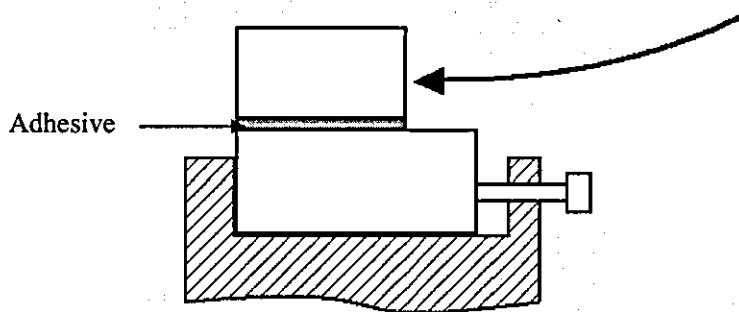


**Figure 3.1 Schematic representation of an impact block test**

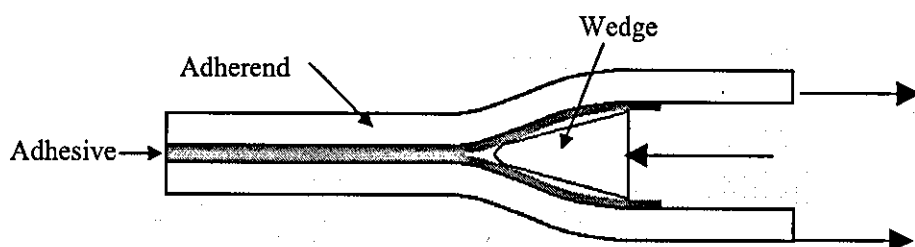


**Figure 3.2 Schematic representation of a wedge impact specimen**

### **3.3. Impact in composites**

High performance FRPC are now well established in many applications such as military aircraft, high speed marine vessels and sports equipment. Increasing usage is also being found in civil aircraft, automotive and building applications. The original reason to use these materials was their high specific (i.e, per unit mass/density) strength and stiffness; however, other potential advantages include reparability, insulating properties, corrosion resistance, possible use in stealth applications and fatigue resistance. In fact, good resistance of FRPCs to fatigue led to an early design philosophy based on quasi-static strength alone. However, with further research and increased studies of components after extended periods in service, it is now recognised that fatigue is potentially damaging to composites and hence is worthy of serious study. Furthermore, fatigue is also linked with two of the main drawbacks of these materials, namely, that initial damage is sub-surface, and hence difficult to detect and, secondly, that the transfer from a stable to unstable crack growth can occur at short crack lengths. Together these two features can mean that the first sign of fatigue damage can be complete failure of the structure. This led to research into fatigue of composites, including the fatigue-related propagation of sub-surface cracks caused by low energy impact, such as the classic scenario of the dropped tool during a maintenance work [5, 95, 96]. Most of this research work has been conducted using SF or, in some cases, simplified versions of load spectra taken from experimental measurements employing techniques such as the rain flow method. However, the in-service load spectra for structural applications can in some cases contain repetitive low-energy impacts, i.e. IF. This type of loading has received little attention to date but has been shown to be damaging to composite materials. The next sub-sections



detail some of the research performed on the analysis of impact and impact-fatigue in FRPC both experimentally and in modelling.

### **3.3.1 FRPC under a impact**

In impacts situations, materials are exposed to different loading conditions compared with static loading since they involve dynamic factors of loads such as inertia; besides materials respond differently to these loading conditions. These were the reasons for researchers to use different ways to analyse experimentally the behaviour of composites exposed to impacts. A description of the principal experimental studies conducted by various researchers for impacts is presented below.

A preliminary step to study FRPCs at impacts is to analyse the load rate sensitivity of materials. In general, it is well known [97-100] that the interlaminar shear strength (ILSS) of carbon fibre/epoxy composites increases with strain rate. In [97], working with a SHPB setup it was suggested that such behaviour could be attributed to the time-dependent deformation of the material, which is a product of the viscoelastic behaviour of the composite matrix. In addition, it was found that even in specimens that do not exhibit failure, the stress-strain behaviour in the unloading part is principally different from that in impacting loading. This was attributed to the heat generated by high strains affecting the structure of the matrix material. A further study [98] showed that the maximum stress supported by the material in a single impact decreased considerably with an increase in the temperature. However, it was concluded in [99], working with a carbon fibre reinforced composite, that increases in ILSS when specimens were tested at impact, were not accompanied by any significant differences in fracture surfaces compared to samples failed under quasi-static loads. For instance, in [101] a relation between the ILSS and the level of the impacting energy was found concluding that the residual ILSS after an impact decreased as the impact energy increased because of the damage size growth.

On the way to understand the effect of an impact, a common method was to define the residual strength of a material that had been previously impacted with a lower energy. In [102], a tensile and compressive strength degradation of CFRP was observed when

they were exposed to impacts being influenced mainly by their level and number; however, that degradation was limited to the region near the impact point. Another way to analyse the influence of impacts in CFRP was to apply a transversal impact over a plate that is clamped using a special device. The transversal impact caused visible damage and delamination in the plate [5] affecting significantly its mechanical properties and being the reason for a high reduction of compression strength [103, 104]. However, such reduction can be decreased by the manufacturing process when woven laminate [105], stitched woven CFRP [106] and pre-tensioned high strength fibres [107] were used.

Another way to analyse the decrease in the mechanical properties of FRPCs is to measure the impact fracture energy necessary to break a pre-impacted specimen. In [108, 109] pre-impacted specimens were tested by a critical impact energy using a commercial CFRP and an instrumented Izod machine, to cause complete failure. The results showed that the energy necessary to break specimens could be divided into three ranges in terms of the pre-impacted energy level: the first range when insufficient damage was produced by the pre-impact to enlarge micro-cracks and debonding; the second range, characterised by a transition zone where micro-cracks produced in the matrix as a result of previous impacts merged generating a debonding zone that decreased considerably the fracture energy; and, finally, a third range when specimens that did not completely failed in the pre-impact had an extremely low quasi-constant fracture energy. For instance, the division into the regions for the IF was also detected in curves of local damage vs. number of impacts [110]. An additional study also showed that an impact could affect the fatigue behaviour of FRPC; in [111], the fatigue life of CFRP laminates was investigated with sinusoidal in-plane loads being combined with a single transversal impact. It was found that fatigue strength of CFRP was affected by the sequence, with the effect being more pronounced in the case when the sinusoidal load followed the impact than in the inverse sequence. Similar experiments have been performed with a glass fibre-reinforced composite (GFRP) [112], where it was found that a single transversal impact had a significant effect on the fatigue life and that behaviour was strongly related to the post-impact residual strength.

### 3.3.2 FRPC under impact and fatigue

Analysis of IF in FRPCs was principally aimed at characterisation of the fatigue life reduction with the increasing load. In [111, 113] the  $S-N$  diagram was used to describe the fatigue life reduction. It was found that an increasing amount of impact damage followed by the cyclic tensile impacts reduced the fatigue performance of the material having, in general, a linear trend in semi-logarithmic coordinates.

However, a more common way to analyse the fatigue life reduction during IF was to use the energy vs. number of cycles curves ( $E-N_F$ ) plotted in the majority of the cases in semi-logarithmic coordinates [88, 108, 114-117]. In [115], working with a jute/vinyl-ester composite in a cyclic Charpy test showed an increase in the material's endurance as the impact energy decreased. Such graphs are divided by some researchers into several regions [116], and in some cases it was possible to identify a threshold energy, below which no visible delamination was observed [108, 114]. However, it was mentioned in [104] that in FRPCs low-energy transversal impacts, which were insufficient to leave any visible damage under the surface, could produce internal damage that could grow under the influence of subsequent cyclic loading. This suggests that not enough experimental work is available to clarify the existence of an endurance limit in FRPCs.

Some research was aimed at analysis of the dependency of IF on the orientation of the fibres in CFRP. In this way in [113], using a Charpy test and different adhesive interlayers and lay-ups it was found that quasi-isotropic laminates have a better fatigue lifetime than cross-ply ones when tested with transversal impacts. However, other variables can increase the transversal impact resistance, e.g. composition of the matrix. In [118] for GFRP tested with a drop weight machine it was observed that a damage area after one transversal impact was highly dependent on the fibres architecture (woven or multi-axial stitched) and resin (brittle or ductile) used. The most critical factor was the matrix composition and it was found that the lowest damage area was observed when a ductile toughened resin was used. However, when similar materials were analysed in IF no difference in the effect of different fibres and matrix was found in the  $E-N_F$  graph, especially, when the energy was normalized in

terms of the penetration energy defined as the energy necessary for a falling weight to penetrate the laminate.

Another kind of variables that are analysed in transversal IF is the interval time defined as a time between subsequent impacts. It was found that increases in the interval time resulted in a lower number of cycles to crack initiation and failure, especially when the applied impact load was small. In addition they found that those results contrasted with test results for standard tensile fatigue. Such behaviour was explained by the fact that at the higher interval time there was enough time to recover deformation confining the damage zone to a small area. However, in the case of low-interval impacts the damage zone is de-localized because the area of contact with the striker increased without the deformation recovering process, increasing the portion of the specimen that can absorb energy in the impact thus resulting in a greater number of impacts to failure.

Researchers also tried to develop models to describe IF in FRPCs. In [119], an investigation of a model for damage and failure of GFRP plates under low velocity IF was carried out. The experimental work conducted by a crank mechanism, introduced transversal cyclic impacts. It was shown that IF caused a reduction in the bending stiffness. And even low-energy impacts produced internal delamination causing a decrease in the laminate strength, even though there was no observable damage. A local damage parameter defined in terms of bending stiffness was suggested; in addition, it was observed that three regions described the damage evolution in the material under IF when damage was plotted against the number of impacts. The first region is linked with initiation and multiplication of delamination, when delamination occurs under the surface; the second zone is characterised by saturation of delamination, when propagation of existing delamination zones and development of new ones are stopped. Finally, the third region is linked with ply cracking with fibre breaking, when damage accelerates until final failure. However, no corroboration of that model with experimental work was presented.

### 3.3.3 Modelling impacts in FRPC

In this section a description of the major work conducted on modelling impact in FRPCs is carried out. The main strategies normally used are mentioned, however, the author recommends [120] for an in depth review of this area.

Criteria of failure for laminate composite structures used in impact conditions were proposed in [121, 122]. Those criteria are described, in general, as a stress-based relation for an account of the delaying effect of compressive stress on delamination initiation. They were verified for simulation of a single low-velocity transversal impact. The criteria involved different damage modes: matrix cracking, matrix crushing and delamination. An interaction between those damage mechanisms was compared with experimental studies and was reported to be in a good agreement. However, other authors [123] also used Chang-Chang's damage criterion, proposed originally for tensile loading [124], to analyse low-velocity transversal impacts in a vessel with and without full internal pressure using their own finite element code. Special attention was taken to define the Hertzian contact law to calculate the contact force between the impact body and the impacted cylindrical vessel. In [125] an extension to Chang-Chang's damage criterion was proposed to predict damage initiation under transversal impacts in CFRP composite. That failure criterion for estimation of delamination was defined in terms of three stress components: plane stress, interlaminar shear stress of the immediately lower ply of the concerned interface and interlaminar shear stress of the intermediately upper one. Some empirical constants were included into the model that should be evaluated by experimental studies. The author concluded that the model-based predictions were in agreement with the test data.

A review of the strategies used by researchers to model delamination with previous transversal impacts was presented in [126]. The strategies were classified into four main groups according to the type of interface between the delaminated and base regions: hybrid elements, a de-equivalence crack, a degraded inter-laminar layer and a sub-structure. In strategies based on hybrid elements the upper plies and lower plies divided by delamination are connected by beams, springs or some type of contact. In the second group an artificial delamination area is included without connection

between these groups of plies. The models with degraded inter-laminar layers have a thin layer placed between plies, and delamination is simulated as a reduction in the elastic properties of the isotropic element. Finally, delamination is treated as a sub-structure when only the delaminated region is modelled, assuming that its thickness is small compared with the upper and lower plies.

However, many works in the area used cohesive elements and continuum damage mechanics to analyse damage evolution under low-velocity transversal impacts. In [127], a two-parameter bi-linear cohesive law was used to describe the interfacial behaviour under mode *I* and mode *II*, calibrated with experimental results. It was concluded that cohesive elements were suitable to simulate the sequence and location of damage areas under transversal impacts response predicting them well in terms of shape, orientation and sizes for a range of impact energies. For instance, in [128] a study of damage in CFRP using continuum damage mechanics (CDM) was conducted, with two damage variables being used to represent fibre-matrix debonding and transverse cracks effects. It was mentioned that with the use of CDM eliminates the critical problems with the refined mesh or necessity to know the crack path to generate a mesh using classical fracture mechanics.

### **3.4. Impact in polymers**

Much research in the area of impact and dynamic testing of polymers has been conducted in an attempt to model the most severe conditions that such material can withstand. In general, impact in polymers is tested using the Charpy and Izod methods, and it has been concluded that, in general, the presence of a notch or stress concentrator and high load rates make those materials predisposed to brittle failure. In [129], that phenomenon was explained by the increase in the yield stress as a consequence of increases in the constraint as well as the material rate-dependency. Despite of all the work conducted to understand behaviour of polymers in single impact conditions, little research has been performed in the area of IF to develop theories of failure under such loading condition. For instance, most of research until recently was concentrated on experimental analysis of the phenomenon, and in some cases it was concluded that it was a critical-load scenario that should be taken into

account in design because it could affect the material [8]. Below, a short experimental review in the area of IF in polymers is given.

One of the oldest work on IF in polymers with debatable conclusions was reported in [130]. There, the results obtained in a single impact were compared with those found in IF for a pre-cracked Charpy specimen and using various polymers in a drop weight machine. It was found that in a single impact of a brittle polymer failure occurred catastrophically once the maximum load is reached; in contrast, in a ductile polymer about 60% of the absorbed energy was consumed in propagation. The analysis on IF of those materials, demonstrated that for a brittle polymer the force vs. displacement relation did not change as the number of impact grows. However, for the ductile polymer that relation changed as the number of impact increased, decreasing the maximum force reached at the impact and increasing the displacement as the crack grew due to the effect of fatigue.

Experimental results also showed that crystalline polymers and toughened modified ones generally required higher impact energies to have a failure in a constant number of impacts than non-crystalline and non-toughened modified materials. A parameter called the retained energy for each impact was used and defined as the difference between the impact energy and the energy returned to the impact block. That parameter was used to analyse the fracture energy during IF and a single impact. It was found that for both cases that parameter had a constant value that was higher in the case of IF for similar materials. The author explained the difference found between those fractures energy levels by an additional energy dissipation process in IF suggesting that could be heat generation. Analysing those results with the theory of fatigue, especially with fatigue crack growth, it was found that a constant value for the fracture energy release rate during entire crack propagation resulted in the extremely unstable crack propagation caused fatigue resulting in a nearly vertical portion of the fatigue crack growth graph in IF.

As usual, the fatigue life and the fatigue crack growth analyses were used to study fatigue under impact conditions. In [131] studies with PMMA demonstrated that the Paris law could be used to analyse IF in polymers. For instance, performance of such

materials in standard and *impact-fatigue* was compared by testing samples in four-point bending using a SHPB system. They found that both impact and standard fatigue demonstrated the convectional S-shaped character on the fatigue crack growth graph; however, it was obvious that the material was more resistant to crack propagation under IF than under standard fatigue. In addition, it was observed that those S-shaped graphs depended also on the level of load imposed during IF; as the load decreased, the material was more resistant to crack propagation. That conclusion was also supported by the dependency of  $K_{IC}$  on loading conditions: for impact loads,  $K_{IC}$  was several times the value predicted for standard fatigue, decreasing for both cases as the imposed force increased. More work to obtain  $K_{IC}$  for PMMA was conducted in [132];  $K_{IC}$  for PMMA also reduced when the impact velocity was increased.

The fatigue-life studies were also used to analyse IF. In [133], working with polycarbonate/acrylonitrile-butadiene-styrene material and a drop weight impact tester, it was observed that the impact life increased as the impact energy decreased and the data points seemed to follow an exponential curve. In addition, an accumulation energy term was used to compare the energy necessary to produce failure in specimens with a single impact. It was found that the higher the impact life, the higher the accumulation energy, the term being 35-45 times higher than for a single impact.

A comparison of the results found under IF and under standard fatigue was conducted in [134] for an epoxy resin with and without silica particles. Various ways to analyse the behaviour of those materials were used. In the case on the fatigue life using  $S-N$  diagrams, it was observed that specimens tested under standard fatigue had a higher fatigue life than those tested in IF. For instance, analysing the fatigue crack growth in those materials, it was found that highest crack growth rates were observed during IF than standard fatigue. The results also showed that tendencies of the fatigue behaviour for each composition for specific loading condition could not be used to predict the behaviour for other loading conditions, concluding that different fracture mechanisms existed for each shape and structure of the silica used. Results that corroborated



previous work with those materials demonstrated also the volume fraction of silica also affected IF [135].

### **3.5. Impact in adhesives**

In this section a description of the experimental and modelling works conducted with adhesives is given, defining some mechanism of failure presented in those materials especially due to impact. Some works in the area of IF for adhesives and adhesive joints is reviewed; however, in general, this area is characterised by the lack of research work.

#### **3.5.1 Adhesives under an impact**

Research into impact loading of adhesive joints is mostly limited to study of their response to a single impact showing, except for some cases, which the tensile strength increases as the load rate increases. Some researchers reported similar results for impact and quasi-static conditions, e.g. for a single lap joint tested in a pendulum impact machine in [136]. In [137], higher strength was measured in impact loading; it was supposed that the result was due to the strain-rate sensitivity of the adherends. An analysis of the shear response of a joint with thick adherends, subjected to various stress waves generated by impact, showed that their type of fracture was associated with the level of the incident stress wave [138].

Investigations in the area of single impacts in adhesive joints using the SHPB test [139, 140] demonstrated a considerable increase in the tensile strength magnitude with the loading rate; that also depended on the type of adherends. In that study, an optimum adhesive thickness was identified when the effect of the type of adherends vanished. Similar results were observed in [141] for a commercial epoxy in a DCB specimen concluding that as the test speed increased joint strength also increased. However, in [90] it was found that increases in the energy absorption (area under the graph force vs. displacement) at higher strain rates were observed only for some adhesives.

On the way to analyze impact in adhesive joints researchers studied interaction between the specimen's geometry, loading rate and fracture toughness-crack velocity relationship. It is well known that most of the adhesives are viscoelastic materials and, consequently, are loading rate-sensitive. In [142], in tests with a commercial epoxy bi-component adhesive using SHPB it was found that as the load rate increased the compressive and tensile elastic modulus did not demonstrate high variations; however, a large increase in the yield stress was detected for both cases. For instance, it was concluded that the influence of the load rate in tensile conditions was higher than in compression. Researchers also proposed viscoelastic models to model adhesives at high loading rates, using the Voigt model with five elements demonstrated where a good relation between experimental and predicted results for SHPB tests of an epoxy adhesive has been observed [143]. On the other hand, in analysis of dynamic conditions, stress wave can undergo reflection and amplification increasing momentarily its level for a short time hence increasing stresses especially in regions with stress concentrators. The response of adhesive joints for specimens with similar overlap length was analysed in [143] concluding that the dynamic stress concentrators were higher in single lap joints than in tapered lap joints and scarf joints. It was suggested that the most effective geometry to reduce the stress concentration for the geometries analyzed in dynamic and static conditions was the scarf joint.

A third factor that also affects the dynamic crack growth is the relationship between toughness and the crack velocity. According to the theory of fracture mechanics, cracks can grow under quasi-static conditions when there exists an energy balance between the applied energy and the energy dissipated in crack growth and plastic deformations of the adherends. It was mentioned in [144] that in rate-dependent materials a quasi-static crack growth could also exist, and there should be an equilibrium between the driving force for the crack propagation and the energy dissipated. When the energy available for the crack growth exceeds the energy necessary to generate a new surface and deform plastically the adherends, the system becomes unstable and the crack propagates dynamically. However, the way that the crack would propagate depends on the relation between fracture toughness and the load rate. It is summarized in [145, 146] that for a toughened modified epoxy

adhesives under quasi-static conditions,  $G_c$  usually decreases with increase in the load rate, having a slip-stick behaviour at lower load rates and a continuous crack propagation at higher rates. Researchers proposed two general types of crack propagation: continuous (stable) and intermittent stick-slip type (unstable) [147] and differentiated each mainly by the fracture surface and the force vs. displacement graph when specimens are tested in displacement control under quasi-static conditions. It is defined that for stick-slip crack propagation there exists a non-continuous force growth tendency that is described as a succession of rapid and arrest periods. In contrast, under stable crack growth conditions the force has a more continuous behaviour in the force vs. displacement graph [148]. The stick-slip response of the epoxy adhesive is attributed mainly to the combination of two mechanisms: blunting mechanism and viscoelastic adhesive behaviour. The blunting mechanism [147] describes that in cases when a blunt crack is formed, it generates a lower stress concentrator than a sharp tip; consequently, a higher applied stress is required to reach critical stress intensity factor for the material at a specific distance. For instance, the yield behaviour in the vicinity of the crack tip controls the plastic deformation that occurs locally and as the yield stress decreases due to the application of lower load rates, the crack blunting mechanism becomes more severe. Finally, dynamics of stick-slip mechanism is explained as follows: after a crack arrest, a plastic zone is formed near the crack tip that is highly blunted so that crack can grow again until the highest value of  $G$  known as strain energy release rate initiation ( $G_i$ ) is reached; after that a fast crack is observed propagating through the virgin material and crack arrests at the value of  $G_{arr}$ .

### 3.5.2 Adhesives under impact fatigue

In contrast to the high level of research into the single-impact loading of adhesive joints, IF has so far received very little attention. In many cases the analysis of repetitive impacting has been limited to relatively short series of impacts. A representative study in the area of IF has been dedicated to analysis of modified adhesively bonded impact blocks bonded with an epoxy adhesive and tested using a drop-weight method; various contact times were applied in the tests [149]. It was demonstrated that the joint's IF strength depended on the stress magnitude and the

loading time applied. For instance, the longer the contact time, the shorter the maximum force necessary to generate failure under a constant number of impacts and the larger the absorbed energy per impact (the difference between the impactor kinetic energy after and before an impact). Some researchers [145] tried to analyse IF in an adhesive using a Charpy specimen made of a toughened epoxy adhesive. It was reported that no evidence for a threshold value of the applied energy was found; in addition, the fatigue crack growth was found to be a suitable technique to analyse the damage accumulation process in IF.

A comparison of responses of single lap joints in IF and standard fatigue was conducted in [150] using fatigue life diagrams. It was observed that IF presented a more rapid decrease in the number of cycles to failure than standard fatigue. Additionally, the IF behaviour depended on the overlap length identifying that the overlap increasing length resulted in the increased number of cycles to failure at the same load.

### **3.5.3 Modelling impacts in adhesives**

An initial description of modelling of adhesive joints was presented in Section 3.2. Most of the publications on impact in adhesive joints deal with crack propagation or stress propagation under a single impact. In [144] it was found that cohesive zone elements (CZE) could be suitable to reproduce cracks in an adhesively bonded wedge specimen with a load rate-dependent adhesive. The obtained experimental result demonstrated that cracks could have both stable and unstable behaviour; hence two types of CZE were defined to reproduce those behaviours. The first type of CZE has a trapezoidal traction-separation law that was used to model a quasi-static crack growth; these elements are defined mainly by two essential parameters fracture, namely: toughness and cohesive strength (obtained experimentally). The shape of the law is necessary to reproduce properly the elastic-plastic deformation of the adhesive. The second type of CZE has a triangular-shaped traction-separation law that was used to reproduce brittle behaviour that was observed experimentally. The latter elements were defined with the similar cohesive strength and slopes (initial and final) as the trapezoidal CZE but avoiding the plateau region. The experimental study

concluded that a crack changed from the stable to unstable behaviour by a stochastic mechanism, and such changes could be more frequent at higher load rates. Obviously, a non-physical mechanism was used to include these elements into the models. Implementation of both types of CZE was only carried out in order to reproduce the distribution of different crack behaviour observed experimentally. The FEM results allowed a conclusion that the proposed CZE were rate-independent and the fracture toughness of the brittle mode was about four times lower than that for a quasi-static crack growth. In addition, it was established that most of the energy available in the system was consumed by the friction between the wedge and the adhesive.

Another way to analyse impact in adhesive joints was based on the analysis of the effect of a transversal impact on a SLJ using CFRP as an adherend [151]. The adhesive was modelled as an elastic-plastic material with kinematic hardening exposed to a transversal impact over the adhesive region as seen in Figure 3.3. It was found with the use of a dynamic FEM that such conditions produced a mixed mode load but as the crack propagated through the adhesive; mode II became the main loading mode.

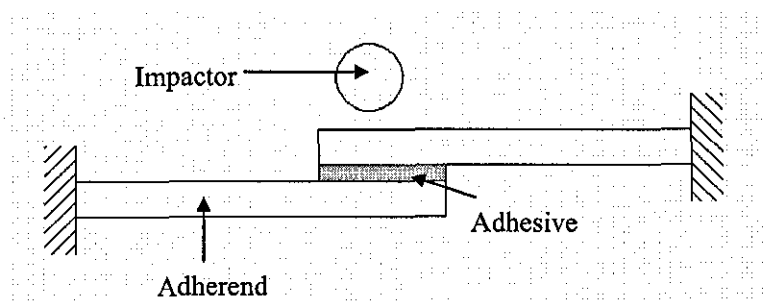


**Figure 3.3 Schematic of impact of SLJ in [151]**

### **3.6. Phenomenological models of impact fatigue**

Researchers, working mainly with steels, proposed various models to study the IF behaviour. A review of these models is presented below.

### 3.6.1 Fatigue life

In [152], a phenomenological model was proposed to analyse the IF behaviour in special under plain carbon steel (The results obtained in that study are not relevant for this research; however, emphasis are taken on the methodology used for analyse the results). The model is based on the fact that the effect of IF conditions on a material can be presented in an  $E-N_F$  graph. Two types of models were proposed-one for high-cycle IF and the second one for low-cycle IF. In the case of high-cycle fatigue it was shown that the phenomenon could be described by the equation:

$$E_i = E_0 + E_k N_F^{-p}, \quad (3.1)$$

where  $E_0$  is the fatigue limit proposed as a material constant,  $E_k$  and  $p$  are the IF parameter and IF exponent; for steels  $p$  has a value of 0.6. In the case of low-cycle fatigue  $E_i$  and  $E_0$  are related by the equation

$$E_i = E_0 + m N_F^{-q}, \quad (3.2)$$

where  $E_0$ ,  $m$  and  $q$  are material parameters that can differ for various steels. An empirical relation between  $q$  and  $m$  was proposed:

$$q = \log_e m + D, \quad (3.3)$$

where  $C$  and  $D$  are constants. Finally, it was suggested that a material under IF can be modelled with the following relation:

$$E_i = E_0 + \exp\left(\frac{q-D}{C}\right) N_F^{-q}. \quad (3.4)$$

### 3.6.2 Accumulated load-time model

Researchers identified that under cyclic impacts, the IF strength depended on the impact stress and the loading time, and proposed empirical relations to characterise

IF. The most popular approach is to relate the cumulative time  $N_F T$  to the maximum stress amplitude in the impact  $\sigma_{\max}$  [134, 135, 154]:

$$\sigma_{\max} (N_F T)^m = C, \quad (3.5)$$

where  $N_F$  is the number of cycles to failure and  $T$  is the loading time,  $C$  and  $m$  are empirical impact-fatigue parameters. In this work, the relation described by equation 3.5 will be referred to as the accumulated load-time model.

### 3.7. Summary

After its initiation in the 19<sup>th</sup> century, the field of IF was nearly forgotten although from the very beginning it was shown that IF is an extremely important loading case, which was erroneously underestimated. Most studies incorporating FRPCs limited their analysis mainly to the effect of a single, or several, transversal impacts on structures supposing it to be the worst scenario of impact loading. Notwithstanding limitations of this study, IF seems to be a dramatic load condition, for which more work should be conducted in order to understand fully the phenomenon. In many studies, the problem of impact in structures was reduced to the effect that it can produce on plates; however as these plates are connected to another structures, e.g. in adhesive joints, such joints are also exposed to the effects of the impacting force. The study of single tensile or repetitive low-velocity impact has, to date, attracted little attention of researchers, and there is an obvious need for significant research effort in this area, where dynamic responses of the material, fatigue, contact boundary conditions, stress concentrations and other factors interaction make any progress very challenging.

In spite of various experimental and modelling studies conducted for impacts, most of them were concentrated on analysis of single or transversal impacts; little attention was paid by researchers to tensile in-plane impacts of FRPCs plates.

In this chapter, existing literature on fracture and impact is analysed in depth to enable good understanding of the subject area and to formulate objectives for this research.

In the next chapter, the methodology of our experimental work is described, providing details on the materials, specimen preparation and testing procedures.



## **CHAPTER 4**

### **Material and Experimental techniques**

#### **4.1. Introduction**

The main aim of this chapter is to describe the materials, joint configurations, and experimental test procedures used. The chapter contains the following:

- A description of the materials used in this research; including the material properties of adhesives and adherends.
- A description of the technique used to manufacture bulk adhesive specimens in order to measure the adhesive material properties.
- A description of the joint configurations used.
- A description of the cyclic impact machine used and test parameter used in the impact fatigue testing.
- A description of the machine used for the constant amplitude fatigue test and the test parameter used.
- A description of the techniques used to measure crack propagation.
- A description of the method used to analyse the fracture surface.

## 4.2. Materials

The materials used in this research were selected from those commonly used in aerospace applications. Two structural adhesives and two adherend materials were used. These are described below.

### 4.2.1 Composite adherends

One of the adherends used in this study was the carbon fibre reinforced composite (CFRP) T800/5245C. The matrix is Rigidite 5245C from BASF, which is a bismaleimide based thermosetting polymer. This is a high temperature resin considered as brittle compared with other common resins used in aerospace CFRP [155]. The properties of 5245C are given in Table 4-1. The carbon fibre used as reinforcement in the composite is the intermediate-modulus fibre T800 supplied by Toray Industries Ltd. The properties of this fibre are given in Table 4-2. Unidirectional (UD) pre-preg material with a nominal fibre volume fraction of 0.6 was laid up in a 16-ply multidirectional (MD) stacking arrangement of (0/-45/+45/0)<sub>s</sub>. Panels were manufactured by DEFRA (QinetiQ) Farnborough. The plates were cured for 2 hours at 182°C, with an initial autoclave pressure of approximately 600 kPa, according to suppliers recommendations. The thickness of the cured plates was approximately 2mm. All the CFRP plates were scanned ultrasonically in order to identify any possible manufacturing problems.

**Table 4-1: Properties of 5245C matrix at room temperature**  
[156]

Glass transition (°C)	227
Cured Density (g/cm <sup>3</sup> )	1.25
Tensile strength (MPa)	83
Tensile Modulus (GPa)	3.3
Elongation (%)	2.9
$G_{IC}$ (J/m <sup>2</sup> )	158

**Table 4-2: Properties of T800 fibres [157]**

Elastic Modules	Tensile Strength	Fracture strain	Density
(GPa)	(GPa)	(%)	(g/cm <sup>3</sup> )
294	5.59	1.9	1.81

Material data for UD T800/5245C was supplied by QinetiQ and is shown in Table 4-3. The elastic material properties of a MD T800/5245C plate was calculated using elastic laminate, they are given in Table 4-3 as well.

**Table 4-3: Properties of T800/5245C composite at room temperature**

	$E_x$ (GPa)	$E_y$ (GPa)	$G_{xy}$ (GPa)	$\nu_{xy}$	$\nu_{yx}$
UD	174	9.64	7	0.36	0.02
MD	99.8	28.1	25.7	0.69	0.2

#### 4.2.2 Aluminium adherends

The second adherend using in this project was 7075-T6 aluminium alloy. This is a high strength aluminium alloy commonly used in aerospace applications when good fatigue performance, high fracture toughness and high strength are required. The aluminium used was 2.5 mm clad plate. The cladding was a thin film (about 62.5  $\mu\text{m}$ ) of pure aluminium over both surfaces; this is used to increase the corrosion resistance of the material. In Table 4-4, a summary of the material properties is presented.

**Table 4-4: Properties of 7075-T6 in clad conditions [158]**

Elastic Modules	Tensile Strength	Yield Strength	Elongation
(GPa)	(MPa)	(MPa)	(%)
71.7	68-76	58-65	5-9

### **4.2.3 Adhesives**

Two types of rubber toughened epoxy adhesives were used. The first adhesive system used the adhesive/primer combination FM 73M/BR 127 from Cytec Industries Inc. FM 73M is a general purpose aerospace adhesive designed to provide structural performance in the temperature range -55°C to 82 °C, giving good durability in metals bonds and also in complex structural systems where combinations of materials are involved. This adhesive is supplied in films of 0.12 mm nominal thickness and is manufactured using a non-woven polyester scrim which is used to support the adhesive itself and to control the flow and glue line thickness during curing. BR 127 is a modified epoxy-phenolic primer that contains 10% solids, of which 2% is a strontium chromate corrosion inhibitor. The remaining 90% of the solution is methyl ethyl ketone (MEK) solvent.

The second toughened epoxy adhesive used was Hysol EA 9628 from Henkel Corporation. This is a modified epoxy adhesive designed for structural bonds and was supplied as a film with a nominal thickness of 0.24 mm. This adhesive is based on a diglycidyl ether of bisphenol A epoxy, cross-linked with a primary amine curing agent. The toughening agent consists of a carboxyl terminated butadiene acrylonitrile rubber. This adhesive is supplied either unsupported or with a random fibre material carrier. In this work the unsupported adhesive were used and this is termed EA 9628 UNS in this thesis. A water-borne epoxy primer 'EA 9257', also produced by Henkel Corporation was used with the adhesive.

## **4.3. Adhesive material properties**

This section will analyse the material properties of both adhesives used in this study, including a description of the method used to manufacture bulk specimens.

### **4.3.1 Bulk adhesive sample manufacture**

Bulk specimens were cut from cured adhesive plates, where each plate was manufactured by co-curing multiple layers of adhesive film. The adhesive sheet was

first cut into pieces approximately 200 x 200 mm using a scalpel. In the case of the first layer the protective layer on one side of the adhesive was left until all sheets had been laid up subsequent layers were added by laying from one corner of the plate to the other corner (in one direction) avoid to an entrapment. After each added layer the film was rolled with a heavy cylinder. The process was continued until the un-cured plate had a thickness a little larger than that required in the final cured specimen. The adhesive plate was cured in a hot press using a calibrated thickness mould. Un-cured adhesive plates were placed in the mould and the top and bottom surfaces covered with a film of PTFE. Pressure and temperature are applied using the following standard cure cycle: heat up in 30 minutes to 120°C, hold 60 minutes at 120°C±3°C; pressure is maintained constant during the cycle. This process was conducted for FM-73M bulk adhesive, a slightly difference for EA 9628 UNS was conducted and reported in [159].

#### 4.3.2 FM-73M material properties

Material properties for the FM-73M adhesive were obtained by testing nine specimens with gauge length of 25 mm. Bulk specimens were manufactured with the dimensions shown in Figure 4.1, a nominal thickness of 0.6 mm and the curing process cycle described before .

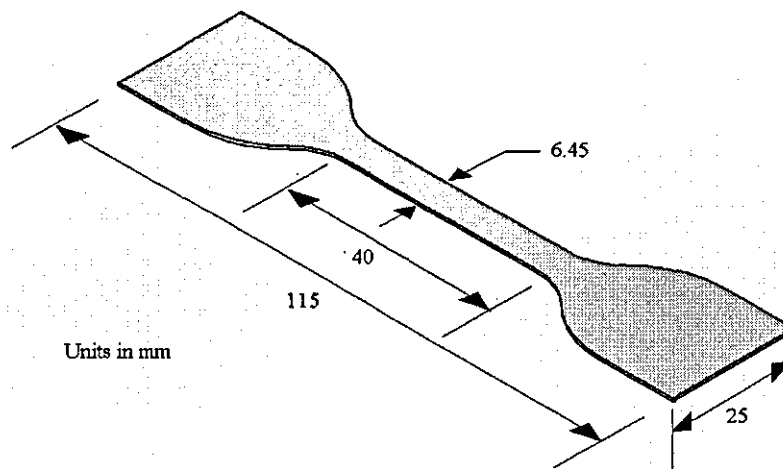


**Figure 4.1: FM-73M Bulk adhesive specimens**

Testing was carried out with a calibrated Instron 3366 universal testing machine using an extensometer. Load rate dependency was investigated by using three different displacement rates; 1, 10, 100 mm/min. The effect of displacement rate on tensile strength can be seen in Figure 4.2. It is noticed that response of the tensile strength has a dependency with displacement rate. Additional analysis conducted of the maximum elongation does not show a strong dependency in terms of the displacement rate. Typical stress-strain curves at different displacement rate are shown in Figure 4.3. The average elastic modulus was found to be 2050 MPa with a standard deviation of 139 MPa.

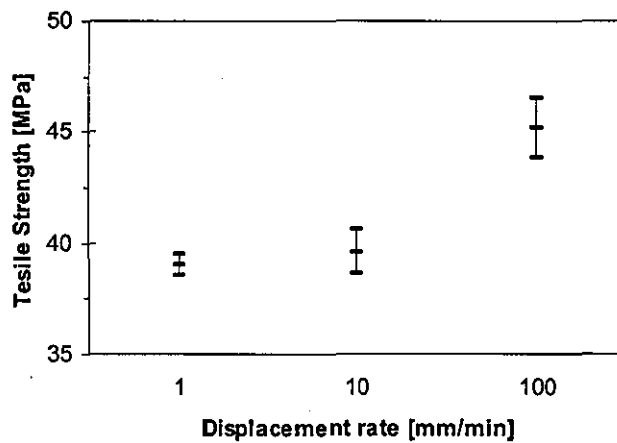
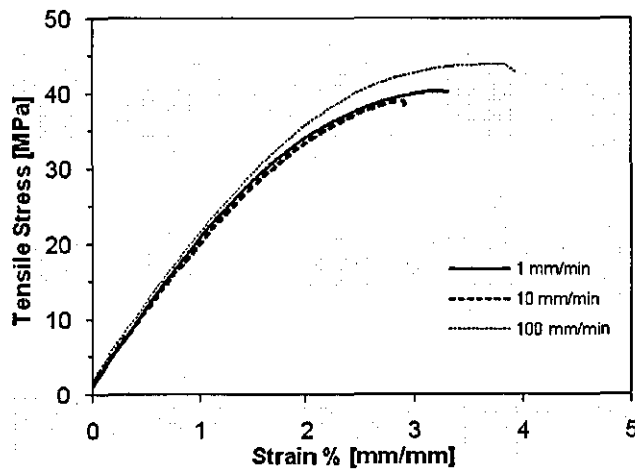


Figure 4.2: Changes in the tensile strength in FM-73M as increasing of the displacement rate



**Figure 4.3 Stress-strain curves for bulk adhesive (FM-73M) at different displacement rates**

#### **4.3.3 Material properties of EA 9628-UNS**

The mechanical properties of EA 9628-UNS have been reported in [159] using bulk specimens. In that work, specimens were designed to have a gauge length of 25 mm and 4 mm thick. The samples were cut from pre-cured adhesive plates following a similar technique to that described in Section 4.3.1. The final shape was achieved using a vertical milling machine. Four cross displacement rates (0.1, 1, 10, 100 mm/s) were used in the testing in order to determine the displacement-rate dependency of the materials properties.

The results obtained in those tests are summarized in Figure 4.4 and Figure 4.5. It can be seen that low displacement rates are related to low tensile strength, however, the increase of tensile strength with displacement rate asymptotically tends to a plateau. Analysis for the maximum elongation and elastic modulus did not provide a conclusive tendency. Typical stress-strain curves for different displacement rates are shown in Figure 4.5. The average elastic modulus was found to be 2037 MPa with a standard deviation of 97 MPa.

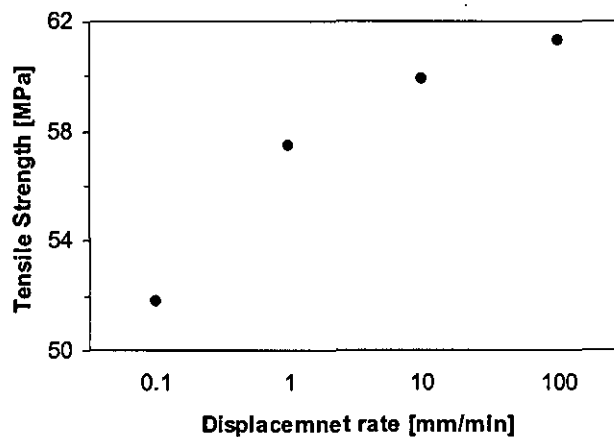


**Figure 4.4 Changes in the tensile strength in FM-73M as increasing of the displacement rate**

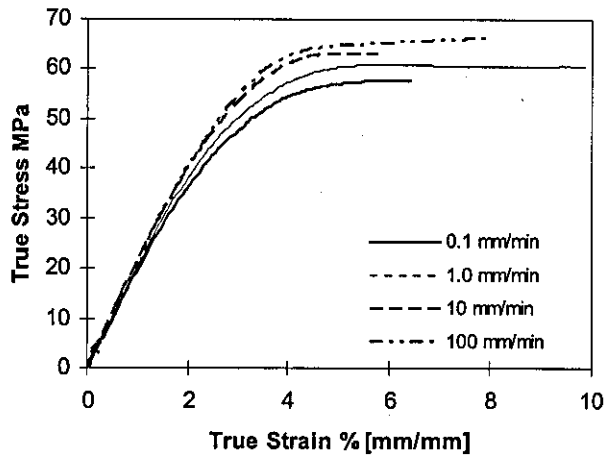


Figure 4.5 Typical stress-strain curves for bulk adhesive at different displacement rate (EA 9628-UNS)

#### 4.4. Surface preparation

The surfaces of the adherends were subjected to a surface treatment prior to bonding in order to improve adhesion and increase repeatability in the tests. The aluminium adherends were grit blasted with alumina ( $400\text{ }\mu\text{m}$ ) at a pressure of 137 kPa; the method was selected due to its convenience and speed. The roughness of a typical grit blasted aluminium surface was measured using a non-contact profilometer (Talysurf CLI 2000) based on the white light interferometer technique. The results are shown in Figure 4.6. The average roughness was  $3.12\text{ }\mu\text{m}$  with a highest height roughness profile of  $21.9\text{ }\mu\text{m}$ .

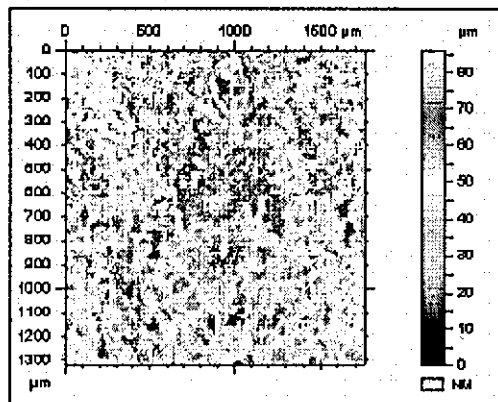


Figure 4.6 Image of a typical aluminium (7075-T6) surface after grit blasting



After grit blasting the aluminium was ultrasonically degreased with acetone. Specimens were then dried at room temperature for 30 minutes.

A similar process of grit blasting and degreasing with acetone was also used for the composite plates, however no specifications are available for pressure and alumina size used in this process.

## **4.5. Adhesive joint configuration**

Two different types of adhesive joint were used:

- Single Lap Joint (SLJ)
- Lap Strap Joint (LSJ)

Two sizes of SLJ configuration were used in the test programme. These were termed as SLJ<sub>short</sub> and SLJ<sub>long</sub> and will be discussed in Section 4.5.1. Additionally, two sizes of LSJ configuration were used and termed as LSJ<sub>long</sub> and LSJ<sub>short</sub>.

### **4.5.1 Single Lap Joints**

SLJ's were used in this research to investigate the fatigue life of bonded joints because failure is easy to define as the moment when both adherends are separated completely. Specimens were manufactured using aluminium 7075-T6 as adherends and FM-73M/BR-127 adhesive/primer system. SLJ<sub>long</sub> were manufactured following ISO 9664:95 standard as shown in Figure 4.7.

The sizes SLJ<sub>short</sub> joint were designed to fit in the Resil impactor machine (Section 4.6.3). The dimensions of the SLJ<sub>short</sub> joint are shown in Figure 4.8.

Joints were manufactured in two stages. After grit blasting and degreasing the adherends, a thin film of BR 127 primer was applied to the bond area and dried for 30 minutes at room temperature. This was then cured at 120°C for 30 minutes. A sheet of FM 73M was cut into pieces of 12.5 mm x 26 mm. One piece of the cut adhesive was

placed at the overlap between the adherends for each sample and any adhesive excess cut off. Bonding was achieved by fixing the adherends using clamps and curing for 60 minutes at 120°C. No special mechanism was used to control the thickness of the adhesive, however, the carrier help to keep a relatively uniform thickness. Adhesive thickness was measured and found to be between 0.14 mm and 0.15 mm. End tabs were bonded to the samples to aid grip in the fatigue tests and also to provide load alignment.

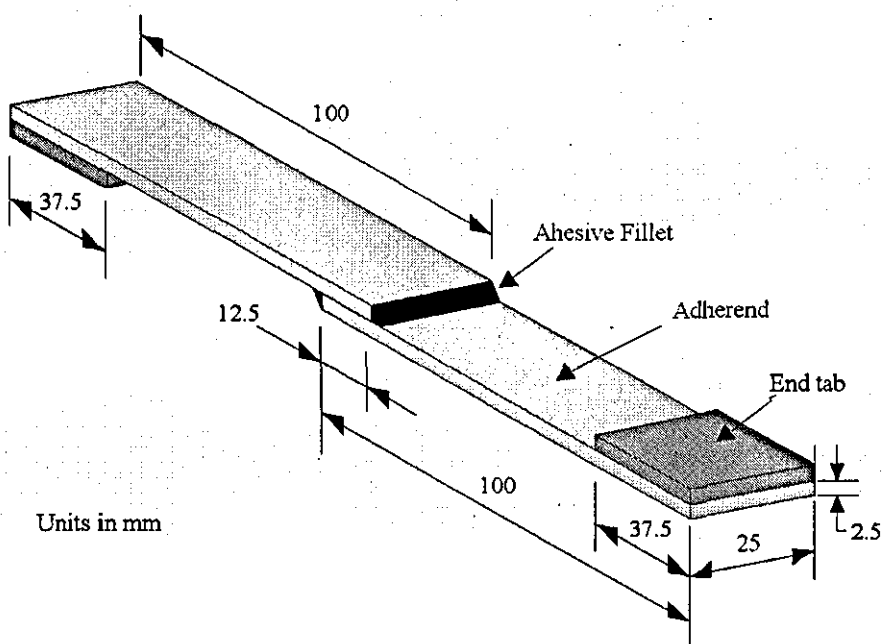


**Figure 4.7 Dimensions of  $SLJ_{long}$**

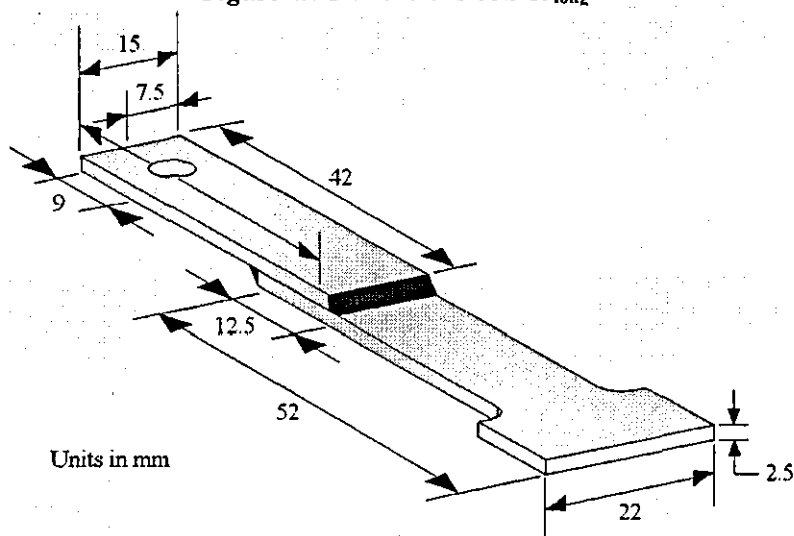


**Figure 4.8 Dimensions of  $SLJ_{short}$**

#### 4.5.2 Lap Strap Joints

LSJ's were used in this research to analyse fatigue crack growth in adhesively bonded joints because it has only one fillet, from which crack can propagate, making it easy to identify it and to observe its growth. The LSJ's were manufactured by adhesively bonding cured T800/5245C (CFRP) panels. This is known as secondary bonding and is distinguished from co-bonding in which the adhesive and CFRP are cured together. The advantage of secondary bonding is that different (optimum) curing cycles can be used for the adhesive and CFRP and that distortion of the CFRP in the joint area during curing can be avoided. Also there is potentially greater freedom in the manufacturing process and there may be cost savings involved in being able to make parts in smaller assemblies. However, the obvious disadvantages are the time and cost penalties of replacing a single process with two.

The process to produce the LSJ's began with grit blasting (taking care not to damage the matrix and fibres making) and acetone cleaning of the pre-cured CFRP panels. The assembled joints of EA 9628 adhesive and CFRP panels were cured in an autoclave at 600 kPa for 60 min at 120°C. Quality verification of cured panels and bonded joints was carried out using an ultrasonic scanning machine. Samples with a bondline thickness of ~0.15 mm were cut from the bonded panels using a diamond saw. End tabs were bonded to the samples to aid grip in the fatigue tests and to provide load alignment. Holes were drilled in LSJ<sub>short</sub> joints to fix specimens to the impact machine using 3 different diameters of drill to minimise problems of delamination in the composite.

Two types of LSJ specimens were used. A long LSJ (LSJ<sub>long</sub>) with the dimensions shown in Figure 4.9(a) and a short (LSJ<sub>short</sub>) shown in Figure 4.9(b).

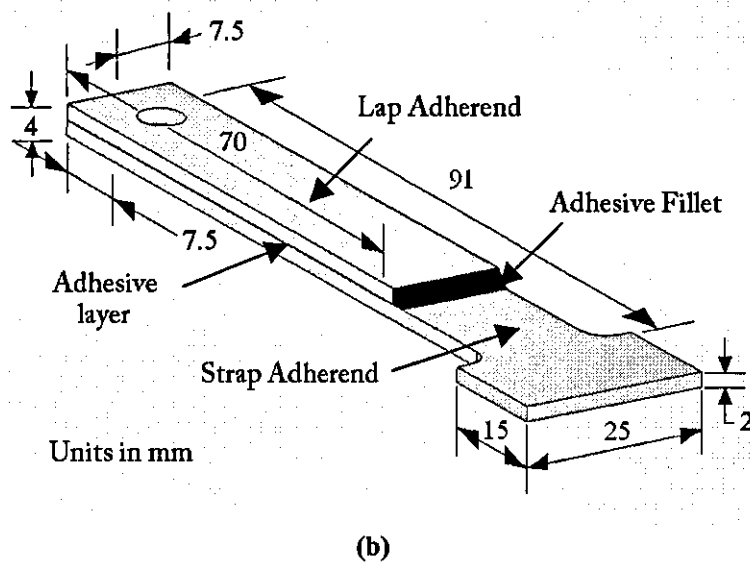
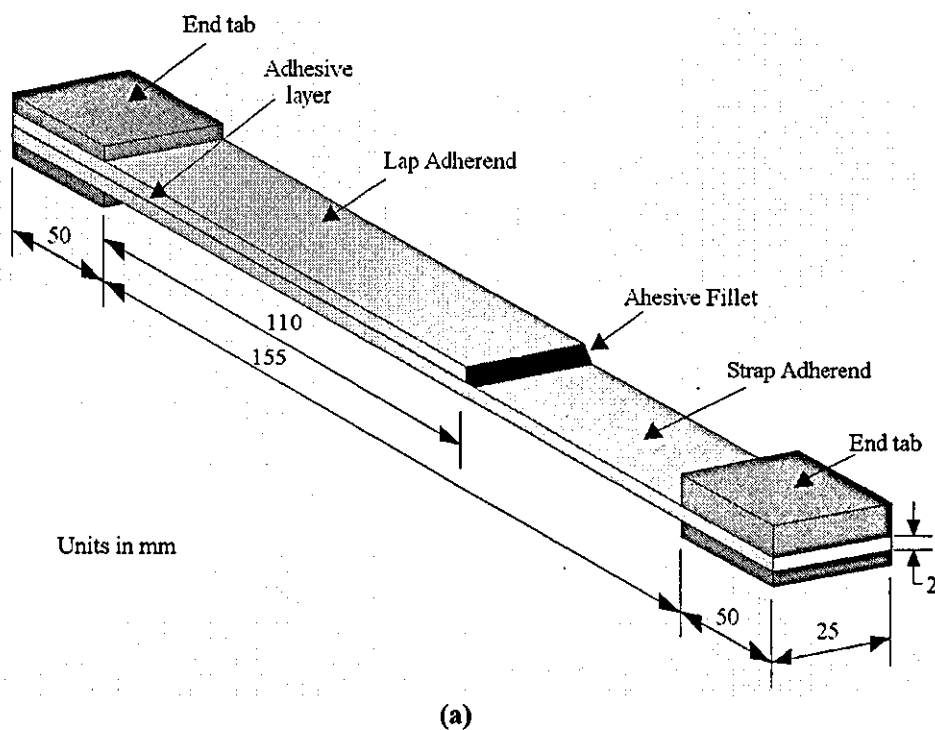


**Figure 4.9 Dimensions of lap strap joint specimens. a) LSJ<sub>long</sub> for SF; b) LSJ<sub>short</sub> for IF**

## **4.6. Experimental Test Procedures**

The following sections describe the mechanical test conducted on the bonded joints.

The tests can be divided as follows:

- Quasi-static tests
- Standard fatigue
- Impact fatigue
- Combined of Impact and Standard fatigue

### **4.6.1 Quasi-static (Qs) testing**

A servo-hydraulic fatigue testing machine with digital control and computer data logging was used in the quasi-static and standard fatigue testing. The quasi-static failure load was calculated as the average of the maximum force reached by two specimens tested at a displacement rate of 0.005 mm/s (SLJ) and 0.05 mm/s (LSJ).

### **4.6.2 Standard fatigue (SF)**

SF tests were conducted using a servo-hydraulic fatigue testing machine with digital control and data logging. A sinusoidal waveform with a constant load amplitude, a load ratio (minimum load/maximum load) of  $R = 0.1$  and frequency of 5 Hz was used for all the tests. This type of loading is referenced to as Standard fatigue (SF). All tests were in ambient laboratory environmental conditions where temperature and relative humidity varied between 18-25°C and 50-60%, respectively.

SF tests with the SLJ's were continued until failure, which is defined when the laps of the specimen are fully separated. The maximum loads used in these tests specimens were selected as proportions of the failure load in quasi-static testing. A fatigue threshold, was defined as the highest maximum load in a load that a sample could survive  $10^6$  cycles with no observable damage using an optical microscope.

SF tests for the  $LSJ_{short}$  and  $LSJ_{long}$  samples were carried out with a maximum load of approximately 60% of the quasi-static failure load, since that load level was suitable to reproduce a fatigue crack growth. Crack propagation were measured over surfaces using the methods described in Section 4.7 combining different techniques like optical, crack gage and backface strain.

Temperature measurements were taken continually over the specimen's surface using a thermocouple, no changes were obtaining during the fatigue test of those specimens.

#### 4.6.3 Impact fatigue (IF)

Impact-fatigue was carried out using a modified CEAST Resil impactor. The basis of this method, as illustrated in Figure 4.10, is that a specimen is supported at one end by an instrumented vice and its opposite end is struck repeatedly by a controlled pendulum hammer, resulting in a dynamic uniaxial tensile loading. In this work, a calibrated impact hammer with mass of 0.951 kg and nominal length of 0.2297 m was used. This hammer can generate an impact of up to 4 J at 2.9 m/s, which corresponds to an initial angle of  $150^\circ$  to the striking position. The instrumented vice shown in Figure 4.11 consists of a piezoelectric force transducer rigidly fixed between the specimen support and a fixed vice. A calibrated impact block is joined to the free end of the sample. This consists of two plates joined by bolts. Variation in the magnitude of the initial impact energy and velocity was achieved by changing the initial angle of the hammer. This angle is maintained constant during an impact-fatigue test by automatic repositioning after braking in each cycle of loading. The impacting frequency produced by the modified Resil impactor is 0.1 Hz.

A pre-test analysis of energy loss due to mechanical friction and aero dynamical losses was implemented by measuring the initial and final angles of the pendulum hammer in a single cycle without a specimen. The result was subtracted from the measured amount of energy dissipated in the specimen in each cycle of impact loading.

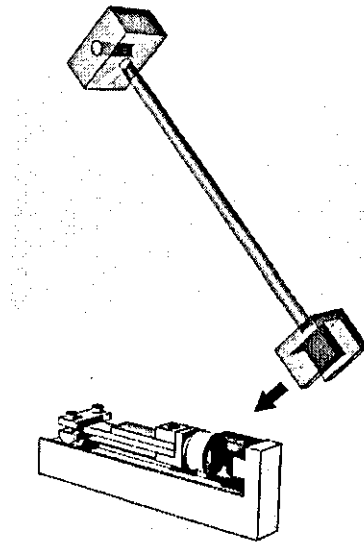


**Figure 4.10 Schematic of specimen fixture for impact fatigue**

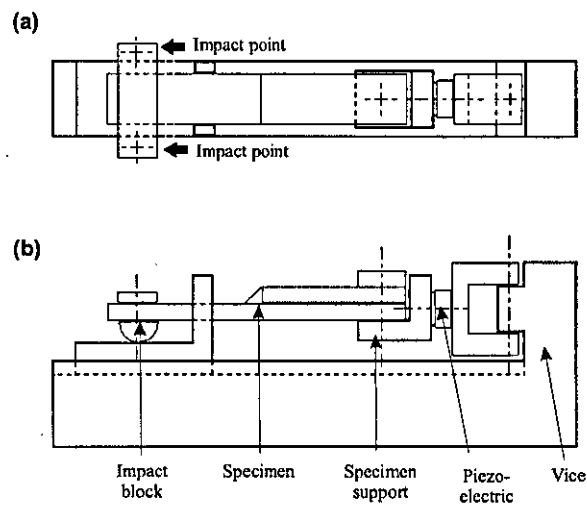


**Figure 4.11 Schematic of the instrument vice on the impact fatigue machine, a) top view, b) front view**

A logic diagram of an impact-fatigue test is shown schematically in Figure 4.12. The pendulum is released from a pre-selected initial angle. Impact with the sample produces a change in the electrical resistance of the piezo-electric sensor, which is captured by the data acquisition equipment. This signal is registered with a pre-selected sampling frequency of 833 kHz, with up to 8000 data points recorded per

cycle. In order to decrease the data noise a 1 kHz filter was used. The amplified and filtered data was downloaded to a computer as magnitudes of force and time and this data was then used to calculate velocity  $V$ , displacement  $d$  and energy  $E$  for each impact. These parameters were calculated using the following relations:

$$V_i = V_{i-1} - \Delta t \left( \frac{F_{i-1} + F_i}{2m} - g \right) \quad (4.1)$$

$$d_i = d_{i-1} + \frac{\Delta t}{2} (V_{i-1} + V_i) \quad (4.2)$$

$$E_i = E_{i-1} + \frac{\Delta t}{2} [(FV)_{i-1} + (FV)_i] \quad (4.3)$$

where the index  $i$  is relates to the current time and  $i-1$  corresponds to the previous measurement, with a time difference of  $\Delta t$ . The initial condition of these equations was assumed as initial displacement and energy in equations (4.2) and (4.3) equal to zero. However, in order to identify the initial velocity  $V_0$  in equation (4.1), a linear momentum conservation analysis was used. In this analysis, it was assumed that after impact; the impact block, specimen and hammer are moving together. In order to continue with the next impact, the impact-fatigue software first compares the maximum energy with the initial potential energy of the hammer, defining failure of the joint when this difference is higher that 50%.

Different levels of initial potential energy for the hammer were used to identify the behaviour of the SLJ<sub>short</sub> specimens in IF conditions. In order to identify the repeatability of the results, two groups of specimens were tested which were manufactured at different times.

The IF tests used for the LSJ<sub>short</sub> joints were carried out with an initial potential energy of 1.07 J, impacting the striking anvil at a velocity of 1.5 m/s. These conditions were kept constant for all LSJ specimens tested in IF. In addition, IF tests used for the SLJ<sub>short</sub> joints were carried out with different initial potential energy – over the range



of 0.13 J to 3.15 J – corresponding to impact speeds varying from 0.66 m/s to 3.32 m/s.

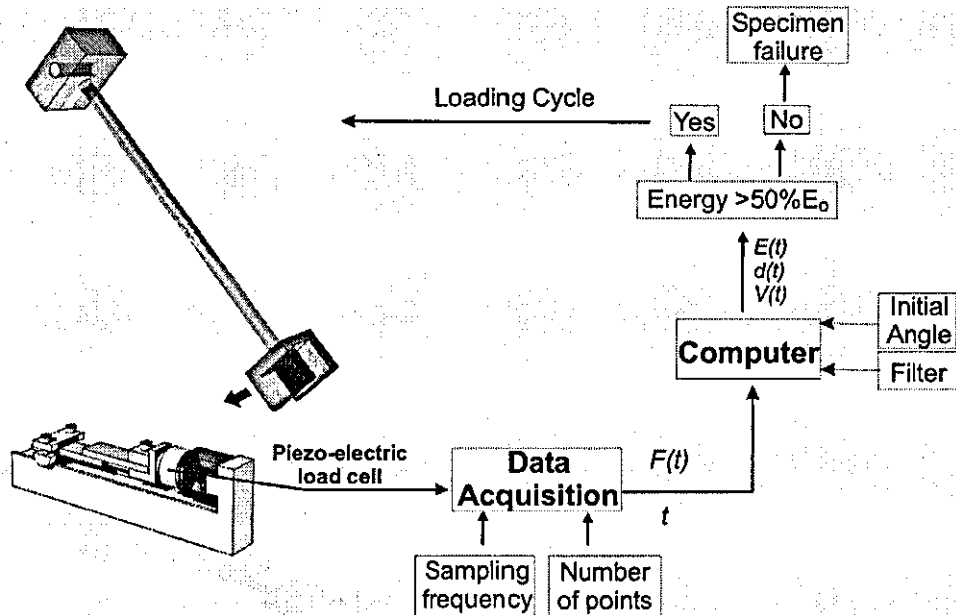


Figure 4.12: Schematic of impact-fatigue test and data acquisition

#### 4.6.4 Combined impact and standard fatigue (CISF)

Combination of IF and SF (CISF) were also carried out on LSJ<sub>short</sub>. The load spectrum consisted of IF-blocks with 100 tensile-impacts followed by samples SF-blocks of 5000 sinusoidal cycles. The IF tests were with an initial energy of 1.07J. The SF cycles had a maximum load of 7.8 kN, load ratio of 0.1 and frequency of 5 Hz.

#### 4.7. Crack growth measurements

Crack growth during fatigue was determined using several methods: optical measurements, crack gauge, and backface strain technique. In the following section each of these methods is described and the methods compared.

#### 4.7.1 Optical measurements

This is a simple and reliable method for monitoring crack length in bonded joints. A high magnification camera is used to record a digital image of the sample at certain times. The digital images are then analysed to determine the crack size. In order to highlight the crack, the edges of the sample are painted white using correction fluid. This generates good contrast between the crack and the sample surface. Marks at 5 mm intervals were made in the paint using callipers. Crack size measurements were made from the digital images using the Screen Callipers V3.3 software, using marks for calibration. The precision of this method was analyzed and calculated to be 0.3 mm. However the precision of this technique depends directly on the quality of the digital image and although that it is a simple technique, it is not completely automated and is time consuming.

For application of this technique in SF conditions, a video camera, Canon MV750, with magnification up to 440X was used. Measurements were programmed to be made every  $10^3$  cycles during crack propagation period and every  $2 \times 10^3$  cycles when there was no visible cracking on the sample surface. It was found using this technique that crack close effects were present in LSJ specimens, even though they were tested with a positive load ratio. This effect made identification of the crack tip by optical methods difficult when no load was applied. To solve this problem in SF conditions, cycle sinusoidal blocks were automatically stopped after a certain number of cycles and a single quasi static load applied to the joint with a maximum tensile value equal to the maximum value of the sinusoidal load. This opened the crack sufficiently for it to be captured by the video camera.

Measurements of crack size in IF condition by optical measurements is a variation of the technique previously described. During cycle impacts, it is not possible to capture image when the crack is open because the hammer interferes with observation of the surface. In order to avoid this problem, images were taken using a microscope with a magnification up to 200X. This operation was carried out by reaming the specimen from the machine at a pre-selected number of impacts and taking an image of the crack with a data image capturing microscope. In order to avoid the crack close effect a simple three point bending support was used to open the crack enough to make a

suitable measurement. Several images of the crack were taken to improve among of the measurement. Image analyse, as described previously, was used in the crack length measurement. The precision of this method was determined to be 0.01 mm, this being the size of a pixel in the image.

#### **4.7.2 Crack gauge and Fractomat system**

This expensive, accurate, commercial technique consists of gluing a special crack gauge to one side of the sample along the bondline. The crack gauge is a thin metal foil, 5 $\mu$ m thick that tears during crack propagation. Changes in the crack size generate changes in the electrical resistance of the crack gauge that are measured by a piece of equipment called the "Fractomat" and converted to a crack length. The Fractomat equipment is a two way amplifier that shows using a digital screen to display the crack size. Conditioned output voltage signals are also produced by the Fractomat equipment that can be captured and recorded in real time by a computer. The precision of this technique is reported by the manufacturer to be  $\pm 0.1\mu$ m for the crack gauge and  $\pm 0.01$  mm for the Fractomat, exceeding by a factor of 10 ASTM-647 [160]. Limits of this technique have been described by the manufacture and identified in the cases when there are large plastic zones, oblique cracks more than  $\pm 5^\circ$  from the centre line and crack bifurcation. Major limitation of both optical and Fractomat is only surfaces cracks measurements.

Care must be taken not to damage the gauge or the solder attaching the wires to the gage. The care with which there is damage makes the technique difficult to apply to IF.

#### **4.7.3 Backface strain**

Backface strain (BFS) is a non destructive technique that entails attaching a strain gauge to the back face of the sample and measuring changes in the strain value with respect to time. The technique is based on the fact that changes in the crack size modify the strain distribution over the joint. These changes can be related directly to the crack size, making the BFS technique a useful tool to determine crack initiation and propagation [161-163].

Initial work with this technique was presented in [161] for welded SLJ. BFS results and FE analyses were compared to identify the cycle where a non-symmetric fillet crack appeared on specimens. Recently work [163] using adhesively bonded SLJ's has shown that the BFS technique can be used to characterise the fatigue life of bonded joints using BFS; the fatigue life was divided into three regions: an initiation period, a period of stable crack growth and a fast crack growth leading to failure. A step forward in the application of this technique was described in [164] where, in conjunction with FEA, an expression was defined that identified crack growth rate as a function of the BFS rate for a specific maximum fatigue load. The technique is described by the authors as a useful tool to measure crack propagation when a crack is not clearly visible.

Two types of strain gauge were used in the back face strain measurements. In SF tests standard electrical resistance strain was used whereas in IF tests semiconductor strain gauges were used. Strain gauges were glued to the specimens using the adhesive recommended by the strain gauge manufacture; M-bond AE-15 from Vishay Measurements Group. This is a two components epoxy adhesive that needs to be mixed before spreading over the region where the strain gauge is to be glued. After attaching the strain gauge, the adhesive is cured for one hour at 75°C, following the manufacturer's recommendations. The electrical resistance strain gauges used in this study were EA-13-120LZ-120 from Vishay. They have an electrical resistance of 120Ω, a gauge factor (a change of resistance by a level of strain) of 2.085 and gauge length of 3 mm. These strain gauges were connected to a strain gauge amplifier using a half-bridge configuration. A dummy strain gauge was glued to a non-loaded aluminium plate, as a non-active element in the half-bridge.

The second type of strain gauge used in this study was the semiconductor strain gauge KSP-2-120-E4 from Kyowa electronic instruments. It is well known that in standard strain gauges, changes in strain produce changes in electrical resistance. In the case of semiconductor strain gauges, changes in strain also produce changes in the electrical resistance. This results in a much larger gauge factor making it easy to detect small changes in strain. The electrical resistance of the gauge was 117.3Ω with a gauge factor of 121. This kind of strain gauges can be connected directly to the Resil

machine impactor, making it easy to capture strain data corresponding to an extra port that is provided with the equipment for other proposes.

In the standard fatigue tests, strain gauges were placed on both the strap and lap adherends, and 7.5 mm from each face, in the locations shown in Figure 4.13. For the impact fatigue tests, the strain gauge was only placed on the strap adherend.

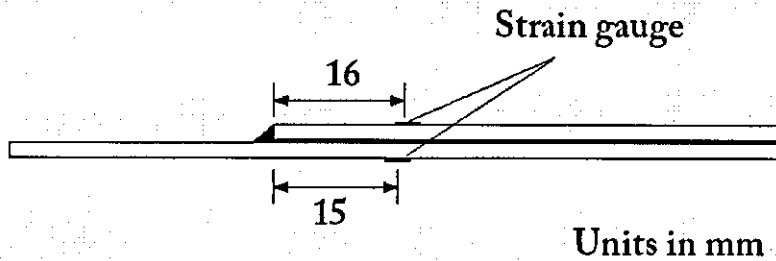


**Figure 4.13 Positions of the back face strain gauges**

#### **4.7.4 Comparison between crack gauge and optical measurements**

A comparison between the crack gauge and optical measurement systems was made using a  $LSJ_{long}$  specimen in order to identify the accuracy and reliability of the second method. The results found are shown in Figure 4.14. It is seen that the two methods show a good correlation. In addition, it is seen that the initial stages of crack growth can be studied optically before the crack reaches the crack gauge. Optical measurement is not a precise method to identify crack initiation phenomena as only surface cracking is detected. To attempt the delay subsurface damage, the BFS technique can be used.

It is observed in Figure 4.14 that as the number of cycles increases a small difference in the magnitudes of the crack size for two techniques begins to happen. The reason for this difference could be due to the fact that the geometry of the crack tip was not exactly perpendicular to the surfaces edges; the crack was somewhat bigger over the surface that was measured with the crack gauge. In previous works based on X ray measurements for the crack tip with a similar joint geometry, it was seen that that the crack tip was not a perfect line and some local dendrite-like pattern was observed.

The pattern was explained as resulting from the stochastic response of a real material during fatigue. In this case a crack surface is higher bigger; however, those differences do not affect the complete crack growth behaviour.

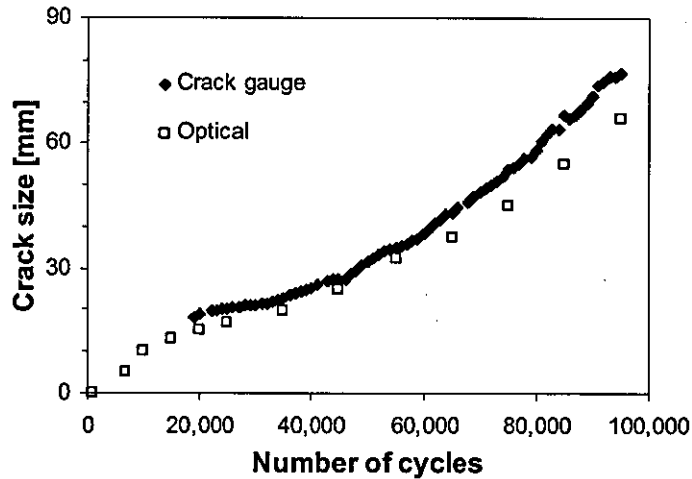


Figure 4.14 Comparison between crack gauge and optical crack measurements

#### 4.8. Fatigue crack growth rate

Measurements of the crack propagation rate were obtained using a graphical method which consisted of fitting a high polynomial to experimental data of crack length against number of cycles. Accuracy of the curve fitting was identified via coefficient of determination ( $R$ ). The criteria used was that  $R$  must be greater than 0.97, guaranteeing a good fit of the polynomial to the experimental data. It was found that this technique was suitable when data points followed a smooth, increasing curve. However, in some cases, especially in IF tests, high crack rate changes resulted in poor fits. In this case difficult higher order polynomials were fitted to difficult region of the experimental data to ensure a good fit over the whole data range. In order to guarantee continuity of the derivative between both polynomials, approximate 5 shared data points were included in adjunct polynomials. For the majority of the IF tests two third order polynomials were fitted to the experimental data. In the case of SF a single polynomial of order 5 was usually used.

#### **4.9. Fractography**

After testing, both edges of the sample and the fracture surfaces were examined with an optical microscope. In order to retain good resolution over large areas, six pictures were taken over the fracture surface and then merged using Photostitch V 3.1 software.

High-magnification studies were also performed using a LEO 440 scanning electron microscope (SEM). A voltage range between 15-25 kV was used with a secondary electron detector. As the adhesive was a poor electrical conductor, the samples were gold coated prior to SEM examination. This process was carried out in a vacuum coating machine (Morfield vacuum coating machine) working at a pressure of  $10^{-2}$  mmHg applying a current of 13 Amp to fine gold wire for about 60 seconds.

#### **4.10. Summary**

This chapter has outlined the experimental methods and techniques used to characterise the adhesive properties and to test adhesively bonded joints under various conditions. A description of specimen configurations and preparation has described for each specimen type used.

For both the adhesives tested, the results show that tensile strength increases considerably as the test speed increases. Analyses on the elastic modulus, on the other hand, do not demonstrate significant changes with the growing test speed.

## **CHAPTER 5**

### **Finite Element Modelling Methods**

#### **5.1. Introduction**

Finite element analysis (FEA) has been extensively used in recent years as a tool to support the study of adhesively bonded joints. With the use of FEA it is possible to locate regions of stress concentration and to investigate the effect of specimen geometry on stress distributions over the joint. The small thickness of the adhesive layer compared with the dimensions of the adherend and the inclusion in the model of geometry singularities makes it difficult to generate a finite-element mesh with a high enough density to avoid excessive mesh distortion but without an unnecessary increase in the number of elements.

The aim of this chapter is to develop a FEA model for LSJs that can be used to:

- Analyse BFS in SF and IF as method to predict fatigue crack growth;
- Analyse the strain energy release rate in LSJs under SF and IF.

#### **5.2. Development of quasi-static model**

The development of a finite-element model for LSJs is aimed at understanding the fatigue crack growth behaviour in joints during SF. However, commonly researchers have analysed this kind of loading with FEA employing a quasi-static model and applying typically the highest load level of the sinusoidal load pattern [27]. In the



following sections a description of each steps of the process used to develop a quasi-static and a BSF models in LSJ are described.

### 5.2.1 Material

Mechanical properties of the T800/5245C composite with a  $[(0/-45/+45/0)_2]_S$  lay-up and the EA 9628 UNS adhesive are given in Table 4.3 (Chapter 4). Structural adhesive materials are considered in general as an elastic-plastic material [165], having in the case of EA 9628 UNS a typical stress-strain diagram showed in Figure 4.5. EA 9628 UNS was modelled in various scenarios, firstly as a purely elastic material in the cases of fully elastic conditions and, secondly, assuming that it was an elastic-plastic material. In the second case, the adhesive was modelled as a piecewise linear material, having isotropic hardening, dividing the plastic range into three work hardening slopes. The von Mises yield criterion was used as the condition of yielding with a yield point defined as a 0.1% of the permanent plastic deformation. Typically, structural adhesives can be considered as time-dependent materials, where creep and a load rate affect the material. However, in most cases, when fatigue is analysed using FEA, the material's load-rate dependency is small and the material is modelled using experimental data obtained from quasi-static tests. In this study the effect of load rates was introduced, however, not in terms of a viscoelastic material model. Rather it is assumed that at specific load rate conditions the stress/strain behaviour has a respective form, determined in experiments and this form is used only to model tensile impacts of specimen. Furthermore, similar work-hardening properties are supposed for the adhesive at high and low rates.

In order to decrease the complexity of the model the CFRP adherend was modelled as an orthotropic solid. This assumption is plausible for a crack growth in the adhesive, however it is less suitable for the crack growth inside CFRP.

### 5.2.2 Geometry and Boundary conditions

The geometry of the lap strap joint used in the experiments as described in Chapter 4 and the geometry of the respective FEA model is given in Figure 4.9, with dimensions in Table 5-1. The boundary conditions of the FEA models used in standard fatigue are

shown in Figure 5.1. In region S1 the boundary conditions represent a rigid clamp, fixing the specimen in the x-direction at its end and in the y-direction along the clamped edge. In region S2 the load is applied in the x-direction while displacement in the y-direction is restricted along the clamped edge.

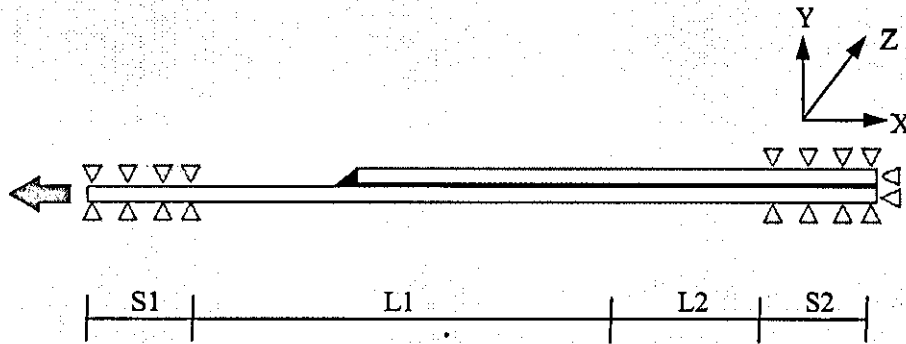


**Figure 5.1 Boundary conditions of a generalized LSJ specimen**

**Table 5-1 Lap strap dimensions**

Dimensions (mm)	LSJ <sub>long</sub>	LSJ <sub>short</sub>
Bond-line thickness:	0.2	0.2
CFRP thickness:	2	2
Lap length (L1+S1):	160	75
Strap length (S1+L1+L2+S2):	255	113
Specimen width:	25	15
Support 1 (S1):	50	15
Support 2 (S2):	50	20

### 5.2.3 Element choice

Two types of quadratic elements (low and higher order) were used to study their effects on the accuracy; the models had the same mesh and elements were chosen from the extensive element database of MSC Marc. A four-node, isoparametric (i.e. element formulation that enables the use of elements with varying shapes) with bilinear interpolation as a low order element was selected. That element was used

with a strain formulation method developed by MSC Marc specifically to improve the accuracy of the results in cases with bending.

As a higher order-element, an eight-node, isoparametric element, with an arbitrary quadrilateral formulation was used. The element employs a bi-quadratic interpolation functions to represent displacements. Two versions of that element were used -fully integrated and reduced integrated- in order to identify computational reduction of this option. Marc uses the reduced integration to decrease the number of numerical integration points, i.e. in the case of four-node quadrilateral element those are reduced from 4 to 1 and in the case of an 8-node quadrilateral element the number of integration points are reduced from 9 to 4. This reduction affects directly the CPU time necessary to calculate the stiffness matrix, decreasing the computation time.

#### **5.2.4 Mesh convergence**

In order to increase the accuracy of simulations when high stress gradients are present, a high-degree mesh refinement technique is normally used. This technique is based on a local refinement over this region including a smooth transition between refined and coarse elements in order to avoid excessive computational requirements. However, this technique is appropriate when stress/strain levels are not sought in areas with geometrical singularities. Geometries of bonded joints are usually difficult to mesh due to two main reasons: difference in dimension and inclusion of geometric singularities. Geometrical singularities are expected in bonded joints due to the presence of theoretically sharp corners; this can be avoided when the stress distribution is analysed areas not affected by them . However, there are also other singularities when stresses and strains are analyzed near the crack tip. In order to sort out this problem, the strain energy release rate is used as a criterion of convergence. This criterion has the advantage that it could be useful to understand the relation between the strain energy release rate and the mesh density. Two numerical techniques were used in simplifications in order to evaluate this parameter in FEA - VCC and the J-integral.

A series of cohesive pre-cracked CFRP LSJ<sub>long</sub> models as seen schematically in Figure 5.2, were used to determine numerical errors and compromise between solution time and accuracy at each mesh density used. They assumed a completely elastic material behaviour, tension at 11 kN with different mesh densities, element types, element formulations and numerical methods to estimate the a LFM parameter. An analytical model described as a Brussat model [39] was also included in order to have a reference for the magnitude expected for  $G$ . A first comparison conducted was for a relation between  $G$  and the element size, presented in Figure 5.3-(a) and using a low order element type. A first numerical method used to obtain  $G$  was VCC; that method is capable to identify the strain energy release rate produced by each mode load-peel stresses with  $G_I$  and shear stresses with  $G_{II}$ . The total strain energy release rate ( $G_T$ ) is obtained by the combination of  $G_I$  and  $G_{II}$ . The results show that  $G_T$  has a quasi constant level until a drastic increase for meshes with element size lower than 0.01 mm. A second method that was used to obtain  $G$ , is the J-integral, with the path-independent integral being equal by definition to  $G_T$  in the linear-elastic analyses. The path-independency of the J-integral was analysed using three paths around the crack tip with their value denoted as  $J_1$ ,  $J_2$  and  $J_3$ ; they were numbered from the closest path at the crack tip as 1 to the farthest (3). The results show that in general terms, there is no significant differences between the J values for all three paths, however, a weak difference is found when the paths that surrounds the crack tip exceeds the equivalent at two element distance. Comparing the results obtained using VCC and J-integral it is observed that both have the same tendency until the discussed low element size is achieved in the first approach when the drastic change of  $G_T$  is observed.

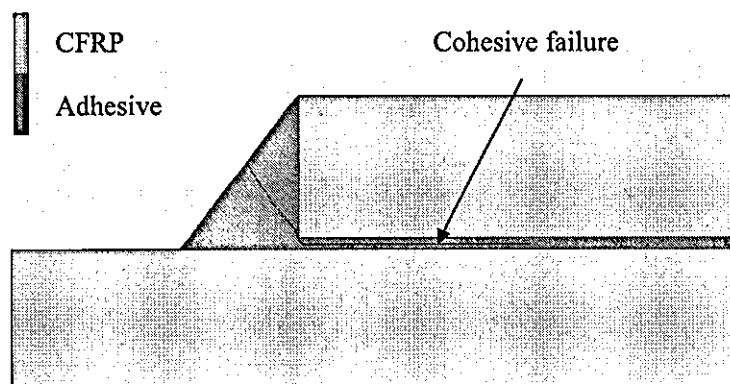
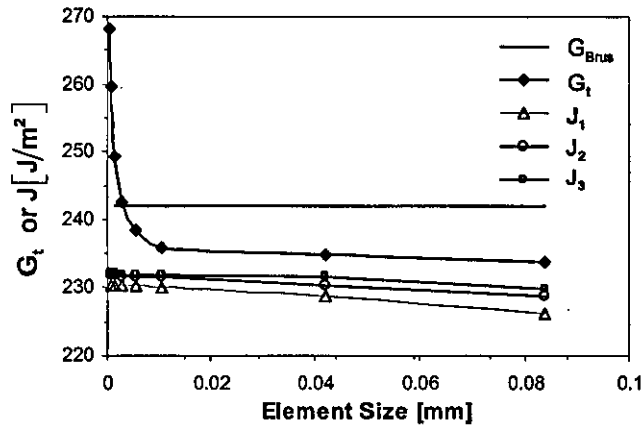


**Figure 5.2 Detail of a cohesive failure in a LSJ<sub>long</sub> specimen**

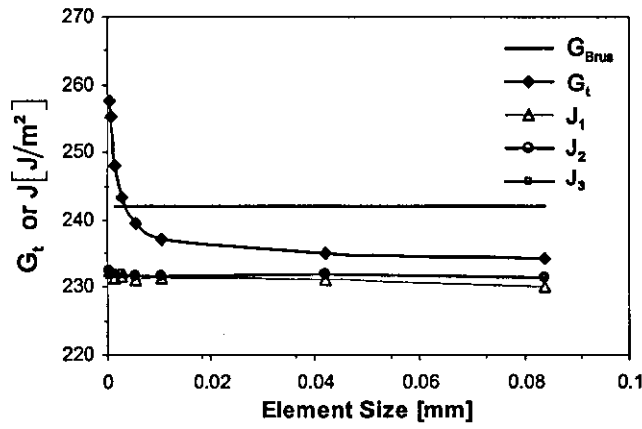
A second analysis was conducted using similar meshes that were developed for the models described above but using a high order element (but without  $\frac{1}{4}$  node formulation to capture the singularity), including both integration formulations. Analysing the results, non significant changes were found for different integration formulations. In addition, no increase in the accuracy or changes in the trends of relations were found in simulations based on lower order elements (Figure 5.3-b). A subsequent analysis conducted for  $G_T$  identified the dependency of the mixed mode ratio calculated as  $G_I/G_{II}$  on the element size. Unexpectedly, it was found that the mixed mode ratio diverged at the same element size that was found for  $G_T$ ; however, the magnitude of the studied element size range was lower than that predicted by the Brussat model. In addition, over the region where the mixed mode was stable, a high difference with the Brussat model was observed. It was observed that the Brussat model gave an erroneous result because the model assumed that a LSJ specimen was loaded mainly in Mode *I* contradicting the definition of this joint configuration.

Reasons for the divergence found for  $G_T$  values at extremely low element sizes can be explained by the singularity accounted for in the model with the crack tip. It is well known that with the decrease in the element size near the crack tip the level of stresses would grow infinitely due to the singularity; this increase would affect the numerical values for the nodes that are close at the crack tip. However, from the results of simulation, a critical element size was found above which the effects of the geometrical singularity is low.

Finally, as expected no element-size dependency was found when  $G$  was obtained using the J-integral method. In addition, similar conclusion can be easily extended to the case of VCC for the element size below the critical value, for which the divergence tendency for  $G$  was detected. It was also found that meshes with the element size higher than 0.01 mm produced correct values but in order to have appropriate element size ratios the size of elements near the crack tip should be no larger than 0.04 mm.



(a)



(b)

Figure 5.3 Comparison of energy release rate using different methods in a cohesive failure of 3.35 mm: a) low order element; b) high order element

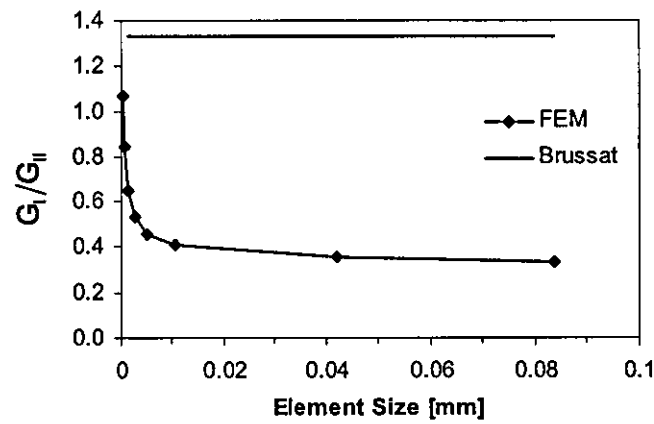
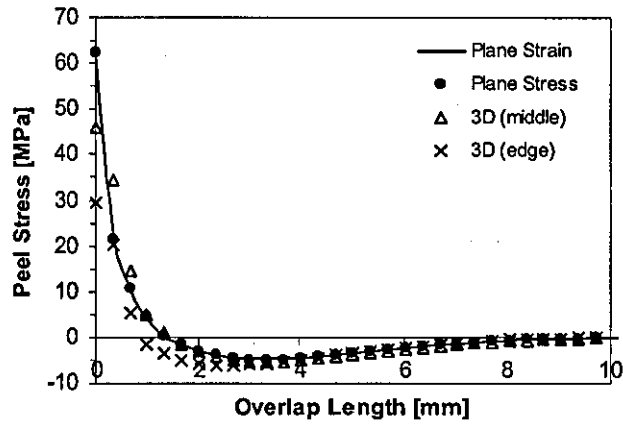


Figure 5.4 Mixed mode dependency on element size

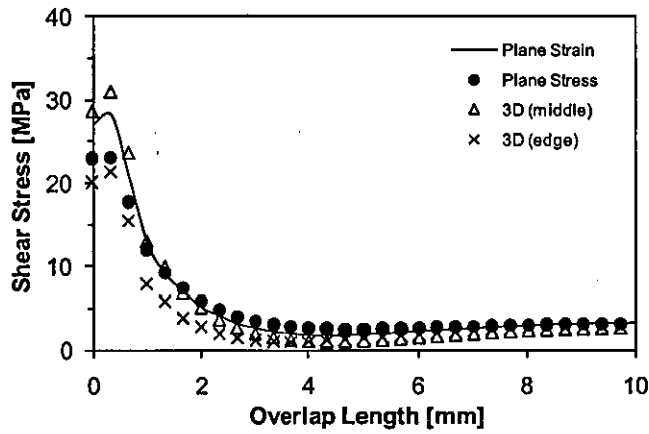
### 5.2.5 Geometrical consideration

As previously explained, meshing of a bonded joint is a difficult task that could result in increases in the CPU time. In order to decrease the CPU time, it is a usual practice in modelling to simplify the problem's geometry reducing its dimension from 3D to 2D. Various additional simplifications can be used in the modelling of lap joints, one of these being the use of the symmetry. There is also a possibility to use various 2D formulations - consider a plain stress and plain strain state for a respective cross section. These different options to model a lap joint in the specific case of a LSJ, may produce different effects on the stress/strain behaviour or even result in values of stress/strain components that can be affected by errors. In order to analyse these differences, a strain distribution over the middle adherend for a LSJ<sub>long</sub> configuration is analysed in order to compare results of the 3D and the 2D models based on different formulations. A four node element, with an assumed strain formulation, was used in 2D models with plane stress and plane strain formulations. In the case of a 3D model eight node iso-parametric brick elements with assumed strain formulation were used. All models were simulated in quasi-static conditions assuming a linear elastic material behaviour for the adhesive with a distributed load on one end.

Figure 5.5 shows the peel and shear stress distributions in the middle adhesive obtained for those models in concordance with findings presented in [166]. They are compared with results of simulations with the 3D model for two regions of the full middle adhesive area: one for a middle plane of the specimen and a second for its edges. In general, a similar tendency was found for stress distributions for both models (2D and 3D). In addition, no difference was detected for the peel stresses for 2D plane stress and plane strain models. But when the shear stress in the middle of the 3D model and in the 2D plane strain model are compared, it is obvious that they are slightly higher in the 3D. Similar differences and trends were found for the shear stresses at the edge (3D model) and for the plane stress formulation of the 2D model. Additionally, the shear stresses in the case of the 3D model are higher in the middle of the specimen; this is supported by results of the 2D model showing that the plane strain state has a higher level of shear stresses than the plane stress state. A comparison of the CPU necessary to solve both models (2D and 3D) showed that a transfer from the 3D model to the 2D results in a decrease in the CPU time by 87%.



(a)



(b)

**Figure 5.5 Comparison of stress distributions over the middle adherend in 2D and 3D FEA models: (a) peel stresses; (b) shear stresses.**

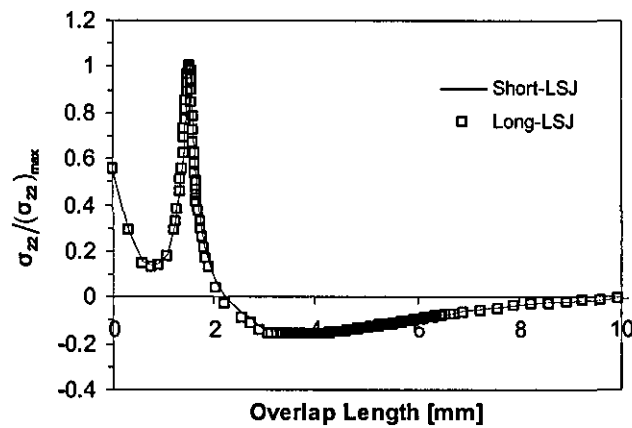
Finally; it is concluded that the 2D model, either plane stress or plane strain, results in a drastic decrease in the CPU time without compromising the precision and character of the stresses obtained for comparable areas of the 3D model. Hence, the studies below will be simulated with the 2D plane strain model unless different model is mentioned.

### 5.2.6 Specimen size differences

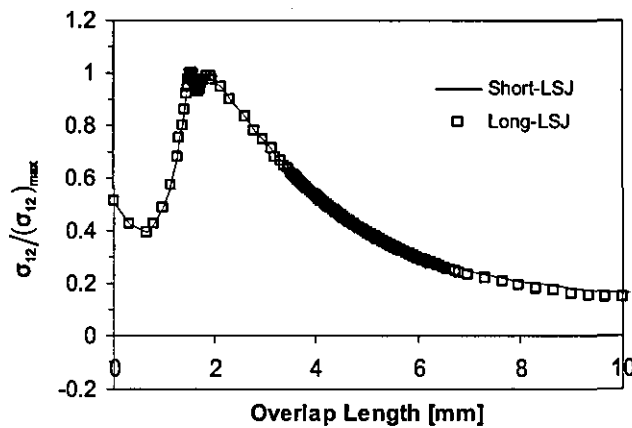
After an analysis of mesh dependency and choosing the 2D model to decrease the CPU process time, it is necessary to understand how differences in the specimen size



affect the stress/strain distributions in the joint. As mentioned in Chapter 3 two geometries of LSJ specimen were used in this study -LSJ<sub>short</sub> and LSJ<sub>long</sub>. The 2D models (including fillets having the same geometry as real specimens) using four noded elements and linear elastic material properties was employed to compare shear ( $\sigma_{12}$ ) and peel ( $\sigma_{22}$ ) stresses over the middle adhesive line for LSJ<sub>short</sub> and LSJ<sub>long</sub> geometries. Figure 5.6 shows the normalized peel and shear stresses for both specimens; the specimens have similar stress distributions that are not affected by changes in the specimen size. It should be also noted that inclusion of the fillet into the 2D model does not affect the stress distribution outside it; however, the stress distribution over the fillet has a specific character.



(a)



(b)

**Figure 5.6 Comparison of stress distributions over the adhesive middle line for short and long LSJ specimens: (a) peel stress; (b) shear stress.**

### 5.2.7 Back face strain gauge in LSJs

In order to identify suitable places where useful strain measurements can be taken to analyse fatigue crack growth in LSJs, a special FEA model of the overlap should be developed. A  $LSJ_{long}$  geometry with the low order elements was used to simulate quasi static loading conditions. The back face strain in the X direction (see Figure 5.1) obtained in simulations for two points given in Figure 4.13 are presented in Figures 5.7 and 5.8. Figure 5.7 shows the strain changes as the crack grows for various positions of points over the lap, measured from the fillet. A general pattern is seen with the strain decreasing steadily until the crack reaches the position along the bondline corresponding to the location of the strain gauge on the back face. At this point there is a dip in the curve and the strain becomes compressive. After the crack has grown beyond this point, the strain gauge is on the part of the lap adherend that is no longer attached to the strap adherend and, hence, is unloaded. So the strain signal vanishes and it is no longer sensitive to the crack growth. It can be seen then, that the ability to detect the crack growth is highly dependent on the position of the strain gauge and the position of the crack. Hence, a different gauge location may be chosen if the aim of the experiment is to predict the first signs of cracking as compared to the aim to monitor the crack growth along the length of the sample.

The results of BFS simulations for a point in the strap as the crack grows are shown in Figure 5.8. Again it can be seen that the strain gauge's location has a strong effect on crack monitoring. The first thing to note is that the strain levels and the difference between maximum and minimum strains are greater than for the gauge on the lap adherend. This is potentially useful in decreasing the effect of experimental scatter, depending on the noise in the strain gauge system. For this adherend, the trend is a steady increase in strain as the crack progresses, followed by its large decrease as the crack passes the location of the gauge, after which strain increases again. This result is due to the fact that as the crack size increases the rotation effect around the crack tip also moves affecting the mix mode. Initially, strain in X direction over the strap at a specific direction increases due to the bending effect; however, as the crack grows this bending effect will be transformed into rotation decreasing the strain level. However, as the crack continues to grow the strain in a point tends to have the initial strain levels. The big advantage of placing the gauge on the strap adherend is that the gauge

can be placed at the site of most interest but will still be able to monitor the crack growth along the whole length.

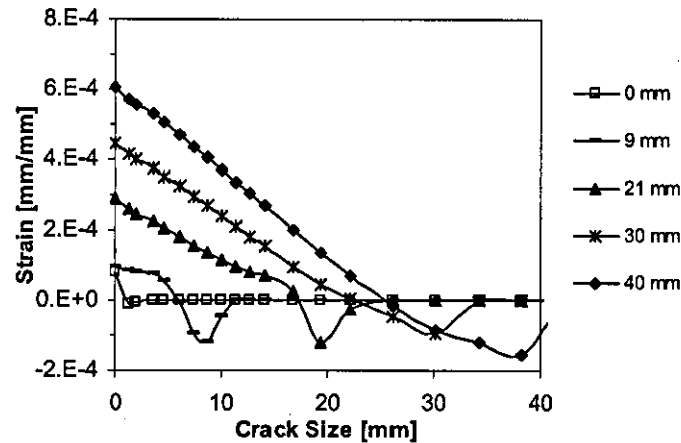


Figure 5.7 Back face strain for different location on the lap adherend

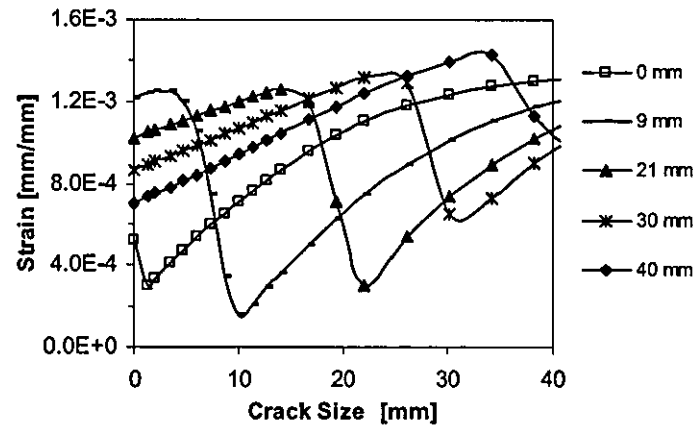


Figure 5.8 Back face strain for different locations on the strap adherend

### 5.3. Development of dynamic model

The aim of development of a dynamic FEA model for LSJ is proposed to study features of the fatigue crack growth behaviour in joints during IF. Still, the finite-element model is developed for a single dynamic impact to analyse the effect of dynamic loading supposing that fatigue crack propagation is related with the maximum load conditions that is reached during the impact.

The process to develop the model capable to reproduce the dynamic situation for LSJs implies more steps than for the quasi-static model. Under dynamic conditions, the interaction of the bodies that are in contact during the impact are extremely important. In order to develop an adequate dynamic model for LSJs, a calibration of the boundary conditions is conducted using the more simple specimen geometries as well as using simulations of un-cracked LSJs.

### 5.3.1 Dynamics of single impact

In order to get an understanding of dynamics of an impact, a simple tensile-impact test was conducted with an aluminium 7075-T6 plate. The plate was manufactured using the geometry and dimensions of the strap of the LSJ<sub>short</sub> specimen. A semiconductor strain gage glued to the face at the middle of the plate was used to measure the dynamic strain for that point during the impact produced with the testing machine as described in Section 4.6.3. However, in the experimental work it was found necessary to measure the strain response on the opposite face of the specimen. In order to have a second recorded set of the data and trying to use the same software and controller of the testing machine, the aluminium plate was rotated, and the strain for the opposite face was measured. That technique is difficult since the strain over opposite surfaces should be captured using two signals that are not measured simultaneously. However, in order to match both signals, they were positioned at the time that a change in the signal was observed. Although this is not a direct method, as explained below, it gives good results. The reaction force and the matched strain data for both top and bottom positions of the gauge were measured during the hammer with energy of 0.77 J and a velocity of 1.27 m/s, (showed in Figure 5.9) of the impact block joined to the aluminium plate.

Experimental measurements of the reaction force are presented in Figure 5.10 (a). It is seen that this signal corresponds to a quasi-perfectly-elastic impact; its symmetry suggests that the approach time is similar to the restitution period. No problems with refractions in the tensile direction were detected by the sensor except to a small disturbance of the signal at approximately 2.5 ms. In addition; these measurements show that the experimental setup has special support conditions practically eliminating reflections at least along the axes of impact, thus avoiding problems of

superposition of signals in the test. Analysing the reason for this, it is seen the pin connecting the vice support and the vice (Figure 4.11) was not perfectly adjusted to the hole of each piece. So when a tensile force reaches the support due to this clearance it would not be reflected since the part would move by a small clearance distance without any restriction. Additionally, it was detected in tests that the force signal suffered a small decrease (around 0.3 ms) during the approach period. That short decrease could be a result of a bouncing between the hammer and the impact block for a short period. As shown in [129], that could be explained by the value of the coefficient of restitution ( $e$ ) (with 1 representing a perfectly elastic collision, while 0 corresponding to a perfectly inelastic one), with  $e=0.57$  being the limit for a continuous bouncing and a transition to a dying-out conditions. However, the force-signal measurement showed that the bouncing phenomenon is extremely limited being present only in one test and not changing the smooth increasing tendency that the signal should have for the case of a perfectly elastic impact.

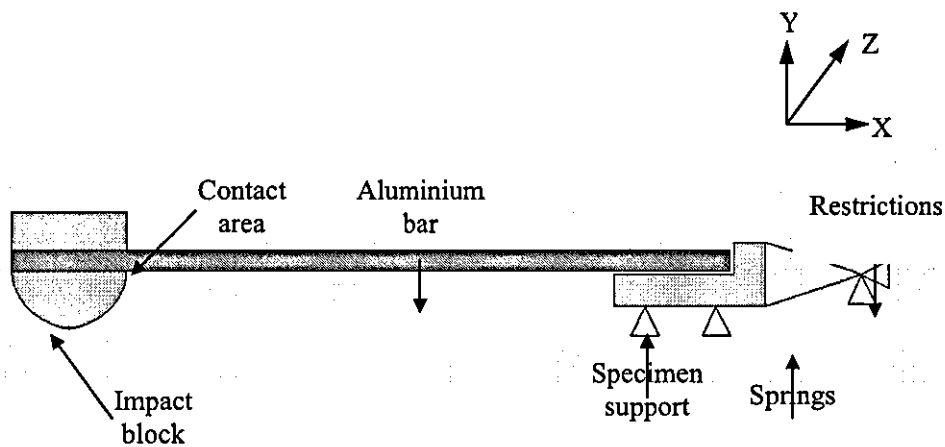


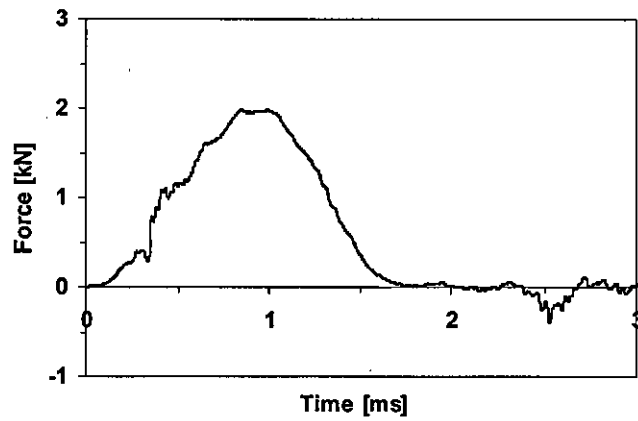
**Figure 5.9 Schematic representation of aluminium bar**

The second type of data that was captured for that simple test was the strain on the top and the bottom of the aluminium plate. In general, both strain signals had a significantly different behaviour, showing that the deformation effect in the specimens was different from the theoretical signal expected during a pure tensile impact. It is known that in a pure tensile impact the strain signal should be similar to the force signal but out of phase. The last feature is due to the time necessary for the stress wave to travel from the middle aluminium plate to the support with the force sensor (unfortunately, our experimental measurements did not have the precision to

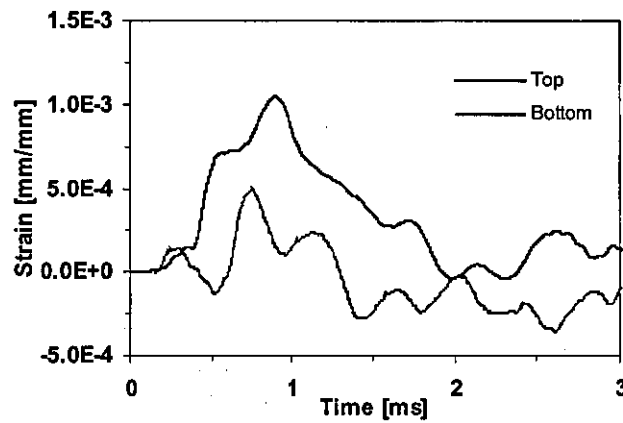
measure exactly this phase shift). In addition, it was calculated that the theoretical expected maximum strain for a 7075-T6 bar with a rectangular section of 15 mm x 3.2 mm, with a Young's modulus of 71.7 GPa, hit in tension with a peak load of 2 kN should be around  $5.8 \times 10^{-4}$  mm/mm.

Despite of the differences between both signals, some relations for specific periods were detected. Though both signals were supposed to be measured at the same time but after some period, a change on the tendency was found: after around 0.5 ms the top strain began to grow and the bottom one to decrease, loosing the symmetry. Such behaviour can be explained by a rotational effect in the plate counter clock wise with regard to the impact block (see Figure 5.12). After that, a decrease in the slope of the top signal was detected with the bottom having a high slope increase. Then, at approximately 1 ms, an increasing symmetry was detected due to the bending deformation mechanism with the quasi-constant tensile effect still characterizing the deformation; the top strain picked while the bottom signal had a local decrease. After reached the maximum strain on the top a continuous decrease was observed, where with both rotation and tension decreasing. However, after 2 ms when there was no interaction between hammer and the aluminium plate, an opposite bending model was registered in the specimen as a product of small amplitude vibration of the plate.

An additional analysis over the total contact time (in the case of the force) and the entire period from the moment of the start of measured deformation and the time when both signals vanished suggests that after the hammer disengage from the impact block, a remaining bending effect is due to the fact that the position of the plate before the impact differs from that just after it. After a short period, the remained bending wave would have some reflections that would disappear rapidly. Their magnitude was around 20% of the maximum strain reached during an impact in the case of the first reflection.



(a)



(b)

**Figure 5.10 Experimental data for aluminium plate in tensile impact:**  
(a) reaction force; (b) strain measurements

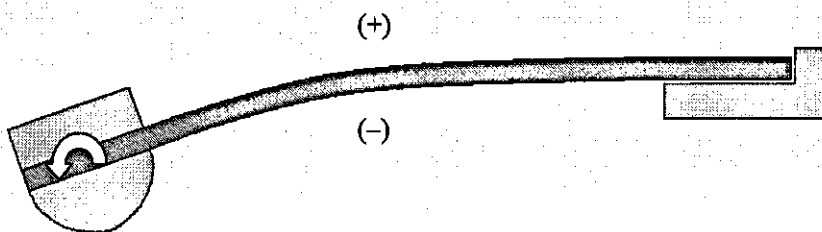


**Figure 5.11 Bending effect in the aluminium bar**

### 5.3.2 Support calibration

In order to understand the impact in more detail and also to identify the reason for the rotation of the aluminium plate, a geometrically nonlinear dynamic implicit 2D model was developed. The transient analysis was implemented using a single step integration method known as “the single-step Houbolt” method [167]. That algorithm was suggested in [18] for a dynamic implicit contact analyses.

The model is composed basically of four elements -a hammer, a specimen, an impact block and a specimen support. The hammer is modelled as a body with a real 2D geometry, using a variable thickness for each section and materials, representing the features of the real component. Corroboration of the weight and inertia were accounted in order to represent as close as possible the real pendulum hammer of the testing machine. In order to decrease the time of simulations, the hammer was modelled an instant before of the vertical position was attained with an initial velocity of  $V_0 = 1.27 \text{ m/s}$ . A special restriction imposed by two linear spring elements was included into the model, connecting the specimen support and a fully restricted support. The springs were used to introduce the compliance effect of the anvil into the model, and eventually, to model the response in the system as closely to the experimental one as possible. The impact block was included into the model, with the size, thickness, contact shape and weight of the original; a perfectly union bond between the impact block and the specimen was supposed. Finally, a contact restriction without friction between the hammer and the impact block was included.

#### 5.3.2.1 Effects of stiffness

As mentioned previously, the developed model employed the fact that elastic reactions are supposed to be the part of the response of the support in order to include the compliance effect of the vice. The value of the spring constants are found by direct simulations for a range of stiffness starting with an infinite one for a perfectly restricted support and decreasing it gradually until a certain value producing reaction forces and contact time close to the measured ones. The decrease in stiffness of the spring produced a decrease in the reaction force and, subsequently, an increase in the contact time.



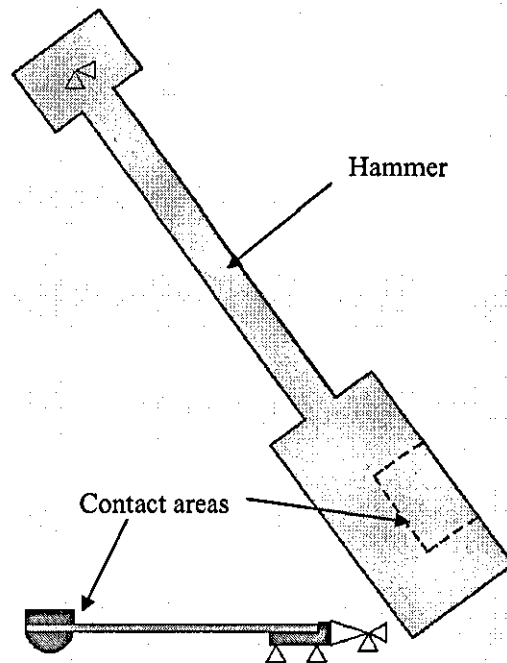
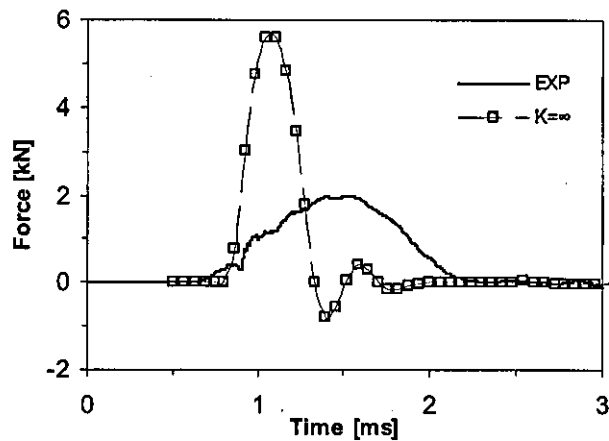


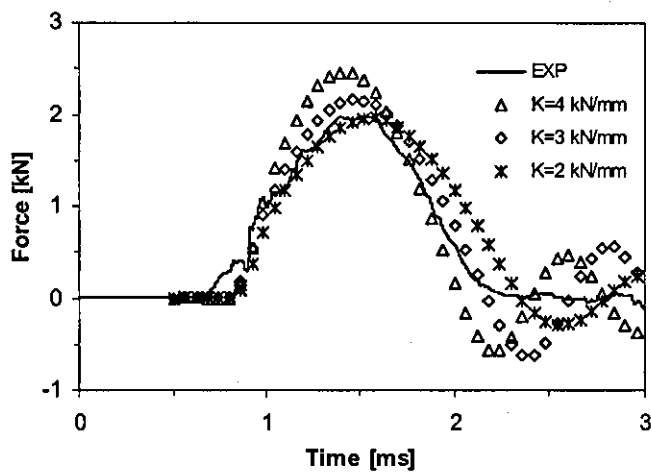
**Figure 5.12 Description of a 2D model of impact**

Results of finite-element simulations of a rigid support are shown in Figure 5.13-a. In this case, the maximum reaction force in simulations increased considerably being significantly higher than the experimental results. As mentioned before, decreasing the value of the spring constant decreased the reaction force and increased the contact time. Thus, by trial and error, the values were changed (it was supposed that both springs had the same stiffness) until the optimum magnitudes of around 3 kN/mm were found (Figure 5.13-b). They provided a good match between the experimental data and the simulations for the period of interaction between the hammer and the aluminium bar. However, comparing both types of data (experimental and simulation) after detachment of the hammer from the impact block it was obvious that small-amplitude fluctuations are presented in the model but not in the experiment. Mathematically, such fluctuations can be eliminated in the model by means of the damping effect on the support. However, when this effect was included into the model the symmetric shape of the reaction force changed. In addition, it was concluded that due to the presence in the machine of a not completely rigid restriction (a pin), the

waves were not reflected (at least, in the tensile direction), avoiding the effect of reflection in the aluminium bar. Finally, it was observed that the critical part to be simulated is the period when the hammer is in contact with the impact block.



(a)



(b)

**Figure 5.13 Comparison between experimental and calculated reaction force: a) completely rigid support; b) elastic support.**

### 5.3.2.2 Calibration of contact area

The second analysed variable was the interaction between the hammer surface and the impact block. A small misalignment between both flat surfaces interacting during the

impact can produce variations in the direction of the forces in the aluminium plate. The optimum impact point was defined as the moment when the hammer reaches a vertical position after being released from its initial angle producing the impact on the hammer block that initially was also modelled as a flat surface. The change of the impact instant can be achieved in the model by moving the hammer block with regard to the vertical position of the hammer. The results of simulations demonstrated no significant changes when the instant of impact was moved back from the optimum impact instant. However, when it was moved forward, a rotation of the aluminium plate was detected but in the clock wise direction, in contrast to the experimental results (i.e. contrary to what is seen in Figure 5.11).

An additional analysis was implemented for cases with the increasing or decreasing distance between the specimen and the hammer's rotation point. The obtained results demonstrated that in order to obtain bending similar to that in experiments (Figure 5.10) that distance should be changed significantly contrary to experimental observations. Finally, it was concluded to include changes of the contact surface of the impact block in order to achieve a rotation effect in the aluminium plate, but keeping the impact duration. Physical inspection of the impact block showed that the impact surface has a small angle with vertical position of the hammer. In addition, it was found that this angle was in clockwise direction, so that when the hammer hit that surface, a tensile force and also a counter-clockwise rotation of the impact block were initiated. An optimal value of that relative angle was obtained by trial and error for an angle of  $1^\circ$  a match with experimental observations was found. Figure 5.14 gives a comparison between the experimental and FEA results, showing a good correlation.

### **5.3.3 Impact in LSJ without crack**

After calibration of the boundary conditions of the model in order to reproduce the impact in the Resil-Impactor testing machine, a comparison of computational results with experimental data for LSJ specimen without a crack was conducted to validate the model. The dynamic model using a non-cracked LSJ<sub>short</sub> geometry, low element order, linear elastic material behaviour for the CFRP adherend and adhesive, and the boundary conditions described above was used to compare the reaction impact force

and signal of the BFS connected to the strap at a distance of 15 mm from the overlap and in the middle of the specimen.

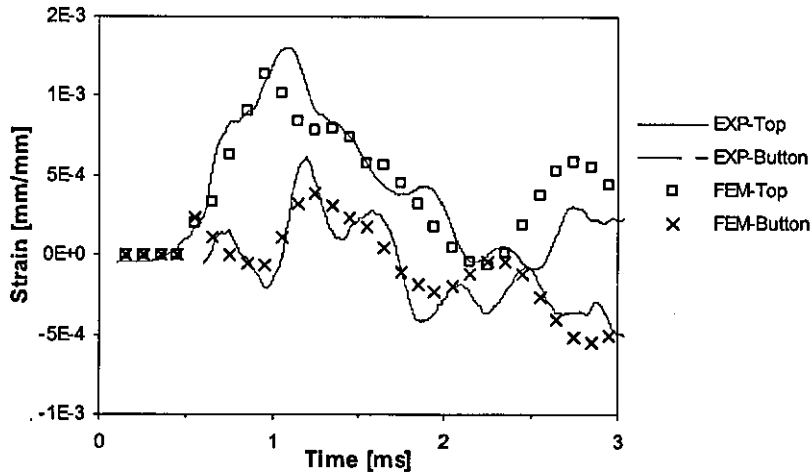


**Figure 5.14 Comparison of experimental and FEA BFS for aluminium plate**

The first comparison is for the reaction force (Figure 5.15). A good agreement between both signals was found with a similar maximum reaction force and a nearly equal contact time. However, in contrast to the case of the aluminium plate, a small reflection with an amplitude of about 16% of the maximum value is found for a reflected initial wave. Similar conclusions can be drawn for strains in the X direction predicted by the model and measured in experiments in the point of a strap that was 15 mm away from the fillet (Figure 5.16). In addition, it was noticed that the strain tendency predicted by the FEA model was in a good agreement with the experimental data, especially in the region of loading and unloading. Still, for the moment when the maximum strain is expected there is some difference with experimental data. This difference can result from a small change on the boundary conditions when another specimen type was tested.

In addition, during the development of the dynamic, nonlinear, implicit model with the elastic material behaviour and solved using a constant time step, shows that the strain response at a point at 15 mm away from the filled was influenced by the time step that was selected. With the decrease in the time step a numerical error in the predicted strain level with a high level of noise occurred. As a result of that analysis,

the optimal time step for simulations was defined as 4  $\mu$ s. It is the lowest time step value that can predict the strain tendency without significant fluctuations of the numerical result.

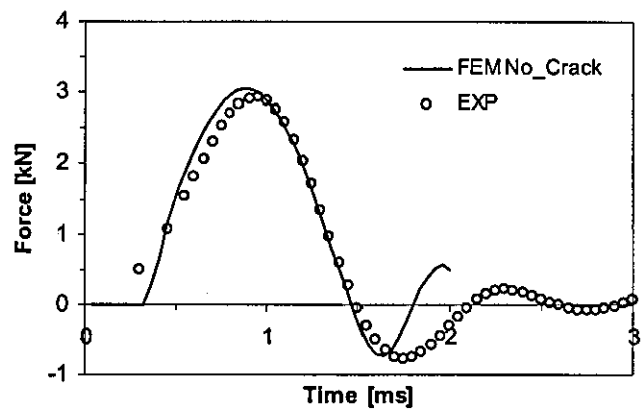


**Figure 5.15 Comparison of experimental and FEA results for force in support. Specimen without damage**

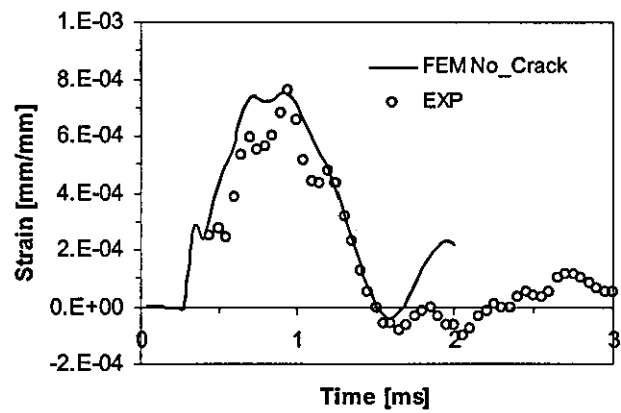


**Figure 5.16 Comparison of experimental and FEA results for axial strain in strap at 15 mm from the fillet. Specimen without damage**

### 5.4. Model to determine the strain energy release rate

In the following section a description of the methodology used to determine the strain energy release rate  $G$  for cracked LSJs under quasi-static and dynamic loading is given. Various methods were used to obtain this parameter such as the VCC for linear models and the J-integral when the effect of plasticity was included in the analyses.

### 5.4.1 Quasi-static model

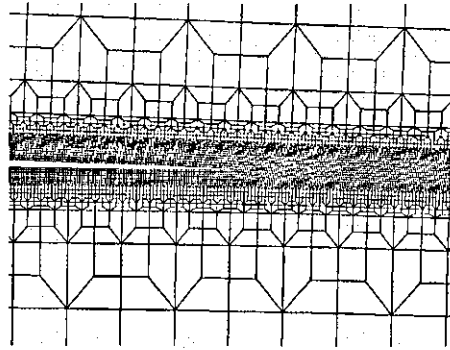
To analyse changes in  $G$  for a crack growing in a LSJs specimen, a direct study with the model using an  $LSJ_{short}$  configuration should be conducted. A description of scenarios of crack localization and the principal directions of crack propagation is presented below.

#### 5.4.1.1 Crack growth scenarios

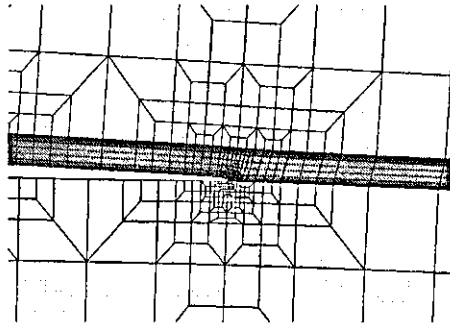
Three scenarios of cracking were explored in the models, shown in Figure 5.17: (i) a crack in the centre of the adhesive layer (Figure 5.17 (a)); (ii) a crack at the interface between the CFRP strap adherend and the adhesive layer (Figure 5.17 (b)); and (iii) a crack in the first ply composite of the strap adherend adjacent to the adhesive layer (Figure 5.17 (c)). The three models are aimed at representing the three loci of failure observed experimentally (discussed in Chapter 6). However, the interface model is rather contentious as the experimental failure was not along a well defined interface between two materials and there is the problem of theoretical singularities when determining fracture parameters at bi-material interfaces.

#### 5.4.1.2 Principal stress direction

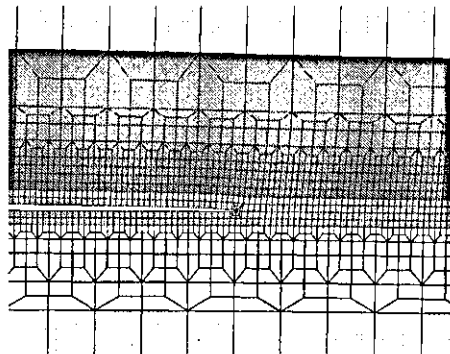
In numerical simulations for any of the three scenarios of crack growth, a variation on the principal stress direction over the crack tip can be determined, influencing the orientation on the crack growth. The direction of crack propagation at each stage of simulations is obtained supposing that the crack propagates in the direction defined as the greatest tension. Then the increments of crack growth can be expressed in terms of the stress intensity factors for modes I and II as [168]:



(a)



(b)



(c)

**Figure 5.17 Finite-element meshes of areas with cracks: (a) cohesive fracture of adhesive, (b) interfacial fracture, (c) fracture in 1<sup>st</sup> ply of CFRP (adhesive layer in grey)**

$$d_x = \frac{3 \frac{K_{II}^2}{K_I^2} + \sqrt{1 + 8 \frac{K_{II}^2}{K_I^2}}}{1 + 9 \frac{K_{II}^2}{K_I^2}}, \quad (5.1)$$

$$d_y = \frac{3 \frac{K_{II}}{K_I} - \frac{K_{II}}{K_I} \sqrt{1 + 8 \frac{K_{II}^2}{K_I^2}}}{1 + 9 \frac{K_{II}^2}{K_I^2}}. \quad (5.2)$$

The stress intensity factors were calculated using the values of  $G$  based on the VCC technique and the respective relation described in Chapter 2.2.2.1. Equations 4.1 and 5.2 are defined for a Cartesian coordinate system, presented in Figure 5.1

A comparison between the angle of crack propagation, which is the angle between the horizontal plane and the direction with the maximum  $d$ , and the crack size was conducted with the geometrically non-linear model using a cohesive crack scenario. The calculated results are presented in Figure 5.18. It was found that the angle of crack growth was always negative with respect to the positive  $X$  direction shown in Figure 5.1. With an increase in the crack size, the negative angle of the crack direction increases. This means that as the crack grows in the adhesive in the direction of the greatest tension, it tends to jump from the adhesive to the CFRP strap that is the direction.

#### 5.4.2 Dynamic model

The simulation of the LSJs under dynamic conditions were conducted using the boundary conditions described in Section 5.3.3 using the same crack growth scenarios presented in Section 5.4.1.1



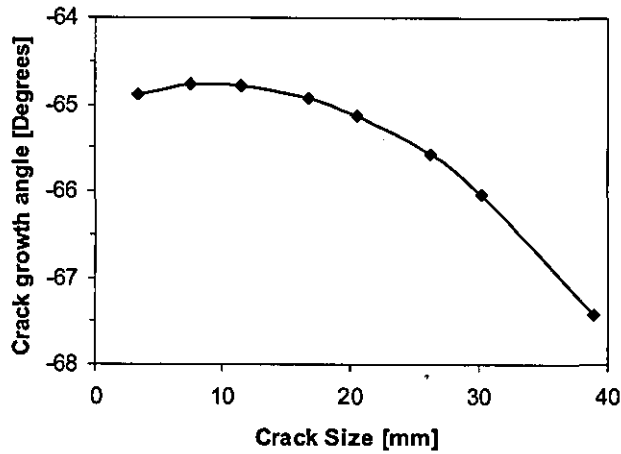


**Figure 5.18 Changes of crack propagation direction for cohesive failure in short LSJ**

## 5.5. Summary

This chapter presented the methodology to develop finite-element models for LSJs under quasi-static and dynamic load conditions. The BSF technique was used to understand the deformation behaviour of LSJs for further studies of the crack growth under SF and IF. An experimental study of the boundary conditions and dynamics of an impact were conducted to calibrate the dynamic finite-element model of LSJs.

A comparison between the energy release rates calculated with different methods such as VCC and three different patterns of J-integral (in terms on the element size) shows no significant differences in the obtained values. However, as the element size decreases, the VCC technique begins to produce an error in the solution. Additionally, it was found that the type of element that were used – a low order element (four nodes) and a high order element (eight nodes) – does not significantly affect the results even though the CPU time increases dramatically. As expected, results for three regions around the crack tip confirmed that the J-integral is not path-dependent. Comparisons between the VCC and J integral with an optimal element size do not produce considerable differences with an analytical model (Brussat model); however, this model shows erroneous values for mix mode fracture.

## **CHAPTER 6**

### **Quasi-static testing and fatigue life of aluminium bonded single lap joints**

#### **6.1. Introduction**

The main aim of this chapter is to understand and quantify the fatigue life of adhesive lap joints when exposed to impact fatigue (IF). The chapter deals with a detailed experimental analysis of single lap joints (SLJs) loaded in IF conditions. Various characteristics of the joints response to such loading are studied and some new parameters to characterise the process are introduced. Results from standard fatigue (SF) tests are used as a basis to evaluate the danger of neglecting (IF) in the durability analysis of bonded components and structures.

This chapter presents the experimental work carried out to obtain the fatigue life behaviour for two load conditions: SF and IF. To reach this aim, the research is focused on the following objectives:

- To conduct quasi-static tests to obtain the mechanical properties of SLJs;
- To conduct fatigue tests for SLJs in SF;
- To study the fatigue life of SLJs in IF;
- To study the stress wear-out of SLJs under SF and IF;
- To compare the fatigue life of SLJs in IF and SF;
- To determine the repeatability of the fatigue life in IF conditions for SLJs;

- To perform a detailed microstructural study of fracture surfaces for specimens tested in SF and IF conditions.

## 6.2. Quasi-static testing of SLJs

Two different sizes of SLJs were used, as described in Section 4.5.1, with details of the dimensions of each type given in Figures 4.7 and 4.8. The following subsections will present the experimental data for quasi-static tests on SLJ<sub>short</sub> and SLJ<sub>long</sub>, analysing the fracture surfaces and finalising with a comparison of the stress distribution of both types of specimens.

### 6.2.1 Test results

Experimental data from tests conducted using the procedure described in Section 4.6.1 shows that the type SLJ<sub>short</sub>, required an average force of  $5.56 \pm 0.27$  kN to break the specimen ( $F_{Qs}$ ). A typical plot of force against displacement for this case is presented in Figure 6.1. It can be seen that at low force values, a non-linear tendency describes the behaviour of the joint until a transition to linear behaviour at approximately 0.5 mm extension. The initial non-linear response may be associated with grip slip. Similar behaviour was found for the SLJ<sub>long</sub> joint tested in quasi-static conditions, which had an average failure load of  $9.39 \pm 0.59$  kN. A typical plot of test results for a SLJ<sub>long</sub> specimen is shown in Figure 6.2. A comparison of  $F_{Qs}$  in both SLJ specimens can be conducted defining the  $F_{Qs}$  per unity of width, in the case of SLJ<sub>short</sub> this variable is 0.37 kN/mm and in SLJ<sub>long</sub> is equal to 0.371 kN/mm. This comparison shows that both SLJs specimens show a similar quasi-static behaviour.

### 6.2.2 Fracture surface

Typical fracture surfaces for samples tested under quasi-static loading conditions are shown in Figures 6.3 and 6.4. It is seen that the fracture has a rough, cohesive character, with the crack growing approximately through the middle of the adhesive layer. The presence of small voids inside the adhesive can also be seen; there are caused by air or moisture entrapment during the curing process.

The schematic representation in Figure 6.4 describes the symmetric crack growth in the joints. Specimens were produced with small fillets at both ends of the adhesive joint, formed by the flow of the epoxy during the curing period. In the early periods of crack propagation, the cracks grow inside the fillet at approximately 45° to the plane of bonding, initiating in the region of the singularity point, referenced as “a” in Figure 6.4

SEM analysis of the fracture surface provides a higher magnification view. Figure 6.5 shows a nearly uniform distribution of holes produced, presumably, by the cavitation process of the rubber toughening particles in the adhesive. The lower magnification micrograph in Figure 6.6 demonstrates that failure also involves damage of the carrier fibres. Flakes can also be seen in the epoxy which can be a consequence of mode II loading. However, in this case it is seen that the orientation of the flakes is influenced by the direction of the carrier fibres.

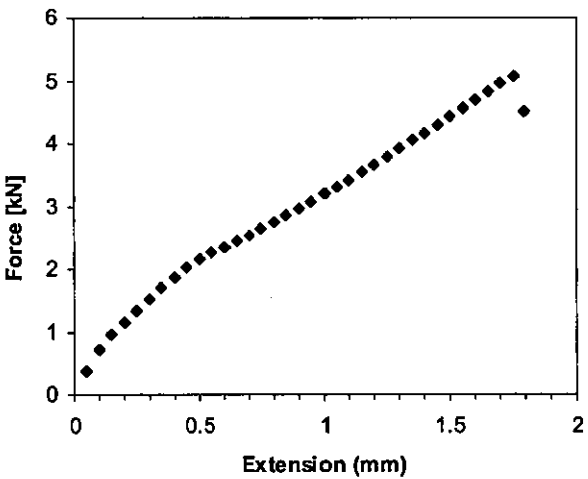


**Figure 6.1** Force-displacement plot for SLJ<sub>short</sub> specimen tested under quasi-static loading

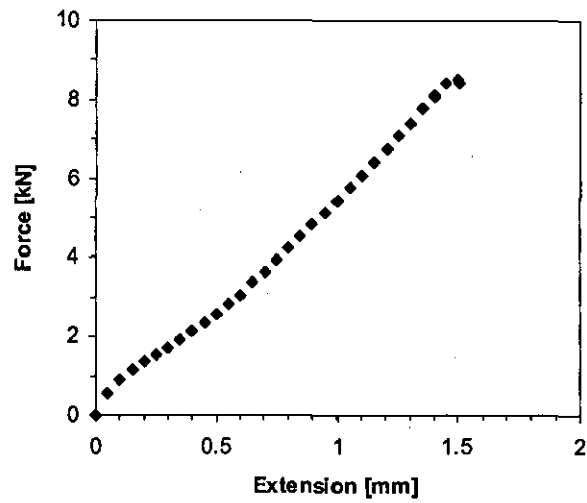
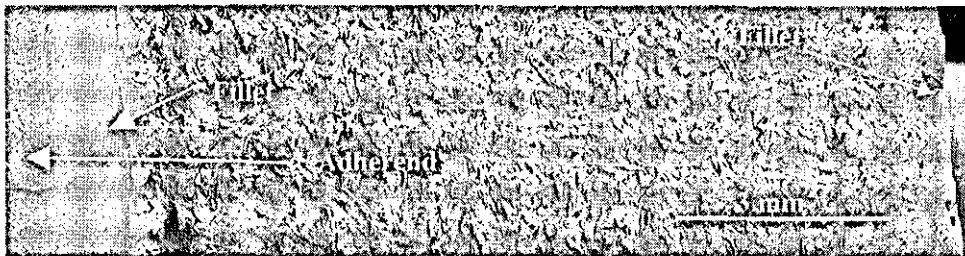
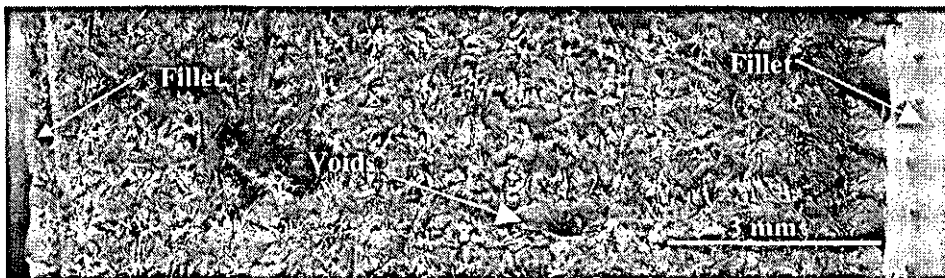


Figure 6.2 Force-displacement plot for SLJ<sub>long</sub> specimen tested under quasi-static loading



(a)



(b)

Figure 6.3 Opposing fracture surfaces after quasi-static testing: (a) upper adherend, (b) lower adherend

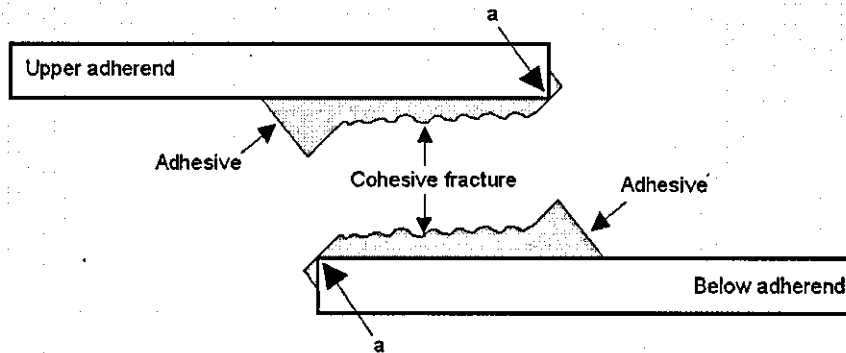


**Figure 6.4 Schematic representation of fracture path in specimens tested under quasi-static loading**

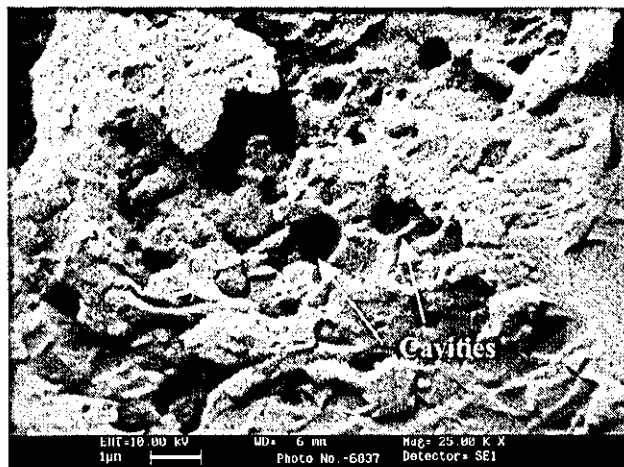


**Figure 6.5 High-magnification SEM of specimen tested under quasi-static loading conditions**

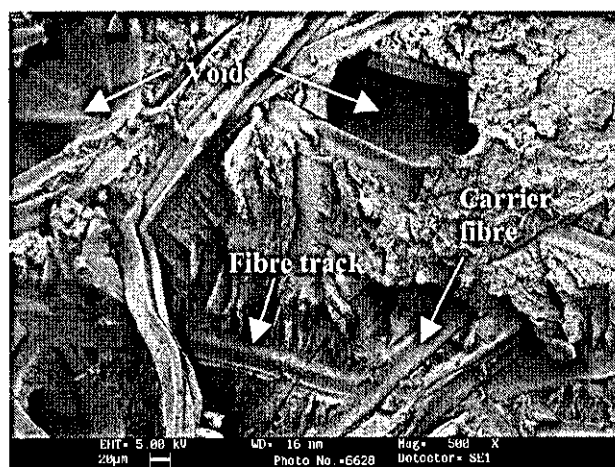


**Figure 6.6 Detail of a typical failure under quasi-static conditions**

6.2.3 Discussion

A comparison of the shear strength of  $SLJ_{short}$  and  $SLJ_{long}$  specimens based on equation 2.20, shows that  $\tau_{SF}^{max} = 30.05 \text{ MPa}$ , and  $\tau_{IF}^{max} = 29.7 \text{ MPa}$ . These results suggest that even through the specimens are geometrically dissimilar, they can support similar magnitudes of shear and peel stress distribution when tested in tension.

Finite element analysis was used to predict the stress distribution in the adhesive under tensile quasi-static loading in  $SLJ_{short}$  and  $SLJ_{long}$  specimens. The geometry and boundary conditions of the FEA models can be seen in

Figure 6.7, with dimensions in Table 6-1. A symmetric boundary condition was applied along the line of symmetry shown in

Figure 6.7. In region S2, a distributed load acting in the x direction was applied, with a magnitude equal to the average force to break the specimen.

Figure 6.8 and Figure 6.9 present a comparison of the subsequent adhesive stress distributions in terms of the x-distance from the line of symmetry of points situated in the middle of the adhesive layer for both types of specimens under quasi-static loading. Stress distribution inside of the fillet is avoided in the graphs.

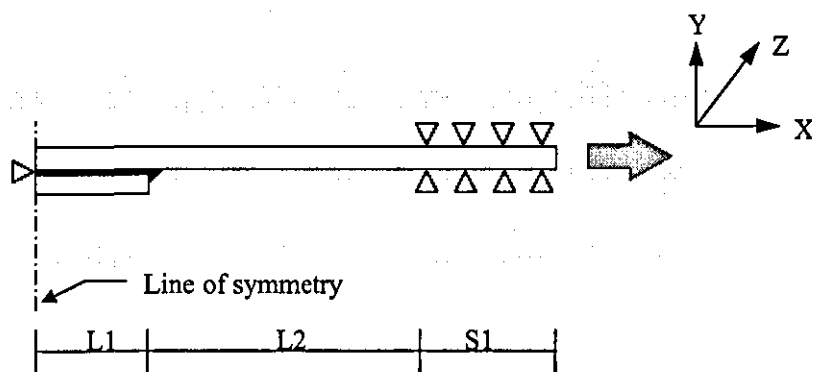


Figure 6.7 Description of a generalized SLJ specimen

It can be seen from these analyses that the SLJ's had similar stress distributions in both specimens concluding that the results found for both configurations can be compared to each other if normalised with respect to quasi-static fracture load.

Table 6-1 Single lap dimensions

Dimensions (mm)	SLJ <sub>long</sub>	SLJ <sub>short</sub>
Bond-line thickness:	0.15	0.15
Aluminium thickness:	2.54	2.54
Overlap (2×L1)	12.5	12.5
Overall length (2×L1+L2+S1):	100	45
Specimen width:	25	15
Support length (S1):	37.5	15

### 6.3. Fatigue life of SLJs in SF

#### 6.3.1 Test results

The following subsections present the results obtained from the SF tests on SLJ<sub>long</sub> and SLJ<sub>short</sub> samples. Various methods are used to analyse the fatigue life and the deterioration of the joints during fatigue testing.

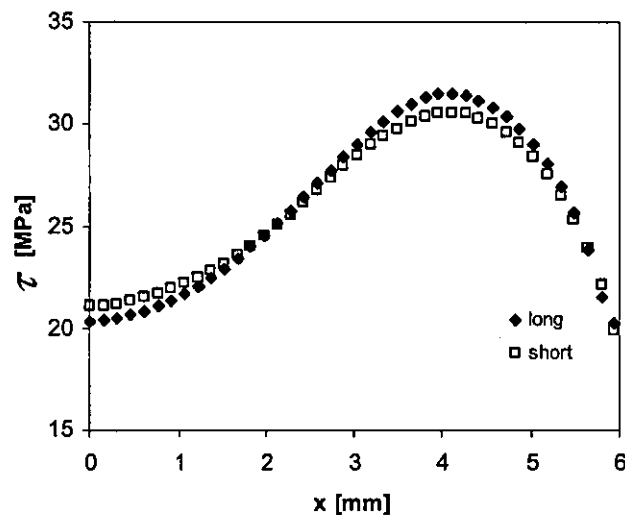
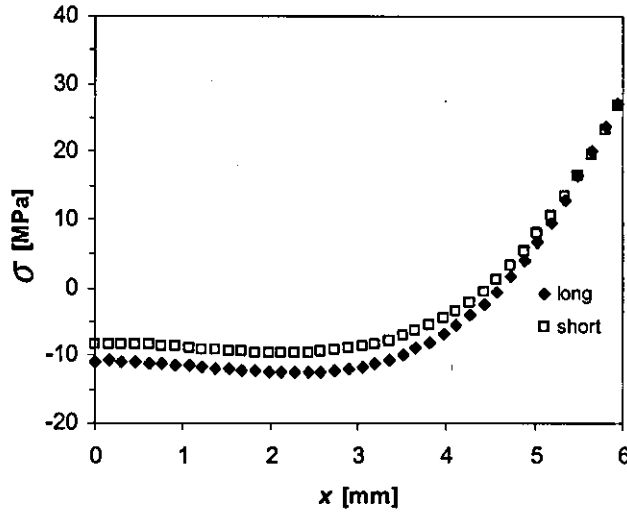


Figure 6.8 Shear stress distributions for SLJ<sub>long</sub> and SLJ<sub>short</sub> specimens in quasi-static loading





**Figure 6.9 Peel stress distribution comparison for SLJ<sub>long</sub> and SLJ<sub>short</sub> specimens in quasi-static loading**

#### 6.3.1.1 Load-life plots

To determine the SF behaviour for SLJs specimens, a sinusoidal load under load control with  $R = 0.1$  and frequency 5 Hz was used, as described in Section 4.6.2. Load controlled tests apply a non-changing magnitude of  $F_{\max}$  during the fatigue life, i.e.  $F_{\max} = \bar{F}_{\max}$ . In order to use comparable parameters for both SLJ<sub>short</sub> and SLJ<sub>long</sub>, Force vs. number of cycles to failure ( $N_F$ ) graphs in SF are plotted in terms of load normalized with respect to the quasi-static fracture load,  $F_{Qs}$ , for each type of specimen. In Figure 6.10, the  $F$  vs.  $N_F$  plot for SLJ<sub>long</sub> and SLJ<sub>short</sub>; shows that SF exhibits three typical regions. There is a low cycle fatigue (LCF) region below approximately 500 cycles and a high cycle fatigue (HCF) region between 500 and  $10^6$  cycles. In this region, there is a nearly linear relation between the normalized  $\bar{F}_{\max}$  and the logarithm of  $N_F$ . A third region is described by an infinite life where specimens could support  $10^6$  cycles without failure. The  $10^6$  fatigue limit of SLJ<sub>long</sub> specimens was approximately 30% of the quasi-static strength of the joint. A comparison of the experimental data for SLJ<sub>long</sub> and SLJ<sub>short</sub> samples shows good agreement.

### 6.3.1.2 Energy - Life plots

Another way to analyse fatigue in SLJs during SF is in terms of the energy that is introduced to the system in each cycle until failure. This parameter is useful when comparing the results from SF and IF because this is a controllable variable under impact conditions. However, identification of a comparable parameter for SF requires additional study. The introduced energy per cycle in SF can be evaluated by means of integrating the force-displacement plot for each cycle. As the SF specimens were tested under force-control, this means that the displacement that a specimen has when the force reaches its peak value in the cycle of the sinusoidal loading will increase during the fatigue life as damage propagates. Similarly, the displacement corresponding to the minimum value of sinusoidal load also increases. To define an energy parameter that can be used in a comparison of the experimental data for SF and IF, the average accumulated energy in SF is calculated as:

$$\bar{E}_t = \frac{1}{2N_f} \sum_{j=1}^{N_f} (F_{\max} \times d_{\max}) , \quad (6.1)$$

based on the assumption of linearity of the force-displacement relationship. The  $\bar{E}_t - N_f$  plot for SLJ<sub>long</sub> samples is given in Figure 6.11. The energy parameter is normalized with respect to the energy necessary to break a SLJ<sub>long</sub> specimen in quasi-static conditions ( $E_{Qs}$ ), which was calculated by integrating the force-displacement diagram in Figure 6.2.

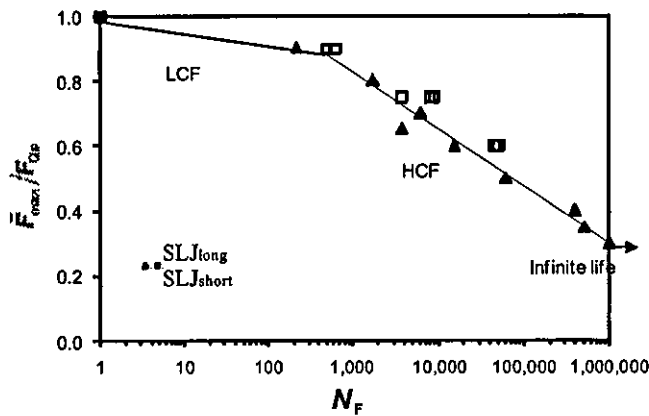


Figure 6.10  $F - N_F$  diagrams for SLJ in standard fatigue

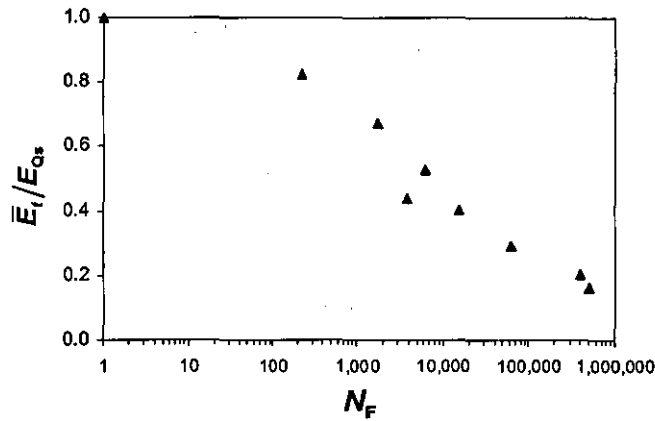
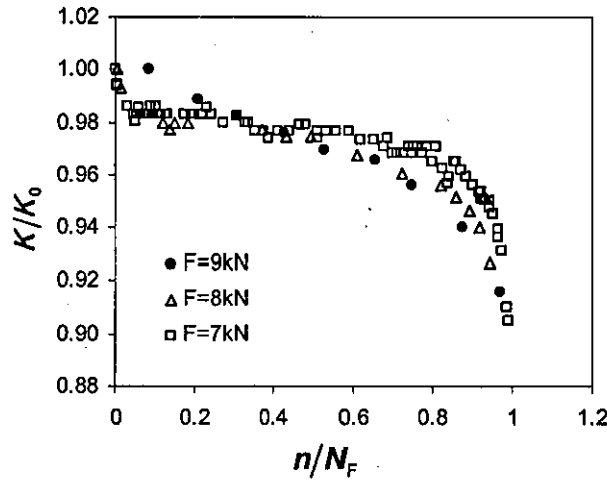


Figure 6.11 E -  $N_F$  diagram for SLJ<sub>long</sub> samples standard fatigue

### 6.3.1.3 Stiffness deterioration

The SLJ can be analysed as a system with its stiffness decreasing during the time that it is suffering fatigue degradation as a product of the number of cycles ( $n$ ). Analysing Figure 6.1 and Figure 6.2, it is seen that the joint has a quasi-linear response after an initial curve in the force-displacement graph. A similar quasi-linear response was found for specimens that had been fatigue damaged. The stiffness deterioration in terms of the fraction of the fatigue life ( $n/N_F$ ) for SLJ<sub>long</sub> in SF is seen in Figure 6.12. It is observed that decrease in the stiffness follows three regions. A first region, where a small decrease is detected until approximately 5% of the fatigue life, a second region which is characterised by a quasi-constant decreasing slope, and a third region at approximately 80% of the fatigue life that exhibits a rapid stiffness deterioration. It is seen that the majority of the stiffness deterioration is under this third region. In addition, it was seen that the minimum value of stiffness before complete failure in the specimens was when it reached a value about 80% of the initial stiffness. Previous work has shown similar changes in the residual strength of SLJs under fatigue loading and related this to damage evolution in the joints and measurements of BFS [163]. In this work it was suggested that damage evolution follows three stages: an initial damage stage, a stable fatigue crack growth stage and an unstable crack growth to failure. These stages varied with fatigue loading. It is likely that the three stages of stiffness degradation in Figure 6.12 correspond to the three phases of damage evolution described in [163].



**Figure 6.12 Deterioration of  $SLJ_{long}$  stiffness as damage accumulate during SF for three specimens tested at a maximum load of 9, 8, and 7 kN**

#### 6.3.1.4 Strength wear out ( $F_{w0}$ )

Strength wear out was investigated using  $SLJ_{short}$  samples. Specimens were tested at a maximum fatigue load equivalent to 70%, 60% and 50% of  $F_{Qs}$  with  $R$  and frequency as described in Section 4.6.2. Specimens were tested at approximately three ranges of the fatigue life, based on the number of cycles to failure presented in Figure 6.10. After SF testing for a percentage number of cycles of  $N_F$  at each maximum load condition, a quasi-static test was conducted following the procedure described in Section 4.6.1 in order to measure the strength wear out as a function of the number of cycles tested.

Figure 6.13 shows the strength wearout of  $SLJ_{short}$  samples in terms of the fraction of the fatigue life tested under SF. As expected, specimens that have been tested for a low number of cycles have a higher strength than those that have been tested at high cycles; however, significant scatter is seen in the results. This can be attributed to the normal stochastic variation in fatigue life of bonded joints. The experimental data shows decreases in the strength of the joints of 30% to 40% at approximately 80% of the number of cycles to failure and a decrease of 10% to 20% at around 40% of the total fatigue life.

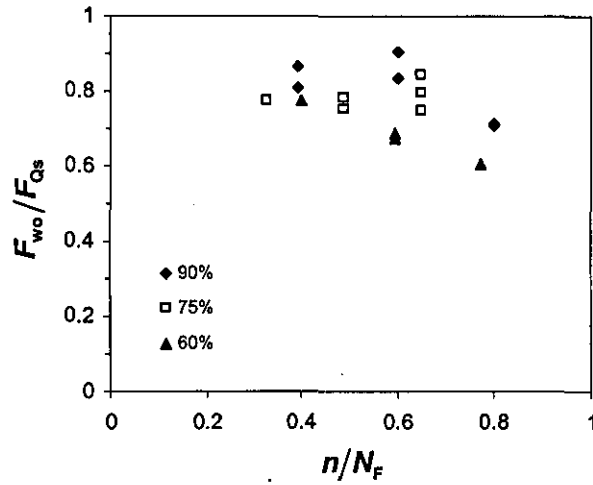


Figure 6.13 Strength wearout of SLJ<sub>short</sub>

### 6.3.2 Examination of fracture surface

In this section, the fracture surfaces of failed SLJ<sub>long</sub> samples tested under SF conditions are investigated using optical and scanning electron microscopy. The samples exhibited two main mechanisms of failure. A cohesive failure of the adhesive was detected in specimens tested at high-load/low cycle fatigue regimes and a mixed fracture path was found in specimens tested when the maximum fatigue force was below 65% of  $F_{Qs}$ .

#### 6.3.2.1 High load/low cycle fatigue

Cohesive failure in the adhesive layer was found in specimens that were tested with maximum force levels above 65% of  $F_{Qs}$ . This type of fracture shown in Figure 6.14(a), looks similar to that seen under quasi-static loading. The higher magnification view in Figure 6.14(b) shows that the toughening mechanism of the rubber particles is active when the adhesive fails, as evidenced by the cavitation in the fracture surface.

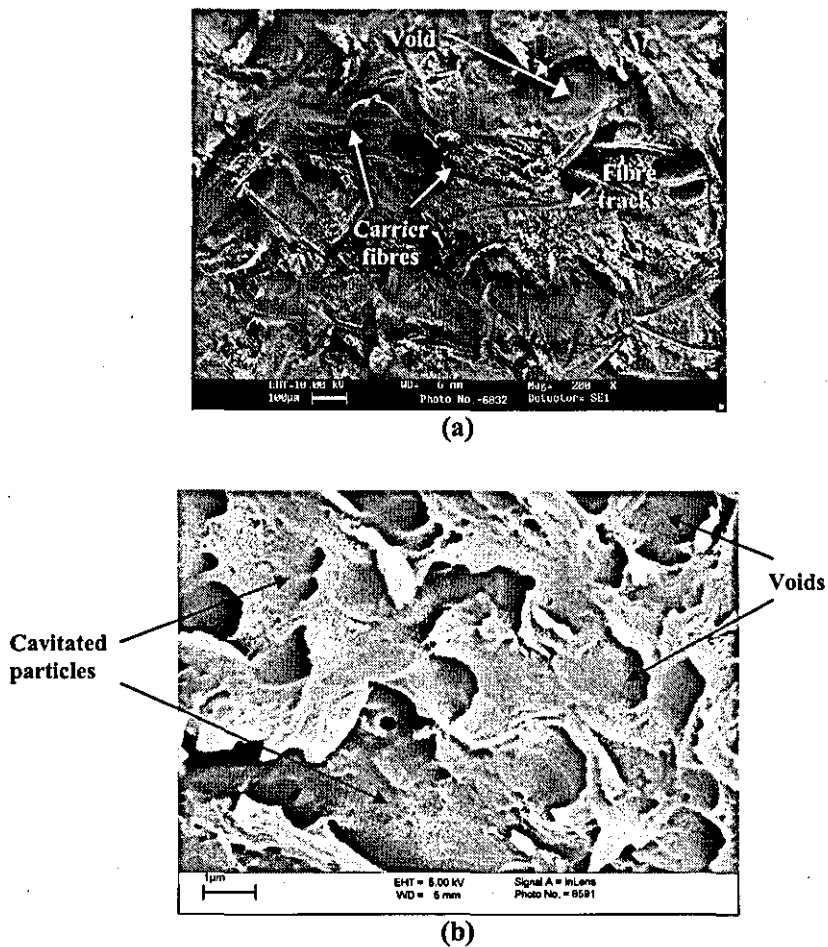
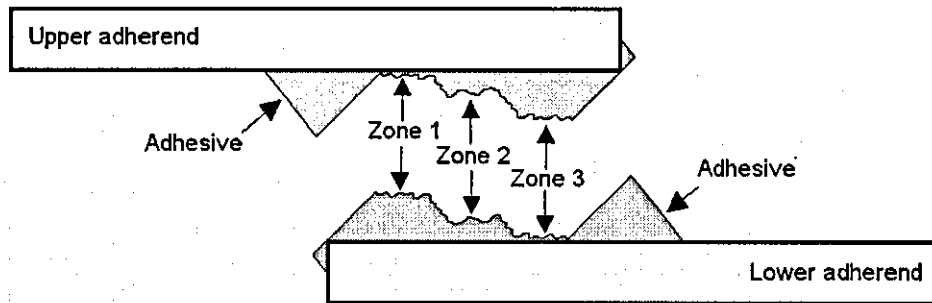


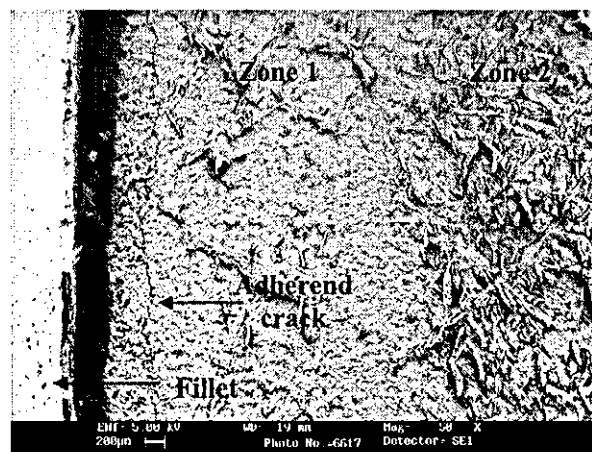
**Figure 6.14 Failure in SF conditions at high force levels (90% of  $F_{Qs}$ );  
(a) general image, (b) zoomed-in image**

### 6.3.2.2 High cycle fatigue fracture

A mixed fracture path was observed in specimens tested in the high cycle fatigue region of SF. Two zones were detected and differentiated by the fracture mechanisms presented in them, as indicated in Figure 6.15. Zone 1 and 3 represent failure in the interfacial region between adherend and the adhesive, whereas Zone 2 represents cohesive failure of the adhesive.



(a)



(b)

**Figure 6.15 Fracture surface of SF specimens tested at 35% of  $F_Q$ : (a) schematic presentation, (b) macroscopic image**

High-magnification analyses of the fracture surfaces in Zones 1 and 3 showed that the apparent interfacial failure was actually in the adhesive/primer adjacent to the adherend. Figure 6.16 shows the primer on the surface, with the inclusion of voids. A typical fracture surface in Zone 2 is shown in Figure 6.17. It has a similar pattern of failure to that seen in specimens tested in the low cycle region. It was found that flake orientation in the fracture surface was dependent on both crack direction and the orientation of the carrier fibres.

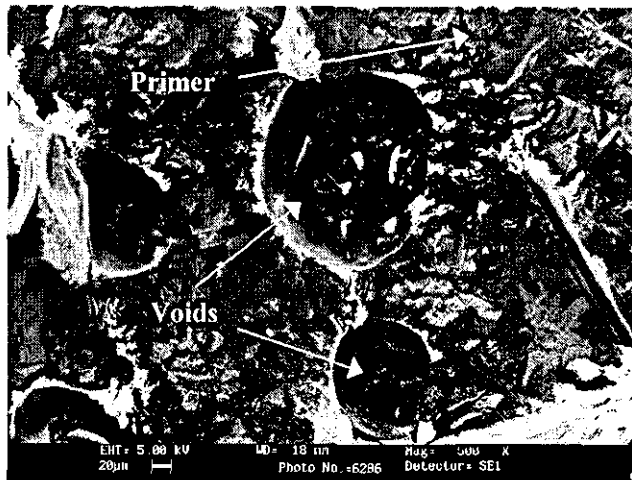


**Figure 6.16 Fracture surface of Zone 1 in specimens tested in SF conditions at 50% of  $F_{Qs}$**

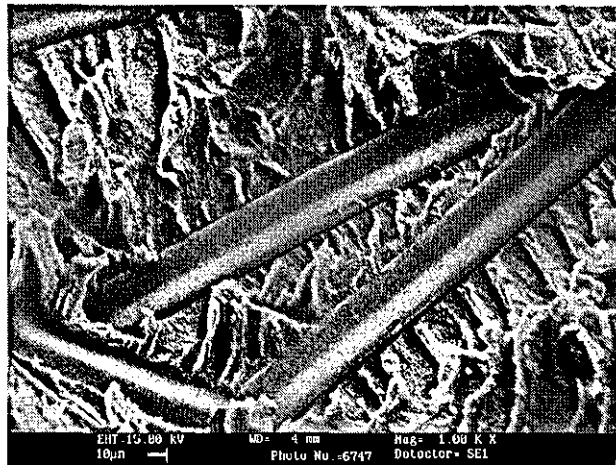


**Figure 6.17 Fracture surface in Zone 2 in specimens tested in SF conditions at 50% of  $F_{Qs}$**

### 6.3.3 Discussion of SF

Analysis of the fatigue life in SLJs has shown that small geometrical differences in similar SLJ's do not significantly affect the number of cycles to failure when specimens are tested using a similar percentage of the quasi-static value. Stiffness deterioration showed that damage inside the specimen begins in the initial cycles but accelerates towards the end of the life. Comparing the results obtained from the strength wearout and the stiffness deterioration tests, it is clearly seen that a sudden failure when the level of damage reaches a critical value.



## 6.4. Fatigue life of SLJs in IF

The following subsections present the results obtained from testing  $SLJ_{short}$  samples in IF. Various methods are used to analyse the fatigue life and the fatigue damage in the specimens.

### 6.4.1 Test results

IF tests were carried out using the modified CEAST RESIL impactor described in Section 4.6.3. A pendulum hammer that transmits a maximum energy of 4 J was used. Different energy levels were used in the IF, in the range from 0.13 J to 3.15 J. This corresponds to impact speeds varying from 0.66 m/s to 3.32 m/s, respectively. Variations in the initial impact energy and velocity were achieved by changing the initial angle of the hammer. The angle was maintained constant during a particular IF test by automatic repositioning after an impact in each cycle of loading.

#### 6.4.1.1 Force and contact time evolution in IF

Impact tests were conducted in energy control, this means that the applied force is not a directly controllable variable as it is affected by the deterioration of the specimen as a result of fatigue. Typical graphs showing the evolution of the force response to impacts at various stages in a sample's life are presented in Figure 6.18.  $F(t)$  is the force response as a function of time and  $F_{max}^0$  is the maximum force reached by the initial impact. It is obvious that the largest effect is due to the propagation of the first tensile wave. The influence of successive stress waves caused by the same impact due to reflections from the edges and their interactions is considerably lower, being below 20% of the maximum force ( $F_{max}$ ). Damage is identified as a deterioration of  $F_{max}$  under continuing impact cycles and a drastic change in response of the specimen is seen in the final breaking impact.

In order to introduce additional parameters to model the deterioration of mechanical properties under conditions of IF, the loading time was investigated. Previous studies of impact loading have suggested various points on the force-time diagram to be used

in the analysis. In [154], the parameter  $T'$  is defined as the time measured from the initial load change until the force begins to decrease after it has attained the maximum value, as illustrated in Figure 6.19(a). A second loading time was also proposed in [135], the time period when maximum force is applied, which is denoted  $T''$  in Figure 6.19(a). In this study, a new parameter,  $T_F$ , is introduced, that is called loading time. This is defined as the time interval between the initial loading point and the moment that the applied force diminishes to zero, as shown in Figure 6.19(b).

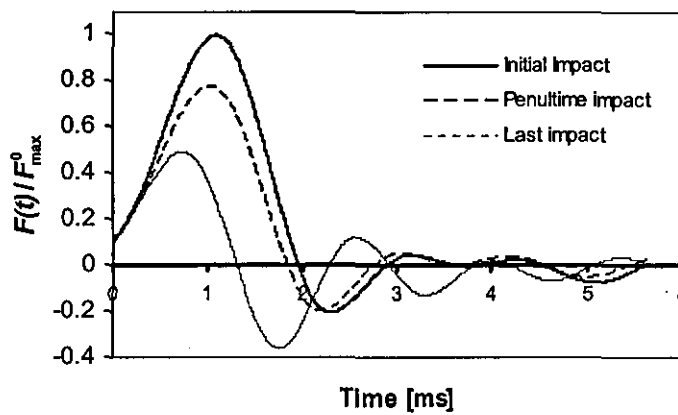


Figure 6.18 Evolution of forces in  $SLJ_{short}$  in various cycles of impact fatigue

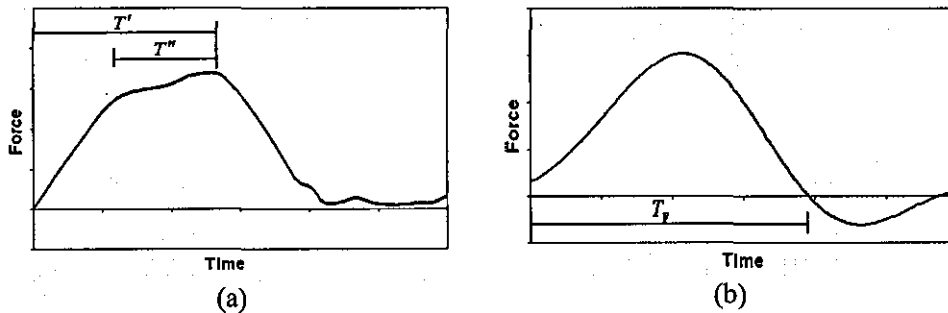


Figure 6.19 Definitions of loading time in Tanaka's model [135] (a) and in the current model (b)

Damage evolution in IF can be analysed in terms of the deterioration of the maximum force and diminishing loading time with the increased number of impacts. Typical curves showing the evolution of these parameters during an impact-fatigue test are given in Figure 6.20. These parameters are normalised respectively by the maximum force  $F_{max}^{10}$  and loading time  $T_F^{10}$  for the 10<sup>th</sup> impact. The 10<sup>th</sup> impact is used rather

than the first in order to avoid possible errors that can be introduced in the system by small misalignments between the pendulum hammer and the impact block in the initial stages of the experiment. It can be seen in Figure 6.20 that the loading time decreases rapidly in the initial stages of fatigue but becomes more stable after approx. 10% of the fatigue life. The mean of maximum force also shows a sharp decrease initially, transferring to a nearly constant deterioration level. With regard to their initial values, it is seen that  $\bar{F}_{\max}$  decreases by some 20% during the test whilst diminishment in the loading time is considerably lower, at approx. 7%. This behaviour illustrates the deteriorating ability of the joint to withstand the impacts, caused by damage evolution in the adhesive. A small increase in the force is seen at approximately half of the fatigue life. This behaviour was possible the result of small misalignments between the hammer and the impact block that can occur during operation.

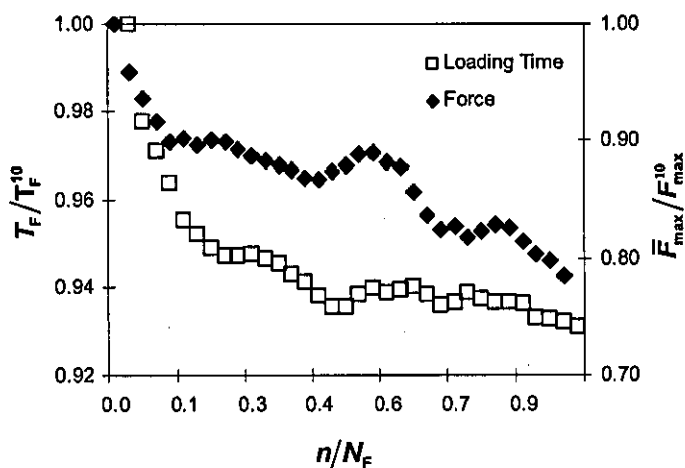


Figure 6.20 Evolution of maximum force and loading time during IF

#### 6.4.1.2 Force – Life plots

In order to compare IF with SF, suitable parameters need to be defined. In the SF test, the maximum force remained constant whereas, as shown above, this varies in IF. To overcome this obstacle, an additional parameter is introduced; the mean maximum force  $\bar{F}_{\max}$ , which is defined as:

$$\bar{F}_{\max} = \frac{1}{N_f} \sum_{i=1}^{N_f} F_i^{\max} \quad (6.2)$$

where  $F_{\max}$  is the maximum force reached in the  $i^{\text{th}}$  impact and  $N_f$  is the total number of impacts until failure. The mean maximum force in each specimen is normalized with respect to the maximum load supported by a similar specimen tested under quasi-static loading  $F_{\max}^{\text{static}}$  in Figure 6.21 and plotted as a function of the number of cycles to failure. The results show a progressive decrease in the number of cycles to failure as the mean maximum force increases. It is seen that even for short loading histories, the IF strength of the joint is below 30% of the quasi-static strength.

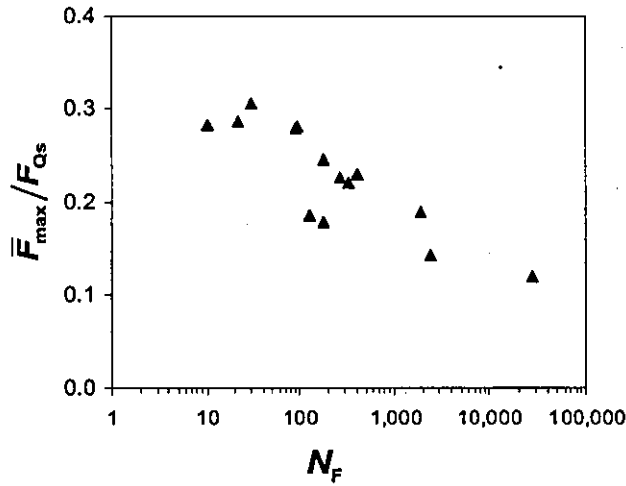


Figure 6.21  $F$ - $N_F$  diagrams for SLJ's under impact fatigue

#### 6.4.1.3 Energy – life plots

The  $E$ - $N_F$  fatigue curve is used to visualise the effect of multiple impacts on the life of joints in terms of energy. Changes in  $F(t)$  during an IF test also affect the energy absorbed by each impact,  $E_j^*$ . As  $E_j^*$  is not constant during the fatigue life, new parameters are required to characterise impact-fatigue. The total energy absorbed during the entire life of the specimen up to its failure  $E_i^*$  is defined as

$$E_i^* = \sum_{j=1}^{N_f} E_j^* \quad (6.3)$$

Here  $E_j^*$  is the amount of energy calculated using Equation 4.3 for the entire of the  $j^{\text{th}}$  impact. A specific energy (i.e. the average absorbed energy per impact) can also be introduced as:

$$\bar{E}_t = \frac{E_t^*}{N_f} \quad (6.4)$$

The effect of specific energy on the specimen's life under impact-fatigue is shown in Figure 6.22. This graph demonstrates a nearly linear decline of fatigue life for energies within the range 0.5 J and 3 J in semi-logarithmic coordinates. Below approx. 0.2 J there is a change in gradient with the curve asymptotically approaching the  $N_f$ -axis. This graph shows that if there exists an IF threshold in terms of energy, it would be at an extremely low energy level.

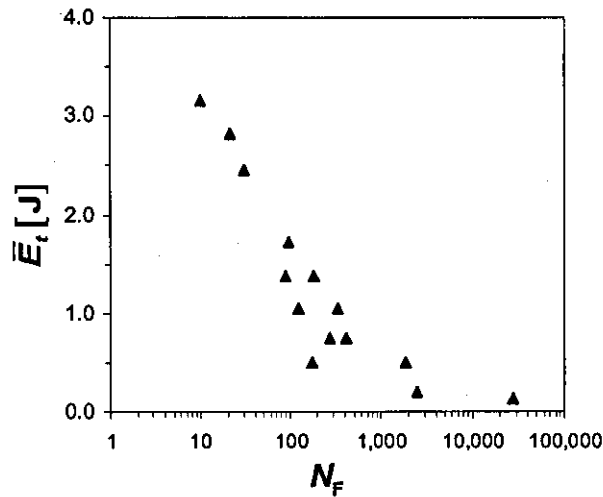
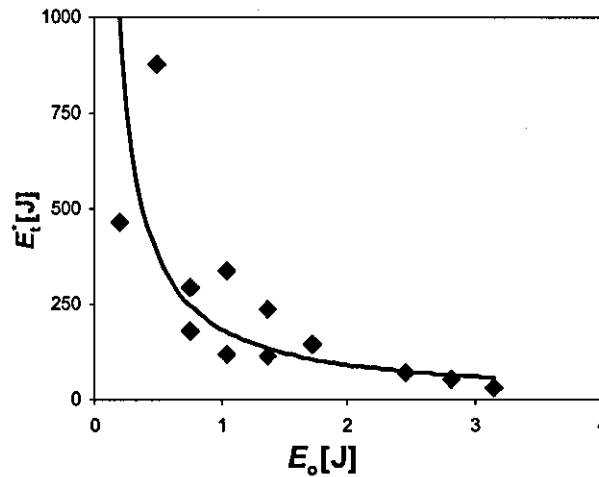


Figure 6.22  $E$ - $N_F$  diagrams for IF

#### 6.4.1.4 Effect of the initial energy

The total amount of energy that is necessary to break the joint in IF can be related to the level of the initial potential energy  $E_o$  of the hammer at the beginning of each cycle, as shown in Figure 6.23. This graph demonstrates that the total energy  $E_t^*$  associated with failure of a specimen in impact-fatigue is not constant, but depends on  $E_o$ . As  $E_o$  increases there is a sharp decrease in  $E_t^*$  up to  $E_o \approx 1$  J, after which  $E_t^*$

decreases more gradually. For values of  $E_o$  higher than 1 J the plot asymptotically approaches the value at which a single impact will produce failure in the specimen. Additional experiments have shown that this will occur at  $E_o \approx 4$  J.



**Figure 6.23 Effect of initial energy of hammer on total energy absorbed in IF to failure**

Analysis of the specific energy,  $\bar{E}_i$ , demonstrates that this is also dependent on the initial energy  $E_o$ . The parameter of energy restitution is defined as the ratio of  $\bar{E}_i$  to  $E_o$ , and represents the fraction of energy that a specimen can absorb on average, during impact-fatigue. This ratio is close to unity when there is little energy dissipation effect. Obviously, it would be expected that in most cases the value of this parameter would be below 1. In the tests with bonded joints, the aluminium adherends are considerably stiffer than the adhesive and most of the energy dissipated in the system will be due to the adherend. Some part of the energy will be transformed into noise generated by the impact but previous research [149] indicates that this amount is negligibly small. In addition, as described previously, losses due to mechanical and aerodynamic friction are automatically accounted for in the experimental measurements. All these facts support the idea that the capacity to dissipate energy in the system is directly related to the level of  $E_o$  as shown in Figure 6.24. Specifically, it is found that the response of the system is less inefficient at higher levels of energy.

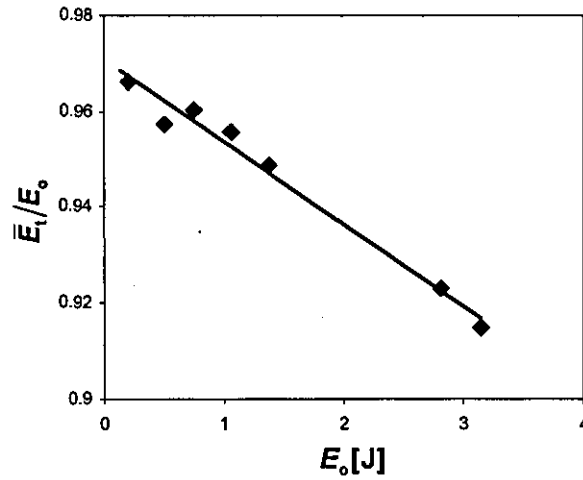


Figure 6.24 Effect of initial energy on energy dissipation in impacts

#### 6.4.1.5 Stiffness deterioration

Stiffness deterioration in terms of the fatigue life for  $SLJ_{short}$  samples in IF is shown in Figure 6.25. It can be seen that the stiffness data has a larger scatter than under SF. However, a similar trend of decreasing stiffness with fatigue cycles is seen and similar regions of deterioration as described for SF are observed. The first region is not easily detectable in Figure 6.25, however, the second and third regions are quite clear. The second region is characterised by a quasi-constant decreasing slope. This is followed by the third region that begins after a decrease in the stiffness of about 5% and a fatigue life of approximately 70% of the total life. The stiffness deterioration leads to complete failure when the stiffness reaches about 85% of the initial value.

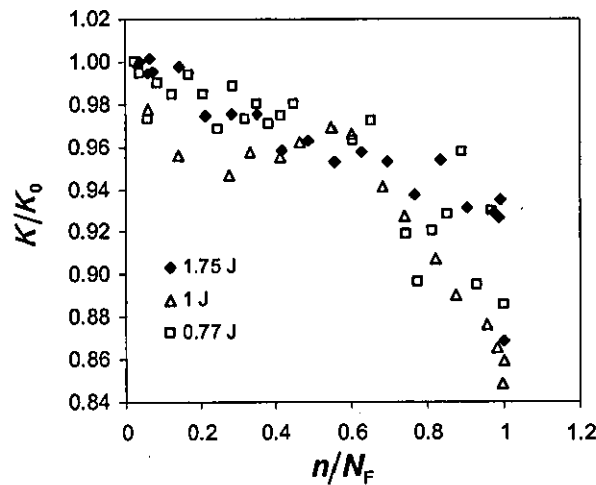


Figure 6.25 Deterioration of the stiffness of  $SLJ_{short}$  samples during IF

## 6.4.2 Examination of fracture surfaces

Studies of specimens tested in IF show that the fracture path is similar to that seen in SF. Cohesive failure is detected in the majority of the specimens tested; however, at energy levels around 0.2 J a mixed-mode fracture has been detected. In the following sections, a description of the fracture path is given, describing micro-and macro-mechanisms of failure in specimens.

### 6.4.2.1 High energy fractures

A study of the fracture surfaces demonstrated that IF at high energy (above 0.2 J) levels resulted in a cohesive failure of the adhesive. A fracture surface can be seen in Figure 6.26, with deformed plastic flakes being a result of the mixed-mode loading. It was seen that IF specimens tested at high energy levels had small signs of plastic deformation in the carrier fibres, as seen in Figure 6.27. SEM analyses performed on the adhesive showed that the cavitation process associated with rubber toughening was active in the epoxy. However, it was found that in some parts of the fracture surface this process was not fully developed as shown in Figure 6.28. In these parts the fracture surface is smooth and can be considered as a result of brittle fracture owing to the reduction of the cavitation process.

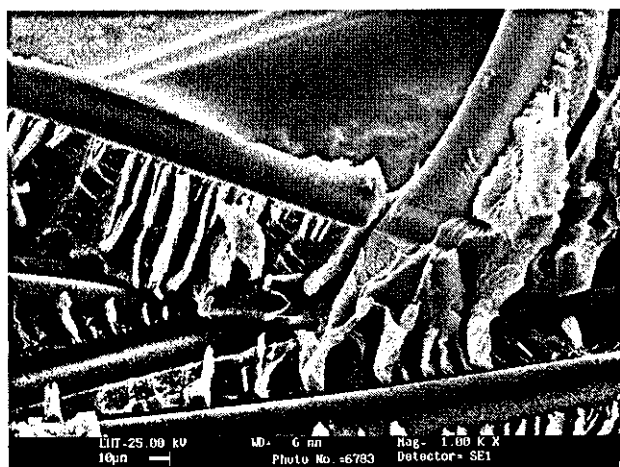
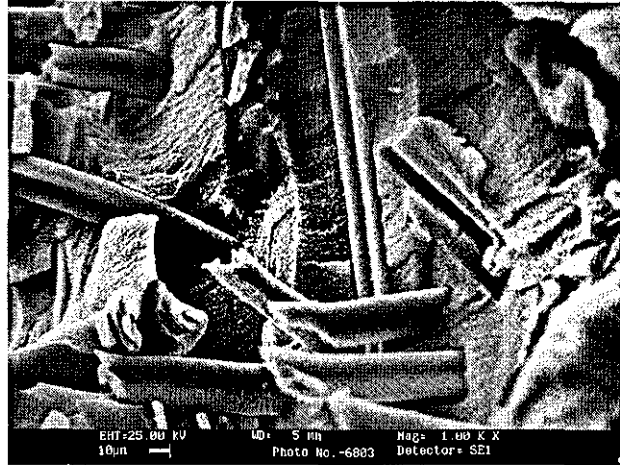
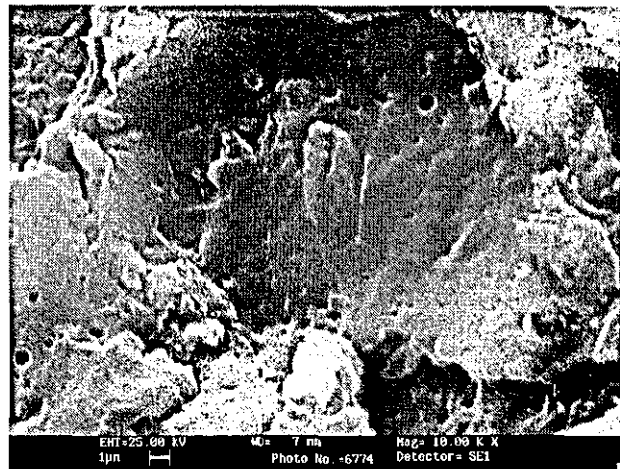


Figure 6.26 Typical fracture surface in adhesive joint after IF at high energy levels in SLJ<sub>short</sub>





**Figure 6.27 Failure in specimen tested at 1 J**



**Figure 6.28 Cavitated rubber particles in IF at high energy levels**

Partial changes in the failure path were detected in some local areas as shown in Figure 6.29, which exhibits both cohesive and interfacial failure.

#### **6.4.2.2 Low energy fracture**

Studies of the fracture path in specimens exposed to low-energy impact fatigue (below 0.2 J) showed mixed-mode fracture, with three zones that are different to those in SF. It was seen in SF that crack growth in Zones 1 and 3 was in the interfacial region in the adhesive and/primer layer near to the adherend (see Figure 6.15). In contrast, at lower energy IF in Zones 1 and 3, crack propagated mainly between the

primer as seen in Figure 6.30. Detailed analysis of Zone 1, demonstrated the presence of small flakes of primer that confirmed this fracture path.

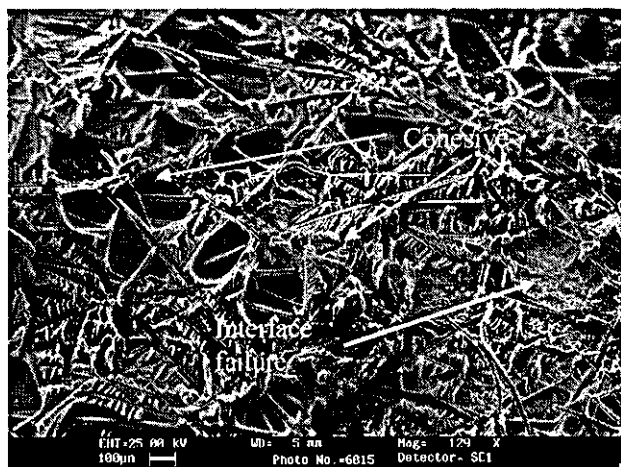


**Figure 6.29 Detail of the cohesive failure at high impact energy in IF**

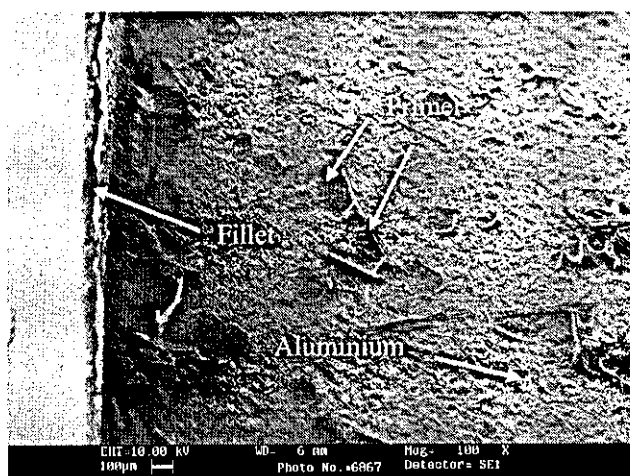


**Figure 6.30 Details of fracture in Zone 1 in low energy IF (adherend side)**

Analysis of Zone 3 in Figure 6.31 shows primer included in the crack path. This confirms that failure at low energy levels occurs between the primer.

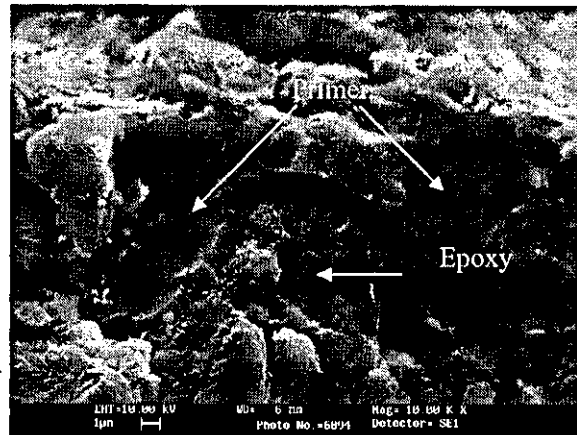


**Figure 6.31 Detail of failure in Zone 3 in low energy IF (adhesive side)**

Voids formation in the epoxy in Zone 1 by cavitation of the rubber particles is very low as can be seen in Figure 6.32.

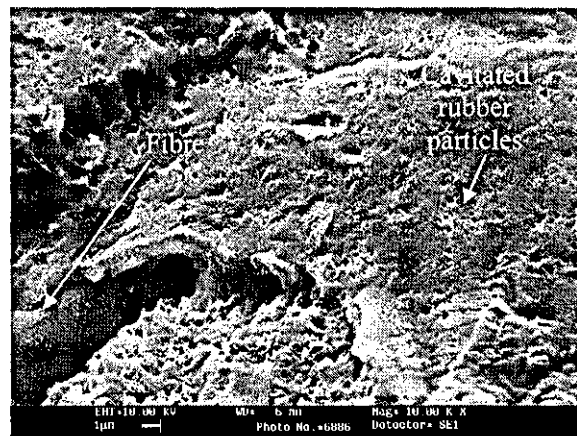


**Figure 6.32 Cavitated rubber particles in impact fatigue at low energy levels**

#### **6.4.3 Repeatability of impact fatigue data**

To confirm the observed trends from IF testing of the SLJ's and to assess the repeatability of results, discussed in Section 6.4.1, a second set of specimens was tested. A set of eight specimens were manufactured using the procedures described in Section 4.5.1 and tested with energy levels in the range of 0.18 J to 3.47 J. A comparison of the average absorbed energy per impact for both sets of samples is presented in Figure 6.33. The figure demonstrates a good match between the data for

the first and second groups of specimens, confirming the repeatability of the previously obtained results. A more detailed analysis of these results brings two principal conclusions. Firstly; the protocol of adhesive joint preparation of adhesive joints described in Section 4.5.1 provides repeatable results. Secondly, the effect of IF on SLJs is a measurable and repeatable phenomenon that causes the gradual deterioration of the material properties of the joint, depending on the level of  $\bar{E}_i$ . In addition, this figure confirms that the average absorbed energy per impact is a precise enough parameter to identify the IF behaviour. A level of scatter is observed in the fatigue tests; however, this is inevitable as fatigue is a probabilistic phenomenon.

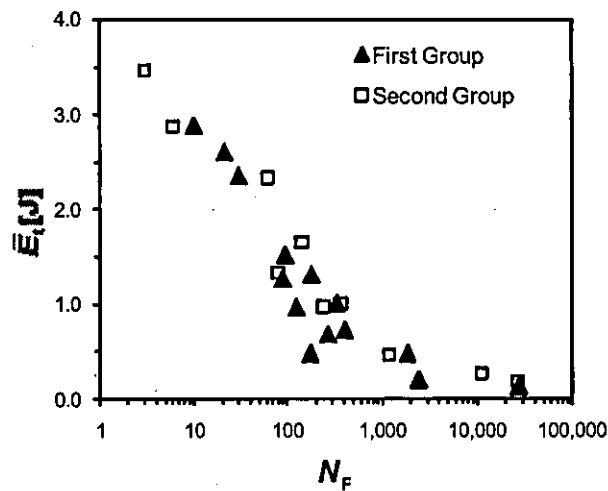


**Figure 6.33  $E$ - $N_F$  diagrams for two groups of specimens in IF**

The asymptotic behaviour of the fatigue life in IF conditions when  $\bar{E}_i \leq 0.2$  J discussed previously is reinforced in Figure 6.33. However, at the levels of energy used in these experiments no absolute durability limit corresponding to an infinite life of the specimens is identified. This behaviour means that even at very low  $\bar{E}_i$  levels, the effect of IF is detectable in SLJs.

#### 6.4.4 Discussion of IF

The results in this section have shown that adhesively bonded joints are susceptible to rapid degradation and failure when subjected to IF. It is also seen that IF can be studied using  $F-N_F$ , and  $E-N_F$  graphs. These graphs show that as the impact force or energy decrease, the number of cycles to failure will increase. From the data that had been tested it is seen that in cases of IF, a fatigue limit is not clearly observable, making this a potential problem in designing against IF. Analysis of stiffness deterioration showed a gradual initial degradation of the adhesive with IF cycles that accelerated towards the end of the fatigue life. Analysis of fracture surfaces indicated that in some areas the toughening mechanism of the rubber particles is not completely active, resulting in semi-brittle behaviour. At high impact energies, failure is in the adhesive layer whereas at low impact energy a mixed fracture was observed including failure between the aluminium oxide layer and primer.

#### 6.5. Comparison of IF and SF

A comparison of  $\bar{F}_{\max}$ , normalized by the static load at failure  $F_{Qs}$ , for IF and SF can be seen in Figure 6.34. This figure shows drastic differences between these two types of loading. The force for a given fatigue life is significantly lower in IF than SF and fatigue failure can be found in IF specimens at force levels below the fatigue limit for SF. A second way to compare the behaviour of IF and SF is using  $E-N_F$  plots, as seen in Figure 6.35. It is seen that at comparable energy levels, the fatigue life is more than two orders of magnitude less in IF than in SF.

Strength and stiffness wearout was similar in both IF and SF, with a gradual initial deterioration followed by a rapid decrease towards the end of the fatigue life. However, greater scatter was seen in the case of IF. Differences were seen in the fracture surface of samples subjected to IF and SF. SF failure was by cohesive fracture of the adhesive, with signs of active toughening of the rubber particles. In IF different mechanisms of failure were detected at different energy levels. At low energy, failure was similar to that seen in SF but with less evidence of the rubber toughening mechanisms. An additional comparison of the severity of damage during

IF is with a comparison of strength wearout in specimens under each fatigue condition. Comparison of the strength wearout in  $SLJ_{short}$  tested in IF and SF is presented in Figure 6.36. It is seen in this graphs drastic differences in the number of impacts or cycles necessary to decrease  $F_{Qs}$  a similar fraction for both load conditions.

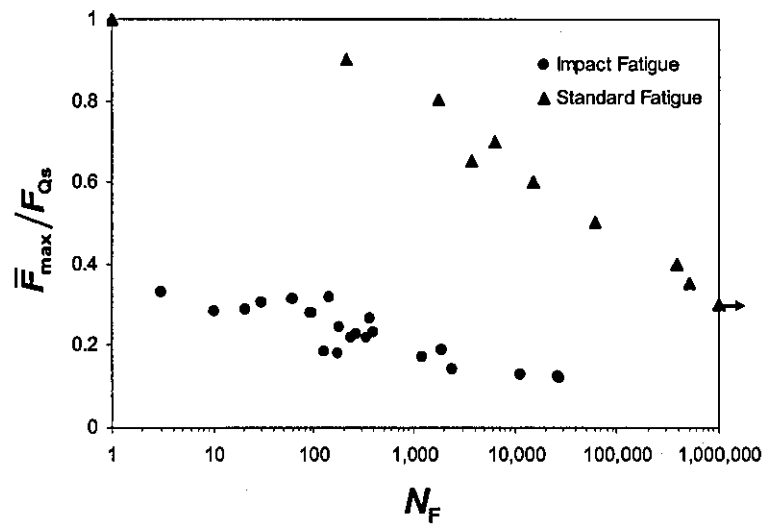


Figure 6.34 Comparison of  $E-N_F$  diagrams for SLJ's in IF and SF

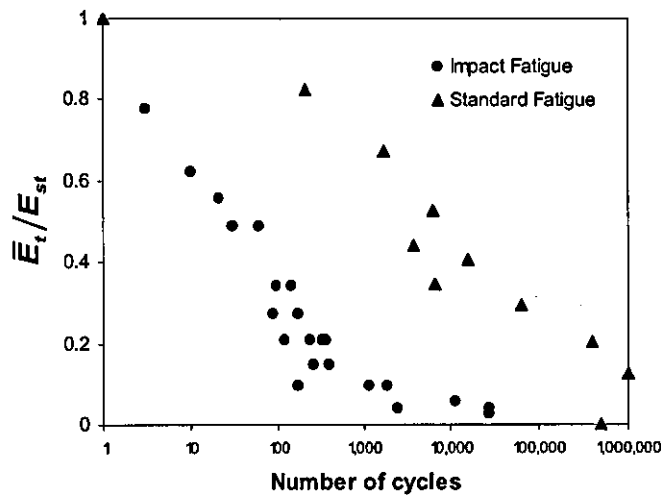
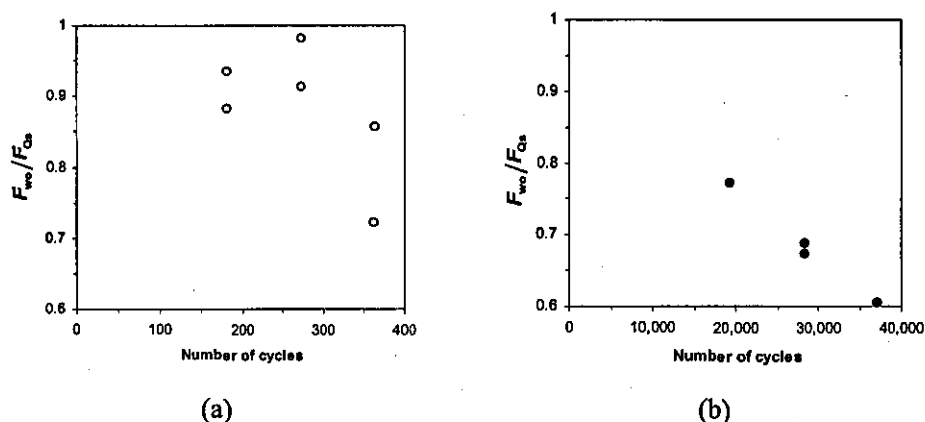


Figure 6.35 Comparison of  $E-N_F$  diagrams for SLJ's in IF and SF



**Figure 6.36 Strength wearout for SLJs, at samples tested at 1J in: (a) IF and (b) SF**

## 6.6. Conclusions

Experimental results obtained from the IF testing of adhesively bonded joints has clearly demonstrated the severity of damage produced by this type of loading and shown that it is more damaging than SF. Moreover, different trends are visible in force-life plots for these two types of loading. In SF, a gradual decrease in the fatigue life with increasing load is observed whereas in IF a significant decrease in life is seen at relatively modest levels of maximum force after relatively few cycles. Comparisons of the fatigue life show a considerably earlier failure in IF than in SF for comparable levels of force and energy. This difference is also seen in  $E-N_F$  plots.

It was found that the energy absorbing capacity of the joint is dependent on the level of impacted energy, with the response of the system being less efficient at higher levels of energy, which could be linked to the more pronounced and rapid damage accumulation. IF result also demonstrated that the maximum force per cycle, loading time, stiffness and strength decreased as a result of damage generated in the sample during IF.

## **CHAPTER 7**

### **Quasi-static and fatigue crack growth in bonded CFRP lap strap joints**

#### **7.1. Introduction**

In recent decades, the aerospace and automotive industries have seen a continuing increase in the use of carbon fibre-reinforced polymer (CFRP) composite materials in structural applications. These developments have necessitated a thorough analysis of fatigue in CFRPs. Records of time-load histories of various components and structures have shown that they are exposed to a variety of cyclic loads that vary through the structure. In some cases, repeated low-energy impacts appear in the load spectrum. The main aim of this chapter is to investigate the fatigue crack growth behaviour of bonded CFRP lap-strap joints (LSJ) subjected to three loading regimes: standard fatigue (SF), impact fatigue (IF) and a combination of impact and standard fatigue (CISF). To achieve this aim the research presented in this chapter is broken down into the following objectives:

- To identify the mechanisms of failure in LSJ and relate these to differences in the fatigue crack growth using specimens with dimensions similar to those used in previous studies [27, 37, 71, 169];
- To conduct quasi static tests using the shortest specimens,  $LSJ_{short}$ , required for IF;
- To determine the fatigue crack growth behaviour in LSJs subjected to SF;
- To determine the fatigue crack growth behaviour in LSJs subjected to IF;
- To determine the effect of CISF on fatigue crack growth.



## 7.2. Quasi-static testing of LSJs

Two sizes of LSJ are used in this work. Full sized samples,  $LSJ_{long}$ , are used to enable comparison with previous work. However, a smaller sample,  $LSJ_{short}$ , is required to fit in the IF testing machine. Details of sample geometry are given in Section 4.5.2. Previously, it was observed using  $LSJ_{long}$  samples reported that the maximum force to produce failure in quasi-static loading of 25 kN. The maximum force supported by the  $LSJ_{short}$  specimen in quasi-static loading was obtained by testing two samples, following the procedure described in Section 4.6.1. The moment of failure of the LSJs was determined by the maximum force in the specimen, which was followed by a rapid decrease in load leading to complete rupture of the joint. After this joint failure, the strap adherend supports the force until it eventually reaches the value for tensile failure of the CFRP. The results from these tests are presented in Figure 7.1, where both joints demonstrate similar behaviour and the average failure load,  $F_{Qs}$ , is 14.24 kN. A comparison of the unity  $F_{Qs}$  in LSJs shows that this variable is equal to 1 kN/mm in  $LSJ_{long}$ ; on the other hand, it is equal to 0.941 kN/mm in  $LSJ_{short}$ . This comparison shows that both LSJs specimens have the same behaviour.

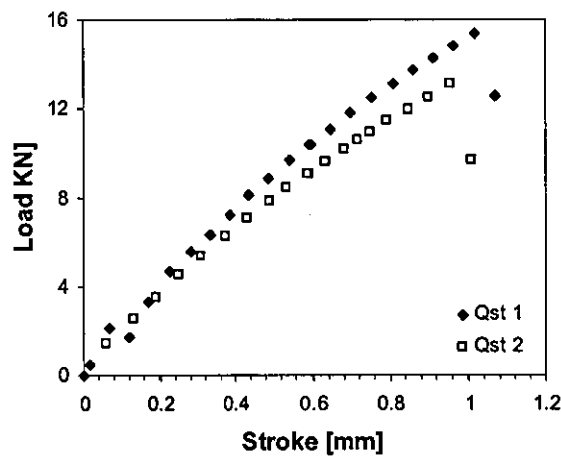


Figure 7.1 Quasi-static value of failure of  $LSJ_{short}$

### 7.3. Fatigue crack growth in LSJs during SF

The FCG behaviour of  $LSJ_{long}$  and  $LSJ_{short}$  was studied using the procedures described in Section 4.6.2.

#### 7.3.1 Fatigue crack growth in $LSJ_{long}$ specimens

To gain an understanding of the fracture process and crack growth behaviour of LSJs in SF, the first part of this chapter deals with the same specimen ( $LSJ_{long}$ ) and SF loading conditions used in previous work [27, 37, 71, 169]. Fatigue testing in one specimen was with a sinusoidal waveform with  $R = 0.1$  and  $f = 5$  Hz. Displacement control was used, with an initial  $F_{max}$  of 14 kN that represents 56% of the quasi-static level for failure. Displacement control was used as this results in a more stable crack growth.

##### 7.3.1.1 Test results

Crack growth in  $LSJ_{long}$  specimens was discussed in Section 4.7.4 where a comparison between crack gauge and optical measurements was made. Results obtained from the two techniques are compared in Figure 4.14. It can be seen that the crack has similar growth pattern at both edges. This demonstrates that measurements are not greatly influenced by which specimen edge or measuring technique is used when measuring the fatigue crack growth. In [170], X-ray radiography was used to analyze the shape of the crack front of LSJs under SF. It was seen that secondary bonded CFRP LSJs tended to have a convex crack front, however, as this shape remained fairly constant it is still legitimate to use edge measurements to determine crack growth rates.

Analysis of the fatigue crack growth (FCG) rate in  $LSJ_{long}$  specimens was conducted as described in Section 4.8, using optical measurements of crack size. The fatigue crack growth rate in  $LSJ_{long}$  specimens is seen in Figure 7.2 as a function of the crack size. It is seen that the FCG in the initial stages has a decelerating tendency, before changing to an acceleration process at approximately 18 mm. A slightly change in the acceleration is seen at about 32 mm.

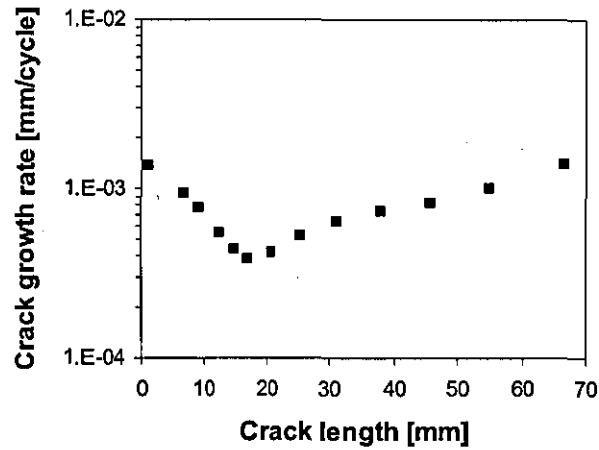


**Figure 7.2 Crack growth rate of  $LSJ_{long}$  in standard fatigue**

A third method used to analyse crack propagation in  $LSJ_{long}$  specimens were the back-face strain (BFS) technique, as described in Section 4.7.3. Figure 7.3 shows a comparison of FEA predicted and experimental BFS plots from the SF tests. Figure 7.3(a) shows results with the strain gauge bonded to the back face of the lap adherend at a position of 16 mm from the end of the overlap. It can be seen that although there is some scatter in the experimental strain gauge reading, there is excellent agreement between the predicted and experimental results. Thus, it can be seen that placing a strain gauge at this position provides a good monitor of the crack length until the crack is approximately 20 mm in length, after which the strain gauge is insensitive to further crack growth. Figure 7.3(b) shows the predicted and experimental results for a strain gauge bonded to the back face of the strap adherend at a distance of 15 mm from the end of the overlap. Again, there is excellent agreement between the predicted and experimental strains. The scatter is reduced in this case, which can be attributed to the higher strains, thus reducing the effect of noise in the measuring system. This result shows that the back face strain on the strap adherend can be used to monitor crack length over the length of the sample, however, it should be noted that greatest positional accuracy will be gained from this technique where the strain gradient is highest, i.e. around the position at which the gauge is placed.

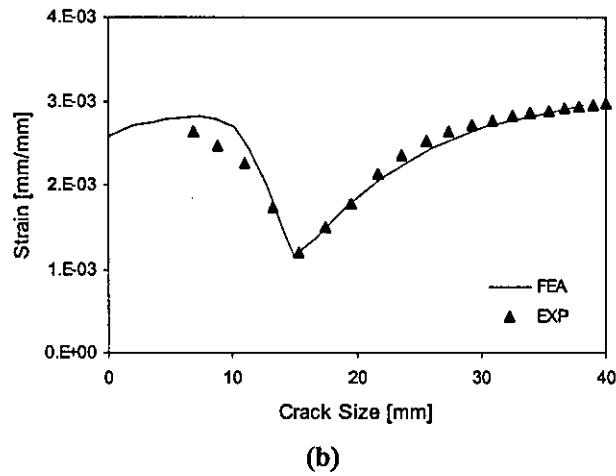
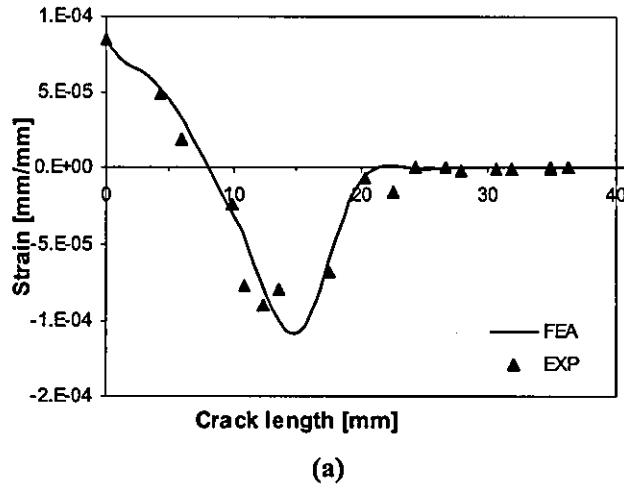


**Figure 7.3 Comparison between experimental and FEA back face strains (a) gauge at 16 mm from the fillet on the lap adherend, (b) gauge at 15 mm from the fillet on the strap adherend**

### 7.3.1.2 Examination of fracture surfaces

Fracture surface analysis of the  $LSJ_{long}$  samples after SF indicated the presence of three different fracture regions, as shown in Figure 7.4. The first region (region I in Figure 7.4) corresponds to cohesive failure in the adhesive layer. A second region (region II in Figure 7.4) is a transition region, in which a mix of failure in the adhesive and in the  $0^\circ$  ply of the CFRP adjacent to the adhesive is observed. In region III, the failure process is dominated by fracture in the CFRP ply adjacent to the adhesive. These results are in agreement with previous studies [71]. Examination of

the type of fracture in the adhesive fillet region showed that the crack was inclined at an angle of approximately  $45^\circ$  to the bond line. Previous work attributed this behaviour to the direction of principal stresses in the adhesive fillet region, these being perpendicular to the fracture surface in the fillet [35]. A minor variation of this crack path was also seen in which the cracks propagated along the fillet/lap interface for a short distance before propagating through the fillet, as shown in Figure 7.5.

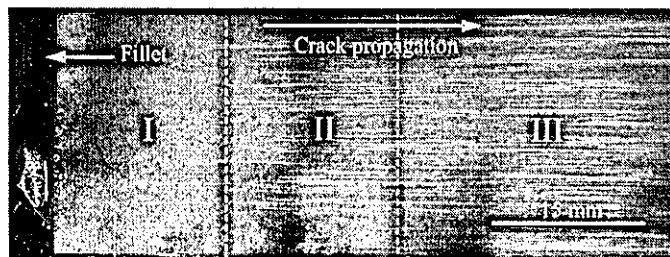


Figure 7.4 Failure surface of sample tested in standard fatigue using  $LSJ_{long}$

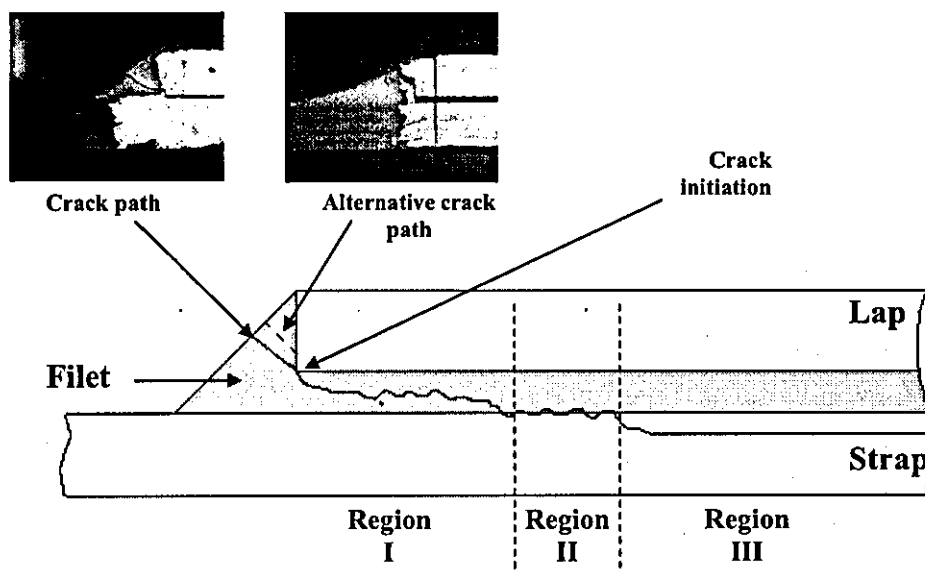
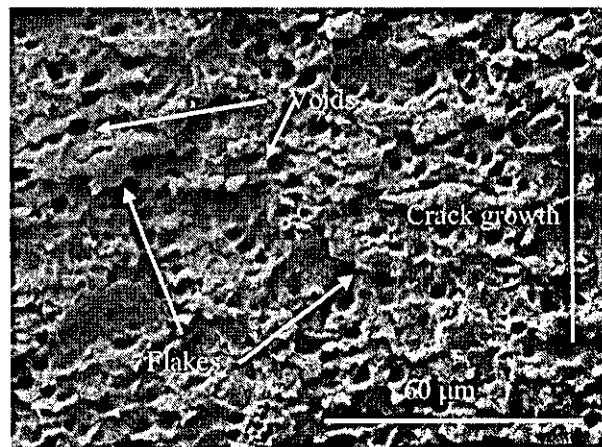


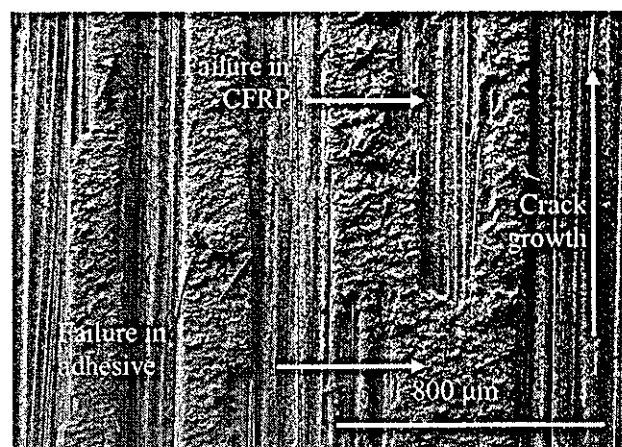
Figure 7.5 Crack initiation and propagation in standard fatigue using  $LSJ_{long}$

Scanning electron microscopy (SEM) was used to study the fracture surfaces in greater detail, as shown in Figure 7.6. In Figure 7.6(a) a typical micrograph of fracture in the adhesive (region I failure) is shown. The cohesive fracture surface is characterised by the presence of flakes that are partly orientated against the direction of the crack growth. Voids with diameter 1 to 5  $\mu\text{m}$  are distributed over the adhesive

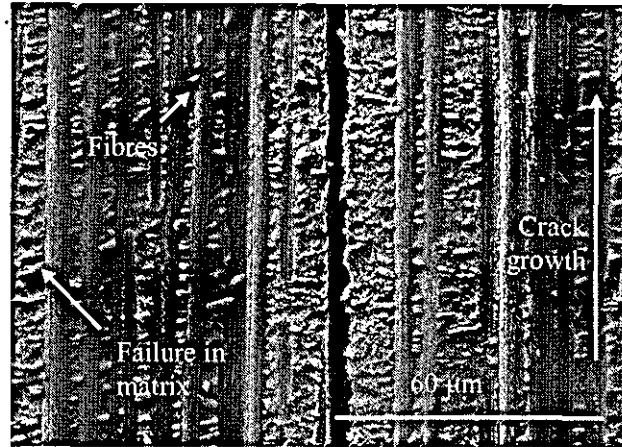
fracture surface resulting from air inclusion during the manufacturing process. Figure 7.6(b) shows the transition region (region II), in which failure both in the adhesive and in the CFRP can be seen. Figure 7.6(c) and (d) show region III of the fracture surfaces, in which failure is predominantly in the 0° ply of the CFRP adjacent to the adhesive. It can be seen that there is a mix of failure in the matrix and fibre debonding. Shear cusps are visible in the areas of matrix failure, which are associated with mode II fracture [99]. Some fibre breakage is also observed in the fracture surface; however, the main crack front does not break through the fibres and hence remains on the surface of the ply adjacent to the adhesive. Figure 7.6(d) demonstrates the transformation of the cusps to rollers as a consequence of friction between surfaces during fatigue.



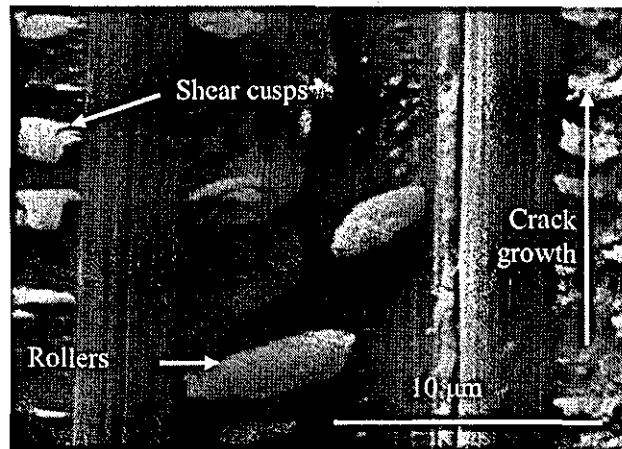
(a)



(b)



(c)



(d)

**Figure 7.6** Scanning electron micrographs of fracture surfaces in  $LSJ_{long}$  samples tested in standard fatigue: (a) region I; (b) region II; (c) and (d) region III

### 7.3.2 Fatigue crack growth of $LSJ_{short}$ specimens in SF

As discussed in Section 4.5.2, a new specimen  $LSJ_{short}$  was designed to study SF and IF, owing to the size restriction in the impact testing machine. The effect of SF on this specimen was tested using the loading condition described in Section 4.6.2. The maximum load was 7.9 kN, which represents 56% of the quasi-static failure load,  $F_{Qs}$ . This was the same proportion of quasi-static failure load used to test  $LSJ_{long}$ . However, force control was used rather than displacement control in order to analyse acceleration in FCG rate when crack growth is in the composite.

### 7.3.2.1 Test results

FCG in  $LSJ_{short}$  specimen was measured using the optical technique described in Section 4.7.1. Failure was defined as the moment when the crack reached a length of 40 mm measured from the fillet.

A comparison of the FCG measurements of two specimens (SF1 and SF2) tested under SF is presented in Figure 7.7. It is seen that in the initial period both specimens have similar FCG behaviour. However this similarity is interrupted when SF2 experiences crack growth acceleration at a crack length of approximately 20 mm. The comparison of crack growth rates for the two samples shown in Figure 7.8 corroborates this observation. It is found that the crack propagation rate in the initial stages is around  $3 \times 10^{-4}$  mm/cycle for both specimens, with a slight decelerating trend. Crack growth continues to decelerate throughout the fatigue life in SF1, when there is an abrupt change in FCG rate in SF2 at 20 mm.

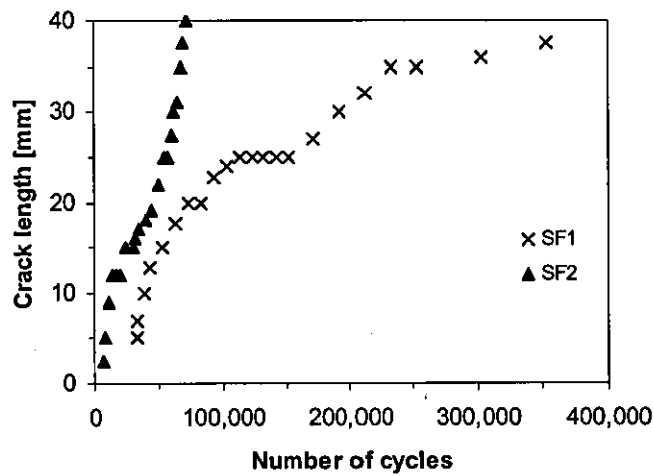
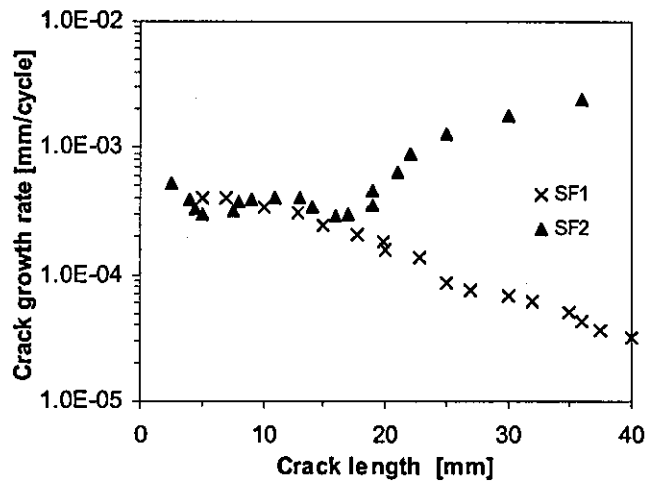


Figure 7.7 Crack growth of  $LSJ_{short}$  specimens in SF





**Figure 7.8 Crack growth rate of LSJ<sub>short</sub> specimens in SF**

Analysis of BFS in LJS<sub>short</sub> specimens tested in SF corroborates the results found when the technique was used with LSJ<sub>long</sub> specimens. It was found that the strap adherend had a notorious strain change as a function of the number cycles that had been tested as a responds of the crack growths. Measurements in the maximum BFS of a strain gauge bonded to the back face of the strap adherend at a distance of 15 mm from the end of the overlap in the SF2 specimen are shown in Figure 7.9.

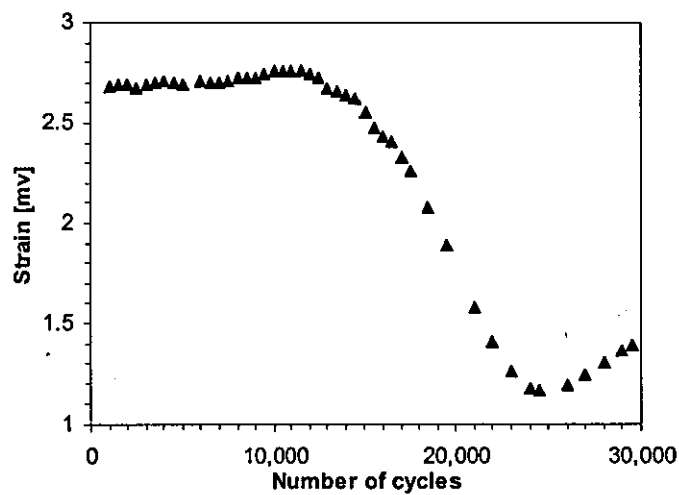


**Figure 7.9 BFS on the strap adherend in LSJ<sub>short</sub> specimen SF2**

### 7.3.2.2 Examination of fracture surfaces

Study of the fracture surfaces of  $LSJ_{short}$  specimens loaded in SF indicated two different types of fracture surface. The first type (SF1) exhibited cohesive failure in the adhesive layer, subsequently termed simply cohesive failures, over the entire fracture surface. Figure 7.10 shows a typical fracture surface, exhibiting ductile tearing, voiding and the cavitation of rubber particles [9, 11]. The ‘wavy’ fracture surface indicates a mixed-mode fracture process.

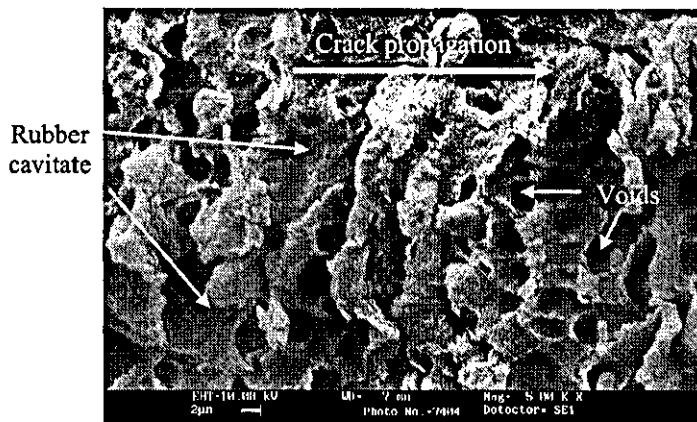


**Figure 7.10 Detail of cohesive failure in SF1  $LSJ_{short}$  specimen tested in SF**

The second type of fracture, as seen in specimen SF2, was more complex. Based on the definition of regions reported for  $LSJ_{long}$  in Section 7.3.1.2, two different regions were found here, as shown in Figure 7.11. The first region (region I in Figure 7.11) corresponds to cohesive failure in the adhesive layer. The second region (region II in Figure 7.11) is a transition region, in which a mixture of failure in the adhesive and in the  $0^\circ$  plies of the CFRP, adjacent to the adhesive, can be seen. The difference between these specimens and the results for long LSJs under similar conditions (Section 7.3.1.2) is that fracture in short LSJs is characterised by the absence of region III, in which failure is entirely in the CFRP. It is suggested that these differences are a consequence of the specimen size, concluding that to obtain a fully developed composite strap failure it is necessary that the crack has more length to propagate.

In Figure 7.11 it can be seen that region I is similar to SF1 type failure. In region II failure in the CFRP is located predominantly in the  $0^\circ$  ply adjacent to the adhesive. It can be seen that fracture is a mix of failure in the matrix and fibre debonding. Rollers and plastically deformed shear cusps can be seen in the areas of matrix failure. Incipient shear cusps are generally related with fracture in static conditions. However, in fatigue, these are more prominent showing a high plastic deformation. In addition, it is observed that when mode II loading is present in fatigue, these cusps are transformed to matrix rollers due to the effect of the continuous fretting of the surface. Some fibre breakage is also seen in the fracture surface; however, the main crack front does not break through the fibres and hence remains in the plane parallel to the ply adjacent to the adhesive.

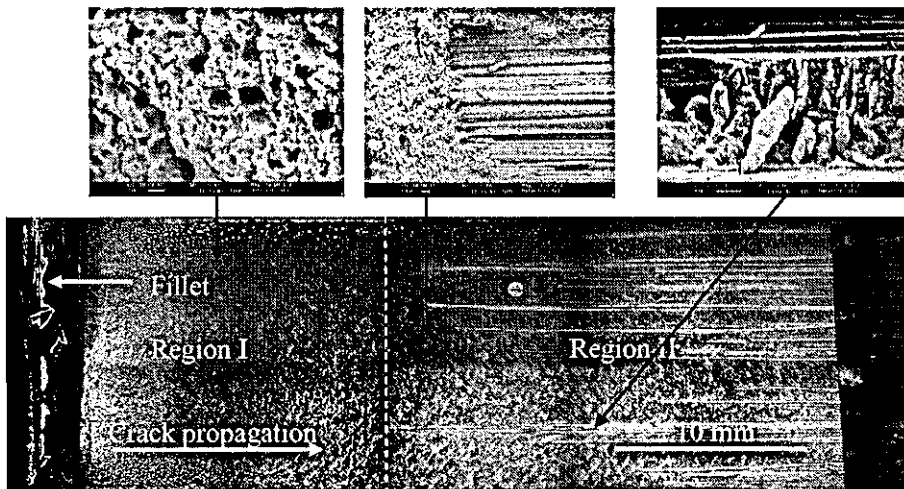


**Figure 7.11 Type SF2 crack propagation of  $LSJ_{short}$  in standard fatigue**

A polished transverse cross section through region II of an SF2 fracture surface is presented in Figure 7.12. It is seen that the crack propagates in some regions in the adhesive and in others in the composite.

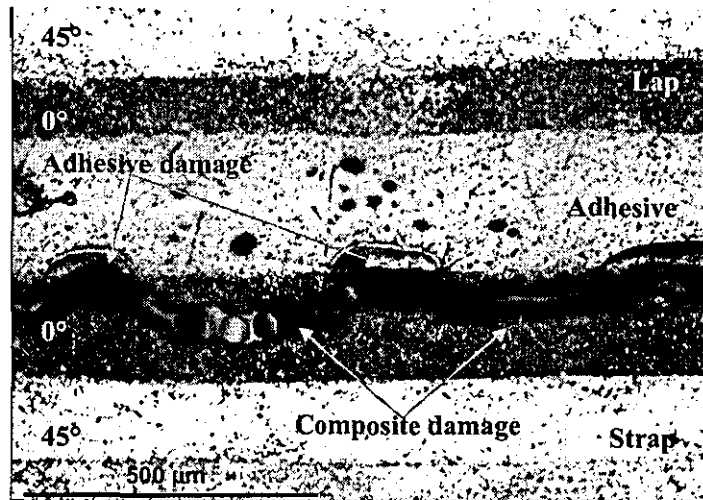


Figure 7.12 Transverse cross section through region II fracture surface in  $LSJ_{short}$

### 7.3.3 Discussion of FCG in SF

Comparing the FCG rates in the  $LSJ_{long}$  and  $LSJ_{short}$  samples, it is seen that they have similar values and tendencies when samples with similar fracture surfaces are compared. This indicates that it is valid to compare samples with different size as long as the maximum fatigue load used is the same percentage of the quasi-static failure load.

It is seen that fatigue damage in CFRP  $LSJ_{short}$  specimens can occur in different forms, and the type of fracture mechanism determines the crack growth rate. In cases when the mechanism of failure changes from cohesive failure of the adhesive to fracture in the composite, a drastic acceleration of the crack growth rate is seen. Similar observations were made in [170] using co-bonded and secondary bonded CFRP LSJs. This may be attributed to the addition of a rubber phase to the adhesive to increase toughness and the lower resistance of the CFRP to crack propagation than the adhesive. In addition, when cracks grow inside the adhesive, there can be more than one path producing damage over a larger area resulting in a higher consumption of energy than when damage is localized in one plane.

A further explanation for the change in fracture mechanism mentioned in [169] is the surface damage of the CFRP on grit blasting. In Section 5.4.1.2, an FEA was used to show that during crack propagation in a LSJ, the direction of the principal stresses influence the direction of crack growth with regard to the orientation of the strap. This explains why cracks tend to be driven towards the CFRP strap. However, it is possible to affect this pattern by changing the resistance to fatigue failure of the different components of the joint

#### **7.4. Fatigue crack growth of short LSJ in IF**

IF tests were carried out using seven LSJ<sub>short</sub> specimens that were subjected to repeated impacts with a pre-selected initial angle of 60°. This angle was kept constant throughout the test and corresponded to a potential energy of 1.07 J and impact velocity of 1.9 m/s. It should be noted that the IF specimens were tested with a maximum force of approximately 21% of the quasi-static strength of the joint, whereas in the SF tests the maximum force was 56% of the quasi-static failure load

##### **7.4.1 Fatigue crack growth**

The FCG of LSJ<sub>short</sub> specimens in IF was obtained using optical measurements and is plotted in terms of the number of cycles in Figure 7.13. In this figure the results can be divided into two main groups. Very rapid FCG was found in two specimens (IF6 and IF7); and a mixed FCG behaviour was seen in the other five specimens. Crack initiation varied, but in the majority of the specimens was observed to occur at a maximum of  $2 \times 10^2$  cycles.

Plots of FCG rate as a function of crack length in IF are seen in Figure 7.14. A general trend in these specimens is an initial crack speed of approximately  $10^{-2}$  mm/cycle, similar to that seen on the specimens with fast FCG (IF6 and IF7). A reliable crack growth rate for IF6 could not be obtained because of the low number of impacts to produce complete failure; however, a crack growth rate of approximately  $10^{-2}$  mm/cycle was calculated over the entire fatigue life of IF7, as shown in Figure 7.14. Once a crack length of around 10 mm was reached, a decrease in the crack growth

rate was observed. The decreasing trend changed when the crack reached a length of approximately 27 mm, when a constant rate plateau was observed for some samples. Some variation of this FCG rate behaviour was observed, especially with IF2 where an acceleration in the FCG rate is seen when the crack reached a length of approximately 27 mm. Analysis of the fracture surface in the next section gives the reason for this acceleration behaviour.

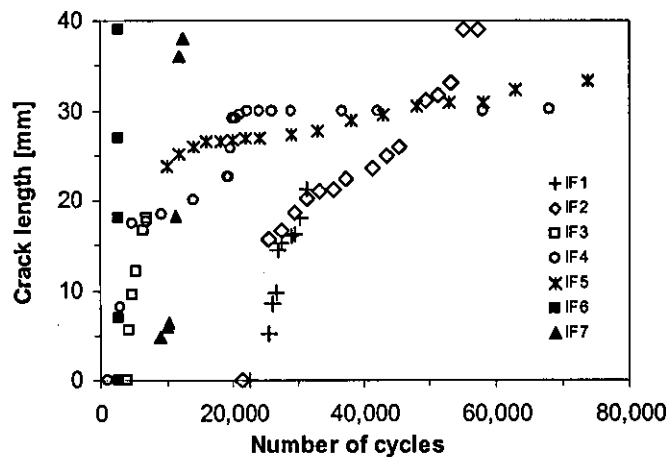


Figure 7.13 Crack growth of LSJ<sub>short</sub> specimens in IF

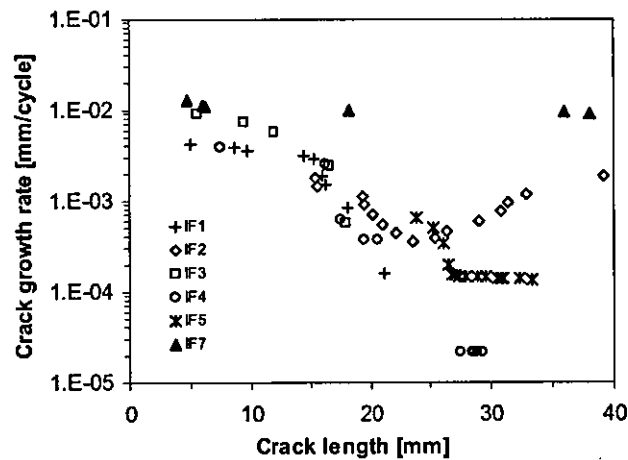
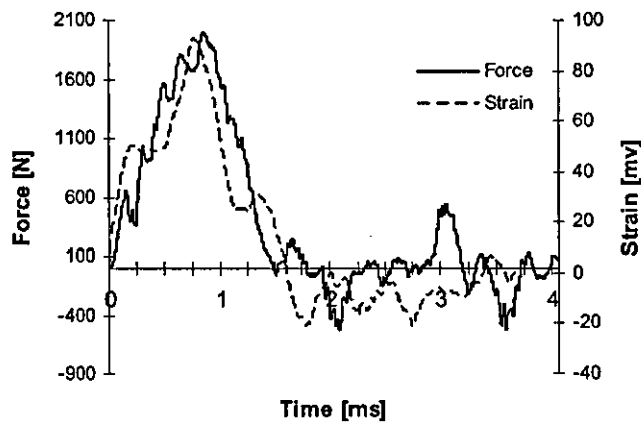


Figure 7.14 Crack growth rate of LSJ<sub>short</sub> specimens in IF

BFS measurements during IF were conducted using a special strain gauge described in Section 4.7.3. A comparison of the signals from the semiconductor strain gauge attached to the strap adherend and the piezo load transducer attached to the sample

grips for a typical impact are presented in Figure 7.15. It can be seen that the load and strain signals generally show good correlation. The force and strain responses are dominated by an initial peak at approximately 1 ms, with subsequent peaks of much smaller amplitude. It should be noted that the maximum load in the impact fatigue is considerably less than that in the standard fatigue testing. There is no obvious time lag between the two signals or difference in damping behaviour, however, there are small differences in the two signal paths, which are likely to be a consequence of scatter rather than systematic. It should be noted that similar experiments with standard electrical resistance strain gauges were not able to generate usable results because of the high noise and lower frequency response.



**Figure 7.15 Force and strain results for a typical impact in impact fatigue and  $LSJ_{short}$**

The evolution of the back-face strain signal as the crack grows in impact fatigue is seen in Figure 7.16, which shows that the signal varies as the crack progresses. The centre of the gauge is at 15 mm from the overlap, and it can be seen that there is a reduction in the peak load as the crack reaches the position of the gauge. It is also noticeable that once the crack has passed the position of the gauge there is a significant negative strain in the strap after the first tensile peak. It is produced because as the crack growth the inertia of the specimen changes and this decreases over the cracked specimen, increasing the possibility bending occurring by small vibrations after an impact.

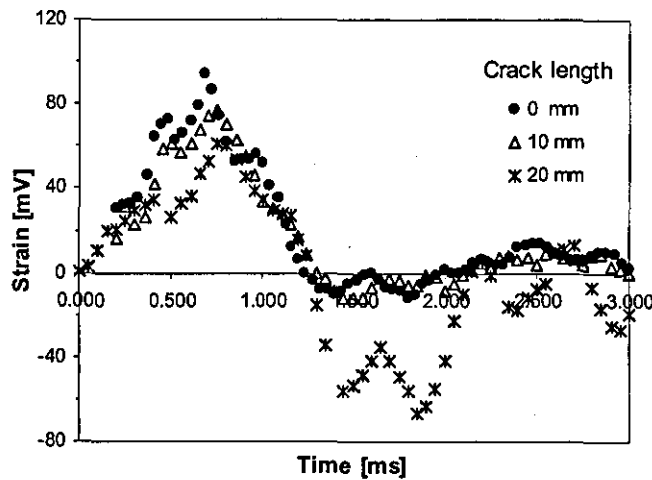


**Figure 7.16 Change in back face strain with crack length during IF using LSJ<sub>short</sub>**

Comparison of the maximum BFS with that predicated using FEA is presented in Figure 7.17. Maximum BFS measurements shows an initial increasing tendency until a maximum value is reached, after that, a decreasing tendency is seen as the crack approaches the position of the gauge. There is then an increase in strain as the crack progresses beyond the position of the gauge. Differences between the experimental and the predicted values can be seen, especially after the crack reaches a size about 10 mm, where a similar trend is seen but moved forward with respect to the predicted FEM strains. These differences can be explained in terms of the crack shape. It has been supposed during the majority of this work that the specimen can be analysed using a 2D plane strain model. In this kind of model it is supposed that the crack front is a strait line. However, if a convex crack shape is formed inside the specimen, the strain at a point in the strap (specifically at centre of the specimen and at 15 mm from the overlap) will show higher values than those expected when the crack is only measured from the edges of the specimen.

#### **7.4.2 Examination of fracture surfaces**

A macroscopic examination of specimens tested under IF conditions shows patterns of failure similar to those observed for LSJ<sub>long</sub> specimens in SF, as seen in Figure 7.18. The first region, denoted A in Figure 7.18, was predominantly cohesive failure of the adhesive. This was followed by a transition region (region B), with a mixture of



failure in the adhesive and CFRP. In region C, crack growth was predominantly in the  $0^\circ$  composite ply adjacent to the adhesive. However, a deviation from the general behaviour was seen in specimen IF2 where the failure in region C was combined with delamination between  $0^\circ$  and  $45^\circ$  plies at the specimen edges and failure in the  $0^\circ$  layer adjacent to the adhesive in the middle of the sample. This explains the acceleration in FCG in region C of IF2, as seen in Figure 7.14.

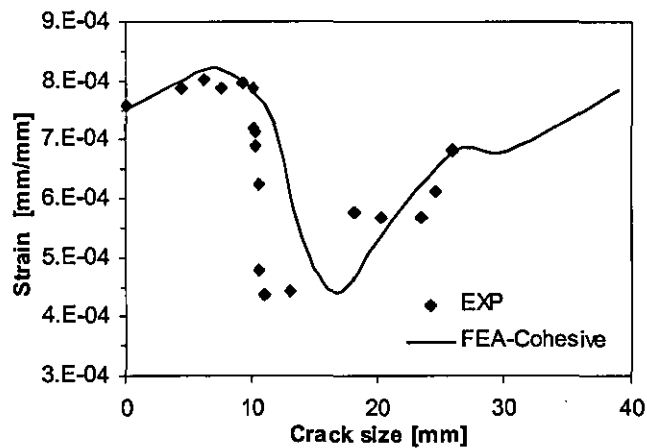


Figure 7.17 Comparison between experimental and FEA back face strains of  $LSJ_{short}$  specimens under IF

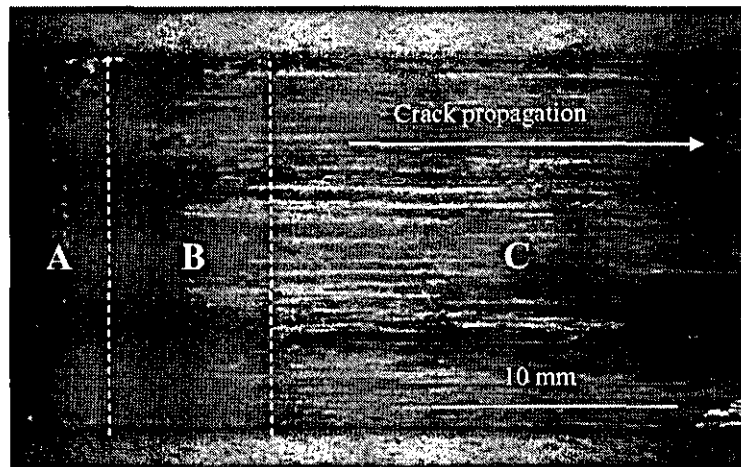
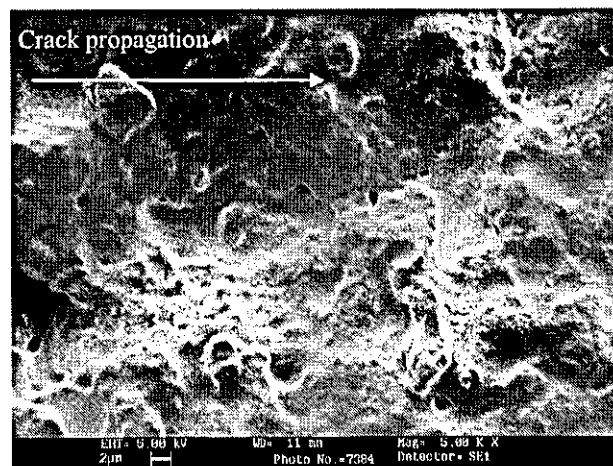


Figure 7.18 Failure surface of  $LSJ_{short}$  tested in impact fatigue

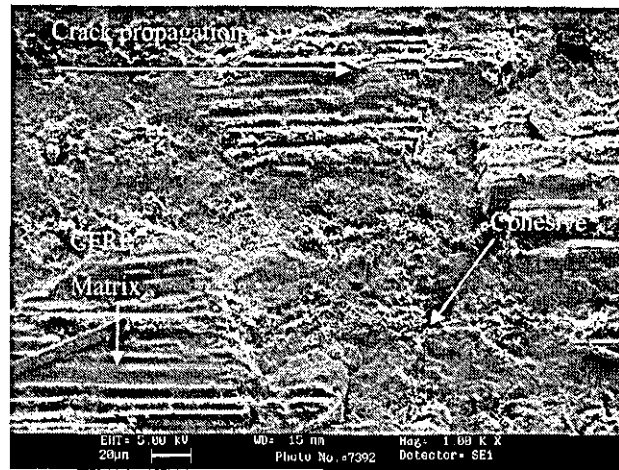
Additional analysis of the fracture surfaces was carried out using SEM. Figure 7.19 shows a micrograph of region A for a specimen with fast FCG. The fracture surface is characterised by a lack of cavitating rubber particles. In a previous study [171], it was

found that rubber particles could remain intact in fast FCG region, resulting in an indistinct difference between the epoxy matrix and the rubber in micrographs. It was shown in [172] that under certain load conditions the cavitation process could be suppressed. No differences were found in the fracture toughness of rubber modified and unmodified epoxies when this was the case. This behaviour was explained as a consequence of the decrease in the shear banding effect due to insufficient levels of plastic deformation caused by the rubber particles. In this work, it is seen that the cavitation process in a rubber toughening modified epoxy adhesive can be suppressed when specimens are tested under IF.

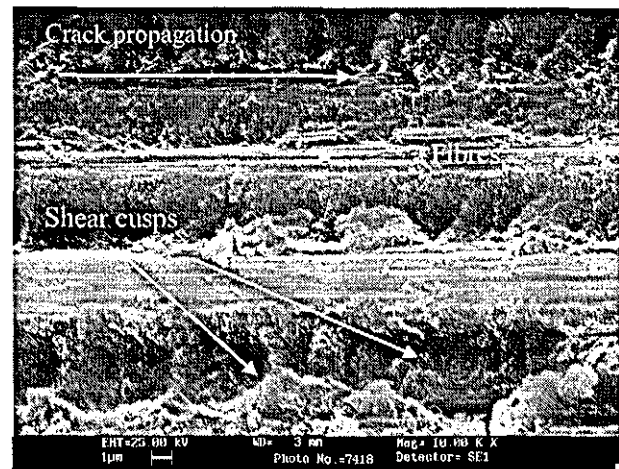
Analysis of region B in IF7 shows that this region exhibits a non-uniform fracture behaviour, as illustrated in Figure 7.20(a). This is characterised by the presence of “islands”, i.e. changes in the fracture path, when a crack propagation mechanism suddenly changes from cohesive failure to damage in the composite and later returns to cohesive failure of the adhesive. This behaviour can be explained by the nucleation of micro cracks in front of the main crack front, generating a local pattern of failure that in time merges with the main crack. Previous studies [71], based on X-ray radiography for similar type of specimens, showed small regions of secondary debonding ahead of the main crack that can cause this behaviour. In region C, damage occurs predominantly in the composite-matrix ply adjacent to the adhesive, as shown in Figure 7.20(b). Fracture in the matrix demonstrates a brittle character, with none of the rollers found in SF.



**Figure 7.19 Fracture in region A in specimens with fast crack growth tested in impact fatigue conditions IF7**



(a)

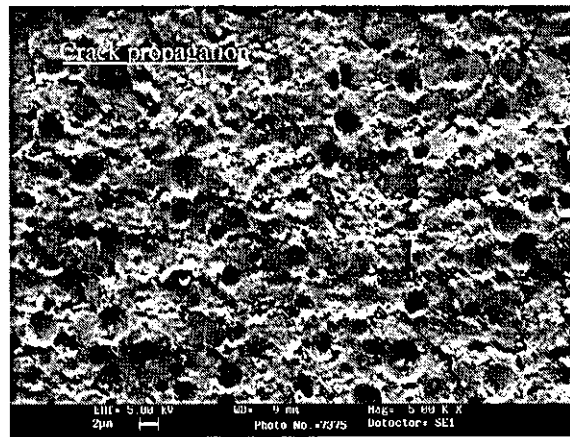


(b)

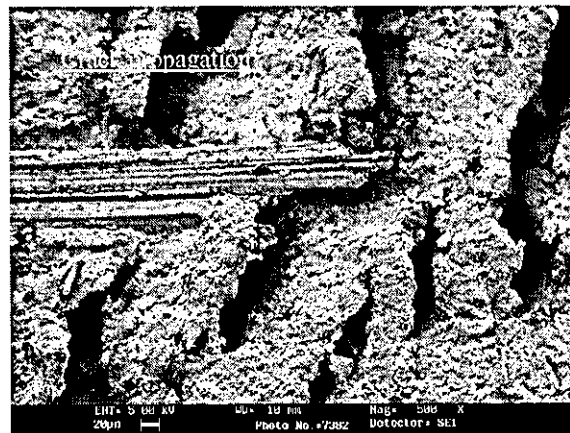
**Figure 7.20 Failure in IF specimen IF7 with fast FCG behaviour: (a) details of failure in region B of the lap; (b) details of failure in region C**

A decelerating FCG rate in IF was seen in two specimens (IF4 and IF5 in Figure 7.14) when the crack reached a length between 15 mm and 25 mm. This behaviour can be explained by a change of the FCG mechanisms. Figure 7.21(a) shows a fracture surface in region A of IF5 and although some voiding is present, there are no signs of rubber cavitation. The fracture surface in region B is shown in Figure 7.21(b) where signs of multiple damage initiation and termination sites can be seen. In some areas there are imprints of fibres on the fracture surface indicating that damage is close to or in the composite but then returns to the adhesive layer. Micrographs from region C of the IF fracture surface are presented in Figure 7.21(c) and (d). It can be seen that the

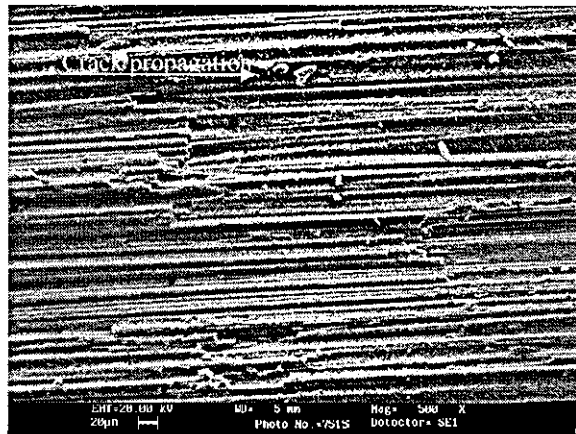
fracture of fibres is a common mechanism, this is explained by the level of bending that is produced during IF of the free specimen end, increasing considerably the tensile stress in the fibres. Fracture in the composite matrix can be observed more clearly in Figure 7.21(c). In contrast to the fast FCG in IF, shear cusps can be seen randomly distributed over the matrix. However, the matrix demonstrates a general brittle behaviour, as seen in Figure 7.21(d).



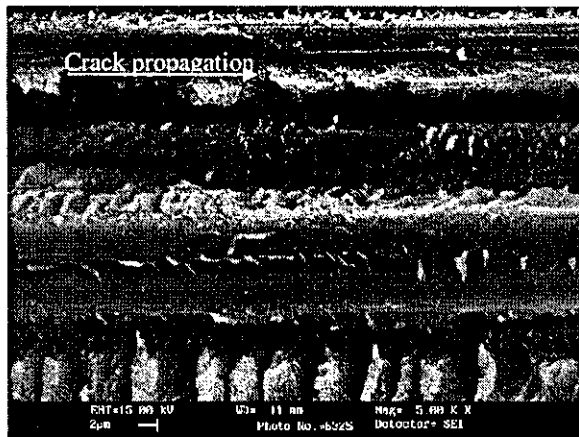
(a)



(b)



(c)



(d)

**Figure 7.21 SEM of fracture surfaces in sample IF5 tested in IF with a slow FCG behaviour. (a) Region A, (b) Region B of the lap, (c) and (d) region C.**

Additional analysis of fracture in the vicinity of the crack front was performed by cutting and polishing fractured specimens. It was seen that cracks in region C can combine matrix composite failure in the  $0^\circ$  ply of the strap with delamination between the  $0^\circ$  and  $45^\circ$  plies.

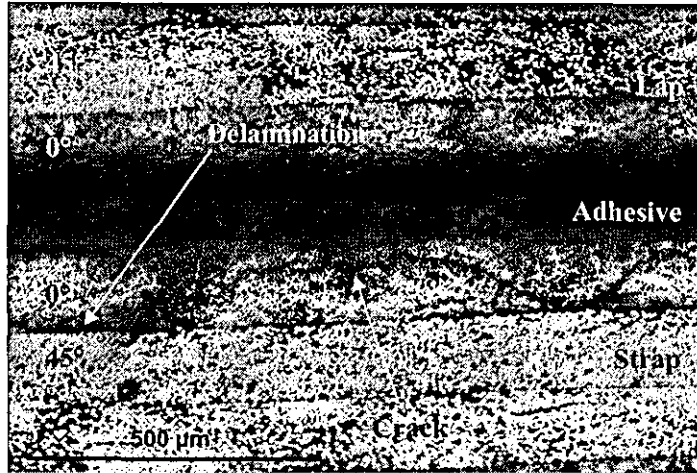


Figure 7.22 Damage across the strap width near to the crack tip under IF

## 7.5. Fatigue crack growth in LSJ short specimens in CISF

A study of combined impact and standard fatigue (CISF) was implemented by means of testing two specimens under the load conditions explained in Section 4.6.4.

### 7.5.1 Fatigue crack growth

Optical measurements of the FCG during CISF were conducted using the technique described in Section 4.7.1. The FCG of both specimens tested during CISF is presented in Figure 7.23. Two tendencies of FCG were observed: fast crack growth in specimen CISF 1 and slower crack growth in specimen CISF 2. It is seen that for both cases stable crack growth behaviour is observed until the crack reaches a length of 10 mm, after that the FCG in CISF 1 becomes unstable. A reliable crack growth rate for CISF 1 after 10 mm could not be obtained because of the unstable behaviour; however, the FCG rate in the early stages of this specimen is similar to that found in CISF 2. The FCG rate in the CISF tests is presented in Figure 7.24. It was found that the FCG rate tends to decrease until a crack size of around 15 mm was reached. Then, a transition occurred to a practically constant average value of crack growth rate of approximately  $8 \times 10^{-3}$  mm/cycle until eventual failure.

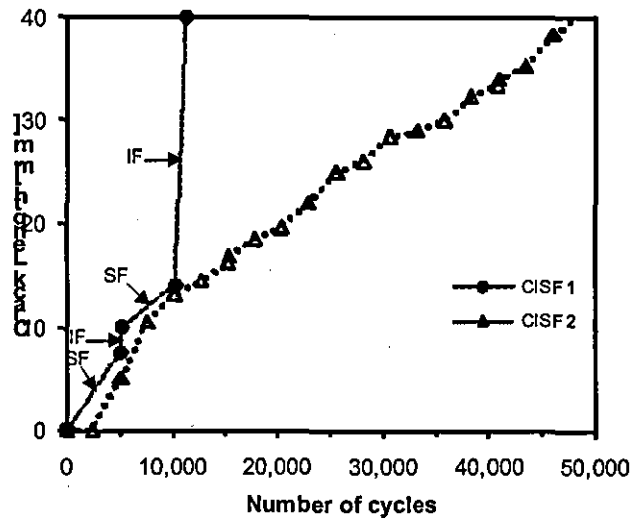


**Figure 7.23 Crack growth in combined impact and standard fatigue**

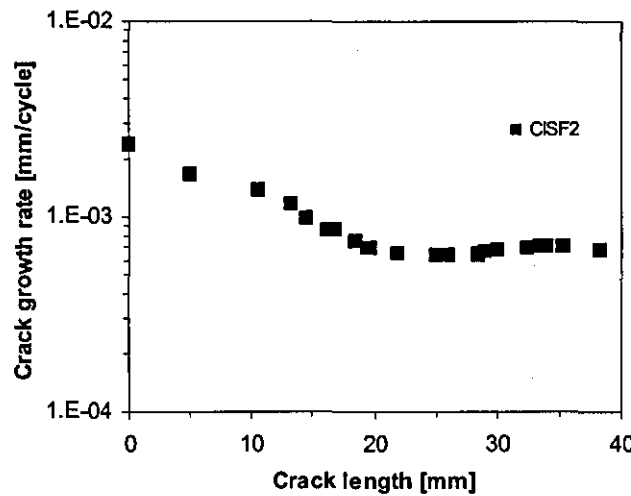


**Figure 7.24 Crack growth rate in combined impact and standard fatigue**

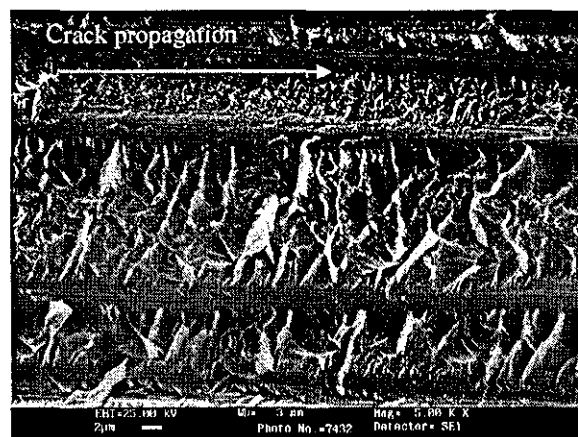
### 7.5.2 Examination of fracture surfaces

Macroscopic analysis of the fracture surfaces revealed two main mechanisms of failure. In the case of fast FCG failure, an intermittent adhesive-CFRP mechanism was seen (specimen CISF1). The specimen who shows slow FCG (CISF 2) exhibited cohesive failure. Results of SEM performed for the fast FCG specimen tested in CISF conditions are presented in Figure 7.25. Analysis of region A, as seen in Figure

7.25(a), shows a number of cavitating rubber particles, demonstrating that the toughening effect is active before the onset of the unstable crack growth in some regions. In addition, a significant number of broken fibres are observed; these being more common near the boundary between regions B and C. Matrix damage in the ply adjacent to the adhesive is seen in Figure 7.25(b). This is characterised by the presence of small and poorly developed shear cusps



(a)



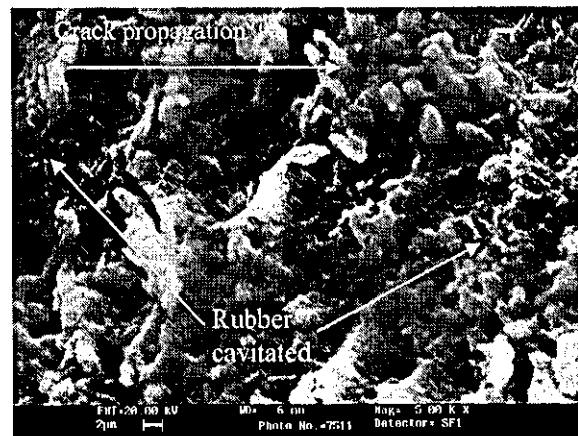
(b)

**Figure 7.25 SEM of fracture surfaces in samples with a fast FCG behaviour tested in CISF: (a) region A, (b) region C**

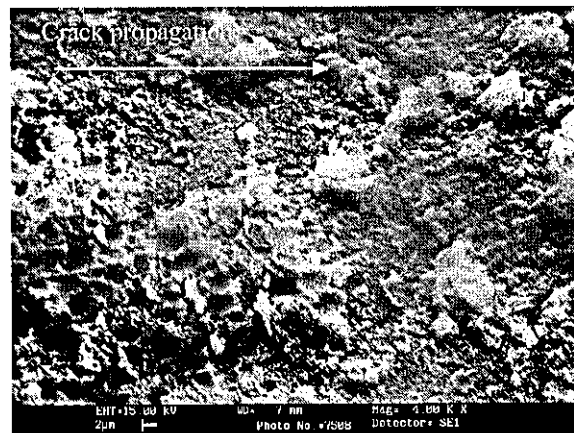
SEM analysis of the cohesive fractured surfaces revealed that IF affects the uniformity of the fracture (Figure 7.26(b)). Changes in the failure mechanism are localised in specific areas and are characterised by the presence of small valleys where smooth adhesive fractured surfaces are present. Additional studies showed that



the toughening mechanism due to cavitation was active during the SF block of the test but resulted in irregular hole sizes. A comparison of the hole size for IF and SF load blocks (Figure 7.26(a) and (b)) shows that, as failure changes from IF to SF, there is a gradual increase in cavitation of rubber particles, until at some point holes reach the maximum size producing the maximum toughening effect. In general, it is seen that the mechanism of fracture exhibits a fracture pattern similar to that in specimens tested in SF when a similar fracture path is compared. This mechanism of failure can be explained by the fact that the crack growth depends on the loading history, being affected by the damage zone ahead of the crack front, where micro-damage can be initiated.



(a)



(b)

**Figure 7.26 SEM of fracture surfaces in specimens with a cohesive failure tested in CISF: (a) SF region, (b) IF region.**

Analysis of the FCG and fracture surfaces revealed the presence of two main mechanisms of failure: a fast FCG associated with an intermittent adhesive–CFRP failure mechanism and a slow FCG with predominantly cohesive failure.

### 7.5.3 Discussion of FCG during CISF

A comparison of the FCG rates for LSJ under SF and CISF samples showing cohesive failure can be seen in Figure 7.27. It is seen that in general the FCG rate under CISF is always higher than that measured during SF. It is seen that the FCG rates under CISF are approximately one order of magnitude higher than those seen in SF. In addition, it was seen that in the cases when the FCG rate could be measured during the IF load block the values were extremely high, as seen in Figure 7.27. In general, it is observed that the inclusion of a small number of impacts in a SF load pattern significantly affects the FCG rate.

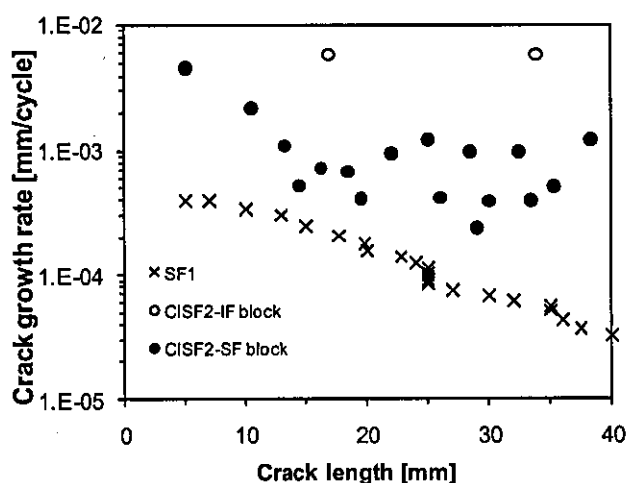


Figure 7.27 Comparison of the crack growth rate in CISF and SF

## 7.6. Discussion

Various differences in the FCG under IF and SF were seen in this Chapter. The first notable difference is that crack initiation was seen under IF at significantly lower load levels. Previous work [173] using similar LSJ<sub>long</sub> specimens observed a fatigue limit

in this specimens under similar SF loading condition with a maximum load equivalent to 44% of the quasi-static value of failure, when in this work damage was seen in IF at only 21% of the quasi-static failure load. Another difference is that during the early stages of crack propagation, when crack growth is in the adhesive, the FCG rate during IF was at least one order of magnitude higher during IF than in SF even though the force levels during SF were about two and a half times higher than in IF. These results show that FCG in LSJs is highly sensitive to IF loading. It is well known that FCG is highly sensitive to geometric parameters, material's properties, local stress, and strain fields, among others factors, however as results observed here and stated in reference [174], the time and size scales also affect this process and, hence, should be included into the analysis of cracks that are initiated at the microscopic scale but later extended to the macroscopic one.

SEM studies of fracture surfaces of specimens failed in IF and SF conditions demonstrate significant differences at the microscale, which could be responsible for the higher FCG rates at the macroscale. SEM showed that although superficially similar, the IF fracture surface were more representative of high energy, brittle failure than those seen in SF.

A starting point to explain reasons for the increased damage in IF is to compare the strain rates seen in the joints with those seen in SF. The loading time for a single cycle of fatigue with a positive stress ratio and frequency of around 500 Hz would be required to achieve similar loading rates to those seen in IF, whereas the SF experiments were performed at 5 Hz, i.e., at loading rates 100 times lower than in the IF tests. It was shown in studies of SF at variable frequencies (between 0.25 and 25 Hz) [175] that a decrease in the frequency reduces the threshold value of  $G_{max}$  and accelerates the crack growth in toughened adhesive joints. This behaviour is attributed to the visco-elasticity of polymer materials. This was because an increase in the load application time in experiments performed at positive load ratios and low frequency, makes the effect of creep behaviour more prominent. The comparison of IF and SF in this work demonstrated that the FCG was higher at the high loading seen in IF, notwithstanding a considerably lower magnitude of force in IF. This behaviour

contradicts the conclusions of reference [175]; hence it can be concluded that the effect of accumulated creep is not a significant factor in this case.

Another mechanism that can be responsible for specific features of cracking in adhesives, suggested in reference [176], is hysteresis heating during the loading–unloading cycle in fatigue testing of toughened adhesive joints that can affect the adhesive properties around the crack tip. It is well known that increases in temperature, especially near the glass transition range, can significantly change the mechanical behaviour of epoxy materials. However, temperature measurements performed on the surface of specimens in this work, using thermocouples and infrared cameras, did not show significant temperature changes during fatigue testing. This indicates that hysteretic heating cannot be one of the main mechanisms affecting the character of failure in tested adhesively bonded joints.

It is unlikely that the acceleration of the failure process in IF compared with SF conditions, can be explained in terms of a single-factor effect. An interaction of several mechanisms, acting at various time and space scales, is more likely to be responsible for this. A high-strain-rate loading regime, characteristic to impacting, results in a more brittle response of the adhesive (and adherends), increasing its propensity to generation of microdefects – microcracks and secondary delamination zones. These defects, though being predominantly limited to the process zone within the vicinity of the propagating crack front, are randomly distributed and can be initiated both in the volume of the adhesive layer, at – or near to – adhesive–adherend interfaces and even inside the adherends. Each impact within a series causes propagation of a rapidly decaying stress wave that interacts with (i.e. reflects from and/or propagates through) these defects as well as with the existing macroscopic crack. These complex interactions affect the dynamics of FCG and can be responsible for ‘switching’ between various damage mechanisms, depending on their respective state of development. A relatively short range of these mechanisms, which are mostly limited to the process zone, result in a quasi-stable propagation of delamination at some stages (where there is no changes between mechanisms) with a practically constant crack growth rate for thousands of impacts. Another important factor that causes a more rapid failure process under conditions of IF than in SF is a more

effective use of energy dynamic fracture processes. It is well known [174] that while in quasi-static loading a large part of energy is used to stretch the entire specimen, in dynamic loading it is effectively concentrated near the crack tip, making it easier for a crack to propagate.

The inclusion of small IF blocks in a SF test (CISF) reveals that in cases when similar fracture surfaces are compared, the FCG rate is higher in CISF than in IF (as seen in Figure 7.27). The brittle behaviour of the adhesive under IF is perceived to be responsible for the production of micro-cracks in the process zone under the IF block that affect the rate of damage in the process zone. As a result of the micro-defects formed in front of the crack tip, the propagation of the main crack under SF will be higher than in a pure SF test.

## **7.7. Conclusions**

A detailed comparative analysis of SF and IF in adhesively bonded joints has conclusively demonstrated that the latter loading regime is considerably more dangerous. One of the most prominent features of IF is its potential to initiate a crack – and to cause its rapid propagation – at levels of loading that are significantly lower than quasi-static and dynamic strengths and even the fatigue durability limit of joints. This is important as this range of loads is generally considered as safe for components exposed to fatigue with varying load amplitude.

Two typical patterns of failure were seen; a cohesive failure in the adhesive, which is related to slow fatigue crack growth, and a mixed-mechanism failure that is associated with fast fatigue crack growth. It was also seen that a change in the pattern of failure from cohesive to the mixed-mechanism path acted as an accelerator of the crack growth in specimens tested in SF. In IF, a mixed-mechanism path was seen in all samples tested. Differences between IF and SF were also seen with regard to the crack speed. It was found that in the initial stages of the crack propagation, the crack rate was 10 times higher in IF than in SF.

It was found that the introduction of a relatively small number of in-plane impacts between blocks of SF drastically changed the dynamics of fracture in the specimen, with the IF blocks having a damage accelerating effect.

Macroscopic analysis of the crack growth has shown that for IF and SF in CFRP LSJs, failure initiates in the adhesive layer and then propagates into the 0° ply of the CFRP adjacent to the adhesive layer. However, higher-magnification examination of the fracture surfaces shows that the failure mechanisms involved in impact-fatigue are very different to those in standard fatigue. In the adhesive failure region there is some cavitation of rubber particles and the formation of regular flakes oriented with respect to the direction of crack growth after standard fatigue. However, in the corresponding region after impact-fatigue the flakes are less regular, and there is no cavitation of rubber particles, the crack depth varies more and there are signs of multiple damage initiation and arrest events. In SF fatigue, fracture in the composite failure region is dominated by regular shear cusps and matrix rollers in the matrix failure areas and fibre debonding. After impact-fatigue the composite failure region is less uniform, with higher incidence of fibre breakage and a more brittle appearance to the matrix failure areas. It is concluded that the toughening mechanism of the rubber particles present in the adhesive is affected by cyclic in-plane impacting. The rapid crack growth in the adhesive associated with IF was characterised by a lack of rubber particle cavitation.

It can be concluded that the back face strain technique can be used to monitor crack growth in LSJs in SF and IF, however, the location of the gauge is critical, with the best location being on the strap adherend and placed along the length at the position in which the greatest accuracy is required. Ideally, a series of crack gauges along the length of the strap should be used. It is also seen that in impact, a piezo strain gauge should be used rather than a standard electrical resistance gauge, both for noise suppression and to achieve the high sampling rates needed to characterise the strain response during an impact.

## **CHAPTER 8**

### **Predicting Fatigue in adhesively bonded joints under Standard and Impact fatigue**

#### **8.1. Introduction**

The use of adhesive joints has expanded to many application in recent years. These structures are often under the influence of varying load conditions that can generate failure by fatigue. This research, has concentrated on the fatigue behaviour of adhesive joints under cyclic low velocity impacts (IF) and compared this to the fatigue behaviour of similar specimens under constant amplitude sinusoidal fatigue (SF). It has been seen experimentally that IF is more damaging than SF. However, no way of predicting IF behaviour in bonded joints has been proposed to date. In this chapter, methods of predicting IF behaviour will be investigated through the following objectives:

- To identify phenomenological models that are suitable to predict the fatigue life of adhesive joints in IF.
- To propose a method to generate fatigue crack growth rate (FCGR) curves in LSJs under IF and SF.
- To propose a model that can be used to predict fatigue crack growth (FCG) when changes in the fracture path seen.
- To propose a method to predict FCG rate under combined impact and standard fatigue (CISF).

## 8.2. Phenomenological models

### 8.2.1 Energy-life approach

The fatigue life in adhesively bonded joints can be characterised using experimental  $E-N_F$  diagrams and fitting the data to the equation proposed by Johnson [83]:

$$\bar{E}_t = \bar{E}_{lim} + D(N_F)^{-q} \quad (8.1)$$

where  $\bar{E}_t$  is the absorbed energy per impact,  $D$  and  $q$  are the impact fatigue parameter and impact fatigue exponent. Johnson also proposed the existence of an impact fatigue limit [ $E_{lim}$ ], defined as the energy level when specimens can support  $10^6$  to  $10^7$  cycles. From the experimental data in this work, it was observed that IF failure occurred even at very low values of  $\bar{E}_t$  and in the energy range that was used, the maximum number of cycles seen was approximately  $2.6 \times 10^4$  with an impact energy of 0.2 J. Hence, in order to apply Equation 8.1 to the experimental data, it was assumed that  $E_{lim}$  was equal to zero.

The fit of Equation 8.1 to the experimental data is presented in Figure 8.1. The equation fits the data reasonably well but does not reflect the notable change in gradient at approximately 600 cycles. This can be attributed to a change from cohesive failure in the adhesive to a mixed failure mode. An alternative equation that can be fitted to the data is:

$$\bar{E}_t = A \times \ln(N_F) + B \quad (8.2)$$

where  $A$  and  $B$  are experimental constants that depend on the particular adhesively bonded joint system (adhesive/adherend) used and by mechanism of failure. Two sets of constants were obtained, one for cohesive failure and one for mixed fracture, in order to fit Equation 8.2 to the experimental data. The fit of Equation 8.2 to the experimental data is presented in Figure 8.2. It can be seen that this provides a better fit to the data than Equation 8.1.



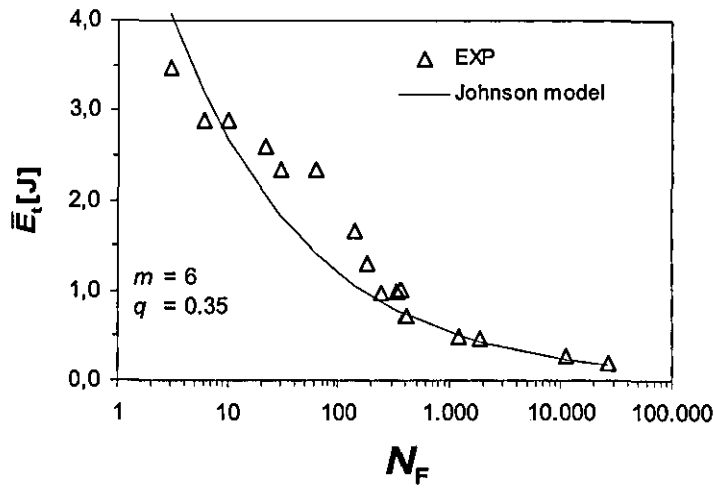


Figure 8.1 Power law fit to energy-life plot for SLJs in IF

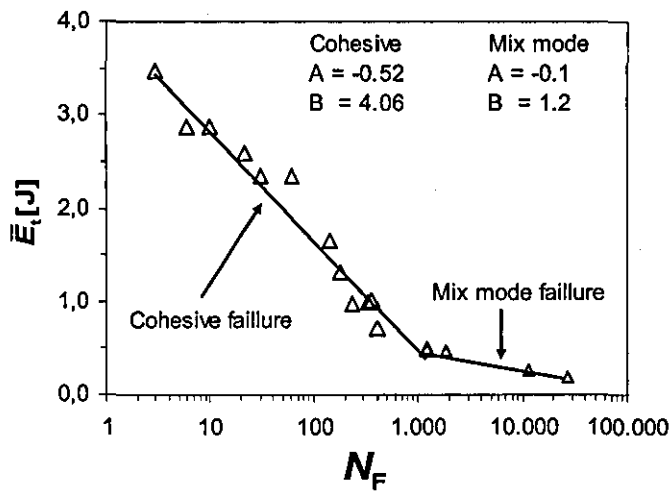


Figure 8.2 Log-linear law fit to energy-life plot for SLJs in IF

### 8.2.2 Stiffness degradation model

Experimental results presented in Sections 6.3.1.3 and 6.4.1.5 show stiffness deterioration during SF and IF as a result of damage formation and propagation in SLJs. It was proposed that this deterioration can be divided into three stages: Stage I is characterised by pre-macrocracking damage, Stage II is defined when a macro-crack propagates until a fraction of 0.8 of the fatigue life. A rapid unstable decrease in

stiffness is seen in Stage III, leading to sudden failure. Following this description, an expression to model this behaviour is proposed. The expression proposed is based on the observed sigmoidal appearance of the strength wearout plot. The fraction of stiffness deterioration ( $K(n^*)$ ) can be expressed as:

$$K(n^*) = K_0 \left[ (H \times n^* + G) \left[ \frac{(1 - m_1 \times (n^*)^{m_2})}{(1 - m_3 \times (n^*)^{m_4})} \right] \right] \quad (8.3)$$

where  $H$ ,  $G$ ,  $m_1$ ,  $m_2$ ,  $m_3$  and  $m_4$  are constants and  $n^*$  represent the fraction of the fatigue life ( $n/N_f$ ). The first term of Equation 8.3, represents the linear behaviour seen in stage II, which can be used to obtain the constants  $H$  and  $G$ . The values of  $m_2$  and  $m_4$  are obtained from the percentage of the fatigue life where the inflection points in the stiffness plots are experimentally observed. The  $m_2$  constant is the percentage of the fatigue life in the change from stage I to II and  $m_4$  is the negative of the percentage fatigue life where the experimental graph changes from stage II to III. The system now only depends on the two constants  $m_1$  and  $m_3$ , where the first one is related to the deterioration in stage III and the second is related to the deterioration in stage I. The fit of Equation 8.2 to the SF experimental data is presented in Figure 8.3. It can be seen that this expression matches very well the experimental results in all the stages.

The second step in this analysis was to extend the use of Equation 8.2 to the IF experimental data. The fit of the Equation 8.2 to the IF experimental data is presented in Figure 8.4. Again, it can be seen that the equation fits the data very well, albeit with more scatter in the experimental data in this case.

A first comparison between Figure 8.3 and Figure 8.4 suggests that a greater decrease in stiffness, especially under stage II, is detected in IF than in SF. The use of stiffness deterioration plots from fatigue measurements can be used for to predict crack initiation and propagation during SF and IF, as proposed in [58]. This method can be described as an enrichment of the fatigue life graphs, giving information about the fraction of damage that is present in the specimen.

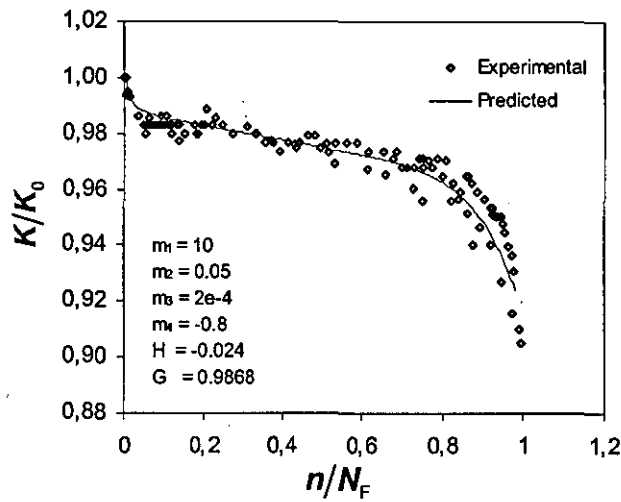


Figure 8.3 Stiffness deterioration during SF

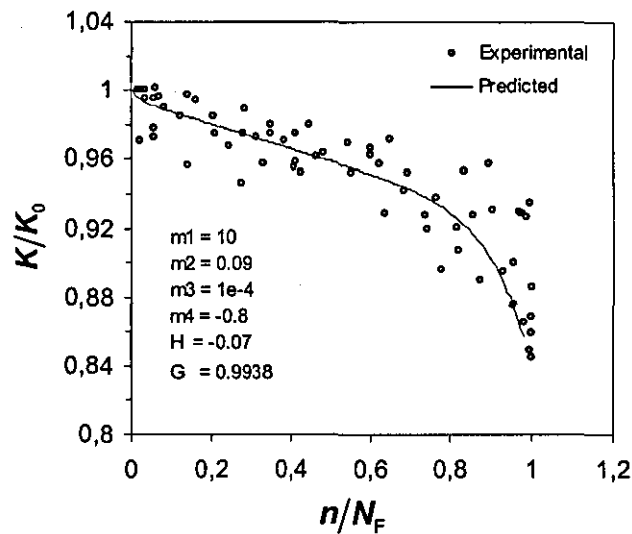


Figure 8.4 Stiffness deterioration during IF

### 8.2.3 The modified load-time model

The IF behaviour of materials can be modelled in terms of the loading time, which depends mainly on the material properties of the parts in collision and the boundary conditions. In Section 3.6.2, the *accumulated load-time model* ( $\sigma_{max}(N_f T)^m = C$ ) was introduced. This model basically proposes that for an input stress, a specific

accumulated contact time can be predicted. A modified version of the *accumulated load-time model* is proposed here because a re-definition of the original parameters in the loading time model is desirable to account for the observed variations in the loading time and maximum force. The total cumulative loading time,  $\tau$ , is thus defined as:

$$\tau = \sum_{i=1}^{N_f} T_{Fi} \tag{8.4}$$

where  $T_{Fi}$  is the contact time for the impact  $i$ , as seen in Figure 6.19. Using this definition and also the mean maximum force,  $\bar{F}_{\max}$ , that is reached over each impact, the *modified load-time model* is presented as:

$$\bar{F}_{\max} \tau^{m_s} = C_1 \tag{8.5}$$

The model described by Equation 8.5 is presented in Figure 8.5, together with experimental data (where  $m_s=0.087$  and  $C_1=2344$ ). It can be seen in this figure that the modified load-time model presents a good characterisation of the fatigue behaviour of bonded lap joints subjected to impact-fatigue.

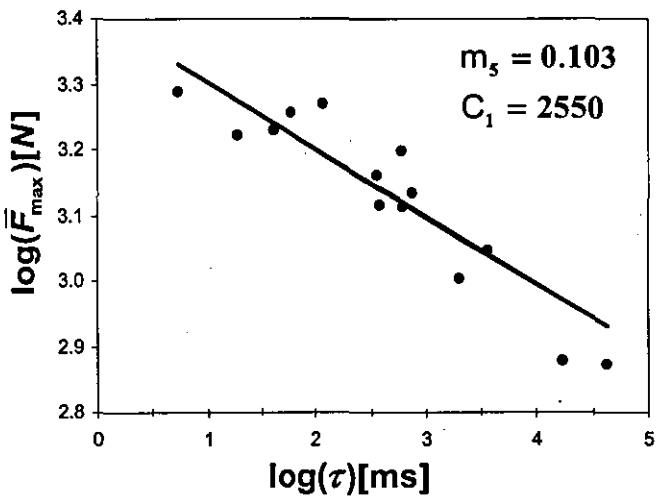


Figure 8.5 Modified load-time model

In Figure 8.5, it is observed that Equation 8.5 can be used to give an average view of the fatigue life. However, as this is defined in terms of the cumulative loading time, considerable experimental data is necessary to determine this model and individual effects in a singular specimen are lost; in conclusion, this model does not have the capacity to predict crack propagation. In order to address this problem, a second model, called the *normalized load-time model* is proposed.

#### 8.2.4 The normalized load-time model

As described previously, during IF the values of maximum and also their consequent contact time vary as damage progress in the SLJs. In order to account for the decrease in the maximum force and relate this with the contact time a second model is proposed. In this model the accumulated loading time before the  $n^{\text{th}}$  impact,  $\tau_n$ , is defined as:

$$\tau_n = \sum_{i=1}^n T_{Fi}, \quad (8.6)$$

this term is related to the decrease in the maximum force caused by damage accumulation in the specimen. Figure 8.6 shows a linear decrease in the normalized maximum force with increasing  $\tau_n$  (which is normalized with respect to  $\tau$ ). These results support the definition of a second model, termed the *normalized load-time model*, which represents the damage deterioration in a specimen as a result of impact-fatigue loading. In the model description in Equation 8.7, the maximum force is normalized with respect to the maximum force of the initial impact and as explained previously, for this analysis this was selected as the 10th impact rather the first to avoid the alignment issues in earl cycles.

$$\frac{F_{\max}}{F_{\max}^{10}} \left[ \frac{\tau_n}{\tau} \right]^{m_6} = C_2 \quad (8.7)$$

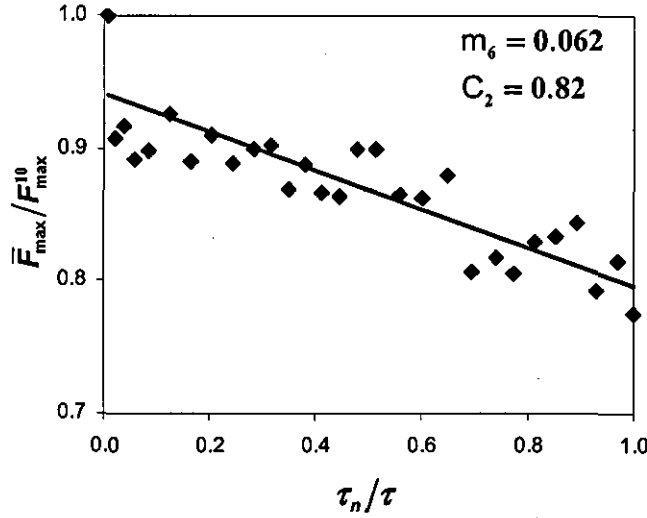


Figure 8.6 Effect of accumulated loading time on damage evolution in SLJ<sub>short</sub>

### 8.3. Fatigue crack growth approach

The fatigue crack growth rate curve has been used previously as a method to characterise failure in fatigue. This was discussed in Section 2.5.2.

#### 8.3.1 Fracture mechanics in LSJs

##### 8.3.1.1 Fracture parameters in SF

Four methods were used to calculate fracture parameters for LSJ<sub>short</sub> specimens. The first method was a simple analytical method proposed in [39] and described in Section 2.3.2.1. This model is based on an elastic analysis of an infinite beam in which the adhesive layer is neglected. The total strain energy release rate ( $G_T$ ) is defined as the sum of the mode I and mode II contributions (i.e.  $G_T = G_I + G_{II}$ ) and for the Brussat model  $G_T$  is termed  $G_{Brus}$ , as defined in Equation 2.21. The other three methods of calculating fracture mechanics parameters were based on the finite element models described in Section 5.2. Strain energy release rate was determined from the linear elastic and geometric non-linear models using the VCC technique [26]. These are termed  $G_{lin}$  and  $G_{gnl}$  respectively. For the model with non-linear adhesive properties

the J-integral fracture parameter proposed was determined for three integral paths around the crack tip.

A first analysis was conducted comparing  $G$  and  $J$  for a cohesive failure using the different calculation methods, as shown in Figure 8.7. Brussat's analytical method predicts a constant value of  $G$  with respect to crack length whereas all the other methods show decreasing values of  $G/J$  with crack length, although an initial increase in  $G$ , to varying degrees, is seen in the first 10 mm. This can be attributed to the fact that the LSJ geometry in the FEA model was far from the infinite length assumption in Brussat's analysis and hence end effects are seen along the length of the sample. It can also be seen that the linear FEA analysis shows the greatest variation in  $G$ , and this is because the geometry is not updated as the sample is loaded. Comparing  $G_{\text{gnl}}$  and  $J$ , it is seen that the latter has a lower value, as can be expected because  $J$  includes the material plastic region, but with a similar decrease tendency.

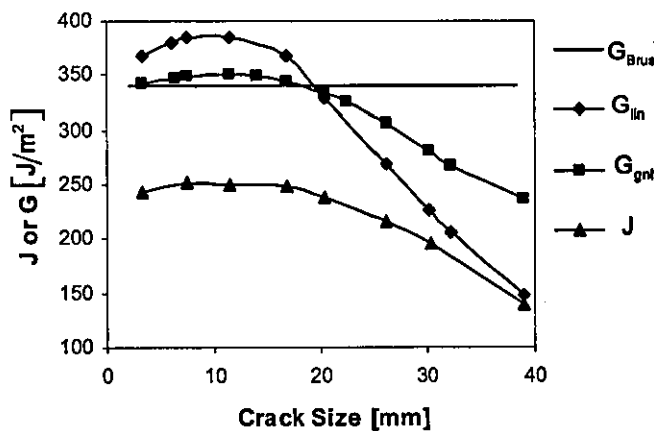


**Figure 8.7 Comparison of different fracture parameters for cohesive fracture of  $\text{LSJ}_{\text{short}}$**

A second analysis was conducted using the geometric non-linear cohesive failure model to investigate mode mixity. Comparison of  $G_I$  and  $G_{II}$  as a function of crack size is presented in Figure 8.8. It is seen that  $G_{II}$  is greater than  $G_I$  but decreases more rapidly after 20 mm crack growth, bringing it close to the value of  $G_I$ .

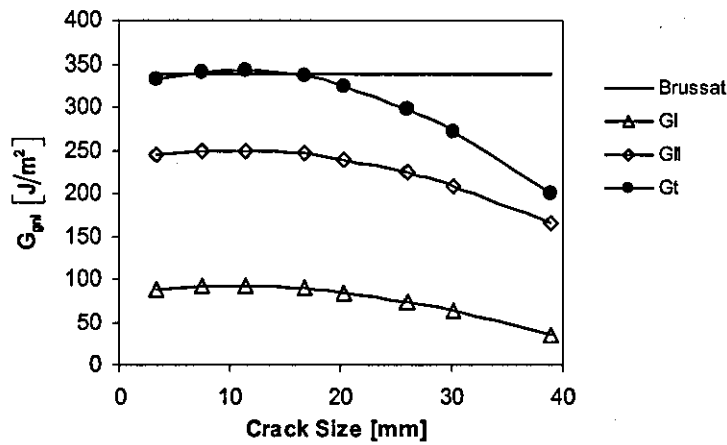


**Figure 8.8** Changes in  $G_I$  and  $G_{II}$  from a geometric non-linear model as a function of the crack size in  $LSJ_{short}$

Finally, the effect of crack location for  $G_{gnl}$  was investigated. Three crack growth scenarios (cohesive, interface and strap; as was described in Section 5.4.1.1) were studied and the results are presented in Figure 8.9. It can be seen that the crack location seems to have only a minor effect on the value of  $G_{gnl}$ . However, Figure 8.10 shows that the same cannot be said for mode mixity, although, it should be noted that the determination of the individual components of  $G$  may be more susceptible to the influence of the singularities at the bi-material interface than for  $G_T$ .

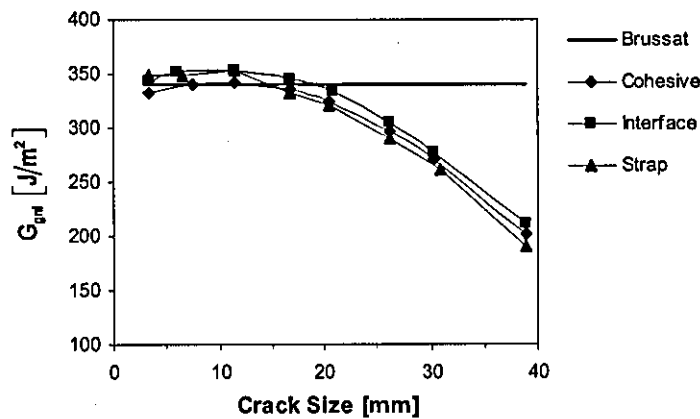


**Figure 8.9** Comparison of  $G_{gnl}$  for different fracture paths



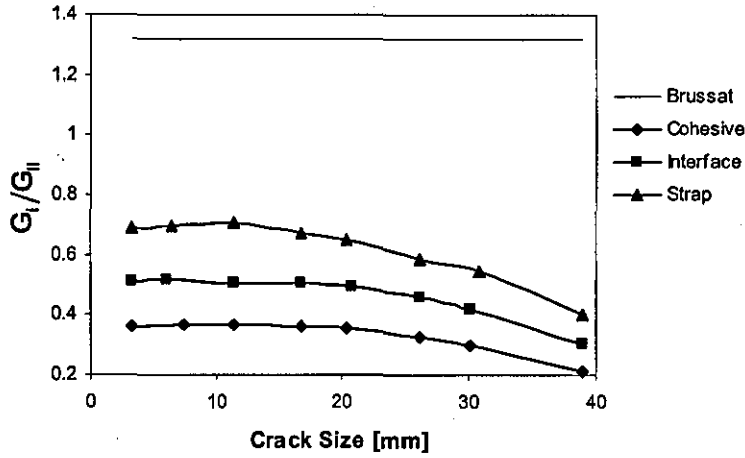


Figure 8.10 Comparison of  $G_{gnl}$  mode ratio ( $G_I/G_{II}$ ) for different fracture paths in  $LSJ_{short}$

#### 8.3.1.2 Fracture parameters in IF

Previously, in Section 5.3, it had been observed that during dynamic conditions the reaction force and the strain at a specific point are highly time dependent. Hence  $G$  is also a time dependent parameter. In order to analyse the dynamic strain energy release rate ( $G_{dyn}$ ) at low velocity impacts, the model presented in Section 5.4.2. was used.  $G_{dyn}$  was obtained using: (i) a geometric non-linear model with elastic material properties ( $G_{dyn}$ ) and (ii) a geometric non-linear model with elastic plastic material properties ( $J_{dyn}$ ).

The first analysis that was conducted analysed the variation of  $G_{dyn}$  during a single impact in a pre-cracked specimen. A FEM model with a cohesive crack size of 11 mm was used. The variation in  $G_{dyn}$  with time for this model is presented in Figure 8.11. It can be seen that there is an increasing tendency that is interrupted for a short period before reaching a maximum before decreasing. A similar pattern was seen in all models with cohesive failure, however, in some cases a more pronounced interrupted period was found. Investigating the reason for interruption in the increasing  $G_{dyn}$  tendency, it was observed that this is the result of a change in the contact point between the hammer and the impact block. At some time the contact point changes giving the option to increase crack opening and consequently to increase  $G_{dyn}$ .

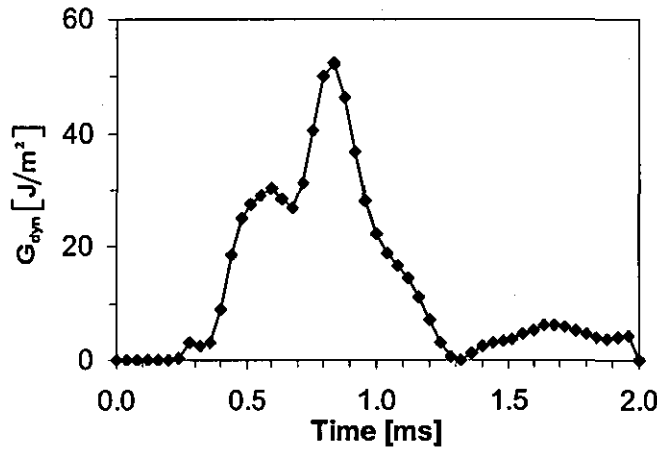


Figure 8.11 Changes in the dynamic strain energy release rate with a cohesive crack size of 11 mm in a LSJ<sub>short</sub>

The second study that was conducted was to analyse the effect of crack location for  $G_{dyn}$ . In this case, it was assumed that crack propagation can be related to the maximum dynamic strain energy release rate ( $G_{dyn}^{max}$ ) reached during an impact. Similar to the study in SF, three cases of crack propagation were analysed (cohesive, interfacial or a composite strap) and the results are presented in Figure 8.12. It is seen that in all three cases the  $G_{dyn}^{max}$  have similar values and a decreasing tendency as the crack increases.

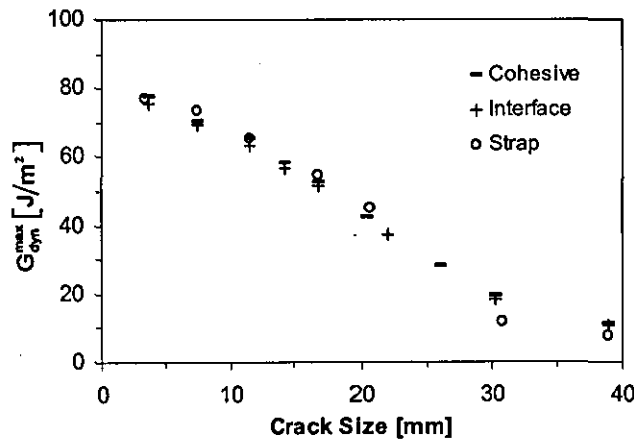


Figure 8.12 Comparison of  $G_{dyn}^{max}$  for different fracture paths in LSJ<sub>short</sub>

The third analysis that was conducted was a comparison of the maximum dynamic strain energy release rate when the crack is modelled as a cohesive crack and the adhesive material is modelled as an elastic material ( $G_{dyn}^{max}$ ) and an elasto-plastic material ( $J_{dyn}^{max}$ ). Figure 8.13 shows the comparison and it is seen that in this case there is no difference in the fracture mechanics parameters when the adhesive is modelled as an elastic or elasto-plastic material. This is explained by the low stress level that exist at the crack tip, with the material below the yield stress.

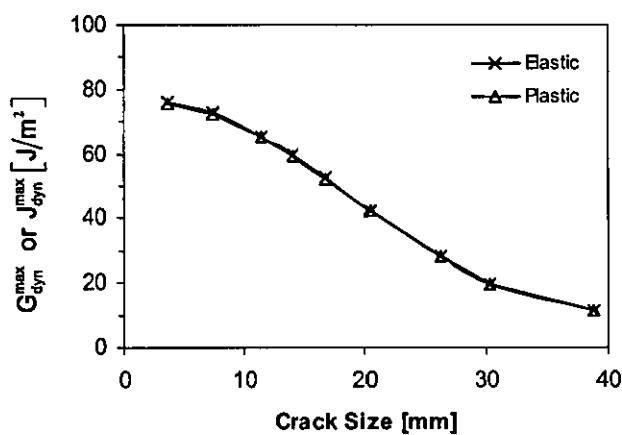


Figure 8.13 Comparison of  $G_{dyn}$  and  $J_{dyn}$  with a linear or elasto-plastic adhesive material in a LSJ<sub>short</sub>

### 8.3.2 Fatigue crack growth rate curves in LSJs

#### 8.3.2.1 Fatigue crack growth rate curve in SF

Experimental data for crack growth rate and numerical simulations of  $G$  with respect to crack size were presented in Section 7.3.2.1 and Section 8.3.1.1, respectively. Those results are used to determine the fatigue crack growth as function of  $G$  in LSJ<sub>short</sub> specimens. In Section 7.3.2.1, it was described that two main mechanism of failure were observed for LSJs in SF. The first cohesive failure in the adhesive, which shows a steadily decreasing crack growth rate as crack length increases. The second is a mixed failure path, with a cohesive failure for a first period; however, once the crack starts to propagate predominantly in the composite there is a sharp increase in the crack growth rate, although this levels as crack length increases further.

Figure 8.14 shows the FCGR curve for the  $LSJ_{short}$  specimens tested under SF. The sample with the cohesive failure shows the classic 3 zone fatigue crack growth behaviour, with a threshold region at approximately  $140 \text{ J/m}^2$  and fast growth region at approximately  $350 \text{ J/m}^2$ . In between these two regions is an area in which  $\log da/dN$  is proportional to  $\log G_{gnl}$ , as proposed by the Paris law. The fatigue crack growth plot for the mixed mode failure is coincident with the cohesive failure plot at high levels of  $G_{gnl}$ , where failure for both samples is cohesive. However, as  $G_{gnl}$  decreases with crack length there is an increase in the rate of crack growth. For a homogeneous type of fracture this would seem a non sensible result, however, it is perfectly explainable in the mixed failure case. It has been shown that for this system, the fatigue resistance of the CFRP matrix is less than that for the adhesive at room temperature [81], thus crack growth rate in the CFRP would be expected to be higher than that for the adhesive for a given value of  $G_{gnl}$ . This would result in different fatigue crack growth plots for failure in the adhesive and the CFRP, as shown schematically in Figure 8.15. It is easy to see from this figure how an increasing crack growth rate with decreasing  $G$  is obtained as the fracture path moves from the adhesive to the CFRP.

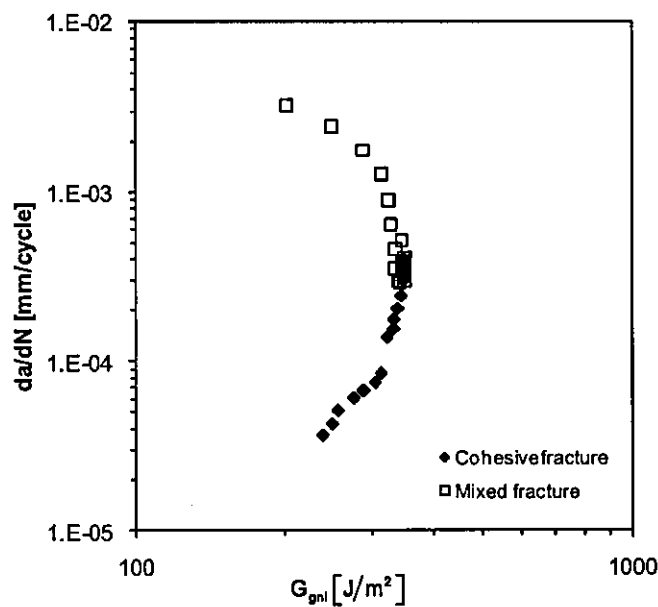
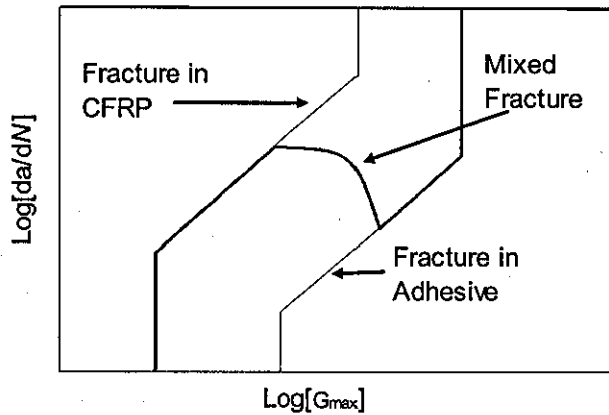


Figure 8.14 Fatigue crack growth during Standard fatigue



**Figure 8.15 Mixed mode fracture model**

### 8.3.2.2 Fatigue crack growth rate curve in IF

Similar to SF, the experimental data and numerical models provided in Section 7.4.1 and 8.3.1.2 were used to generate plots of the crack growth rate in terms of  $G$  during IF. In this case,  $G_{dyn}^{max}$  results were used in the analysis. As described in Section 7.4., it was not possible to measure the fracture in the adhesive because of the extremely fast crack propagation rate. However, the crack propagation rate associated with matrix cracking could be measured.

Figure 8.16 shows the FCGR-curve for an IF specimen with a slow FCG in  $LSJ_{short}$  exhibiting matrix cracking as the main fracture mode. A linear relationship suggests that the Paris's type law can be used to characterise FCG under IF. Values of  $G_C$  and  $G_{th}$  for the matrix cracking failure are approximately  $75 \text{ J/m}^2$  and  $26 \text{ J/m}^2$  respectively, with an  $m$  constant equal to 3.58.

In some specimens a delamination between the adhesive  $0^\circ$  ply and the  $45^\circ$  ply over the strap was observed. This change in failure mode can also be seen in the FCG graph (Figure 8.16). From analysis of the FCG in IF it is seen that the delamination process works as an accelerator for crack growth and a change similar to that found in SF when the failure changed from one mechanism to another is seen.

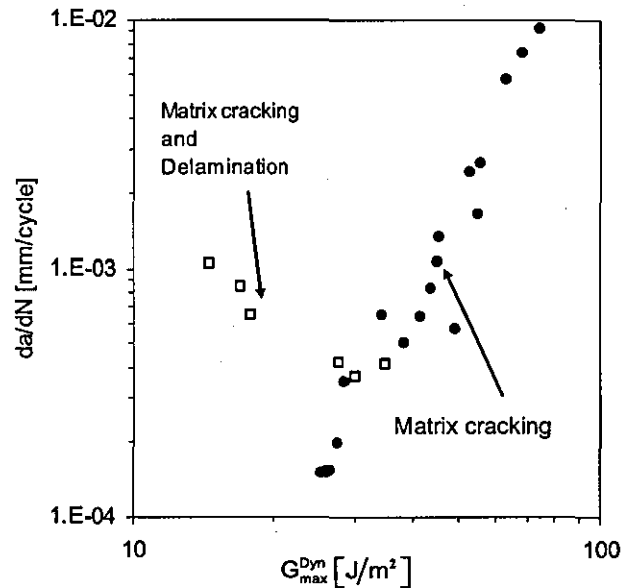


Figure 8.16 Fatigue crack growth during Impact fatigue

### 8.3.3 Mixed mechanism fracture model (MMFM)

Analyzing the results obtained from the SF specimens, it is observed that there is a difference in the fatigue crack behaviour in the case when the crack growth is in the adhesive and the case when the failure is a combination of failure in the adhesive and adherend. It has been described previously, that the mixed mode failure begins as a cohesive fracture and then, progressively changes to a combination of cohesive and matrix failure in the ply next to the adhesive. This means that two completely different mechanisms are present simultaneously, with competing crack growth behaviours. Combining these two behaviours, it is supposed that in general the FCG for a specimen with a mixed mode fracture needs to have a first region following the same FCG as a fully cohesive failure followed by a progressive change to a matrix failure FCG behaviour. In this work, it is assumed that the net FCG rate in mixed mode failure is a percentage of the rates for cohesive and matrix failure that exist in the specimen.

Image analysis has been carried out on the fracture surfaces with the aim of distinguishing between cohesive and matrix composite damage over the fracture

surface. In Figure 8.17, it is possible to observe the different regions of each failure mode, where white represents matrix cracking and black adhesive failure. In order to determine the percentage of each mechanism at a specific crack size, small areas (region with grey colour in Figure 8.17) were taken and then by a subroutine in Matlab that counts pixels, it is possible to find the percentage of each mechanism. It is supposed that the area is small enough to be approximated as a line. Some of the measurements are presented in Figure 8.17.

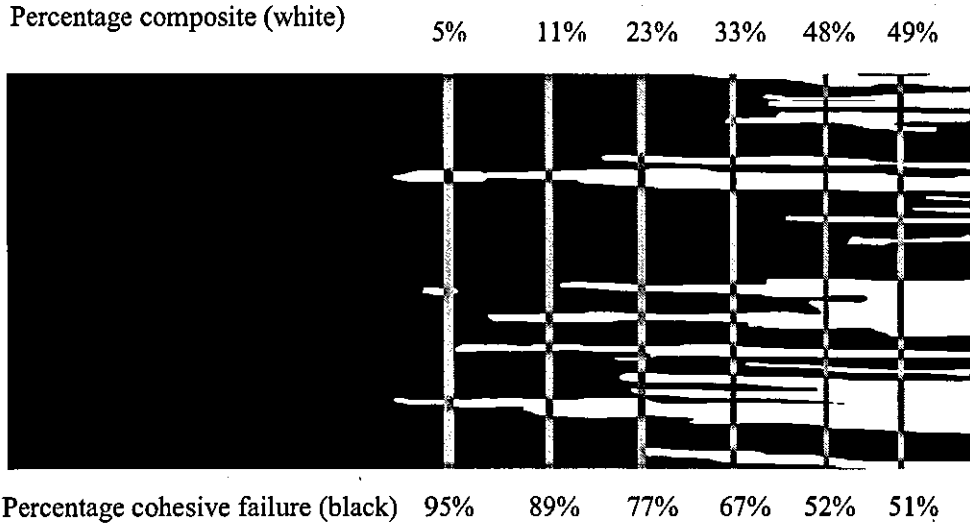


**Figure 8.17 Failure in mixed fracture model under SF.**

The crack growth rate at a specific crack size when both fracture mechanism are observed can be analysed as a percentage combination of the crack growth rate for each mechanism of failure. Linear or non-linear relations can be proposed, in order to have a general rule of mixtures, however this relation needs to be obtained by an optimization of the values. The following expression is proposed and referred to as the mixed mechanism fracture model (MMFM).

$$\text{Log} \left( \frac{da}{dN}(a) \right)_T = A^{\prime 1} \times \text{Log} \left( \frac{da}{dN}(a) \right)_{MC} + B \times \text{Log} \left( \frac{da}{dN}(a) \right)_{Coh} \quad (8.8)$$

where the sub indices T, Coh and MC refer to the mechanism of failure: total, cohesive and matrix cracking; A and B are the percentages of cohesive failure and

matrix cracking respectively and  $n$  is an exponent that is calibrated for the experimental data.

FCG for a fully cohesive failure can be seen in Figure 8.14, however, to obtain the FCG curve for matrix cracking previous work needs to be reviewed. In [81] a DCB specimen with similar adhesive/adherend system to that used in this research was used to define the FCG of this system. It was seen that at room temperatures failure can occur in the adhesive or composite and it was observed that cases when failure was in the composite  $G_{IC}$  was equal to  $200 \pm 50 \text{ J/m}^2$ . However, information on  $G_{Ith}$  and  $m$  (constant of the paris's law) was not presented. It was also mentioned that in cases when specimen were tested at low temperature only composite failure was observed and the parameters for crack growth were:  $G_{IC} = 250 \pm 50 \text{ J/m}^2$ ,  $G_{Ith} = 80 \pm 50 \text{ J/m}^2$ ,  $m = 8.8 \pm 0.9$ . This data is used in this research to define FCG with the mechanism of matrix cracking.

An optimization analysis was conducted for the constant  $n$  in Eqn. 8.8. Figure 8.18 shows the application of Eqn. 8.8. with three values for this constant. It is observed that as  $n_I$  increases the change from cohesive to matrix cracking is faster. From this analysis it is concluded that  $n_I = 2.5$  gives a good approximation to the experimental data.

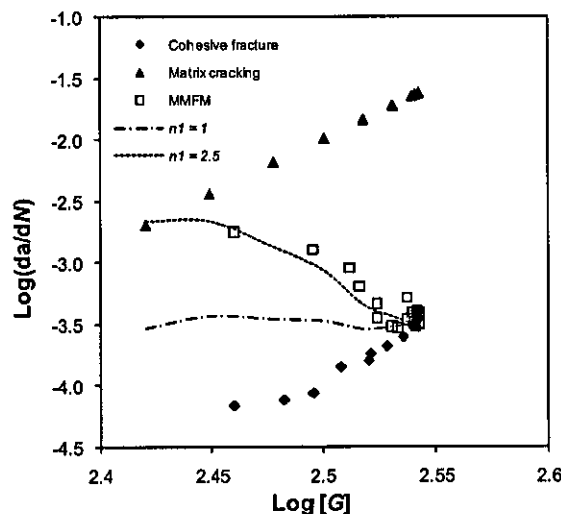


Figure 8.18 Optimization of  $n$  in the mixed mechanism fracture model



## 8.4. Numerical crack growth integration

Numerical crack growth integration (NCGI) was described in Section 2.5.2.2, is an established technique to predict crack growth in variable amplitude fatigue based on the results of constant amplitude fatigue [160]. In this present work, the technique was implemented to analyse CISF based on the results obtained from IF and SF.

### 8.4.1 Cohesive failure during SF

NCGI was used predict crack growth in SF in order to validate the technique and also to corroborate the FCGR-curves shown in Section 8.3.2.1 for LSJs with a cohesive failure. A comparison between the experimental data and the NCGI prediction of cohesive failure in a  $LSJ_{short}$  during SF is presented in Figure 8.19. It is seen that the NCGI gives a good prediction of the experimental data.

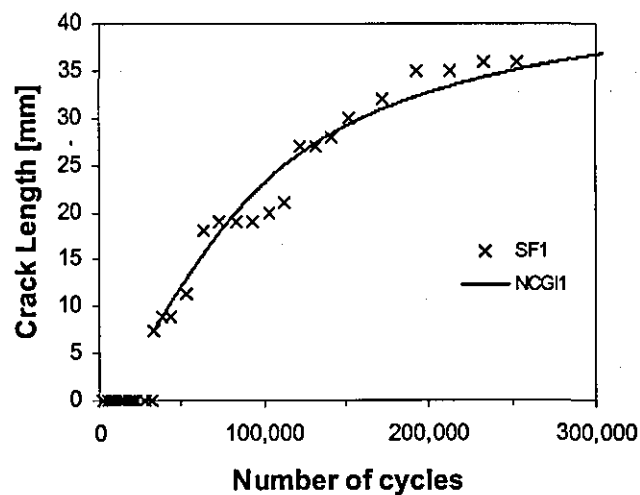
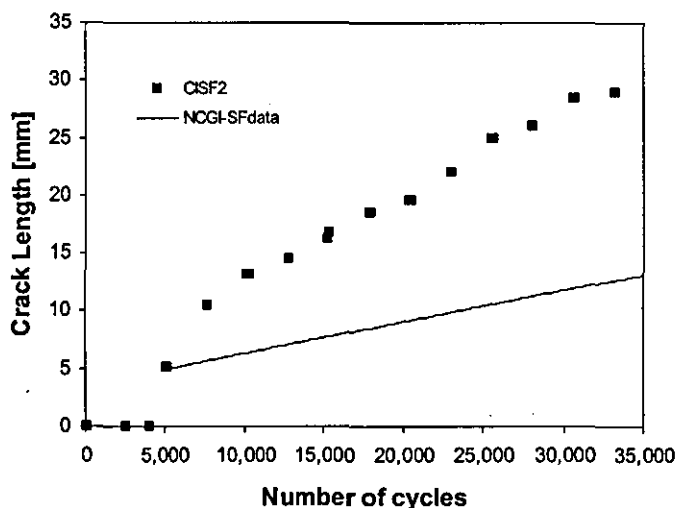


Figure 8.19 NCGI prediction of cohesive failure in a  $LSJ_{short}$  under SF

### 8.4.2 CISF

An extension of the use of NCGI technique is to analyse the FCG in CISF specimens. Experimental data has shown that in some cases a cohesive failure is found when specimens are tested under CISF. A first case was to use NCGI with the  $(FCGR-curve)_{SF}$  to predict failure in CISF. Figure 8.20 shows a comparison of the FCG in a cohesive failure under CISF and the NCGI predicted failure using the  $(FCGR-$

curve)<sub>SF</sub> for a cohesive failure. As expected, the NCGI method underpredicts crack growth as the enhanced crack growth in the IF region is increased. However, the plot usefully shows the significant effect of a proportionally small number of low energy impacts when included in a SF spectrum.



**Figure 8.20 NCGI of a cohesive failure LSJs under CISF**

The next step was to modify the method to incorporate load interaction effects. It was described in Section 7.5 that the FCG rate for a cohesive failure in IF could not be measured because of the high FCG rate and the small area with this type of failure. However, in order to include the effect of IF in the NCGI method, it was assumed that the  $(FCGR\text{-}curve)_{IF}$  could be obtained using a “Damage shift” model (DSM), as explained previously in Section 2.5.2.3. The empirical DSM was originally proposed to account for the inclusion of interaction effects in variable amplitude SF. This model proposes the existence of a function  $\psi_E$  which is associated with a lateral displacement of the FCGR-curve. In this work, it is assumed that the FCGR-curve needs to be moved to the left, in order to predict the FCG rate during CISF for a similar  $G$  to that obtained during SF. Figure 8.21 shows schematically this FCG rates shift. During implementation of the DSM model for CISF it is supposed that during the transition for SF to the FCG rate  $((da/dn)_i)$  changes suddenly from the SF to IF FCG curve, as described by region ‘1’ in Figure 8.21. During the 100 impacts, described as region ‘2’ in Figure 8.21, the FCG follows the  $(FCGR\text{-}curve)_{IF}$ . After IF, a more gradual change to the  $(FCGR\text{-}curve)_{SF}$  is introduced to account for interaction effects, as

represented by region '3' in Figure 8.21. Various scenarios for change from IF to SF were investigated. The first was that the FCG rate changed abruptly from SF to IF, as seen in Figure 8.22 ( $DSM_{abr}$ ), then continued to follow the  $(FCGR-curve)_{SF}$  for the subsequent 5000 SF cycles (described as 'region 4' in Figure 8.21). However, other scenarios were investigated in which damage ahead of the crack tip produced by the IF caused the FCG rate in region '3' to be higher than that predicted by  $DMS_{abr}$ . A second scenario is that a gradual decrease in FCGR is seen over all the 5000 SF cycles, in which case region '4' in Figure 8.21 disappears. This scenario is shown in Figure 8.22 and described as  $DSM_{lin.}$ . A variation of this scenario is when the damage ahead of the crack tip only affects a fraction of the 5000 SF cycles as represented in Figure 8.22 and described as  $DSM_{frac.}$

Following the scenarios of FCG rate deterioration described above, each of these cases was used to predict crack growth in the CISF. The first case was the use of  $(FCGR-curve)_{SF}$  and  $DSM_{abr}$  to predict the FCG behaviour of CISF with a cohesive failure. The value of  $\psi_E$  was obtained by changing the empirical constant  $C$  used in the Paris law (Equation 2.52) and keeping  $m$  constant (i.e. slope of the FCGR-curve) to try to minimize the error between the predicted and experimental data. A comparison of the NCGI and the experimental data is seen in Figure 8.23. The FCG behaviour is described as a step increasing tendency, which is a product of the sudden changes from SF to IF.

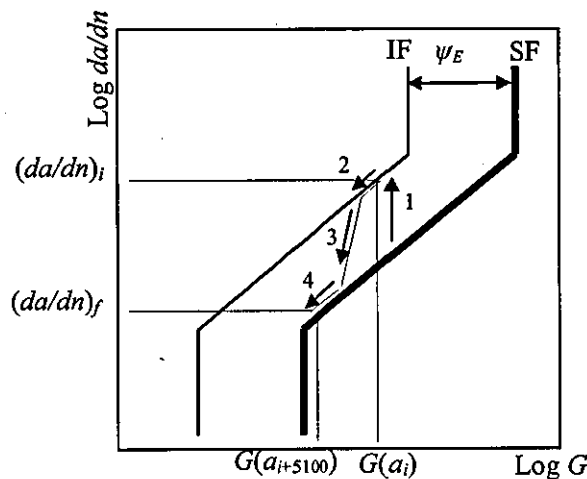


Figure 8.21 Schematic representation of CISF in Damage Shift model

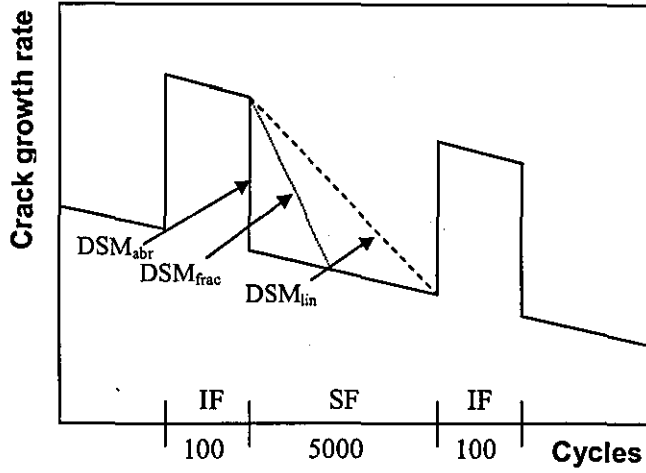


Figure 8.22 Schematic representation of FCG rate changes from IF to SF in CISF

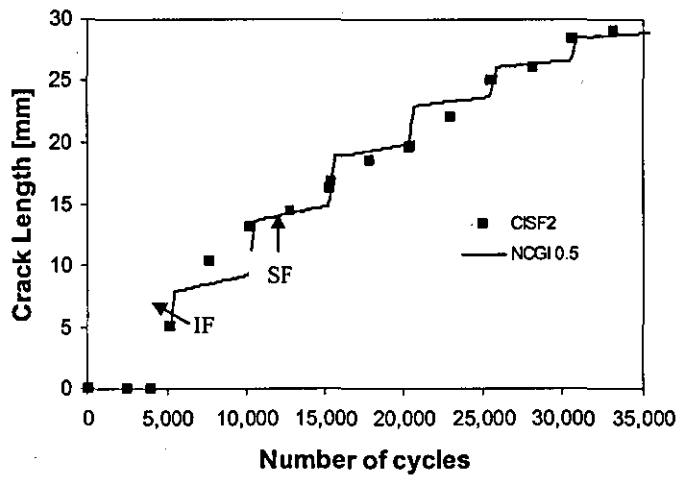


Figure 8.23 NCGI curve using  $DSM_{abr}$

The FCGR-curve of the CISF is presented in Figure 8.24 where the  $(FCGR-curve)_{SF}$  and the constructed  $(FCGR-curve)_{IF}$  are included. As expected, a drastic change from SF to IF is seen. The  $\psi_E$  necessary to obtained the  $(FCGR-curve)_{IF}$  was  $0.26 \text{ J/m}^2$  in log-scale

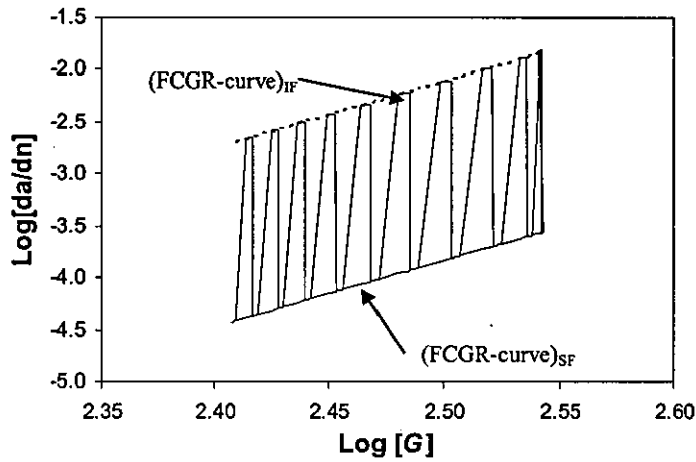


Figure 8.24 FCGR-curve for a CISF assuming  $DSM_{abr}$

The second crack growth scenario investigated was the use of the  $(FCGR-curve)_{SF}$  and  $DSM_{lin}$ . In Figure 8.25 a comparison between CISF data and the NCGI predicted crack growth is seen. A good correspondence between predicted and experimental data can be seen. Comparing Figure 8.23 and Figure 8.25, shows the softening effect of including the more gradual change in FCGR from IF to SF.

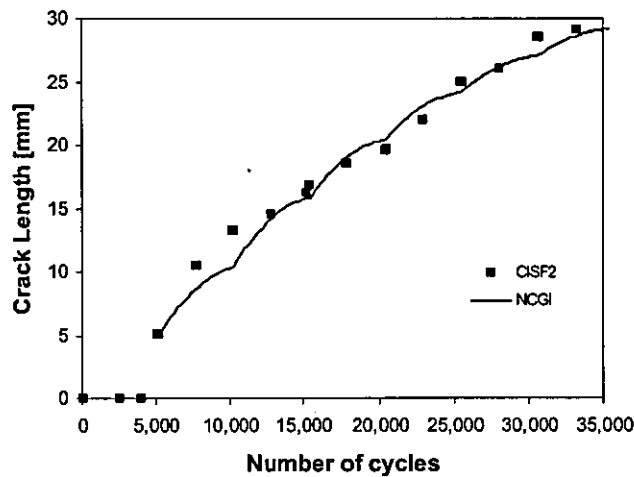


Figure 8.25 NCGI curve using  $DSM_{lin}$

The FCGR-curve for the CISF with the  $DSM_{lin}$  scenario is presented in Figure 8.26. As expected, it is seen that the FCG rate shows a gradual change when varying between IF and SF. The value of  $\psi_E$  was  $0.13 \text{ J/m}^2$  in log-scale.

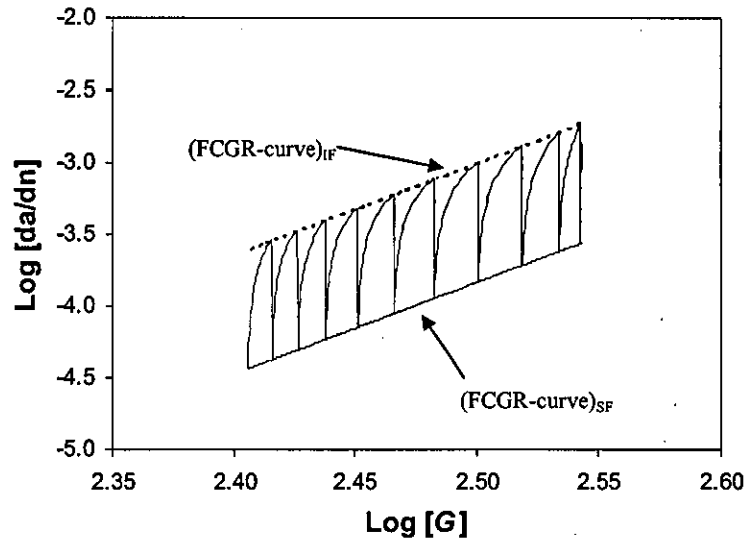


Figure 8.26 FCGR-curve for CISF assuming  $DSM_{lin}$

The third crack growth scenario assumed that IF damage affects only a fraction of the SF load block. In this case it was supposed that only 20% of the SF block was affected by this damage. A comparison between the experimental and the corrected NCGI using the  $DSM_{frac}$  scenario is presented in Figure 8.27. In this case, step increases in FCG are seen; however, they are less abrupt than seen with the  $DSM_{abr}$  assumption. This is also seen in Figure 8.28. In this case  $\psi_E$  was  $0.21 \text{ J/m}^2$  in log-scale.

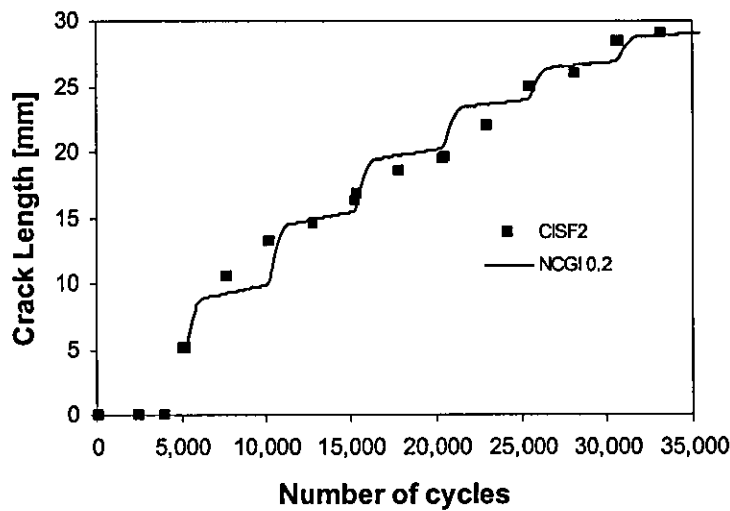


Figure 8.27 NCGI curve using  $DSM_{frac}$

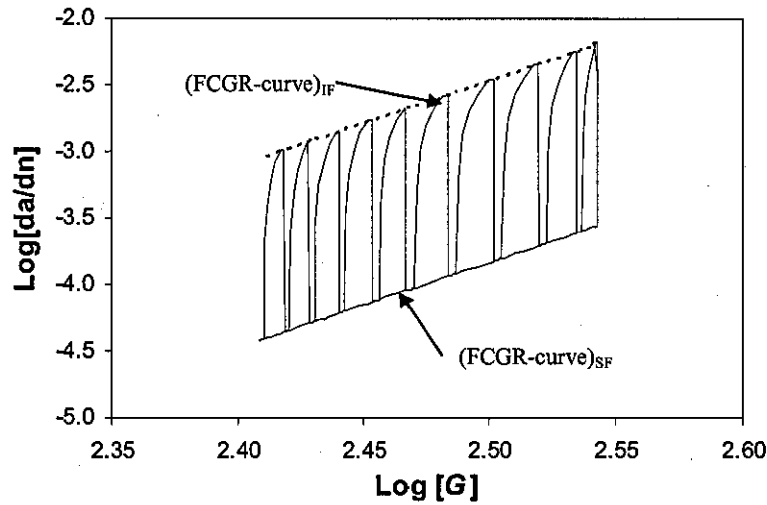


Figure 8.28 FCGR-curve for CISO assuming  $DSM_{fra}$

## 8.5. Discussion

Various phenomenological models were proposed to analyse IF. The first method used was the fatigue-life model, where linear behaviour was observed when the impact energy was plotted against logarithmic number of cycles to failure. In addition, it was observed that changes in the mechanism of failure had a direct impact on this graph.

The second phenomenological model investigated was the stiffness degradation, where a three stage graph was observed. The stiffness degradation was analysed for SF and IF, and similar tendencies were found for both graphs when the stiffness decrease was plotted in terms of the normalized fatigue life. With this data, a method to analyse fatigue is proposed; where the  $E-N$  diagram is used to determine the fatigue life and stiffness deterioration is used to determine the regions of initiation, stable propagation and onset of unstable crack growth in specimens.

Two modifications of the accumulated time-stress model have also been proposed to characterise the impact-fatigue results. The first model was termed the modified load-time model and relates the total cumulative loading time of the primary tensile load wave to the mean maximum force. The second model attempts to characterise sample

damage under impact-fatigue by relating the maximum force normalised with respect to initial maximum force to the accumulated loading time normalised with respect to the total accumulated loading time. This model has been termed the normalized load-time model. It is shown that both models provide a suitable characterisation of impact-fatigue in bonded joints.

A methodology to construct FCG diagrams under SF and IF is proposed. Values of the strain energy release rate obtained numerically have been plotted against experimental results of the crack growth rate in LSJs. Results were compared with previous work conducted in the area and found to be in the range of those reported previously. The FCG graphs in similar load conditions and in the case when a single mechanism of failure exists show a tendency similar at those proposed by the Paris' law, where a threshold, stable and unstable regions are presented. Where changes in the mechanism of failure (at similar load conditions) were observed anomalous crack growth behaviour was observed that could be explained by a transfer from the FCG plot of one mechanism to that of another. To account for this behaviour, a model is proposed where the FCG of the system is a function of the percentage of failure and the crack growth rates in hypothetically unique mechanisms of failure. This model depends on the percentage of damage of each driving mechanism and the crack growth rate that is expected in a hypothetical scenario when only one mechanism exists. Changes from cohesive to a matrix cracking fracture were studied and the proposed mixed failure mechanism crack growth model was used to predict the FCG under a combination of fracture modes in a specimen. This model is a combination of the fraction of each FCG, with a penalty term  $n$  for the matrix cracking that has the highest FCGR. The model was seen to predict the mixed crack growth behaviour well if the correct value of  $n_i$  was selected.

Numerical crack integration was used to predict FCG behaviour in CISF, especially in the case when cohesive failure was seen. Initial approximations using only data from SF underpredicted crack growth. As described in Section 7.5, experimentally it was seen that the inclusion of small number impacts changes drastically the FCG and this was confirmed by this approximation. The use of the damage shift model helps to modify the prediction of the NCGI. In this study, three scenarios of FCG rate change



from IF to SF were studied, where in all of them the (FCGR-curve)<sub>IF</sub> was obtained using the damage shift model. It is seen that the effect of IF on damage in the adhesive can be represented in the model by controlling the rate of change of crack growth in the transition from IF to SF. An abrupt change in crack growth rates represents no interaction effects whereas a gradual change results in an accelerated crack growth in SF because of IF included damage ahead of the crack tip. This is seen to have direct effect on the predicted crack growth behaviour.

## 8.6. Conclusions

Impact energy was seen to be a linear function of the logarithm of cycles to failure in IF.

Changes in stiffness in IF and SF were represented by a sigmoid curve. This curve could be used to predict the percentage of the fatigue life.

The *modified load-time model* and the *normalized load-time model* provide a suitable characterization of IF in bonded joints in different fatigue stages.

The fatigue crack growth rate curve was seen to be a valid representation of fatigue propagation under SF and IF, and it can be constructed by a combination of experimental and FEA technique. It was seen that the Paris law is a suitable relation that can be used to analyse crack propagation in IF as same as in SF.

Changes on the fracture mechanism in specimens were modelled by the mixed mode fracture model (MMFM), reproducing the experimentally observed acceleration on the fatigue crack growth rate when cracks change to growth from high to a low fracture resistance material.

Damage shift model in conjunction of the numerical crack growth integration technique were proposed to analyse CISF proving to be a suitable technique to account for the damage zone (seen experimentally in previous work) that exists ahead of the main crack tip produced especially by small blocks of IF. In the analysis to get

the value of the function  $\psi_E$  which characterise the damage shift model it is concluded that the IF load block affects the complete area of crack propagation for a SF load block.

## CHAPTER 9

### Discussion

#### 9.1. General

The study of *impact fatigue* (IF) started at approximately the same time as standard fatigue (SF), however, little work has been published since. A literature review conducted to understand the effect of IF, especially in adhesives, polymers and composite, shows transverse impacts generated internal damage that considerably decreased the SF resistance of the material. In the area of adhesively bonded joints, the majority of the work concerning impact loading has been concentrated on the effect of loading rate on toughness. However, conclusions from single impact tests cannot be used to predict the behaviour of adhesively bonded joints under IF.

In previous work on IF, it has been observed that energy *vs.* number of cycles plots are a good method to characterise fatigue; however, similar limitations to those seen in the stress *vs.* number of cycles of plots used to characterise SF are seen. It was concluded from the literature review. That research on IF is characterised by a lack of published work, especially concerning cyclic tensile impacts conditions in composites and adhesives that are the subject of this work.

## **9.2. Experimental techniques**

This project was conducted using a pendulum impact machine which produces low velocity tensile impacts. This machine consists of a specimen fixed to a support at one end whilst the other end is hit by a pendulum hammer. It is well known that during an impact, the loading condition depends on the type of contact that exists between the hammer and the impacted surface. The presence of small misalignments can significantly affect the stress distribution in the sample. In this work, a tensile bar was used to understand and calibrate numerically the impact. It was seen that small uncontrollable misalignments in the contact area drastically affected the loading of the sample. However, such misalignments can be analysed by FEA in order to investigate the effect on internal stress distributions. During the boundary conditions calibration, it was necessary to include elastic restrictions on the specimen support in the models as ideal supports produced higher reaction forces and smaller contact times than those obtained experimentally. However, when elastics supports were included in the model, the reaction forces decreased and the contact time increased to correlate well with experiments. This parameter interaction gives the possibility to reproduce approximately the range of forces and contact times that were reached experimentally in the tensile bar and the LSJs specimen.

Experimental testing of bulk FM 73M and EA 9628 UNS adhesive specimens indicated that the tensile strength and yield stress increased with load rate, without a variation in the elastic modulus. This indicates a viscoplastic rather than viscoelastic behaviour when the load rate is increased.

## **9.3. Fatigue life in aluminium bonded SLJ**

### **9.3.1 Standard fatigue**

Small geometrical changes in similar SLJ do not significantly affect the number of cycle to failure when specimens are tested using a similar percentage of the quasi-static strength. Stiffness deterioration showed that damage begins early in the fatigue

life but accelerates towards the end. Strength wearout and stiffness deterioration results showed that rapid failure occurs when the level of damage reaches a critical value.

### 9.3.2 Impact fatigue

During IF, the reaction force and the contact time vary as a product of damage evolution. As damage increases, the contact time, reaction force and consequently the energy absorbed per impact decreases.

Adhesively bonded joints are susceptible to rapid degradation and failure when subjected to IF. The IF can be studied using the force-life ( $F-N_F$ ) and energy life ( $E-N_F$ ) curves. These graphs show that as the impact force or energy decreases, the number of cycles to failure increases. Additionally when data is plotted using the  $E-N_F$  curves, changes in the fracture mechanics can be identified.

Tendencies of the fatigue life in SF showed a smooth transition from a quasi-static test to a fatigue test. This is also confirmed in strength wearout tests of the joints where the quasi-static strength value begins to decrease as the number of cycle's increases. However, during IF a drastic transition from the quasi-static strength is seen, followed by a continuous decrease.

The results from fatigue-life plots for IF and SF show a drastic difference between these two types of loading. It was seen that the number of cycles to failure for IF is much lower than that needed for failure in SF. From the data generated it seems that in the case of IF, a fatigue limit is not clearly observable even though specimens were tested at 13% of the quasi-static strength of the joint. However, during SF, a  $10^6$  fatigue limit was observed at 30% of the quasi-static strength of the joint.

## 9.4. Fatigue crack growth in lap strap joints

The FCG rate in different size LSJs specimens showed that they had similar values and tendencies when samples with similar fracture mechanism were compared. This

indicates that it is valid to compare samples with different size as long as the maximum fatigue load has the same percentage of the quasi-static failure load.

It is seen that fatigue damage in CFRP LSJs can occur in different forms, and the type of fracture mechanism determines the crack growth rate. In cases when the mechanism of failure changes from cohesive failure of the adhesive to fracture in the composite, a drastic acceleration of the crack growth rate is seen. This may be attributed to the addition of a rubber phase to the adhesive to increase toughness and the lower resistance of the CFRP to crack propagation than the adhesive. In addition, when cracks grow inside the adhesive, there can be more than one path producing damage over a larger area and resulting in higher consumption of energy than when damage is localized in one plane.

Differences in the FCG under IF and SF were described as differences in the percentage of the quasi-static strength for crack initiation and differences in the FCG rate during crack propagation. Crack initiation was seen under IF at significantly lower load levels than the  $10^6$  cycle fatigue limit in SF, which was at a maximum load is equivalent to 44% of the quasi-static failure load. During the early stages of crack propagation, when crack growth is in the adhesive, FCG rates were at least one order of magnitude higher in IF than in SF, even though the force levels during SF were about two and a half times higher than in IF. These results show that FCG in LSJs is highly even small number of low energy impacts even in a fatigue system can significantly accelerate damage.

The inclusion of small IF blocks in a SF test (CISF) reveals that in cases when similar fracture surfaces are compared, the FCG rate is higher in CISF than in IF. The brittle behaviour of the adhesive under IF is perceived to be responsible for the production of micro-cracks in the process zone under the IF block that affect the rate of damage in the process zone. As a result of these micro-defects formed in front of the crack tip, the propagation of the main crack under SF will be higher than in a pure SF test.

SEM studies of fracture surfaces of specimens failed in IF and SF conditions demonstrate significant differences at the microscale, which could be responsible for

the higher FCG rates at the macroscale. SEM showed that although superficially similar, the IF fracture surface were more representative of high energy, brittle failure than those seen in SF.

## 9.5. Modelling SF, IF and CISF

### 9.5.1 Modelling impact fatigue

During IF, the accumulated energy per impact and the number of cycles to failure can be related using a natural logarithmic function. Changes in the mechanism of failure produce changes in the experimental constants that are used to model the data.

Measurements of stiffness deterioration have been seen to be a useful method to characterise damage propagation in joints. An expression was defined which included all stages of the stiffness deterioration, which in conjunction with a fatigue-life model can be used to predict fatigue in adhesive joints. This technique can be used for both SF and IF.

Empirical relations between the accumulated contact time (contact time times the number of impacts) and the impacted force can be used in adhesively bonded joints to identify IF. The *modified load-time model* is proposed to correlate the accumulated load time that reaches specimens at different impact level forces. The *normalized load-time model* attempts to characterise sample damage under impact-fatigue by relating the maximum force normalised with respect to initial maximum force to the accumulated loading time normalised with respect to the total accumulated loading time. It is observed that both models provide a suitable characterisation of IF in SLJ.

The FCGR-curve seems to be a suitable method to analyse fatigue during SF and IF, where a linear according to the region of crack propagation is observed and approximated by the Paris law. Comparison of the matrix cracking under SF and IF shows that  $G_{th}$  has drastically decreased, from a value around 200 J/m<sup>2</sup> during SF to 25 J/m<sup>2</sup> during IF (as seen in Figure 8.14 and Figure 8.16). Changes on the slope on the Paris's law relation were observed where it is expected values around 8.8 for SF

and 3.58 during IF. In addition, from the results found in this research, it is expected that  $G_C$  during SF for an adhesive damage will be equal or higher than  $350 \text{ J/m}^2$  in SF when in IF it is expected to be equal or less than  $76 \text{ J/m}^2$ .

### **9.5.2 Mixed mechanism fracture model (MMFM)**

The mixed failure mode crack model is a suitable model to approximated, changes in the fracture surface from one mechanism to other. This model is defined in terms of the FCG rate of each fracture mechanism and the proportion of each mechanism observed at a specific crack size. The model is suitable to predict the FCG rate when a failure changes from an adhesive cohesive failure to a matrix cracking failure. The model predicts an increase in the FCG rate as more matrix cracking appears similar as the experimental data.

### **9.5.3 Modelling CISF**

The damage shift model is a technique which includes effect on the load history in the fatigue behaviour of adhesive joints. A parameter  $\psi$  can be determined experimentally to predict the FCGR-curve in cases when it is not available. In this work, it was used to predict the IF behaviour of a cohesive failure. Various scenarios of FCGR transition were analysed when specimens were tested in CISF; in order to reproduce the FCG rate acceleration when small impact block are included to SF load pattern. From the use of numerical integration of the FCG rate, it is observed that the affected region by the IF cover at least the same region where the crack is propagating during SF.



## **CHAPTER 10**

### **Conclusions and future work**

#### **10.1. Conclusions**

- Variable boundary condition in pendulum tests result in an uncertain stress distribution under impact, however, the dynamics of an impact can be calibrated by combination of experimental testing and FEA.
- The studied epoxy adhesives (FM 73 and EA 9628 UNS) exhibited viscoplastic material behaviour as the load rate or displacement rate increases.
- Similar configuration specimen with different sizes but constant overlap lengths produced different quasi-static strengths, however, the relation quasi-static strength/width was constant.
- Dissimilar size specimens tested under SF at the same quasi-static strength fraction gave similar fatigue lives.
- Damage in SLJs under SF and IF, identified as the stiffness deterioration parameter, begins early in the fatigue life but accelerates towards the end of the fatigue life.

- The reaction force and the contact time can be used as parameters to characterise IF damage in adhesively bonded joints.
- Adhesively bonded joints are susceptible to rapid degradation and failure when subjected to IF.
- Adhesive joints tested under SF have a smooth transition from quasi-static behaviour, which is in contrast to the drastic transition seen in IF.
- The fatigue limit for IF is lower than 13% of the quasi-static strength whereas in SF, it is at 30% of the quasi-static strength.
- Fatigue damage can occur as cohesive failure of the adhesive and or CRFP damage, represented by matrix cracking and eventual delamination, especially during IF. FCG rate acceleration is seen when the damage fracture mechanism change from cohesive failure to matrix cracking and from matrix cracking to delamination.
- Crack initiation during SF and IF shows differences, where it was found that during SF no visible crack appeared in LSJ samples after  $10^6$  cycles when the maximum force was equal to 44% of the quasi-static specimen strength [173], however, during IF it is seen that crack initiated when specimens were tested at loads two and half times lower than SF.
- FCG rates during cohesive damage in IF are at least one order of magnitude higher than those found in SF.
- Inclusion of small IF blocks in a SF load spectrum generates an acceleration in the FCG rate during the SF blocks.
- IF data can be approximated with a natural logarithmic function, where the abscise are the number of the cycles to failure and the ordinate the impacted energy; changes on the equation constant is expected as the mechanism of failure changes.

- Stiffness deterioration in IF and SF can be modelled with a six parameter function representing all stages of the process.
- The proposed modified load-time model and normalized load-time model can be used to characterise of IF in SLJs.
- The FCGR-curve is a suitable method to analyse crack propagation during SF and IF in LSJs.  $G_{th}$  in IF for matrix cracking is about  $25 \text{ J/m}^2$ , with a Paris law exponent constant equal to 3.58.  $G_C$  during SF for an adhesive damage is equal or higher than  $350 \text{ J/m}^2$  whereas for IF it is equal or less than  $76 \text{ J/m}^2$ .
- Changes from one mechanism of fracture to another can be modelled using the mixed mechanism fracture model (MMFM), which is a function of the FCG rate of each mechanism of failure, the fraction damage of each mode fracture and an experimental constant.
- The damage shift model is a suitable technique to predict the effects of load history on fatigue crack growth. Numerical integral method, in combination with the damage shift model, is a suitable method to predict FCG in CISF.

## 10.2. Future work

Future examination of the boundary conditions in the impact Resil machine should be conducted in order to restrict specimen displacements during impacts only in the tensile direction, decreasing the complexity of the FEA necessary to reproduce an impact. An option to produce a pure tensile contact is by the use of a universal joint between the impact block and the specimen in order to absorb rotation and give only a pure tensile impact.

As part of the conclusions in this work, it was seen that FCG in the CFRP is an extremely critical mechanism of failure in bonded composite joints. Attention needs to be directed at the analysis of IF in CFRP laminates. In order to achieve this aim, a large experimental programme needs to be conducted where the problems of matrix

cracking initiation and propagation, including delamination, needs to be conducted. This kind of study implies the use of non destructive techniques to analyse FCG under different scenarios. Criteria of failure combining stress state and fatigue need to be proposed to understand matrix cracking and propagation in IF.

Criteria of failure under IF require further investigation. The fracture behaviour of materials is a mechanism that is a size parameter problem. Fracture mechanism should be further studied, initially with homogenous and crystalline materials, like PMMA. This will help to decrease the complexity of the fracture mechanism and enable analysis of the problem in a more fundamental way.

A useful extension to the work in this thesis could be to analyse IF using the strength wearout data obtained during IF and SF in conjunction with cohesive zone element (CZE) theory. Strength wearout can provide experimental data for use in the development of possible deterioration laws that can be included in the CZE and in this way to analyse fatigue. This would be used to predict impact damage and fatigue deterioration of bonded joints subjected to IF and SF.

## References

- [1] Campbell FC. Secondary adhesive bonding of polymer-matrix composites. in "ASM handbook, Volume 21: Composites". 2001.
- [2] Ekh J. Multi-fastener single lap joints in composite structures. PhD Thesis, Royal Institute of technology, Stockholm. 2006.
- [3] James CW, Edgar AS. Progress in structural materials for aerospace systems. *Acta Materialia*. 2003;51(19):5775-5799.
- [4] Higgins A. Adhesive bonding of aircraft structures. *International Journal of Adhesion and Adhesives*. 2000;20(5):367-376.
- [5] Cantwell WJ, Curtis PT, Morton J. Impact and subsequent fatigue damage growth in carbon fibre laminates. *International Journal of Fatigue*. 1984;6(2):113-118.
- [6] Peters JO, Ritchie RO. Foreign-object damage and high-cycle fatigue of Ti-6Al-4V. *Journal of Materials Science and Engineering*. 2001;A 319-321:597-601.
- [7] Hertzberg RW, Manson, J.A. *Fatigue of Engineering Plastics*. Academic Press. 1980.
- [8] Du Pont. Impact Fatigue the long term toughness parameter. *Materials & Design*. 1988;9:229-230.
- [9] Isik I, Yilmazer U, Bayram G. Impact modified epoxy/montmorillonite nanocomposites: synthesis and characterization. *Polymer*. 2003;44(20):6371-6377.
- [10] Azimi H, Pearson R, Hertzberg R. Fatigue of hybrid epoxy composites: Epoxies containing rubber and hollow glass spheres. *Polymer Engineering & Science*. 1996;36(18):2352-2365.
- [11] Kinloch AJ. Adhesives in Engineering. *Proceedings of the I MECH E Part G Journal of Aerospace Engineering*. 1997;211:307-335.
- [12] Perez N. *Fracture Mechanics*. Kluwer Academic Publishers. 2004.
- [13] Anderson TL. *Fracture Mechanics Fundamentals and Applications*. CRC Press. 2005.
- [14] Griffith AA. The phenomena of rupture and flow in solids. *Philosophical Transactions of the Royal Society of London, Series A*. 1921;221:163-198.
- [15] Irwin GR. *Fracture I*. In *Handbuch der Physik* Edited by S Fluegge Springer-Verlag. 1958;6.
- [16] Inglis CE. Stress in a plate due to the presence of cracks and sharp corners. *Institute of Naval Architecture*. 1913;55:219-241.
- [17] Saxena. *A Nonlinear Fracture Mechanics for Engineers*. CRC Press LLC. 1998.
- [18] Software M. Marc 2007 r1 Volume A: Theory and user information. 2007.
- [19] Rice JR. A path independent integral and the approximate analysis of strain concentration by notches and cracks. *Journal of Applied Mechanics*. 1968;35:379-386.
- [20] Suresh S. *Fatigue of materials*. Cambridge University Press. 1997.
- [21] Maekawa I. The influence of stress wave on the impact fracture strength of cracked member. *International Journal of Impact Engineering*. 2005;32(1-4):351-357.
- [22] Xu RL, Wang P. Dynamic fracture mechanics analysis of failure mode transitions along weakened interfaces in elastic solids. *Engineering Fracture Mechanics*. 2006;73(12):1597-1614.
- [23] Miannay DP. *Time-Dependent Fracture Mechanics*. Mechanical Engineering Series Springer. 2001.

- [24] Morozov N, Petrov Y. Dynamic of fracture. Springer. 2000.
- [25] Rybicki EF, Kanninen MF. A finite element calculation of stress intensity factors by modified crack closure integral. *Engineering Fracture Mechanics*. 1977;9:931-938.
- [26] Sethuraman R, Maiti SK. Finite element based computation of strain energy release rate by modified crack closure integral *Engineering Fracture Mechanics*. 1988;30(2):227-231.
- [27] Wahab MMA, Ashcroft IA, Crocombe AD, Hughes DJ, Shaw SJ. The effect of environment on the fatigue of bonded composite joints. Part 2: fatigue threshold prediction. *Composites Part A: Applied Science and Manufacturing*. 2001;32(1):59-69.
- [28] Ripling EJ, Mostovoy S, Patrick RL. Application of fracture mechanics to adhesive joints. Final Report AD0424287, Materials Research Lab INC Richton Hill. 1963.
- [29] Loch AJK, Shaw SJ. The Fracture Resistance of a Toughened Epoxy Adhesive. *The Journal of Adhesion*. 1981;12(1):59 - 77.
- [30] Yan C, Mai YW, Ye L. Effect of Bond Thickness on Fracture Behaviour in Adhesive Joints. *The Journal of Adhesion*. 2001;75(1):27 - 44.
- [31] Tong L, Steven GP. Analysis and Design of Structural Bonded Joints. Kluwer Academic Publishers. 1999.
- [32] da Silva LFM, Carbas RJC, Critchlow GW, Figueiredo MAV, Brown K. Effect of material, geometry, surface treatment and environment on the shear strength of single lap joints. *International Journal of Adhesion and Adhesives*;In Press, Accepted Manuscript.
- [33] Gledhill RA, Shaw SJ, Tod DA. Durability of adhesive-bonded joints employing organosilane coupling agents. *International Journal of Adhesion and Adhesives*. 1990;10(3):192-198.
- [34] Crocombe AD. Stress analyses. in *Adhesive Bonding Science, Technology and Applications* Edited by RD Adams Woodhead Publishing Limited. 2005.
- [35] Johnson WS. Stress analysis of the cracked-lap-shear specimen - An ASTM round-robin *Journal of Testing and Evaluation*. 1987;15:303-324.
- [36] Papini M, Fernlund G, Spelt JK. The effect of geometry on the fracture of adhesive joints *Int J Adhes Adhes*. 1994;14(1):5-13.
- [37] Ashcroft IA, Wahab MMA, Crocombe AD, Hughes DJ, Shaw SJ. The effect of environment on the fatigue of bonded composite joints. Part 1: testing and fractography. *Composites Part A: Applied Science and Manufacturing*. 2001;32(1):45-58.
- [38] Tong L, Luo Q. Analysis of cracked lap shear joints. in *Modeling of Adhesively Bonded Joints*, edited by Martins-da Silva LF and Ochsner A Springer. 2008.
- [39] Brussat TR, Chiu ST, Mostovoy S. *Fracture Mechanics for Structural Adhesive Bonds*. AFML-T77-163, Air Force Materials Laboratory, Wright Patterson. 1977.
- [40] Yeh-Hung L, Rakestraw MD, Dillard DA. The cracked lap shear specimen revisited--a closed form solution. *International Journal of Solids and Structures*. 1996;33:1725-1743.
- [41] Goland M, Reissner E. The stress in cement joints. *Journal Applied Mechanics*. 1944;66(A-17).
- [42] Davies P. CD. Fatigue and durability of marine composites. in *Fatigue in Composites*, Edited by Harris B, Woodhead Publishing Limited. 2000:709-729.

- [43] Van Paepegem W, Degrieck J. Effects of Load Sequence and Block Loading on the Fatigue Response of Fiber-Reinforced Composites. *Mechanics of Advanced Materials and Structures*. 2002;9(1):19 - 35.
- [44] Degrieck J, Van Paepegem W. Fatigue damage modeling of fibre-reinforced composite materials: Review. *Applied Mechanics Reviews*. 2001;54(4):279-300.
- [45] Lemaitre J, Sermage JP, Desmorat R. A two scale damage concept applied to fatigue *International Journal of Fracture*. 1999;97:67-81.
- [46] Chaboche JL. Continuum Damage Mechanics: Present State and Future Trends *Nucl Eng Des* 1987;1987(105).
- [47] Lemaitre J. How to use damage mechanics *Nuclear Engineering and Design*. 1984;80:133-245.
- [48] Ashcroft IA. Fatigue. in *Adhesive Bonding Science, Technology and Applications* Edited by RD Adams Woodhead Publishing Limited. 2005.
- [49] Crocombe AD, Richardson G. Assessing stress state and mean load effects on the fatigue response of adhesively bonded joints. *International Journal of Adhesion and Adhesives*. 1999;19(1):19-27.
- [50] Palmgren A. Die lebensdauer von kugellagern. *VDI-Zeitschrift*. 1924;68(339-341).
- [51] Miner M. Cumulative damage in fatigue. *Journal of Applied Mechanics*. 1945;12:159-164.
- [52] Erpolat S, Ashcroft IA, Crocombe AD, Abdel-Wahab MM. A study of adhesively bonded joints subjected to constant and variable amplitude fatigue. *International Journal of Fatigue*. 2004;26(11):1189-1196.
- [53] Marco SM, Starkey WL. A concept of fatigue damage. *Transactions of the American Society of Mechanical Engineers*. 1954;76:626-662.
- [54] Owen MJ, Howe RJ. The accumulation of damage in a glass-reinforced plastic under tensile and fatigue loading. *Journal of Physics D: Applied Physics*. 1972;5:1637-1649.
- [55] Gathercole N, Reiter H, Adam T, Harris B. Life prediction for fatigue of T800/5245 carbon-fibre composites: I. Constant-amplitude loading. *International Journal of Fatigue*. 1994;16(8):523-532.
- [56] Adam T, GN, Reiter H, Harris B. Life prediction for fatigue of T800/5245 carbon-fibre composites. II. Variable-amplitude loading. *Int J Fatigue*. 1994;8:533-547.
- [57] Jen-Ming HR, Lee CH. Strength and life in thermoplastic composite laminates under static and fatigue loads. Part II:. *International Journal of Fatigue*. 1998;20(9):617-629.
- [58] Zhang Y, Vassilopoulos AP, Keller T. Stiffness degradation and fatigue life prediction of adhesively-bonded joints for fiber-reinforced polymer composites. *International Journal of Fatigue*. 2008;30(10-11):1813-1820.
- [59] Van Paepegem W, Degrieck J. A new coupled approach of residual stiffness and strength for fatigue of fibre-reinforced composites. *International Journal of Fatigue*. 2002;24(7):747-762.
- [60] Taheri-Behrooz F, Shokrieh MM, Lessard LB. Residual stiffness in cross-ply laminates subjected to cyclic loading. *Composite Structures*. 2008;85(3):205-212.
- [61] Joris Degrieck AWVP. Fatigue damage modeling of fibre-reinforced composite materials: Review. *Applied Mechanics Reviews*. 2001;54(4):279-300.
- [62] Yang JN, Lee LJ, Sheu DY. Modulus reduction and fatigue damage of matrix dominated composite laminates. *Composite Structures*. 1992;21(2):91-100.
- [63] Whitworth HA. Cumulative Damage in Composites. *Journal of Engineering Materials and Technology*. 1990;112(3):358-361.

- [64] Whitworth HA. A stiffness degradation model for composite laminates under fatigue loading. *Composite Structures*. 1997;40:95-101.
- [65] Yao WX, Himmel N. A new cumulative fatigue damage model for fibre-reinforced plastics. *Composites Science and Technology*. 2000;60(1):59-64.
- [66] Hosoi A, Kawada H, Yoshino H. Fatigue characteristics of quasi-isotropic CFRP laminates subjected to variable amplitude cyclic two-stage loading. *International Journal of Fatigue*. 2006;28(10):1284-1289.
- [67] Schaff JR, Davidson BD. Life Prediction Methodology for Composite Structures. Part I--Constant Amplitude and Two-Stress Level Fatigue. *Journal of Composite Materials*. 1997;31:128-157.
- [68] Erpolat S, Ashcroft IA, Crocombe AD, Abdel-Wahab MM. Fatigue crack growth acceleration due to intermittent overstressing in adhesively bonded CFRP joints. *Composites Part A: Applied Science and Manufacturing*. 2004;35(10):1175-1183.
- [69] Paris PC, Erdogan F. A critical analysis of crack propagation laws. *Trans ASME D*. 1963;85:528-535.
- [70] Shivakumar K, Chen H, Abali F, Le D, Davis C. A total fatigue life model for mode I delaminated composite laminates. *International Journal of Fatigue*. 2006;28(1):33-42.
- [71] Ashcroft IA. A simple model to predict crack growth in bonded joints and laminates under variable-amplitude fatigue. *The Journal of Strain Analysis for Engineering Design*. 2004;39(6):707-716.
- [72] Xu XX, Crocombe AD, Smith PA. Fatigue Crack Growth Rates in Adhesive Joints Tested at Different Frequencies. *The Journal of Adhesion*. 1996;58(3):191 - 204.
- [73] Al-Ghamdi A, Ashcroft IA, Crocombe AD, Abdel-Wahab MM. Crack growth in adhesively bonded joints subjected to variable frequency fatigue loading. *The Journal of Adhesion*. 2003;73:1161-1182.
- [74] Mall S, Ramamurthy G, Rezaizadeh MA. Stress ratio effect on cyclic debonding in adhesively bonded composite joints. *Composite Structures*. 1987;8(1):31-45.
- [75] Pirondi A, Nicoletto G. Fatigue crack growth in bonded DCB specimens. *Engineering Fracture Mechanics*. 2004;71(4-6):859-871.
- [76] Schon J, Starikov R. Fatigue of joints in composite structures. in *Fatigue in Composites*, Edited by Harris B, Woodhead Publishing Limited. 2003:621-643.
- [77] Abou-Hamda MM, Megahed MM, Hammouda MMI. Fatigue crack growth in double cantilever beam specimen with an adhesive layer. *Engineering Fracture Mechanics*. 1998;60(5-6):605-614.
- [78] Mall S, Ramamurthy G. Effect of bond thickness on fracture and fatigue strength of adhesively bonded composite joints. *International journal of adhesion and adhesives*. 1989;9(1):33-37.
- [79] Choupani N. Mixed-mode cohesive fracture of adhesive joints: Experimental and numerical studies. *Engineering Fracture Mechanics*. 2008;75(15):4363-4382.
- [80] Xu XX, Crocombe AD, Smith PA. Mixed-mode fatigue and fracture behaviour of joints bonded with either filled or filled and toughened adhesive. *International Journal of Fatigue*. 1995;17(4):279-286.
- [81] Ashcroft IA, Shaw SJ. Mode I fracture of epoxy bonded composite joints 2. Fatigue loading. *International Journal of Adhesion and Adhesives*. 2002;22(2):151-167.



- [82] Pirondi A, Nicoletto G. Mixed Mode I/II fatigue crack growth in adhesive joints. *Engineering Fracture Mechanics*. 2006;73(16):2557-2568.
- [83] Johnson AA. Impact Fatigue - An Emerging Field of Study. *Engineering Integrity*. 2004;15:14-20.
- [84] Report of the Commission Appointed to Enquire into the Application of Iron to Railway Structures. London. 1849.
- [85] Stanton TE, Bairstow L. The resistance of materials to impact,. *Proceedings of the Institute of Mechanical Engineers*. 1908:889-919.
- [86] Hertzberg RW. *Deformation and Fracture Mechanics of Engineering Materials*. Published by Wiley & Sons, New York, 4th edition. 1996.
- [87] Schrauwen B, Peijs T. Influence of Matrix Ductility and Fibre Architecture on the Repeated Impact Response of Glass-Fibre-Reinforced Laminated Composites. *Applied Composite Materials*. 2002;9(6):331-352.
- [88] Jang B. P. KW, Jang B. Z. Impact Behavior and Impact-Fatigue Testing of Polymer Composites *Composites Science and Technology* 1992;44(2):107-118.
- [89] Khosrovaneh AK, Dowling NE. Fatigue loading history reconstruction based on the rainflow technique. *International Journal of Fatigue*. 1990;12(2):99-106.
- [90] Bezemer AA, Guyt CB, Vlot A. New impact specimen for adhesives: optimization of high-speed-loaded adhesive joints. *International Journal of Adhesion and Adhesives*. 1998;18(4):255-260.
- [91] ASTM-D950-2003. Standard test method for impact strength of adhesive bonds. 2003.
- [92] ISO-11343:2003. Adhesives. Determination of dynamic resistance to cleavage of high-strength adhesive bonds under impact conditions, wedge impact method.
- [93] Adams RD, Harris JA. A critical assessment of the block impact test for measuring the impact strength of adhesive bonds. *International Journal of Adhesion and Adhesives*. 1996;16(2):61-71.
- [94] B. R. K. Blackman AJK, A. C. Taylor and Y. Wang. The impact wedge-peel performance of structural adhesives *Journal of Materials Science*. 2000;35:1867-1884.
- [95] Clark G, Saunders DS. Morphology of impact damage growth by fatigue in carbon fibre composite laminates. *Materials Forum* 1991;15(4):333-342.
- [96] Ramkumar RL. Effect of low-velocity impact damage on the fatigue behaviour of graphite/epoxy laminates. in 'Long Term Behaviour of Composites', ASTM STP 813, Ed TK O'Brien, ASTM, Philadelphia USA. 1983:116-135.
- [97] Hosur MV, Waliul-Islam SM, Vaidya UK, Kumar A, Dutta PK, Jeelani S. Dynamic punch shear characterization of plain weave graphite/epoxy composites at room and elevated temperatures. *Composite Structures*. 2005;70(3):295-307.
- [98] Hosur MV, Waliul ISM, Vaidya UK, Dutta PK, Jeelani S. Experimental studies on the punch shear characterization of satin weave graphite/epoxy composites at room and elevated temperatures. *Materials Science and Engineering A*. 2004;368(1-2):269-279.
- [99] Hiley MJ, Dong L, Harding J. Effect of strain rate on the fracture process in interlaminar shear specimens of carbon fibre-reinforced laminates. *Composites Part A: Applied Science and Manufacturing*. 1997;28(2):171-180.
- [100] Lifshitz JM, Leber H. Response of fiber-reinforced polymers to high strain-rate loading in interlaminar tension and combined tension/shear. *Composites Science and Technology*. 1998;58(6):987-996.
- [101] Hosur M.V. AA, Jeelani S., Vaidya U. K. . Studies on the Influence of Through-the-Thickness Reinforcement on Low-Velocity and High Strain Rate

- Response of Woven S2-Glass/Vinyl Ester Composites *Journal of Composite Materials*. 2001;35(12):1111-1133.
- [102] Wyrick D. A. ADF. Residual Strength of a Carbon/Epoxy Composite Material Subjected to Repeated Impact. *Journal of Composite Materials*. 1988;22(8):749-765.
- [103] Ding YQ, Yan Y, McIlhagger R. Effect of impact and fatigue loads on the strength of plain weave carbon-epoxy composites. *Journal of Materials Processing Technology*. 1995;55:58-62.
- [104] Harris B. A historical review of the fatigue behaviour of fibre-reinforced plastics. in *Fatigue in Composites*, Edited by Harris B, Woodhead Publishing Limited. 2000.
- [105] Sanchez-Saez S, Barbero E, Zaera R, Navarro C. Compression after impact of thin composite laminates. *Composites Science and Technology*. 2005;65(13):1911-1919.
- [106] Hosur MV, Adya M, Alexander J, Jeelani S, Vaidya U, Mayer A. Studies on Impact Damage Resistance of Affordable Stitched Woven Carbon/Epoxy Composite Laminates. *Journal of Reinforced Plastics and Composites*. 2003;22(10):927-952.
- [107] Potter KD, Schweickhardt F, Wisnom MR. Impact Response of Unidirectional Carbon Fibre Rod Elements with and without an Impact Protection Layer. *Journal of Composite Materials*. 2000;34(17):1437-1455.
- [108] Sinmazçelik T, Arıcı AA, Günay V. Impact-fatigue behaviour of unidirectional carbon fibre reinforced polyetherimide (PEI) composites. *Journal of Materials Science*. 2006;41(19):6237-6244.
- [109] Bora MÖ, Çoban O, Sinmazçelik T, Cürgül I, Günay V. On the life time prediction of repeatedly impacted thermoplastic matrix composites. *Materials & Design In Press*. 2009;30(1):145-153.
- [110] Çoban O, Bora MÖ, Sinmazçelik T, Cürgül I, Günay V. Fracture morphology and deformation characteristics of repeatedly impacted thermoplastic matrix composites. *Materials & Design In Press*. 2009;30(3):628-634.
- [111] Ding Y.Q. YY, McIlhagger R. Effect of impact and fatigue loads on the strength of plain weave carbon-epoxy composites. *Journal of Materials Processing Technology*. 1995;55:58-62.
- [112] Yuanjian T, Isaac DH. Combined impact and fatigue of glass fiber reinforced composites. *Composites Part B*. 2007;39(3):505-512.
- [113] Yuan Q. FK, Karger-Kocsis J. Low-energy charpy impact of interleaved CF/EP laminates *Applied Composite Materials*. 1995;2(2):19-133.
- [114] Khan B, Rao R, Venkataraman N. Low Velocity Impact Fatigue Studies on Glass Epoxy Composite Laminates with Varied Material and Test Parameters-Effect of Incident Energy and Fibre Volume Fraction *Journal of Reinforced Plastics and Composites*. 1995;14(11):1150-1159.
- [115] Ray D, Sarkar BK, Bose NR. Impact fatigue behaviour of vinylester resin matrix composites reinforced with alkali treated jute fibres. *Composites Part A: Applied Science and Manufacturing*. 2002;33(2):233-241.
- [116] Roy R. SBK, Rana A. K., Bose, N. R. Impact fatigue behaviour of carbon fibre-reinforced vinylester resin composites *Bulletin of Materials Science*. 2001;24(1):79-86.
- [117] Ming-Hsiung H. HJR, Doong J.L, Fung G.P. Impact fatigue of a polycarbonate/acrylonitrile-butadiene-styrene blend. *Polymer Engineering & Science*. 1999;39(4):708-720.

- [118] Schrauwen B. PT. Influence of Matrix Ductility and Fibre Architecture on the Repeated Impact Response of Glass-Fibre-Reinforced Laminated Composites Applied Composite Materials. 2002;9:331-352.
- [119] Azouaoui K, Rechak S, Azari Z, Benmedakhene S, Laksimi A, Pluvinae G. Modelling of damage and failure of glass/epoxy composite plates subject to impact fatigue. International Journal of Fatigue. 2001;23(10):877-885.
- [120] Hampson PR, Moatamedi M. A review of composite structures subjected to dynamic loading. International Journal of Crashworthiness. 2007;12(4):411 - 428.
- [121] Hou JP, Petrinic N, Ruiz C, Hallett SR. Prediction of impact damage in composite plates. Composites Science and Technology. 2000;60(2):273-281.
- [122] Hou JP, Petrinic N, Ruiz C. A delamination criterion for laminated composites under low-velocity impact. Composites Science and Technology. 2001;61(14):2069-2074.
- [123] Changliang Z, Mingfa R, Wei Z, Haoran C. Delamination prediction of composite filament wound vessel with metal liner under low velocity impact. Composite Structures. 2006;75(1-4):387-392.
- [124] Chang FK, Chang KY. A Progressive Damage Model for Laminated Composites Containing Stress Concentrations. Journal of Composite Materials. 1987;21(9):834-855.
- [125] Hyung Yun C, Chang F-K. A Model for Predicting Damage in Graphite/Epoxy Laminated Composites Resulting from Low-Velocity Point Impact. Journal of Composite Materials. 1992;26(14):2134-2169.
- [126] Maranon A. Characterising delamination in composite materials PhD Thesis, Loughborough University, Loughborough. 2005.
- [127] Aymerich F, Dore F, Priolo P. Prediction of impact-induced delamination in cross-ply composite laminates using cohesive interface elements. Composites Science and Technology. 2008;68(12):2383-2390.
- [128] Guinard S, Allix O, Guedra-Degeorges D, Vinet A. A 3D damage analysis of low-velocity impacts on laminated composites. Composites Science and Technology. 2002;62(4):585-589.
- [129] Williams JG. Fracture Mechanics of Polymers. E Horwood. 1984.
- [130] Adams GC. Impact Fatigue of Polymers Using an Instrumented Drop Tower Device. Instrumented Impact testing of plastics and Composite Materials, *ASTM ST, SL* Kessler, GC Adams, SB Driscoll, and DR Ireland, Eds, ASTM, philadelphia, 1987, . 1987:pp 281-301.
- [131] A. I. Gomaa AHHaAM. Subcritical crack propagation under cyclic stress impulse International Journal of Fracture. 1992;53:187-199.
- [132] Maekawa I SH. Characteristic property of impact fracture toughness. . JSME Int J A 1995;38(1):80-83.
- [133] Ming-Hsiung Ho J-RHJ-LDC-PF. Impact fatigue of a polycarbonate/acrylonitrile-butadiene-styrene blend. Polymer Engineering & Science. 1999;39(4):708-720.
- [134] Yamamoto I, Higashihara T, Kobayashi T. Effect of Silica-Particle Characteristics on Impact/Usual Fatigue Properties and Evaluation of Mechanical Characteristics of Silica-Particle Epoxy Resins. JSME Int Journal Ser A Solid Mech Mater Eng Soc Mech Engineers). 2003;46(2):145-153.
- [135] Ninomi M, Uway K, Kobayashi K, Okahara A. Impact Fatigue Properties of Epoxy Resin Filled with SiO<sub>2</sub> Particles. Engineering Fracture Mechanics. 1991;38(6):439-449.

- [136] Harris J. ARD. An Assessment of the Impact Performance of Bonded Joints for Use in High Energy Absorbing Structures Proc Inst Mech Eng C, Mech Eng Sci. 1985;199(C2):121-131.
- [137] Beevers A. EMD. Impact Behavior of Bonded Mild Steel Lap Joints. Int J Adhes Adhes. 1984;4(1):13-16.
- [138] Kihara K, Isono H, Yamabe H, Sugibayashi T. A study and evaluation of the shear strength of adhesive layers subjected to impact loads. International Journal of Adhesion and Adhesives. 2003;23(4):253-259.
- [139] Yokoyama T. Experimental determination of impact tensile properties of adhesive butt joints with the split Hopkinson bar The Journal of Strain Analysis for Engineering Design. 2003;38(3):233-245.
- [140] Yokoyama T, Shimizu H. Evaluation of Impact Shear Strength of Adhesive Joints with the Split Hopkinson Bar. JSME international journal Series A, Solid mechanics and material engineering. 1998;41(4):503-509.
- [141] Crocombe AD. Modelling and predicting the effects of test speed on the strength of joints made with FM73 adhesive. International Journal of Adhesion and Adhesives. 1995;15(1):21-27.
- [142] Goglio L, Peroni M, Rossetto M. Effect of the Strain Rate on the Mechanical Behaviour of Epoxy Adhesives Key Engineering Materials. 2007;347:671-676.
- [143] Sato C, Ikegami K. Dynamic deformation of lap joints and scarf joints under impact loads. International Journal of Adhesion and Adhesives. 2000;20(1):17-25.
- [144] Sun C, Thouless MD, Waas AM, Schroeder JA, Zavattieri PD. Ductile-brittle transitions in the fracture of plastically deforming, adhesively bonded structures. Part II: Numerical studies. International Journal of Solids and Structures. 2008;45(17):4725-4738.
- [145] Bandyopadhyay S. Review of the Microscopic and Macroscopic Aspects of Fracture of Unmodified and Modified Epoxy Resins Materials Science and Engineering A. 1990;125(2):157-184.
- [146] Maugis D. Subcritical crack growth, surface energy, fracture toughness, stick-slip and embrittlement. Journal of Materials Science. 1985;20(9):3041-3073.
- [147] Kinloch AJ, Williams JG. Crack blunting mechanisms in polymers. Journal of Materials Science. 1980;15(4):987-996.
- [148] Ashcroft IA, Hughes DJ, Shaw SJ. Mode I fracture of epoxy bonded composite joints: 1. Quasi-static loading. International Journal of Adhesion and Adhesives. 2001;21(2):87-99.
- [149] Usui Y. SO. Impact Fatigue Strength of Adhesive Joints Bull Jpn Soc Precis Eng. 1984;18(3):213-218.
- [150] Imanaka M, Kishimoto W, Okita K, Nakayama H, Shirato M. On the Impact Fatigue Strength of Adhesive-Bonded Lap Joint. Journal Society of Material Science Japan. 1985;34(386):1296-1300.
- [151] Vaidya UK, Gautam ARS, Hosur M, Dutta P. Experimental-numerical studies of transverse impact response of adhesively bonded lap joints in composite structures. International Journal of Adhesion and Adhesives. 2006;26(3):184-198.
- [152] Johnson AA, Storey R. The impact fatigue properties of iron and steel. Journal of Sound and Vibration. 2007;308(3-5):458-466.
- [153] Yu J, Peter K, Huang M. The impact-fatigue fracture of metallic materials JOM Journal of the Minerals, Metals and Materials Society. 1999;51(4):1543-1851.
- [154] Tanaka T, Kinoshita KI, Nakayama H. Effect of Loading Time on High-Cycle Range Impact Fatigue Strength and Impact Fatigue Crack Growth Rate. JSME

- International Journal Series A, Solid Mechanics and Material Engineering. 1992;35(1):108-116.
- [155] Briançon C, Sigety P, G'Sell C. In situ study of matrix strain in carbon/resin composite materials. *Composites Science and Technology*. 1996;56(7):835-840.
- [156] Beland S. High Performance Thermoplastic Resins and Their Composites. 1991.
- [157] Hegeler H, Brückner R. Mechanical properties of carbon fibre-reinforced glasses. *Journal of Materials Science*. 1992;27(7):1901-1907.
- [158] Alcoa. Alloy 7075 plate and sheet.
- [159] Nelson LJ. The effect of environment and loading rate on the mechanical properties of an epoxy film adhesive. Final project, University of Bath, London. 1999.
- [160] Erpolat S. Variable amplitude fatigue loading of adhesively bonded joints. PhD Thesis, Loughborough, Loughborough University. 2004.
- [161] Zhang Z, Yao D, Shang JK. Fatigue Crack Initiation in Solder Joints. *Journal of Electronic Packaging*. 1996;118(2):41-44.
- [162] Zhang Z, Shang JK, Lawrence FV. A Backface Strain Technique for Detecting Fatigue Crack Initiation in Adhesive Joints. *The Journal of Adhesion*. 1995;49(1):23 - 36.
- [163] Shenoy V, Ashcroft IA, Critchlow GW, Crocombe AD, Abdel Wahab MM. An investigation into the crack initiation and propagation behaviour of bonded single-lap joints using backface strain. *International Journal of Adhesion and Adhesives*; In Press, Corrected Proof.
- [164] Crocombe AD, Ong CY, Chan CM, Wahab MMA, I.A. A. Investigating Fatigue Damage Evolution In Adhesively Bonded Structures Using Backface Strain Measurement. *The Journal of Adhesion*. 2002;78:745-776.
- [165] Camanho PP, Tavares CML, de Oliveira R, Marques AT, Ferreira AJM. Increasing the efficiency of composite single-shear lap joints using bonded inserts. *Composites Part B: Engineering*. 2005;36(5):372-383.
- [166] da Silva L, Öchsner A. Modeling of adhesively bonded joints. Springer, Hildeberg. 2008.
- [167] Chung J, Hulbert GM. A family of single-step Houbolt time integration algorithms for structural dynamics. *Computer Methods in Applied Mechanics and Engineering*. 1994;118(1-2):1-11.
- [168] Knops B. Numerical Simulation of Crack Growth in Pressurized Fuselages. Doctoral thesis, Faculty of Aerospace Engineering, Delft University of Technology, The Netherlands. 1994.
- [169] Ashcroft IA, Hughes DJ, Shaw SJ. Adhesive bonding of fibre reinforced polymer composite materials. *Assembly Automation*. 2000;20:150-161.
- [170] Bishop SMG, R B. Fatigue Crack Growth in Adhesively-Bonded and Co-Cured CFRP Joints Bonding and Repair of Composites; Birmingham; UK; 14 July 1989. 1989:67-74.
- [171] O.Takeshi. The fatigue of toughened epoxy polymers. PhD Thesis, Imperial College of Science, London. 1999.
- [172] Yee DL, A. F., Chen I-W, Chang S-C, Takahashi K. Fracture behaviour of unmodified and rubber-modified epoxies under hydrostatic pressure *Journal of Materials Science*. 1994;29:2205-2215.
- [173] Abdel Wahab MM, Ashcroft IA, Crocombe AD, Shaw SJ. Prediction of fatigue thresholds in adhesively bonded joints using damage mechanics and fracture mechanics. *Journal of Adhesion Science and Technology*. 2001;15(7).
- [174] Slepian LI. Models and Phenomena in Fracture Mechanics. Springer. 2002.

- [175] Moskala EJ. Effects of mean stress and frequency on fatigue crack propagation in rubber-toughened polycarbonate/copolyester blends. *Journal of Applied Polymer Science*. 1993;49(1):53-64.
- [176] Jethwa JK. The fatigue performance of adhesively-bonded metal joints. PhD Thesis, Imperial College of Science, London. 1995.



